Galaxy Clusters and Their Role in Galaxy Evolution

Galaxy Clusters and Their Role in Galaxy Evolution

By Ian Roberts
MSc. (McMaster University, Hamilton ON)
BSc. (Mount Allison University, Sackville NB)

A Thesis Submitted to the School of Graduate Studies in the Partial Fulfillment of the Requirements for the Degree Doctor of Philosophy

McMaster University
Doctor of Philosophy (2020)
Hamilton, Ontario (Physics & Astronomy)

TITLE: Galaxy Clusters and Their Role in Galaxy Evolution
AUTHOR: Ian Roberts (McMaster University)
SUPERVISOR: Dr. Laura Parker
NUMBER OF PAGES: xxi, 253

Abstract

Galaxy clusters are the most-massive, collapsed, galaxy environments in the Universe, and they exist along a spectrum of dynamical state and virialization. Such extreme environments extend the range of physical processes that we can study relevant to galaxy evolution. Therefore, galaxy clusters are important laboratories to advance our understanding of galaxy evolution.

With optical and X-ray observations, along with dark matter only simulations, we test methods for classifying galaxy cluster dynamical state. We show that the shape of the member-galaxy redshift distribution, for a given cluster, is a useful proxy for cluster dynamical state which correlates with cluster X-ray morphology. Applying these classifications to simulated clusters, we show that unrelaxed clusters have experienced recent major mergers as well as active accretion of new galaxies. We also present evidence for enhanced star formation in galaxies within unrelaxed clusters, compared to counterparts in relaxed systems. This trend is likely connected to the shorter times-since-infall for galaxies in unrelaxed clusters.

Interactions between galaxies and the intracluster medium (ICM) play an important role in quenching galaxy star formation. With a sample of SDSS clusters, and archival X-ray observations from the *Chandra* observatory, we investigate galaxy star formation as a function of ICM density. For all masses, the quenched fraction of galaxies increases with ICM density. For low-mass galaxies, there is evidence for enhanced quenching in the densest cluster regions, consistent with ram pressure stripping. To further probe ram pressure in clusters, we use high-resolution imaging to search for galaxies undergoing stripping in the Coma cluster. We present $\sim$40 ram pressure stripping candidates, which are consistent with being stripped on their first infall toward the Coma centre. These galaxies show enhanced star formation rates, suggesting that gas compression from ram pressure may be catalyzing star formation.

Environmentally-driven quenching in galaxy clusters is a function of both, both how long a galaxy has been part of a cluster, and how efficiently cluster processes quench galaxies. The former is informed by accurate characterization of cluster dynamical state, and the latter by detailed studies of quenching mechanisms as a function of galaxy mass, both of which are focal points of this work.

Acknowledgements

First, and foremost, a huge thanks to Dr. Laura Parker for your excellent supervision over the years. Thank you for creating an environment for success, for giving me the freedom to work on the research I found most compelling, and for your infectious enthusiasm and excitement for science which has made these past six years incredibly enjoyable. I look forward to the future collaborations to come. To my supervisory committee, Dr. Bill Harris and Dr. James Wadsley, thank you for always providing sound scientific advice and guidance. Thank you to the McMaster Physics & Astronomy Department, all of the faculty and staff, and especially, all of my friends and colleagues. I've enjoyed every minute of it. I wouldn't be here without the endless support from my family over the years, I look forward to being the only "real" doctor in the family. Most importantly, thank you Ashley for all of your love and support. You make everything better.

Contents

List of Figures

List of Tables

Abbreviations

ΛCDM	Cosmological model with cosmological constant and cold dark matter
AD	Anderson-Darling
AGN	Active galactic nucleus (nuclei)
AIC	Akaike information criterion
BCG	Brightest cluster galaxy
BPL	Broken power-law
B/T	Bulge-to-total
CAS	Concentration-asymmetry-clumpiness
CDF	Cumulative distribution function
CFHT	Canada-France-Hawaii Telescope
CGP	Central galaxy paradigm
CMB	Cosmic microwave background
CRS	Cluster red sequence
DM	Dark matter
FoF	Friends-of-friends
G	Gaussian
HD	Hellinger Distance
IFU	Integral field unit
IMF	Initial mass function
IR	Infrared
ICL	Intracluster light
ICM	Intracluster medium
ISM	Interstellar medium
LOS	Line of sight
MCMC	Markov chain Monte Carlo
MM	Major merger

MMG	Most-massive galaxy
MMP	Most-massive progenitor
MDPL2	MultiDark Planck 2
NFW	Navarro-Frenk-White
NG	Non-Gaussian
PPS	Projected phase space
PSF	Point spread function
S/N	Signal-to-noise ratio
SAM	Semi-analytic model
SDSS	Sloan digital sky survey
SED	Spectral energy distribution
SFH	Star formation history
SFMS	Star-forming main sequence
SFR	Star formation rate
SHMR	Stellar-to-halo mass relation
SMBH	Supermassive black hole
SN	Supernova
SPL	Single power-law
sSFR	Specific star formation rate
SZ	Sunyaev-Zeldovich
UV	Ultraviolet
VDP	Velocity dispersion profile
XRW	X-ray weak

Co-authorship

Chapters 2, 3, 4, 5, 6 of this thesis contain original scientific research written by myself, Ian Roberts. Chapter 2 has been published as a peer-reviewed journal article in the Monthly Notices of the Royal Astronomical Society (MNRAS). The citation for this work is: Roberts I.D., Parker L.C., Hlavacek-Larrondo J., 2018, MNRAS, Volume 475, Issue 4, pp. 4704-4716. This work was co-authored with my supervisor, Dr. Laura Parker. The third author, Dr. Julie Hlavacek-Larrondo, assisted in the X-ray astronomy analysis which was necessary for this work. Chapter 3 has been published as a peer-reviewed journal article in MNRAS. The citation for this work is: Roberts I.D., Parker L.C., 2019, MNRAS, Volume 490, Issue 1, pp. 773-783. This work was co-authored with my supervisor, Dr. Laura Parker. Chapter 4 has been published as a peer-reviewed journal article in MNRAS. The citation for this work is: Roberts I.D., Parker L.C., 2017, MNRAS, Volume 467, Issue 3, pp. 3268-3278. This work was co-authored with my supervisor, Dr. Laura Parker. Chapter 5 has been published as a peer-reviewed journal article in the Astrophysical Journal. The citation for this work is: Roberts I.D., Parker L.C., Brown T., Joshi G.D., Hlavacek-Larrondo J., Wadsley J., 2019, ApJ, Volume 873, Issue 1, pp. 42-57. This work was co-authored with my supervisor, Dr. Laura Parker. The third author, Dr. Toby Brown, derived spectrally-stacked HI gas scaling relations. The fourth and six authors, Dr. Gandhali Joshi and Dr. James Wadsley, ran the simulations required for extracting theoretical galaxy infall velocity distributions. The fifth author, Dr. Julie Hlavacek-Larrondo, assisted in the X-ray astronomy analysis necessary for this work. Chaper 6 has been published as a peer-reviewed journal article in MNRAS. The citation for this work is: Roberts I.D., Parker L.C., 2020, MNRAS, Volume 495, Issue 1, pp. 554-569. This work was co-authored with my supervisor, Dr. Laura Parker. I hereby grant an irrevocable, non-exclusive license to McMaster University and Library and Archives Canada to reproduce the material as part of this thesis.

Stay inside 'til somebody finds us
Do whatever the TV tells us
Stay inside our rosy-minded fuzz

So worry not
All things are well
We'll be alright
We have our looks and perfume on

The National (2007). *Boxer*. Beggars Banquet Records.

1 | Introduction

1.1 The ΛCDM Universe

1.1.1 Cosmological Parameters

The leading model describing the formation and evolution of large-scale structure in the Universe is the *Lambda Cold Dark Matter* (ΛCDM) model, which describes a universe experiencing accelerating expansion, dominated by dark energy (Λ) and cold-dark matter (CDM) (e.g. Mather et al., 1990; Riess et al., 1998; Perlmutter et al., 1999; Planck Collaboration et al., 2018). The Universe began with the "big bang", ∼13.8 Gyr ago (Planck Collaboration et al., 2018), and has been expanding and cooling from this initial hot, dense state since. Initial elemental abundances (primarily hydrogen and helium) were set by big bang nucleosynthesis in the early Universe, and predictions from a hot big bang model agree well with observed elemental abundances (Alpher, Bethe, and Gamow, 1948). Heavier elements (e.g. carbon, nitrogen, oxygen, etc.) were eventually synthesized by generations of massive stars (Wagoner, Fowler, and Hoyle, 1967). As the Universe continued to expand and cool, free electrons combined with protons to form neutral atoms and the Universe became optically thin. The light from this epoch was then able to travel freely, encoded with information on the conditions of the early Universe. As the Universe continued to expand, these ultraviolet (UV) photons were redshifted and eventually observed as the Cosmic Microwave Background radiation (CMB, Penzias and Wilson 1965).

Many observations support this concordance model, but key to this picture was the discovery of the CMB radiation and detailed measurements of the power-spectrum of the CMB fluctuations (COBE, Mather et al. 1990; WMAP, Hinshaw et

al. 2003; Planck, Planck Collaboration et al. 2014). The positions and amplitudes of acoustic peaks in the CMB power spectrum provide tight constraints on the key components of our Universe and their relative contributions (Peebles and Yu, 1970; Sunyaev and Zeldovich, 1970; Hu and Dodelson, 2002). These contributions are commonly parametrized with the density parameter

$$\Omega(z) = \frac{\rho_i(z)}{\rho_c(z)} \tag{1.1}$$

where $\rho_i(z)$ is the density of each individual component (dark energy, matter, radiation) as a function of redshift, z, and $\rho_c(z)$ is the critical density of the Universe. The critical density is the total density (dark energy + matter + radiation) required for a flat Universe, and is given by

$$\rho_c(z) = \frac{3H^2(z)}{8\pi G} \tag{1.2}$$

where H is the Hubble parameter which describes the rate of the expansion of the Universe, and G is Newton's gravitational constant. A present-day value of the Hubble constant (H_0) of $67.66\,\mathrm{km\,s^{-1}\,Mpc^{-1}}$ (Planck Collaboration et al. 2018, however also see e.g. Riess et al. 2019) gives a present-day critical density of

$$\rho_{c,0} = 1.27 \times 10^{11}\,\mathrm{M_\odot\,Mpc^{-3}} = 8.60 \times 10^{-30}\,\mathrm{g\,cm^{-3}}. \tag{1.3}$$

Present-day values of the density parameters for dark energy and matter are (Planck Collaboration et al., 2018)

$$\Omega_{\Lambda,0} = 0.6889 \pm 0.0056$$
$$\Omega_{m,0} = 0.3111 \pm 0.0056.$$

The sum of the density parameters is consistent with unity, therefore the Universe appears flat to high precision. Note in this standard ΛCDM it is assumed that the current radiation contribution is negligible relative to dark energy and matter. That said, the relative contributions of different cosmological components have varied throughout the history of the Universe. Dark energy is consistent with a cosmological constant (e.g. Alam et al., 2017), and therefore the density has no

redshift dependence, ie. $\rho_\Lambda(z) = \rho_{\Lambda,0}$ for all z. The density of the matter and radiation components scale with redshift as

$$\rho_m = \rho_{m,0}\,(1+z)^3 \tag{1.4}$$

$$\rho_r = \rho_{r,0}\,(1+z)^4. \tag{1.5}$$

While radiation is negligible at low redshift, at much higher redshift radiation played an important role in driving the dynamics of the Universe. Finally, the matter component (Ω_m) consists of contributions from baryonic (Ω_b) and dark matter (Ω_c), which have present-day values of $\Omega_{b,0} = 0.04897 \pm 0.00031$ and $\Omega_{c,0} = 0.26067 \pm 0.00199$ (assuming $h = 0.6766$, Planck Collaboration et al. 2018). The "normal" baryonic matter only accounts for $\sim 5\%$ of the energy density budget of the Universe and 95% of the Universe is in the form of dark matter and dark energy.

1.1.2 Structure Formation

In a perfectly homogeneous Universe, structure formation would not be possible. However, quantum fluctuations present in the very early Universe were amplified to macroscopic scales, likely through inflation (Guth, 1981; Linde, 1982), providing seeds for structure growth. These fluctuations are now readily observed as inhomogeneities in the CMB, and have given rise to the formation of galaxies and large-scale structure in the Universe (e.g. Peebles, 1965; Zeldovich, 1972; Peebles, 1980). Density fluctuations, δ, can be described at any point in space or redshift relative to the mean density

$$\delta(\vec{x}, z) = \frac{\rho_m(\vec{x}, z) - \bar{\rho}_m(z)}{\bar{\rho}_m(z)}, \tag{1.6}$$

where $\rho_m(\vec{x}, z)$ is the matter density at a given point in space and redshift, and $\bar{\rho}_m(z)$ is the mean matter density at a given redshift. The initial density pertubations are well described by a Gaussian random field, and initially the overdensities grow according to linear theory while $\delta << 1$ (Press and Schechter, 1974). Above a critical value, $\delta_c \sim 1.686$, overdensities decouple from the linear growth and collapse non-linearly, eventually forming virialized halos (Press and Schechter, 1974).

The timescale for a region to cease expansion and begin collapse is the turnaround time, $t_{\rm turn}$, and a halo will virialize at $\sim 2 \times t_{\rm turn}$ (e.g. Peebles, 1980). Fluctuations on small scales have larger amplitudes and will reach δ_c first and collapse early. Larger structure is built up through merging and the coallescence of smaller halos, which is known as the "bottom-up" growth of structure in the Universe. As the Universe continues to expand, and overdensities continue to grow, larger and larger structures surpass the overdensity required for collapse and virialization. While galaxy-mass halos collapsed and formed primarily at $z \gtrsim 3$, galaxy cluster halos are collapsing and virializing primarily at $z \lesssim 1$ (Mo and White, 2002; Springel et al., 2005).

The structure of the Universe is homogeneous on very large scales ($\gtrsim$ few hundred Mpc, Ntelis et al. 2017), however structure on smaller scales is not smoothly distributed. Instead, structure forms into the "cosmic web" (Bond, Kofman, and Pogosyan, 1996). Galaxies are preferentially found along narrow filaments and sheets, with the nodes of intersecting filaments as sites of galaxy clusters. This filamentary structure is separated by underdense "voids" where the number density of galaxies is relatively low (e.g. Bond, Kofman, and Pogosyan, 1996; Cautun et al., 2014). The cosmic web has been observed by large galaxy redshift surveys (e.g. York et al., 2000; Colless et al., 2001; Driver et al., 2009) and is also ubiquitous in large-box cosmological simulations (Springel et al., 2005; Vogelsberger et al., 2014; Crain et al., 2015; Klypin et al., 2016). Fig. 1.1 shows the distribution of low-redshift galaxies in the Sloan Digital Sky Survey (SDSS), where this cosmic web structure is clearly apparent. On smaller scales, filaments between galaxies and around galaxy clusters have been observed through ionized gas in the X-ray (Connor et al., 2018) as well as weak lensing tracing the dark matter distribution (Epps and Hudson, 2017). Cosmic filaments are dynamic structures which drive flows of gas and galaxies, fueling accretion onto galaxy groups and clusters at the nodes of the cosmic web (e.g. Cautun et al., 2014).

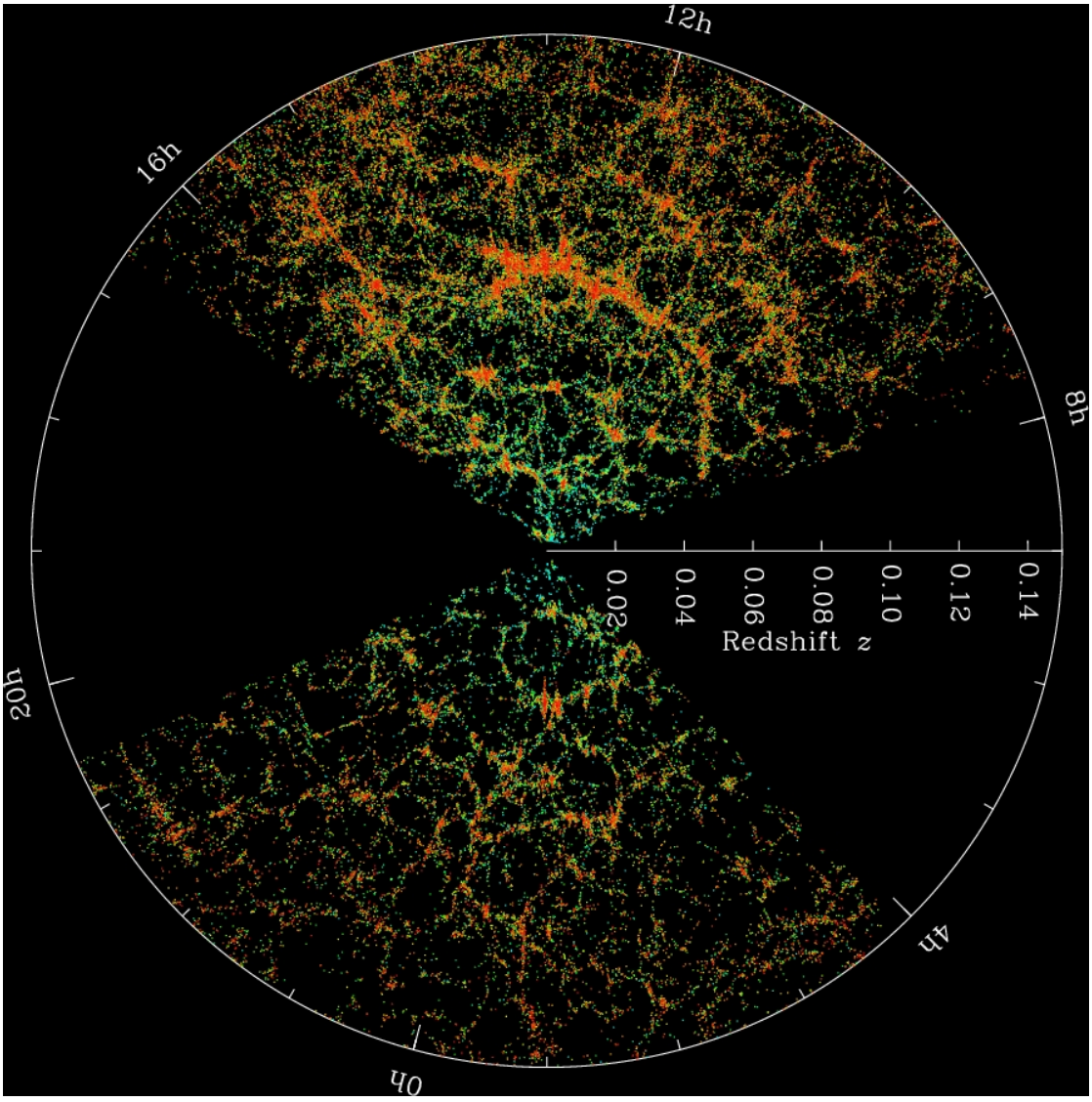

FIGURE 1.1: Distribution of low-redshift galaxies in a slice of the Sloan Digital Sky Survey, showing the structure of filaments and voids comprising the cosmic web. The map extends out to a redshift of $z = 0.15$ or a luminosity distance of $\sim$700 Mpc. *Credit: SDSS.*

1.2 Galaxies

1.2.1 Composition

Galaxies are collections of stars, gas, and dust, embedded within a common dark matter halo. It is the interplay of these components, and the galaxy environment, that ultimately drive the growth and evolution of galaxies.

The largest contributer to the overall mass of a galaxy is dark matter. Dark matter does not interact via electromagnetism, therefore inferring dark matter properties observationally is challenging. Despite this, dark matter properties can be constrained through indirect observations. For rotationally dominated galaxies, the rotational velocity of stars and gas is determined by the total mass enclosed within the orbit of a tracer (e.g. Sofue and Rubin, 2001). For dispersion dominated galaxies the observed line widths of stellar absorption features are used as a probe for the galaxy mass (e.g. Binney and Tremaine, 2008). Additionally, for both early- and late-type galaxies, globular clusters, planetary nebula, or dwarf satellites can be used as tracers of the dark matter potential in order to compute a dynamical mass (e.g. Deason et al., 2012; Posti and Helmi, 2019). In order to estimate the mass of dark matter in galaxies with these methods, spectroscopic observations out to large distances from the galactic center, where the dark matter halo dominates the total mass, are necessary. Alternatively, gravitational lensing also probes galaxy dark matter masses. Dark matter masses from strong gravitational lensing are available for ∼100s of galaxies (e.g. Bolton et al., 2008). The weak lensing signal for individual galaxies is too small to detect, however weak lensing measurements for many galaxies can be stacked to increase the signal and constrain the average dark matter properties of the galaxy stack. Both cosmological simulations as well as weak lensing surveys show clear correlations between galaxy stellar and dark matter mass (Hudson et al., 2015; Matthee et al., 2017), therefore rough estimates of galaxy dark matter masses can be obtained with the observed stellar mass coupled to a stellar-to-halo mass relation.

The stellar component of galaxies is primarily traced by photometric observations and absorption spectroscopy in the rest-frame optical or near-infrared (IR). Stellar emission peaks at $\sim 1\,\mu$m (see Fig. 1.2), therefore galaxy luminosities in

near-IR filters are effective stellar mass tracers. When fluxes have been measured in many photometric filters, stellar masses can be obtained by fitting the galaxy spectral energy distribution (SED, see Section 1.2.2 for a more complete discussion of SED fitting). Stellar masses of galaxies in large surveys within the local Universe typically range between $\sim 10^9$ and $\sim 10^{11}\,\mathrm{M}_\odot$. This lower mass limit is simply a product of the detection limits of large surveys. Nearby galaxies in the Local Group (the Milky Way, M31, and their satellites) are observed with stellar masses $\lesssim 10^6\,\mathrm{M}_\odot$ (McConnachie, 2012), and the shape of the stellar mass function at this low-mass end is still relatively unconstrained.

The gaseous component comprises a multiphase interstellar medium (ISM) made up of warm/hot ionized gas, cool atomic gas, and cold, dense molecular gas. All phases are dominated ($\sim 90\%$) by hydrogen. The warm/hot ionized gas is the most difficult phase of the ISM to measure observationally. In principle this hot ionized gas is detected through X-ray continuum emission, but given the sensitivity limits of current X-ray telescopes as well as the soft X-ray background from the Milky Way, such observations are only feasible for very massive galaxies. Alternatively, this diffuse material can be probed through UV and X-ray absorption spectroscopy with bright active galactic nuclei (AGN) as back-lights (e.g. Yao et al., 2008; Gupta et al., 2012). The cooling of this warm/hot halo gas onto the galactic disc can be an important source of future star-forming gas for galaxies.

The neutral component of the ISM consists of primarily atomic (HI) and molecular hydrogen (H_2). Atomic hydrogen is directly traced through the 21 cm spin flip transition in the hydrogen atom. Emission from this transition is optically thin, therefore the 21 cm luminosity is directly proportional to the atomic hydrogen mass within the observed region (e.g. Roberts, 1962; Catinella et al., 2010). The colder, molecular hydrogen component is rarely observed directly, instead requiring tracer molecules to measure its abundance. The most common tracer of molecular hydrogen is the carbon monoxide (CO) molecule, which has a relative abundance to molecular hydrogen in the ISM of $\sim 1:10\,000$ (e.g. Bolatto, Wolfire, and Leroy, 2013). It is assumed that emission from CO rotational transitions trace the distribution of molecular gas, and therefore the observed CO luminosity, L_{CO},

is converted to a mass of molecular hydrogen, M_{H_2}, as

$$M_{H_2} = \alpha_{CO}\, L_{CO} \tag{1.7}$$

where α_{CO} is the so-called CO-H_2 conversion factor. In practice, the value of α_{CO}, as well as its variation across different types of galaxies and dependence on local metallicity, is a major source of uncertainty (see Bolatto, Wolfire, and Leroy 2013 for a review). Emission from the CO molecule traces ISM gas densities of $\gtrsim 100\,\mathrm{cm}^{-3}$ (Tielens, 2005), denser molecular hydrogen is probed through higher density tracers such as the HCN and HCO^+ molecules (Shirley, 2015).

The ratio of cold-gas to dust in the ISM is on the order of 100:1 (e.g. Cortese et al., 2016). Despite this relatively low abundance, dust plays an important role in catalyzing the conversion of atomic to molecular hydrogen, which in turn is vital for star formation. Dust in galaxies is typically observed with the extinction of UV and optical light, or through mid- and far-IR continuum emission. Given the connection between dust and the creation of molecular hydrogen, dust emission is used as another tracer of the underlying molecular gas distribution within galaxies (e.g. Groves et al., 2015).

The emission of light from these galaxy components span the entire electromagnetic spectrum. This highlights the importance of multiwavelength observations for understanding the interplay of these various components as well as the overall evolution of galaxies.

1.2.2 Star Formation

Star formation in galaxies is closely tied to the gas cycle within the host. The majority of cold-gas mass ($\lesssim$ a few hundred Kelvin) in star-forming galaxies is HI (Saintonge et al., 2017), however it is actually the H_2 gas which is directly tied to star formation. In dense regions of the galaxy, the conversion of atomic to molecular gas becomes efficient as atomic hydrogen cools. The primary sites of star formation in galaxies are cold ($\sim 10 - 20\,\mathrm{K}$), dense molecular clouds which typically have sizes $\gtrsim 10\,\mathrm{pc}$ and masses $\gtrsim 10^4\,\mathrm{M}_\odot$ (André et al., 2014). Dense regions (clumps) in these molecular clouds, the progenitors of stellar clusters and associations, are able to efficiently cool further, first forming dense pre-stellar cores

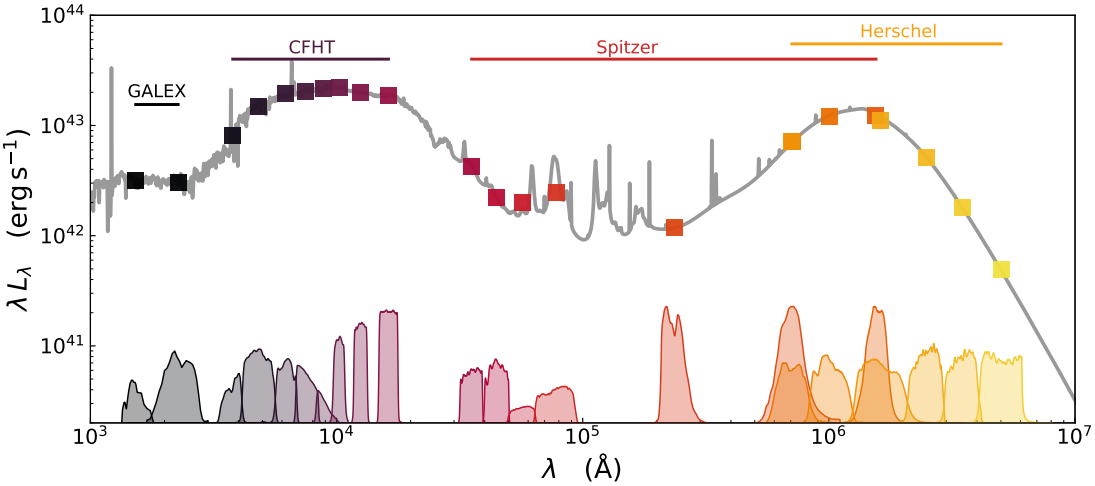

FIGURE 1.2: Model spectrum for a star-forming galaxy from the UV to the far-IR (grey), generated with the BAGPIPES[1] code (Carnall et al., 2018). Filter curves for photometric bands from various telescopes ranging from the ultraviolet to the far-infrared are shown at the bottom of the panel. Square data points show the model fluxes for each filter, which are used to construct a model galaxy SED.

(~ 0.1 pc in size, André et al. 2014) and then eventually stars. Stars are not all formed of the same mass, but instead as a spectrum of masses known as the initial mass function (IMF) – the shape of which may be largely universal across different galaxies (e.g. Bastian, Covey, and Meyer, 2010). According to the empirical stellar IMF, most stars are formed with masses between $\sim 0.5 - 1\,M_\odot$, with more massive stars ($\gtrsim 5\,M_\odot$) being far more rare (Kroupa, 2001; Chabrier, 2003). The lifetimes of stars decrease with increasing mass, meaning that rare, massive stars have the shortest lifetimes. Most stellar mass in galaxies is made up of relatively old, low-mass stars with masses $\sim 0.5 - 1\,M_\odot$. Stellar luminosity scales with mass as $L \sim M^{3.5}$, therefore young, high-mass stars account for a large fraction of galaxy luminosity in star-forming galaxies. High-mass stars have emission that peaks at UV wavelengths, whereas the low-mass stars, which trace galaxy stellar masses, peak at $\sim 1\,\mu$m in the near-IR.

Star Formation Rate Indicators

The level of ongoing star formation in galaxies is measured with the star-formation rate (SFR), defined as the number of solar masses worth of stars that a given galaxy forms in a year. Observationally, SFRs are almost always inferred by observing, either directly or indirectly, young, massive stars in galaxies. Because the lifetimes of massive stars are so short ($\lesssim$100 Myr), the presence of massive stars in a galaxy is an excellent indicator of recent star formation. If there has not been recent star formation within a galaxy then the signatures of massive stars will not be observed. Due to dust extinction within galaxies, SFR indicators are often split into one of two classes: 1. Unobscured (by dust) indicators, and 2. Obscured indicators. These SFR tracers sample various regions of the galaxy SED, and for reference I show a model SED in Fig. 1.2. Below I will introduce a number of the most common methods for estimating SFRs observationally. For a more detailed description see the review by Kennicutt and Evans (2012).

Galaxy Colour. The colour of a galaxy is given by the magnitude difference of the galaxy measured in two filters. Typically this is done with a "blue" and a "red" optical filter, for example, SDSS g-r colours are very common. Another common colour, which incorporates near-UV information is NUV-r. Galaxy colours are used as approximate SFR indicators due to the fact that galaxies with active star formation emit large amounts of short wavelength flux which will result in bluer colours. Conversely, galaxies with no star formation will be dominated by flux at red and near-IR wavelengths and therefore will show red colours. The largest uncertainty when using optical colours as SFR indicators is the effect of dust reddening, which if uncorrected can cause a galaxy to have a relatively red colour despite strong star formation. NUV-r colours are generally considered the best filter combination for tracing SFR due to the large baseline separating the "blue" and "red" filters, however this colour is very sensitive to the presence of dust.

UV Continuum. Massive stars emit primarily in the UV region of the electromagnetic spectrum, and therefore the UV luminosity of a galaxy is an excellent tracer of the unobscured SFR. If the SFR is high, then more massive stars, and in turn more UV photons, are produced leading to a high UV luminosity. For

galaxies with little-to-no ongoing star formation, very few massive stars will be present and the UV luminosity will be correspondingly decreased. Dust strongly absorbs in the UV, and reradiates this energy as IR photons. Therefore the UV luminosity is only capturing UV radiation which has not been absorbed by dust, which may only be a fraction of the total emission within the galaxy. To address this, UV star formation indicators are paired with indicators tracing the emission obscured by dust (such as IR luminosity, see below) in order to account for both the obscured and unobscured components of the SFR.

Hα Emission Line. The most common emission line SFR indicator used in the local Universe is the Hα recombination line. Hα is a spectral line in the Hydrogen Balmer series corresponding to an electron transition from the $n = 3 \rightarrow n = 2$ level, producing a photon at 656.28 nm. Partially ionized HII regions are produced by star formation in galaxies via UV photoionization. These HII regions host a wealth of hydrogen recombination events, producing large Hα line fluxes as recombined electrons cascade down toward the ground state. Similar to the UV continuum, the largest uncertainty for Hα SFRs is the effect of dust obscuration. The ratio between the Hα and Hβ ($n = 4 \rightarrow n = 2$) lines, known as the "Balmer decrement" is often used to estimate the degree of dust obscuration, and therefore correct Hα SFRs. Since the shorter wavelength Hβ line is more strongly influenced by dust than Hα, the ratio between the two is sensitive to the amount of dust present. Hα SFRs are typically measured through rest-frame optical spectroscopy, either via one integrated measurement for a galaxy, or resolved across individual galaxies with integral field unit (IFU) spectroscopy. Hα fluxes can also be estimated with narrow-band photometry, however typical narrow-band filters include both the Hα and [NII] emission lines. Furthermore, careful continuum subtraction must be performed to remove contamination from the rest-frame r-band.

At higher redshift, the Balmer lines are shifted out of the visible range, and other emission lines such as [OII] or [CII] are more commonly used as SFR indicators (Kennicutt and Evans, 2012).

IR Continuum. UV radiation from massive stars is absorbed by dust and re-emitted in the IR, making the IR dust continuum a useful tracer of this obscured star formation. Dust emits as a modified black-body curve in galaxy SEDs from

roughly 10 to 1000 μm, peaking at $\sim$100 μm. 24 μm emission has been established as a reliable SFR indicator (e.g. Kennicutt and Evans, 2012), as it probes warm dust heated by young stars. The total-IR luminosity can also be estimated, which in turn is strongly correlated with SFR. Many calibrations between photometric bands along the dust curve and total-IR luminosity have been derived for this purpose (e.g. Galametz et al., 2013). While total-IR luminosities and SFRs can be derived with a single photometric band, estimates of the total-IR luminosity are more accurate with the inclusion of multiple filters (Galametz et al., 2013) – however this often comes at the cost of resolution. The largest uncertainty in IR SFRs is the fact that IR luminosity is only tracing emission from massive stars reprocessed by intervening dust. This will miss emission along lines-of-sight which are optically thin to UV photons. For very dusty star-forming galaxies, IR SFRs will accurately trace the total galaxy star formation, otherwise IR estimators need to be calibrated against, or combined with, unobscured tracers.

Radio Continuum. The radio continuum consists of a free-free component originating from photoionized HII regions, and synchrotron emission for which the primary source is charged particles from supernovae (SNe). With multi-frequency radio data, this free-free component can be separated from the synchroton (Murphy et al., 2011) in order to provide an unobscured photoionization-based SFR indicator. Due to the long wavelength of emission, the free-free radio continuum avoids the complication of dust attenuation which is present for Balmer line tracers. At lower frequencies where the radio continuum is dominated by synchrotron emission, calibrations with SNe rates, and therefore SFRs, have also been developed (Murphy et al., 2011).

SED Fitting. All of the SFR indicators described above target specific regions of the galaxy SED, however it is also possible to derive SFRs by fitting the SED with stellar population templates. Galaxy SEDs are a collection of fluxes for a galaxy measured at a number of different wavelengths along the galaxy spectrum (see Fig. 1.2), ideally ranging from the UV to the far-IR. SED fitting assumes that galaxy spectra correspond to the flux-weighted sum of the spectra from the individual stars making up the galaxy (allowing for the reprocessing of stellar light by

dust). By combining an assumed IMF, stellar population templates, stellar evolution tracks, dust distributions, nebular emission models, etc., one can produce model galaxy spectra. These spectra can then be convolved with the filter-curves of interest to generate model SEDs which are then compared to observations. The best-fit model SED contains a wealth of information, including stellar masses, SFRs, star-formation histories (SFHs), metallicities, dust content, etc. SED SFRs are most accurate when derived from photometric bands spanning a wide baseline from the UV to the far-IR. This ensures that important galaxy spectral features are well captured, such as the UV continuum, 4000 Å break, stellar continuum, and the dust curve. SED fitting also introduces assumptions, for example with regards to dust extinction laws or star formation histories (SFHs), which can introduce substantial uncertainties (e.g. Walcher et al., 2011). Traditionally, SFHs were assumed to follow simple parametric forms such as exponential, lognormal, or power-law (e.g. Gladders et al., 2013; Carnall et al., 2019), however comparison to simulations has shown that SFHs can be more complex than is captured by simple parametric desciptions (Leja et al., 2019). Recently, flexible SFH models have become popular as they are capable of capturing a wide range of galaxy SFHs, while not relying on strong assumptions regarding the SFH functional form (e.g. Leja et al., 2019).

Finally, a persistent source of uncertainty for most SFR tracers is contamination due to the presence of AGN emission. UV and Hα flux from AGN can contaminate unobscured SFR tracers, and dust heating from AGN can affect IR SFR tracers. AGN contamination will be strongest in the central regions of high-mass galaxies (where AGN are most prevalent), and accurate masking of strong AGN regions in galaxies is crucial for accurate SFRs.

1.2.3 Morphology

The first systematic classification scheme for galaxy morphologies was published by Hubble (1926). This classification scheme (see Fig. 1.3), colloquially known as Hubble's tuning fork, divides galaxies into elliptical and spiral galaxies. Elliptical galaxies are further subdivided by ellipticity, $e = 0, 1, 2, ..., 7$, where $e = 10 \times (a - b)/a$ and a, b are the major and minor axes of the ellipse. E0 is then a

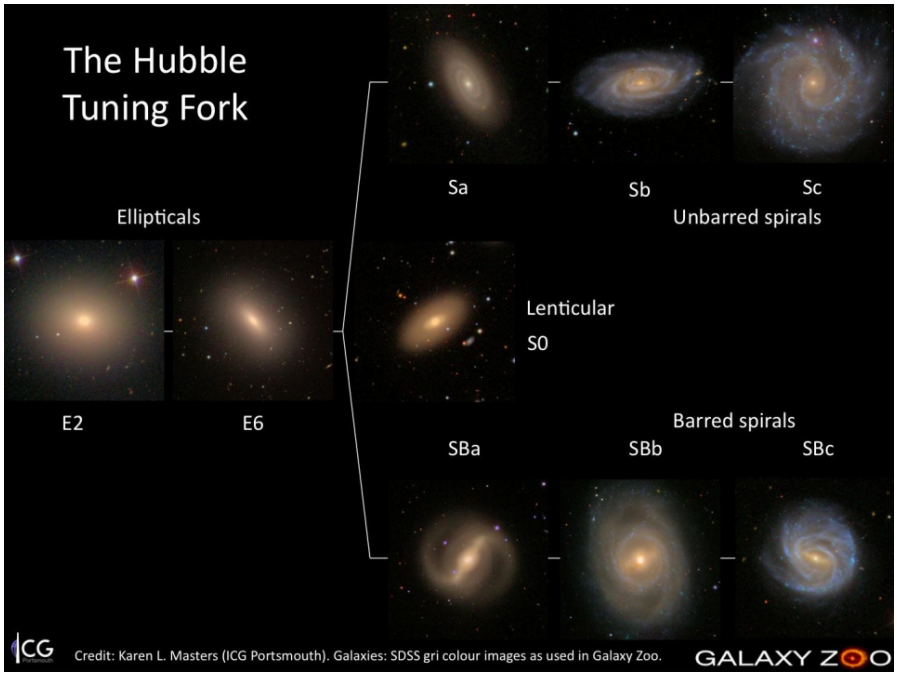

FIGURE 1.3: Hubble's tuning fork diagram of galaxy morphology. *Credit: Karen L. Masters/Galaxy Zoo/SDSS.*

perfectly round galaxy and E7 corresponds to a highly ellongated ellipse. Some of the differences in shape between E0 and E7 galaxies may not be intrinsic, and instead due to projection effects. Spiral galaxies are subdivided into Sa, Sb, and Sc spiral galaxies. Sa corresponds to galaxies with bright central bulges and tight spiral arms, Sc corresponds to galaxies with weak/no bulges and loose spiral arms, and Sb is intermediate to the two. Similar SBa, SBb, SBc classes exist for barred spiral galaxies. S0 or lenticular galaxies in this classification correspond to smooth disc galaxies with no strong spiral arms, and finally, a class for irregular galaxies is often included for galaxies that do not fall into any of the previous classes. Following the original nomenclature from Hubble, elliptical and S0 galaxies are referred to as "early types" and spiral galaxies as "late types". This nomenclature refers only to the positions on the tuning fork diagram and not to any evolutionary sequence (Hubble, 1926).

The earliest techniques for classifying galaxy morphologies were via visual classifications (see Hubble 1926, or more recently, Nair and Abraham 2010). While visual classifications are able to accurately classify galaxy morphology, the time

consuming nature of this practice make it difficult to apply visual classifications to large modern galaxy surveys. Despite this, citizen science projects such as the Galaxy Zoo[2] (Lintott et al., 2008) have made the application of visual classifications to large surveys increasingly viable. Furthermore, advancements in deep learning techniques have led to machine learning derived "visual" classifications which are trained on simulated data and human visual classifications. These deep learning morphologies agree well with human classifications and can be efficiently applied to large data sets (e.g. Domínguez Sánchez et al., 2018). With the advent of large photometric galaxy surveys, many quantitative measures of galaxy structure and morphology have been developed to complement these more qualitative classifications. Examples of quantitative morphological measures include the Sérsic index, bulge-to-total ratio, concentration-asymmetry-clumpiness (CAS, Conselice 2003) classifications, and Gini-M_{20} classifications (Abraham, van den Bergh, and Nair, 2003; Lotz, Primack, and Madau, 2004).

Sérsic Index. The Sérsic index, n, is a free parameter of the Sérsic profile which is commonly fit to galaxy surface brightness profiles. The mathematical form (Sérsic, 1963) of the Sérsic profile is given by

$$\mu(r) = \mu_e + b_n \left[\left(\frac{r}{r_e} \right)^{1/n} - 1 \right] \tag{1.8}$$

where $\mu(r)$ is the galaxy surface brightness as a function of radius, μ_e is the surface brightness at the effective radius, r_e, which encloses half of the total light, and b_n is a pre-factor which depends on the Sérsic index n. Disc galaxies have light profiles which are well fit by small Sérsic indices, with the standard exponential disc given by $n = 1$. In comparison, elliptical galaxies have light profiles which are well fit by larger Sérsic indices. The de Vaucouleurs profile, which has proven to be a good fit for elliptical galaxies (e.g. Vincent and Ryden, 2005), is given by $n = 4$. Sérsic indices are derived from azimuthally averaged surface brightness profiles, and therefore are excellent for capturing the average, smooth component of galaxy light profiles, however may not accurately capture irregular or asymmetric components. For example, spiral arm features are not captured by Sérsic profiles.

[2] `https://www.zooniverse.org/projects/zookeeper/galaxy-zoo/`

Bulge-to-Total Ratio. As opposed to modeling galaxies as a single component, as is the case for the single Sérsic profile, it is common to model galaxy light distributions as a two-component bulge+disc distribution. The bulge and disc components are modelled with separate Sérsic profiles, often assuming an $n = 1$ exponential disc and an $n = 4$ de Vaucouleurs bulge, though it is also possible to model the Sérsic indices for the bulge and disc as free parameters. The best fit Sérsic models can then be integrated to give the total light in the bulge and disc components, and then the bulge-to-total (B/T) ratio is given by the ratio of the bulge flux to the total galaxy flux (bulge+disc). Given that late-type galaxies are dominated by light from the disc component, and early-type galaxies are dominated by light from the bulge component, the B/T ratio is a useful morphological discriminator. For purely elliptical galaxies the B/T ratio will approach unity, and for purely disc galaxies this ratio will approach zero. While in many cases the B/T ratio provides a better model of galaxy light profiles than single Sérsic fits, it is still an axisymmetric model and therefore does not capture asymmetric components such as spiral arms.

CAS System. A three-parameter morphological classification system commonly used to quantify the stellar light distribution of galaxies is the CAS system. The three CAS parameters measure the concentration (C), asymmetry (A), and clumpiness (S) of galaxy stellar light. The concentration is estimated from the sizes of concentric apertures which contain 20% and 80% (or sometimes 30% and 70%) of the total galaxy flux. The concentration parameter, C, is then given by

$$C = 5 \log \left(\frac{r_{80}}{r_{20}} \right) \tag{1.9}$$

where r_{20} and r_{80} are the radii of apertures enclosing 20% and 80% of the total galaxy flux. Elliptical galaxies have typical concentrations from $4 - 5$ and disc galaxies have concentrations ranging from $3 - 4$ (Conselice, 2014).

The asymmetry parameter is measured by taking the difference between the galaxy image and an image of the galaxy rotated by 180°. The sum of the resulting residual map is then an estimate of the galaxy asymmetry. The asymmetry

parameter, A, is given by

$$A = \min\left(\frac{\sum |I_0 - I_{180}|}{\sum |I_0|}\right) - A_{\rm bkg} \tag{1.10}$$

where I_0 is the original galaxy flux image, I_{180} is the galaxy image after a rotation by 180°, and $A_{\rm bkg}$ is a measure of the asymmetry measured over a blank background region. The asymmetry parameter is a quantitative measure of the fraction of a galaxy's flux which is contained in asymmetric components. For elliptical galaxies the asymmetry typically ranges from $0 - 0.05$ and for spiral galaxies between $0.05 - 0.20$ (Conselice, 2014).

Finally, the clumpiness (smoothness) parameter is a measure of the fraction of a galaxy's light which is within clumpy distributions. This is measured by spatially filtering the galaxy images to emphasize the light at high spatial frequencies. The clumpiness parameter, S, is computed as

$$S = 10 \times \left[\left(\frac{\sum (I_{x,y} - I^{\sigma}_{x,y})}{\sum I_{x,y}}\right) - S_{\rm bkg}\right] \tag{1.11}$$

where $I_{x,y}$ is the original image, $I^{\sigma}_{x,y}$ is a blurred version of the original image, and $S_{\rm bkg}$ is the clumpiness parameter measured on a blank sky background region. The width of the smoothing kernel, σ, is determined by the size of the galaxy (Conselice, 2014). The resultant image, $I_{x,y} - I^{\sigma}_{x,y}$, is essentially the original image after filtering with a high-pass filter, leaving only the high-frequency, clumpy components. Elliptical galaxies typically have clumpiness values of ~ 0, whereas disc galaxies typically have clumpiness values between $0.1 - 0.4$ (Conselice, 2014).

Gini-M_{20}. Another multi-parameter classification scheme for galaxy morphologies is the Gini-M_{20} introduced by Abraham, van den Bergh, and Nair (2003) and Lotz, Primack, and Madau (2004). The Gini coefficient is a parameter originating from economics literature, originally used to measure the distribution of wealth across a population. In the economics context, a high Gini coefficient would correspond to a population where much of the wealth is concentrated within a small subset of the population, whereas a low Gini coefficient corresponds to a uniform wealth distribution. In the astrophysical context, the Gini coefficient measures the

homogeneity of flux distributed across galaxy pixels, and is computed as

$$G = \frac{1}{\bar{X}n(n-1)} \sum_{i=1}^{n} (2i - n - 1) X_i \tag{1.12}$$

where $i = 1, 2, 3, ..., n$ for a set of n pixel flux values X_i. A galaxy with all flux concentrated in one pixel corresponds to $G = 1$, and a galaxy with a perfectly uniform flux distribution corresponds to $G = 0$. Gini coefficients for low-redshift galaxies are typically between $0.2 - 0.6$ (Abraham, van den Bergh, and Nair, 2003), with early-type galaxies falling on the high side of this distribution and late-type galaxies falling on the low-side. The Gini coefficient was paired with the M_{20} parameter from Lotz, Primack, and Madau (2004) to form a 2D morphological plane. M_{20} measures the second-order moment of the galaxy image for the brightest pixels in the galaxy image, and is then normalized by the "total" second-order moment for the entire image. Mathematically, the second-order moment for an image is given by

$$\mu_{\rm tot} = \sum_{i=1}^{N} \mu_i = \sum_{i=1}^{n} f_i[(x_i - x_c)^2 + (y_i - y_c)^2] \tag{1.13}$$

where x_i, y_i are the coordinates of the ith pixel, f_i is the flux in the ith pixel, and x_c, y_c are the central coordinates which minimize the total moment, $\mu_{\rm tot}$. The M_{20} parameter is then determined by rank-ordering galaxy pixels by flux and then summing μ_i over the brightest pixels until the cumulative flux reaches 20% of the total flux. Finally, this parameter is normalized by the total moment, $\mu_{\rm tot}$

$$M_{20} = \log \left(\frac{\sum_i \mu_i}{\mu_{\rm tot}} \right), \text{ while } \sum_i f_i < 0.2\, f_{\rm tot}, \tag{1.14}$$

where $f_{\rm tot}$ is the total flux of the galaxy. M_{20} is particularly sensitive to bright galaxy features which are offset from the galaxy centre. Furthermore, galaxies with large negative values of M_{20} tend to have highly concentrated flux distributions where values of M_{20} closer to zero correspond to more diffuse emission.

FIGURE 1.4: X-ray-Optical composite image of the central regions of the Coma Cluster. *Credit: ESA/XMM-Newton/SDSS.*

1.3 Galaxy Clusters

Galaxy clusters are the most massive, virialized objects in the Universe. As the Universe becomes more Λ dominated, it will be harder for overdensities to grow and therefore galaxy clusters may be the most massive structures that will ever virialize (Araya-Melo et al., 2009). Galaxy clusters are collections of galaxies orbiting in a common dark matter halo, with total masses $> 10^{14}\,\mathrm{M}_{\odot}$ – the bulk of which comes from the mass of the dark matter halo. Smaller collections of galaxies ($10^{13} \lesssim M_{\mathrm{total}} \lesssim 10^{14}$) are usually referred to as galaxy groups. As such extreme environments, galaxy clusters are important laboratories to both study environmentally driven galaxy evolution (e.g. Dressler, 1984; Wetzel, Tinker, and Conroy, 2012) as well as test theories of cosmology and large-scale structure formation (e.g. Allen, Evrard, and Mantz, 2011).

1.3.1 Properties

Galaxy clusters consist of four main components, which I will outline below.

1. **The Dark Matter Halo.** The dark matter halo is the most massive component of a galaxy cluster, accounting for $\sim 90\%$ of the total cluster mass. The first evidence for dark matter in galaxy clusters dates back to Zwicky (1933) and Zwicky (1937), who showed that the dynamical mass of the Coma cluster clearly exceeds its luminous mass. Dark matter does not radiate electromagnetically, making it difficult to observe directly. Current knowledge on the existence of dark matter in galaxy clusters is derived indirectly from gravitational lensing measurements (e.g. Richard et al., 2010; Hoekstra et al., 2013) or from luminous tracers of the cluster potential well (e.g. Girardi et al., 1998; Ettori et al., 2013). N-body dark matter only simulations (e.g. Springel et al., 2005; Klypin, Trujillo-Gomez, and Primack, 2011; Klypin et al., 2016) have provided insights into the detailed structure of dark matter halos. In dark matter only simulations, halos on all scales are well fit by a Navarro-Frenk-White (NFW) profile (Navarro, Frenk, and White, 1997), which scales as $\sim r^{-1}$ at small radii and $\sim r^{-3}$ at larger radii. Other popular dark matter halo models are the Hernquist (Hernquist, 1990) and Einasto (Einasto, 1965; Merritt et al., 2006) profiles. The sizes of galaxy clusters are parametrized by the virial radius of the dark matter halo ($R_{\rm vir}$), which is approximated by R_{200}, the radius which encloses an average density equal to 200 times the critical density of the Universe. Typical sizes for galaxy clusters range from $R_{200} \simeq 1000 - 3000\,\mathrm{kpc}$, and typical dark matter masses for galaxy clusters range from $\sim 10^{14} - 10^{15}\,\mathrm{M}_{\odot}$.

2. **The Intracluster Medium.** The intracluster medium (ICM) consists of the hot, diffuse gas between galaxies in galaxy clusters. ICM gas is primarily ionized, with average temperatures ranging between $\sim 0.3 - 10\,\mathrm{keV}$ (Ota et al., 2006). The ICM is observed in the X-ray continuum through thermal bremmstrahlung emission as well as through the thermal Sunyaev-Zeldovich (SZ) effect (Sunyaev and Zeldovich, 1970; Birkinshaw, 1999). The density of the ICM increases radially toward the centre of the cluster, and ICM density profiles are typically parametrized with an isothermal β-model (Cavaliere

and Fusco-Femiano, 1976; Arnaud, 2009) which has the functional form:

$$n = n_0 \left[1 + \left(\frac{R}{R_c}\right)^2\right]^{-\frac{3}{2}\beta} \tag{1.15}$$

where n_0 is the central ICM density, R_c is the core radius, and β is the beta index. The beta model arises from the assumption that the ICM and cluster galaxies are in hydrostatic equilibrium and are isothermal. In this picture, β corresponds to the ratio of the specific energy of cluster galaxies to the specific energy of the hot gas, ie.

$$\beta \equiv \frac{\mu m_p \sigma^2}{k T_{\rm gas}} \tag{1.16}$$

where μ is the mean molecular weight, m_p is the mass of the proton, σ is the one-dimensional galaxy velocity dispersion, and $T_{\rm gas}$ is the temperature of the ICM (assumed to be roughly constant). The bulk of ICM X-ray emission originates from the central cluster regions where the ICM density is high - the X-ray luminosity, L_X, is proportional to the square of the ICM density (e.g. Ettori et al., 2013). The characteristic cluster-centric radius within which ICM X-ray emission is observed is $\sim R_{500}$, the radius which encloses an average density equal to 500 times the critical density of the Universe.

3. **Galaxies.** Rich galaxy clusters host many individual galaxies, with the population of massive galaxies ($M_\star \gtrsim 10^{10}\,{\rm M}_\odot$) numbering in the $\sim$ hundreds and the population of dwarf galaxies ($M_\star \lesssim 10^{10}\,{\rm M}_\odot$) numbering in the $\sim$ thousands (e.g. Kim et al., 2014). The total stellar mass of cluster galaxies only accounts for $\lesssim 1\%$ of the total cluster mass. Galaxies are often used as tracer particles of the cluster dark matter potential, where the observed galaxy velocity dispersion is a reliable tracer of the total cluster mass (for virialized clusters with a high number of tracer galaxies, e.g. Old et al. 2014). In typical galaxy clusters, the line-of-sight galaxy velocity dispersions range between $500 - 1500\,{\rm km\,s^{-1}}$ (Girardi et al., 1993). Galaxies are continually accreted onto galaxy clusters, and this accretion occurs preferentially via the cosmic web. Newly accreted galaxies infall with large velocity offsets from

the cluster systemic velocity, and subsequently approach the cluster velocity centroid over multiple orbits (e.g. Rhee et al., 2017). Additionally, the extreme cluster environment can strongly affect observed galaxy properties such as star formation and morphology (e.g. Wetzel, Tinker, and Conroy, 2012; Wilman and Erwin, 2012). A full discussion of these effects and the physical mechanisms driving them is given in Sections 1.4.2 and 1.4.4.

4. **Intracluster Light.** The intracluster light (ICL) is a low surface brightness, diffuse component of stellar light in clusters, made up of stars which are not bound to individual galaxies. The ICL can make up 5-20% of the stellar mass within a galaxy cluster (e.g. Burke, Hilton, and Collins, 2015; Montes and Trujillo, 2018), however, only accounts for $\lesssim 1\%$ of the total cluster mass. The ICL likely formed through stellar stripping via merging of satellite galaxies and tidal interactions during cluster assembly (e.g. Burke, Hilton, and Collins, 2015; Montes and Trujillo, 2019). In general, the distribution of ICL in clusters seems to follow the distribution of dark matter mass, making the ICL a potentially useful tracer of the cluster dark matter halo (Montes and Trujillo, 2019).

1.3.2 Cluster Finding

Among the earliest cluster-finding methods is the Friends-of-Friends (FoF) group-finding algorithm (e.g. Huchra and Geller, 1982; Press and Davis, 1982). The idea behind the FoF algorithm is that galaxies are linked together according to projected separations in distance and velocity. There are two free parameters in this algorithm, known as linking lengths. Galaxies are linked together if their separations in projected distance and velocity are less than the chosen linking lengths. Clusters are built up in this fashion as more galaxies, and groups of galaxies, are linked together. The FoF algorithm is succinctly summarized by Press and Davis (1982) in saying that all galaxy pairs are "friends" and therefore clusters are built up according to the notion that "any friend of a friend is a friend".

The FoF algorithm is very appealing in its simplicity, especially in the era of large redshift surveys (SDSS, York et al. 2000; 2dFGRS, Colless et al. 2001; GAMA, Driver et al. 2009), where it can be efficiently applied to find groups and

clusters. Additionally, it is able to generate clusters without making any assumptions about the underlying cluster properties or location. The primary shortcoming of the FoF approach is that the linking lengths have to be carefully tuned to ensure accurate identification of clusters and their member galaxies. If the linking lengths are too small there is a risk of unphysically "fracturing" a single cluster into multiple sub-groups, conversely, if the linking lengths are too large then the risk becomes "merging" multiple, physically distinct groups into one cluster (Duarte and Mamon, 2014; Campbell et al., 2015). Comparisons to mock catalogues from simulations are often used to optimize the selection of linking lengths (e.g. Nolthenius and White, 1987). FoF methods are sensitive to spectroscopic completeness and smaller systems may be missed if completeness is too low. Modern cluster finding algorithms often begin with this simple FoF approach and then incorporate phase-space distribution assumptions, variable linking lengths, iterative membership procedures, etc. and are able to reproduce cluster memberships from mock catalogues with high accuracy (e.g. Yang et al., 2005; Yang et al., 2007; Robotham et al., 2011).

While the FoF method relies on spectroscopic redshifts to generate cluster memberships, it is possible to identify galaxy clusters on the basis of rest-frame optical photometry alone. The primary method to accomplish this is known as the cluster red sequence (CRS) method (Gladders and Yee, 2000), which detects clusters with two-filter photometry. The method is based on the fact that virtually all galaxy clusters show a well defined red sequence of elliptical galaxies in colour-magnitude space, therefore it is possible to identify galaxy clusters based on collections of galaxies which are strongly clustered on the sky and also show a tight red sequence. This method is particularly resistant to projection effects as a random projection of galaxies, which are spatially clustered on the sky, will not show the tight red sequence expected for clusters. The CRS method also provides a precise photometric redshift estimate for identified clusters, as the *observed* red sequence colour is strongly redshift dependent – this arises from the fact that the *rest-frame* red sequence colour in clusters seems to be highly homogeneous from cluster to cluster (Gladders and Yee, 2000). The CRS method can be readily applied to large photometric galaxy surveys, making it an extremely efficient technique for identifying clusters. To obtain precise galaxy memberships for CRS clusters, follow-up

spectroscopy to obtain redshifts in the vicinity of the identified cluster is still necessary. Additionally, the CRS method will not work well for unevolved or low-mass systems containing a large fraction of blue galaxies.

Above I have discussed cluster finding techniques which exploit galaxies as tracers of the cluster potential well, however it is also possible to detect clusters by measuring the hot gas permeating clusters, between galaxies. This hot ($\sim 0.3 - 10\,\mathrm{keV}$) ICM is observed in two main ways: 1. X-ray continuum from bremmstrahlung emission, and 2. scattering via the Sunyaev-Zeldovich effect.

Galaxy clusters commonly display diffuse, extended X-ray emission emitted from the hot ICM, therefore galaxy clusters are identified in the X-ray by the presence of this extended emission. This technique avoids any uncertainties due to galaxy projection effects, it also naturally provides a well defined cluster centre (the peak of the X-ray emission), which is more complicated with optical cluster finding techniques. The X-ray observations need to be high enough resolution to identify extended sources, if the point-spread function (PSF) is too large then it is difficult to differentiate between diffuse cluster emission and X-ray point sources such as AGN. This becomes a more significant issue at high redshift where the angular size of galaxy clusters is relatively small. Modern, high-resolution X-ray observatories, such as *Chandra* and *XMM-Newton*, are primarily used for pointed observations, meaning that only a small fraction of the sky has been mapped by high-resolution X-ray observations. Therefore X-ray observations are more often used to confirm the presence of galaxy clusters which have been inferred from other techniques. That said, the upcoming all-sky X-ray survey, *eROSITA*, will drastically increase the number of X-ray identified clusters (Merloni et al., 2012). While most clusters are detected in the X-ray, cluster X-ray luminosities can differ substantially, even at fixed cluster mass (Stanek et al., 2006; Wang et al., 2014). Therefore samples of X-ray detected clusters are biased toward relaxed clusters with dense ICMs, and will identify fewer low-mass or unrelaxed systems.

A second method to detect the ICM in galaxy clusters is to measure the scattering of background photons off of free electrons in the cluster ICM. Electron scattering of CMB photons by galaxy clusters along the line of sight imprints a measureable distortion to the radiation spectrum of the CMB. This is known as the Sunyaev-Zeldovich (SZ) effect (Sunyaev and Zeldovich, 1970; Birkinshaw, 1999),

and is a reliable method for detecting galaxy clusters. The strongest asset of the SZ technique, and in contrast to X-ray methods, is that the sensitivity of SZ effect is independent of redshift. This makes the SZ technique especially powerful for detecting clusters (or proto-clusters) at high redshift, as the sensitivities of all other cluster finding techniques decline strongly with increasing redshift. Similar to X-ray methods, the SZ technique is also biased toward identifying large galaxy clusters with a large, dense ICM.

1.3.3 Dynamical State

Most techniques for determining cluster masses (e.g. dynamical masses, X-ray hydrostatic masses) make assumptions about the relaxed state of galaxy clusters. For galaxy clusters out of virial equilibrium, accurately estimating cluster masses, radii, velocity dispersions, etc. is incredibly difficult and these properties are often overestimated by traditional techniques (e.g. Old et al., 2018). Therefore obtaining accurate measurements of cluster properties is contingent on a detailed understanding of the cluster dynamical state. Examples of clusters which may be far from virial equilibrium include galaxy clusters still in the process of collapse and formation, and galaxy clusters which have recently experienced a merger event with another large halo. These two classes are not independent, as the cluster formation process involves many mergers with smaller group-mass halos (e.g. Kravtsov and Borgani, 2012). Clusters which have been removed from virial equilibrium, if further unperturbed, will approach equilibrium again, however the timescales to do so can be long. If two-body relaxation governs the return to equilibrium, then the timescale to return to equilibrium is likely many crossing times (Binney and Tremaine, 2008; Mo, Bosch, and White, 2010). For typical galaxy clusters, the crossing time is roughly $\sim R_{200}/\sigma_v \sim$ few Gyr. Violent relaxation can expedite this relaxation process, but dynamical perturbations may still persist over multiple crossing times (Mo, Bosch, and White, 2010).

Diagnostics of cluster dynamical state are most often performed with optical observations of galaxy distributions within the cluster, or X-ray observations of the distribution of the diffuse ICM.

X-ray Methods

A relaxed, virialized galaxy cluster is expected to have spatially symmetric X-ray emission from the diffuse ICM and the presence of an ICM cool core at the cluster centre. A cool core is a sharp density increase within the central $\sim$100 kpc of the cluster. The radiative cooling rate in the hot ICM scales with the square of the ICM density (Böhringer and Werner, 2010), therefore such a density cusp corresponds to strong radiative cooling and a subsequent decrease in gas temperature. The central regions of many galaxy clusters show decreases in ICM temperature of a factor of three or more (Böhringer and Werner, 2010). The presence of a cool core is believed to be an evolutionary indicator for galaxy clusters, where evolved, relaxed clusters will have had time to develop strong cool cores through classical cooling flows (e.g. Peterson and Fabian, 2006). In the cluster centre the ICM densities, and therefore the ICM cooling rates, are the highest. As this central gas cools, it loses energy through radiation and a subsonic inflow of gas develops in order to maintain pressure support for the overlying gas at larger radii (Fabian, 2002). This can result in collections of cool gas being deposited in a growing region at the centre of the cluster, therefore developing a central cool core. Based on the assumption that evolved, relaxed clusters will display strong cool cores, the X-ray surface brightness concentration parameter is widely used as an indicator for cluster dynamical state. This concentration parameter is computed as (Santos et al., 2008; Santos et al., 2010; Nurgaliev et al., 2013)

$$c_{SB} = \frac{S_X(R < 40\,\mathrm{kpc})}{S_X(R < 400\,\mathrm{kpc})} \tag{1.17}$$

where $S_X(R < 40\,\mathrm{kpc})$ and $S_X(R < 400\,\mathrm{kpc})$ are the X-ray surface brightnesses within 40 and 400 kpc. The X-ray concentration parameter will be highest for clusters with strongly peaked ICM density profiles, and therefore strong cool cores.

A second X-ray proxy for cluster dynamical state is the asymmetry of the diffuse cluster X-ray emission. For a relaxed cluster, the ICM will trace the virialized, symmetric halo and therefore axisymmetric X-ray emission should be observed. Disturbed, unrelaxed clusters, in particular those with recent mergers, show a much more asymmetric ICM (Nurgaliev et al., 2017). Quantitative proxies for X-ray asymmetries, such as the X-ray centroid shift (e.g. Böhringer et al., 2010) or

photon asymmetry (Nurgaliev et al., 2013), have been developed and extensively tested. Galaxy clusters with high X-ray asymmetries tend to also show low X-ray concentrations, whereas clusters with low asymmetries commonly show high concentrations and strong cool cores (Nurgaliev et al., 2013).

Optical Methods

Optical observations of cluster member galaxies can also be used to classify the dynamical state of the host cluster. These methods can be divided into dynamical measures which consider the distribution of satellite galaxies, or which consider properties of the central, brightest cluster galaxy (BCG). One of the simplest techniques, especially when working with data from redshift surveys, is to consider the shape of the projected-velocity distribution for member galaxies. This method is predicated on the fact that the one-dimensional velocity distributions for virialized clusters are well described by Maxwell-Boltzmann statistics, and therefore have a Gaussian velocity distribution (e.g. Yahil and Vidal, 1977; Bird and Beers, 1993; Hou et al., 2009). In practice, this method is implemented by constructing the spectroscopic redshift distribution for cluster member galaxies and using statistical normality tests to quantify whether the distribution is well-fit by a Gaussian. Clusters which are not well-fit by a Gaussian are considered unrelaxed, and clusters which are well-fit by a Gaussian are considered relaxed. Statistical normality tests commonly used in the literature include the Anderson-Darling test (AD, e.g. Anderson and Darling 1952; Hou et al. 2009; Hou et al. 2013) and the Hellinger Distance (HD, e.g. Ribeiro et al. 2013; de Carvalho et al. 2017). It is also common to classify cluster dynamical state with the spatial clustering of satellite galaxies, since relaxed clusters should have relatively smooth galaxy distributions whereas unrelaxed clusters may have high levels of substructure (e.g. Dressler and Shectman, 1988; Lopes et al., 2018).

A second class of optical relaxation measures consider the properties of the BCG as tracers of the cluster dynamical state. The two most common methods are the luminosity or stellar mass gap between the most massive and second most massive cluster galaxies, or to consider the offset of the position of the BCG from the cluster centre. Since the BCG should sit near the centre of the cluster potential, it will progressively grow in stellar mass by dominating gas accretion within the

cluster, and more importantly, by cannibalizing galaxies through minor mergers (e.g. De Lucia and Blaizot, 2007; Ruszkowski and Springel, 2009; McDonald et al., 2016). This BCG mass growth will therefore drive a gap between the luminosity or stellar mass of the most massive and second most massive cluster galaxies in dynamically old clusters, whereas more unrelaxed systems will have had less time to establish a dominant BCG. In clusters there is no strong consensus regarding the best observational definition of cluster centre, with the position of the BCG, the position of the X-ray peak, and the luminosity or mass-weighted centre all being common choices (e.g. George et al., 2012). For relaxed clusters these centre definitions should all be consistent with one another, however unrelaxed clusters may show significant offsets between different cluster centre choices. Many unrelaxed clusters do host BCGs with large offsets from other cluster centre definitions (e.g. Katayama et al., 2003; Sanderson, Edge, and Smith, 2009; Carollo et al., 2013; Khosroshahi et al., 2017), therefore the offset between BCG position and luminosity-weighted centre is a potentially useful measure of cluster relaxation. It is important to note that all relaxation proxies based on properties of the BCG are reliant on accurate identification of the brightest, or most massive galaxy in the cluster. This is particularly challenging for fibre-based redshift surveys, where fibre collisions in the dense cluster interior can lead to missing galaxy spectra.

1.4 Galaxy Evolution

Large, spectroscopic redshift surveys of galaxies over the past two decades, both in the local universe (e.g. the SDSS and 2dF, York et al. 2000; Colless et al. 2001) and at higher redshift (e.g. COSMOS and DEEP2, Scoville et al. 2007; Newman et al. 2013), have revolutionized the study of galaxy evolution across a wide range of environment and cosmic time. Early seminal works demonstrated that the population of passive, early-type galaxies has increased substantially over the past $\sim 5\,\mathrm{Gyr}$ (Butcher and Oemler, 1978), and that these "red and dead" galaxies are preferentially found within dense galaxy environments (Dressler, 1980). These early observational results have since been confirmed with much better statistics thanks to modern surveys containing millions of observed galaxies. The following

are the major observational results which anchor our current understanding of galaxy evolution.

1. In the local Universe, massive galaxies are preferentially early-type galaxies which are gas-poor and show little-to-no ongoing star formation, whereas, low-mass galaxies are more commonly late-type, gas-rich, with active star formation (e.g. Brinchmann et al., 2004; Baldry et al., 2006; Blanton and Moustakas, 2009; Peng et al., 2010; Kelvin et al., 2014; Brown et al., 2015).

2. Dense environments, such as groups and clusters, host a larger proportion of passive, early-type galaxies than low-density environments. This is true, to some extent, for all stellar masses, however trends with environment are strongest for low-mass galaxies (e.g. Dressler, 1980; Haines et al., 2006; Bamford et al., 2009; Blanton and Moustakas, 2009; Urquhart et al., 2010; Wetzel, Tinker, and Conroy, 2012; Wilman and Erwin, 2012; Haines et al., 2015; Brown et al., 2017).

3. The peak of star formation in the Universe occured at $z \sim 2$ and the average star formation rates of galaxies have been decreasing since then to the present day (e.g. Lilly et al., 1996; Madau, Pozzetti, and Dickinson, 1998; Whitaker et al., 2012; Madau and Dickinson, 2014).

Large efforts in galaxy evolution are now underway to understand the physical drivers of the observed trends highlighted above. For example, what physical processes are responsible for massive galaxies being less star-forming than their lower-mass counterparts? Additionally, why are galaxies in dense environments preferentially passive compared to isolated galaxies? There is a particular focus on which processes are shutting off star formation in galaxies. This cessation of galaxy star formation is commonly referred to as "quenching", a term which will be used extensively throughout this thesis. Given the connection between galaxy cold-gas and star formation, removing or heating cold-gas reserves will lead to star formation quenching. Below I will outline some of the relevant physical processes capable of affecting galaxy properties, as well as expand on these important observed trends.

1.4.1 Internal Processes

There are a number of physical processes operating within galaxies which can strongly influence observed properties. These can be feedback processes, from stars or AGN, dynamical processes affecting the stability of galaxy discs, or processes impeding gas cooling within galaxies.

Stellar Feedback. The process of star formation is self-regulating (Franco and Shore, 1984; Hopkins, Quataert, and Murray, 2011). Gas cooling and collapsing within a cloud is necessary to form new stars, however this cooling is then impeded by feedback from young stars which have recently formed. This feedback can take the form of strong stellar winds, UV heating from massive stars, and feedback from SN explosions once massive stars have reached the end of their short lifecycles (White and Frenk, 1991; Governato et al., 2007). This stellar feedback injects energy into the ISM which can radiatively and/or mechanically heat the surrounding gas, therefore limiting the efficiency of new star formation. Star formation is a clustered process, both spatially and temporally, therefore the combination of stellar winds and SN feedback from clustered massive stars will amplify the effects (e.g. Hopkins, Quataert, and Murray, 2012; Keller et al., 2014). For dwarf galaxies in particular, feedback from SN explosions may be responsible for limiting star formation over the extent of the galaxy and is often invoked to explain the low stellar-to-halo mass ratios in low-mass galaxies (e.g. Sawala et al., 2010). Simulations have shown that realistic implementations of SN feedback are required for producing simulated galaxies with sensible star formation histories (e.g. Scannapieco et al., 2012).

AGN Feedback. A second form of strong feedback, especially in high-mass galaxies, is that from AGN. AGN arise from supermassive black holes (SMBHs) at the centres of galaxies which are actively accreting surrounding material. The energy released from this accretion manifests itself in energetic jets which are launched from just outside the SMBH, or from powerful winds being driven from the accretion disk. This feedback can extend out to scales of tens or even hundreds of kiloparsecs. These jets can inject energy into the ISM over galactic scales, both

through radiative and kinetic modes, heating gas and potentially halting (or reducing) star formation (see Fabian 2012 for an observational review). Feedback from AGN is most important for galaxies with stellar masses $\gtrsim 10^{10.5}\,M_\odot$ where AGN are observed to be prevalent (e.g. Kauffmann et al., 2003; Pimbblet et al., 2013). Direct constraints on the effectiveness of AGN feedback are difficult to obtain, both through observations and simulations, largely due to the dynamic range involved from scales of a few A.U. where the jet/winds are launched out to 100s of kiloparsecs where the feedback may reach (Fabian, 2012; Wurster and Thacker, 2013). Indirect constraints on the relation between AGN and star formation are mixed, with evidence for both enhanced and suppressed star formation in galaxies hosting AGN (Santini et al., 2012; Gürkan et al., 2015; Lanzuisi et al., 2015; Mullaney et al., 2015; Stanley et al., 2015; Ellison et al., 2016). AGN emission can also contaminate common SFR estimators, further complicating the issue.

Virial Shock Heating. Analytic models and simulations predict that galaxies with dark matter masses $\gtrsim 10^{12}\,M_\odot$ support a stable halo of virial shock heated gas ($T \gtrsim 10^{5-6}\,K$, Birnboim and Dekel 2003; Cattaneo et al. 2006; Gabor and Davé 2015). Simulations suggest that long cooling times, as well as AGN feedback, allow this gas halo to remain hot over long periods, impeding gas cooling and therefore limiting star formation (Cattaneo et al., 2006; Gabor and Davé, 2015). In this model, galaxies with dark matter masses $\lesssim 10^{12}\,M_\odot$, on average, do not support a stable hot halo and therefore are able to continue to feed star formation through cold-flow accretion. Qualitatively, this is very similar to the "starvation" process described in the following section, where the hot group/cluster halo prevents gas cooling in member galaxies. Therefore a similar physical mechanism may play an important role in both the dependence of star formation on mass and environment (Gabor and Davé, 2015).

Morphological Quenching. For galaxies which transit from disc to progressively spheroidal morphologies, star formation may be quenched due to this morphological change alone, without the need for specific gas heating or removal mechanisms. Star-forming disc galaxies contain both stellar and cold-gas discs. Instabilities in the gaseous component can lead to fragmentation, collapse, and eventually star formation. The stability of galactic discs is typically described by the Toomre Q

parameter (Toomre, 1964), given by

$$Q = \frac{\kappa\sigma}{\epsilon G\Sigma}, \tag{1.18}$$

where κ is the epicyclic frequency, σ is the velocity dispersion, Σ is the surface density of the disc, and ϵ is a constant of order unity which differs for stellar vs. gaseous discs. For a two-component disc (stellar + gas), an effective Toomre Q is defined as (Jog and Solomon, 1984; Martig et al., 2009)

$$Q^{-1} = \alpha_g Q_g^{-1} + \alpha_s Q_s^{-1}, \tag{1.19}$$

where α_g and α_s are constants of order unity and Q_g, Q_s are the Toomre parameters for the gas and stellar components. It can be shown that discs with $Q \lesssim 1$ are unstable to collapse (e.g. Safronov, 1960; Toomre, 1964). For galaxies where all of the stellar mass is contained in a pressure supported spheroid you will then have $Q_s \to \infty$, and the lack of self gravity from a stellar disc can stabilize the gaseous disc against collapse (Martig et al., 2009). Therefore morphlogical quenching suggests that the transition from disc to spheroidal morphology is sufficient to stabilize the gas disc against collapse, and therefore prevent star formation. Morphological quenching still requires some mechanism to drive a morphological change within galaxies. One candidate is galaxy mergers, as both major and minor mergers are capable of transforming galaxy morphology (Mihos and Hernquist, 1994a; Mihos and Hernquist, 1994b). Additionally, dynamical instabilities such as the formation of a bar can cause substantial gas flows toward the centre of the galaxy, leading to high central mass concentration and the eventual build-up of a significant bulge component (e.g. Wyse, Gilmore, and Franx, 1997).

1.4.2 Environmental Processes

Galaxies residing in dense environments, such as massive groups and clusters, are subject to a host of physical processes which are not experienced by galaxies isolated in the field. These environmental interactions can be broadly divided into two classes: 1. Dynamical (gravitational) interactions between cluster galaxies or between galaxies and the cluster halo, and 2. Hydrodynamic interactions between

galaxies and the dense ICM. Dynamical interactions include mergers (e.g. Mihos and Hernquist, 1994a; Mihos and Hernquist, 1994b), impulsive galaxy interactions ("harassment", e.g. Moore et al. 1996), and tidal interactions (e.g. Mayer et al., 2006; Chung et al., 2007), and hydrodynamical interactions include ram pressure stripping (e.g. Gunn and Gott, 1972), viscous stripping (e.g. Nulsen, 1982), and starvation/strangulation (e.g. Larson, Tinsley, and Caldwell, 1980; Peng, Maiolino, and Cochrane, 2015). All of these physical processes are capable of driving changes in galaxy star formation and/or morphology, therefore constraining the efficiency of these various processes is necessary for a comprehensive understanding of galaxy evolution in dense enviroments. Below I will provide a brief discussion of these various environmental processes and the influence that they may have on galaxy morphology and star formation.

Mergers. Galaxy mergers are commonly divided into two classes, major and minor mergers, depending on the mass-ratio between the two galaxies. Mergers involving galaxies of similar mass ($M_1/M_2 \lesssim 3-4$) are classified as major mergers, and those involving galaxies with a large mass difference ($M_1/M_2 \gtrsim 3-4$) are considered minor mergers (Lotz et al., 2011) – also known as accretions. Major mergers are known to induce strong bursts of star formation, as is apparent for Ultra-Luminous Infrared Galaxies (ULIRGS). These extreme galaxies show some of the highest SFRs in the local Universe and are often associated with merger events. Furthermore, observations of close pairs of galaxies show enhanced star formation with decreasing pair separation, consistent with merger induced star formation (Ellison et al., 2008; Davies et al., 2015). These strong starbursts associated with mergers can quickly exhaust galaxy gas reserves, potentially quenching star formation. A major merger consisting of two late-type galaxies typically results in a single, early-type galaxy once the two progenitors have coalesced. Therefore major mergers strongly impact galaxy morphology along with star formation.

Less extreme, minor mergers can also induce starburst behaviour in the primary galaxy. This is due to tidal forces between the two galaxies which can funnel large amounts of gas toward the galaxy centre, catalyzing strong star formation (e.g. Mihos and Hernquist, 1994a). Minor mergers are much more common than major mergers (e.g. Lotz et al., 2011), and so potentially play a substantial role

in transforming galaxies. Observations of galaxies in minor pairs show that star formation is typically enhanced in the primary galaxy, but suppressed in the lower-mass secondary (Davies et al., 2015). Similar to major mergers, this star formation enhancement in the primary may result in significant gas depletion, leading to reduced star formation over the long term. Due to the substantial mass difference, minor mergers do not typically drive large scale morphological transformations (i.e. late-type to early-type), however subtle morphological signatures from minor mergers, such as tidal streams, are observed as the secondary is absorbed by the primary galaxy.

Galaxy groups and clusters are host to above average galaxy densities, and are natural environments for frequent mergers. In order for two galaxies to merge, they must be near to each other but also have low relative velocity. For mergers to occur, relative velocities between galaxies must be low. Because of this, mergers are actually far more frequent in galaxy groups compared to galaxy clusters (Jian, Lin, and Chiueh, 2012), where the lower velocity dispersions in groups are more conducive to mergers.

Impulsive and Tidal Interactions. Beyond mergers, there are further dynamical interactions which can occur between galaxies that do not result in the eventual coalescence of two galaxies. These take the form of impulsive, fly-by interactions (often referred to as "harassment") or tidal interactions. Similar to mergers, high-speed, impulsive galaxy interactions can induce bursty star formation and repeated close encounters can strongly funnel gas toward the central galaxy regions fueling star formation (Fujita, 1998). Galaxy harassment is also capable of introducing morphological changes, in particular, driving galaxies from discs to spheroids (Moore, Lake, and Katz, 1998).

Tidal interactions between central and satellite galaxies can lead to the stripping of not only gas, but also dark matter and stars, giving rise to galaxy tidal tails and also contributing to the build-up of the ICL. The tidal stripping of gas removes the fuel for star formation, which can therefore lead to quenching. Even if tidal forces are not capable of directly stripping gas, tidal interactions can transport gas outwards allowing it to be more easily stripped by other mechanisms (e.g. ram pressure, see below; Mayer et al. 2006; Chung et al. 2007).

Ram Pressure Stripping. As galaxies orbit through galaxy clusters, they move at high velocities relative to the ICM. This leads to galaxies feeling a ram pressure wind, opposite to the direction of motion, which is capable of directly stripping gas from galaxies. The strength of this ram pressure depends on both the density of the ICM as well as the velocity of the galaxy relative to the ICM, and is given by

$$P_{\rm ram} = \rho_{\rm ICM} v^2 \tag{1.20}$$

where $\rho_{\rm ICM}$ is the density of the ICM and v is the galaxy velocity relative to the ICM. As galaxies typically infall onto clusters at large velocity offsets, the ram pressure is strongest during the first infall. Characteristically, galaxies undergoing ram pressure stripping leave a wake of stripped material opposite to the direction of motion. This stripped material is commonly observed with the atomic hydrogen 21 cm transition or the Hα line tracing ionized gas (Kenney, van Gorkom, and Vollmer, 2004; Chung et al., 2009; Poggianti et al., 2017), however can also consist of more densely bound galactic components such as molecular gas and dust (Sivanandam, Rieke, and Rieke, 2010; Sivanandam, Rieke, and Rieke, 2014; Jáchym et al., 2019). By directly stripping gas from galaxies, ram pressure is capable of quenching star formation very effectively. With very efficient gas stripping, especially of the star-forming molecular gas, star formation can be quenched on $< 1\,$Gyr timescales (Quilis, Moore, and Bower, 2000). Those short quenching timescales assume very efficient gas stripping, however for less efficient stripping gas may remain bound to the galaxy over multiple orbits (McCarthy et al., 2008).

Ram pressure stripping is not expected to have any strong effect on the intrinsic galaxy morphology, as it primarily influences gas content without any strong pertubations of the stellar distribution. That said, ram pressure will quench star formation in galaxies from the outside in, as the loosely bound gas in galaxy exteriors is more easily stripped. This can lead to an observed "fading" of the star-forming disc relative to the central bulge, leading to galaxies appearing more early-type – though this is not sufficient to completely explain the morphologies of cluster galaxies (Christlein and Zabludoff, 2004; Bundy et al., 2010).

Starvation. For isolated galaxies, cold-gas reserves are replenished through cold accretion from gas cooling out of the hot galaxy halo. In dense environments, this

halo gas can be stripped from the galaxy (either through ram pressure or tidal effects) preventing this future accretion. Additionally, the high ambient temperature of virialized group and cluster halos can impede the efficiency of this gas cooling. It is this prevention of the replenishment of cold-gas reserves in a galaxy which is known as starvation. Once a galaxy has been cut off from these future gas reserves, the quenching timescale is then set by the depletion times for the consumption of a galaxy's existing gas reserves. As a result, the quenching timescales associated with starvation are relatively long, $\sim 2-10\,\mathrm{Gyr}$ (Balogh, Navarro, and Morris, 2000; Wheeler et al., 2014; Fillingham et al., 2015; Peng, Maiolino, and Cochrane, 2015; Wetzel, Tollerud, and Weisz, 2015). Evidence for starvation is often inferred through long derived quenching timescales (e.g. Balogh, Navarro, and Morris, 2000), however starvation can also be constrained through observations of galaxy gas halos (Wagner, McDonald, and Courteau, 2018) or galaxy metallicity trends (e.g. Peng, Maiolino, and Cochrane, 2015). Starvation is not expected to drive morphological changes in galaxies, but is often invoked to explain the prevalence of passive, red disc galaxies in dense environments (e.g. Kawata and Mulchaey, 2008).

1.4.3 Galaxy Mass and Star Formation

The strongest predictor for galaxy star formation in the local Universe is stellar mass. Low-mass galaxies tend to be strongly star-forming whereas high-mass galaxies are the most quenched (e.g. Peng et al., 2010). Among star-forming galaxies, there is a tight relation formed between SFR and stellar mass known as the star-forming main sequence (SFMS). For galaxies on the SFMS, SFR increases with stellar mass roughly as a power-law with a slope between 0.5 and 1 (see Whitaker et al. 2012 and references therein). The SFMS is clear in the left-hand panel of Fig. 1.5. To normalize for this increasing trend with stellar mass it is useful to consider the SFR per unit stellar mass, known as the specific star formation rate ($\mathrm{sSFR} = \mathrm{SFR}/M_\star$). For all local galaxies, sSFR decreases clearly with increasing stellar mass – at least for galaxies with $M_\star \gtrsim 10^{8-9}\,\mathrm{M}_\odot$. Per unit stellar mass, low-mass galaxies show the strongest star formation at low redshift. This is true for isolated galaxies as well as for galaxies in dense clusters. Over cosmic time,

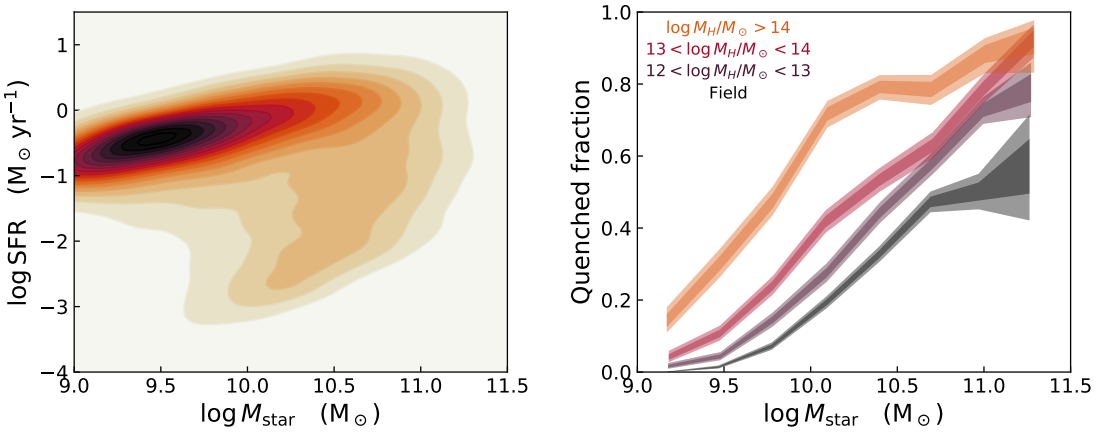

FIGURE 1.5: *Left:* Star formation rate versus stellar mass (left) and quenched fraction versus stellar mass and environment (right), for low-redshift SDSS galaxies. The tight correlation between stellar mass and star formation rate in the upper half of the panel is known as the "star-forming main sequence". Passive, quenched galaxies fall below this main sequence. *Right:* The fraction of quenched galaxies as a function of stellar mass. Different line colours correspond to galaxies within environments ranging from isolated field galaxies up to galaxies in massive clusters. The shaded regions denote 68 and 95% confidence intervals following Cameron (2011).

$L^{\star}$-like galaxies have been most efficient at converting their baryons to stars (e.g. Behroozi, Wechsler, and Conroy, 2013; Hudson et al., 2015).

When plotted as a histogram, the sSFRs of local galaxies form a bimodal distribution of star-forming and quiescent galaxies, roughly divided at sSFR = $10^{-11}\,\mathrm{yr}^{-1}$ (Wetzel, Tinker, and Conroy, 2012). As a result of this clear bimodality, it makes sense to consider the fraction of passive galaxies within a given population, known as the quenched fraction, f_Q. The quenched fraction depends strongly on stellar mass and is highest for high-mass galaxies (e.g. Wetzel, Tinker, and Conroy, 2012). Strikingly, low-mass galaxies ($\sim 10^{8-9}\,\mathrm{M}_{\odot}$) which are isolated in the field, show quenched fractions which are virtually zero ($<1\%$, Geha et al. 2012), clearly demonstrating the mass-dependence of star formation. The mass-dependence of quenched fractions is also clear from the right-hand panel of Fig. 1.5 which shows galaxy quenched fraction vs. stellar mass for low-redshift galaxies from the SDSS. The extremely low quenched fractions for isolated galaxies at $\sim 10^9\,\mathrm{M}_{\odot}$ is seen in the grey trend line in Fig. 1.5 which corresponds to field galaxies.

This clear relation between star formation and mass is likely linked to the internal mechanisms experienced by galaxies, as described in Section 1.4.1. Mechanisms such as AGN feedback and virial heating will only be effective for high-mass galaxies, which may be responsible for the fact that quenched fractions for high-mass galaxies are so large. The fact that quenched fractions are so small for low-mass ($\sim 10^9\,\mathrm{M}_{\odot}$), isolated galaxies suggests that internal mechanisms are not efficient when it comes to quenching lower-mass galaxies. As is discussed in the subsequent section, quenching of these low-mass galaxies at low-redshift is likely driven by environmental processes.

1.4.4 Galaxy Environment and Star Formation

It is now firmly established that galaxy star formation shows a clear dependence on local environment. In the right-hand panel of Fig. 1.5, I plot the quenched fraction of low-redshift galaxies as a function of both stellar mass and environment. As discussed in the previous section, there is a strong correlation between galaxy mass and quenched fraction, with the highest mass galaxies being the most quenched. However, there is a second relationship between quenched fraction and environment apparent in the same figure. At fixed stellar mass, galaxies residing in higher mass

halos (high-mass groups and clusters, red and orange lines) have systematically higher quenched fractions compared to galaxies in low-mass groups or the field (purple and black lines). This is true at all stellar masses, however is most clear for low-mass galaxies with $M_\star \lesssim 10^{10-10.5}\,\mathrm{M}_\odot$ (Haines et al., 2006; Bamford et al., 2009; Peng et al., 2010).

In Fig. 1.5 I have shown the correlation between quenched galaxies and cluster halo mass. This relation has also been established by many previous works (e.g. Kimm et al., 2009; Wetzel, Tinker, and Conroy, 2012). A connection between galaxy star formation and environment is also seen for other estimators of local galaxy environment, such as the Nth nearest neighbour number density, Σ_N. Σ_N is determined by measuring the distance from a given galaxy out to its Nth nearest neighbour, d_N, where N is an integer number of galaxies – typical values of N range from 3 to 10. d_N is then converted into a projected number density as

$$\Sigma_N = \frac{N}{\pi d_N^2}. \tag{1.21}$$

Σ_N is easily computed without a priori information regarding the presence of galaxy groups or clusters, however the major disadvantage is that it can artificially link cluster galaxies which appear close in projection but are actually distant in three-dimensional space. Measured spectroscopic redshifts for galaxies go a long way to mitigate this, however redshift space distortions still need to be carefully considered. First employed by Dressler (1980), numerous studies have since confirmed that the quenched fractions of galaxies clearly increase with Σ_N (e.g. Woo et al., 2013; Kawinwanichakij et al., 2017).

Galaxy star formation also depends strongly on environment within individual halos, traced by the projected cluster-centric distance. Many works have shown that the fraction of quenched galaxies increases with decreasing cluster-centric radii (e.g. Blanton and Roweis, 2007; Li, Yee, and Ellingson, 2009; Rasmussen et al., 2012; Haines et al., 2015). There are multiple potential explanations for this trend, which are difficult to disentangle. For example, given that high-mass galaxies show high quenched fractions, it may be that there are more high-mass galaxies in the centres of clusters. This is true to some extent, however the strength of this "mass segregation" is relatively mild for clusters of galaxies (Roberts et al., 2015;

Kafle et al., 2016). Simulations have shown that the time-since-infall for cluster galaxies (i.e. the time since the galaxy first crossed the cluster virial radius) is longer for galaxies near the centre of the cluster, and shorter for galaxies in the exterior. Therefore, it is possible that galaxies in the centres of clusters have simply experienced the cluster environment for longer, which in turn is effective at shutting off star formation. Finally, the ICM density as well as the cluster tidal field both increase towards the cluster centre, therefore cluster-specific quenching mechanisms (such as ram pressure or tidal stripping) are both more effective in the dense cluster interior. In reality, it is likely a superposition of all of these effects (and perhaps others) which give rise to observed increase of quenched galaxies toward the cores of galaxy clusters.

Pre-processing

The build-up of large scale structure in the Universe is a hierarchical process, where massive galaxy clusters grow through the accretion of lower mass galaxy groups. A key question regarding the environmental quenching of star formation is, what are the characteristic environments within which star formation is quenched? The idea that galaxy star formation can be quenched within a galaxy group, prior to accretion onto a larger galaxy cluster, is known as "pre-processing". Given the prominent red sequence observed in galaxy clusters, many studies have attempted to constrain what fraction of red cluster galaxies were pre-processed in groups versus quenched within the galaxy cluster (e.g. Fujita, 2004; McGee et al., 2009; von der Linden et al., 2010; Haines et al., 2015). Constraining pre-processing is also important for understanding the physical nature of environmental quenching, as some quenching mechanisms are likely more efficient in groups (ie. mergers) and others in clusters (ie. ram pressure stripping).

Large Scale Environment

Thus far, I have only discussed galaxy environment on relatively small scales, such as membership in a group/cluster or nearest neighbour galaxy densities. That said, the large scale, cosmic web environment (described in Section 1.1.2) can also

be considered. Previous studies have made efforts to elucidate the effects of large-scale structure on galaxy star formation, typically by separating filament and void galaxies. Such results have been mixed, but there is some evidence that galaxies in voids show higher star formation compared to denser, filamentary environments (e.g. Alpaslan et al., 2015; Moorman et al., 2016; Kuutma, Tamm, and Tempel, 2017).

1.5 This Thesis

The broad goals of this thesis are to: (a) improve observational classifications of the galaxy cluster environment, and (b) better understand the physical mechanisms driving star formation quenching in galaxy clusters. To accomplish this, we use high-quality observations of galaxy clusters at both optical and X-ray wavelengths, allowing the study of various components of the cluster environment. Specifically, this thesis will explore three main questions:

1. What are the best observational techniques for identifying relaxed and unrelaxed galaxy clusters?

2. Do the star-forming and morphological properties of galaxies in relaxed galaxy clusters differ from those hosted by unrelaxed clusters?

3. Which physical mechanisms are responsible for quenching star formation in dense environments?

In Chapter 2 we explore the relationship between optical and X-ray observational proxies for cluster dynamical state. We compile a sample of SDSS galaxy clusters which also have archival X-ray observations from either the *Chandra* or *XMM-Newton* X-ray observatories. With this sample, we are able to compute numerous relaxation estimators for each individual cluster, with both the optical and X-ray wavebands. This allows us to explore which optical relaxation measures are best correlated with observed X-ray morphologies, thereby testing which cluster relaxation proxies are most effective. We demonstrate that the shape of the member-galaxy velocity distribution (ie. Gaussian or non-Gaussian as traced by

the Anderson-Darling test) traces cluster X-ray morphology, on average for a large sample of galaxy clusters.

In Chapter 3 we follow up the work in Chapter 2 by investigating the properties of relaxed and unrelaxed galaxy clusters in a large, cosmological dark matter simulation. We project the simulated halos along a line-of-sight and measure the shape of their one-dimensional velocity distributions analogously to observational techniques. This gives us a sample of relaxed and unrelaxed clusters in the simulations which were identified in projection and are therefore comparable to observational samples, but yet still give us access to "un-observable" information from the simulation such as merger and accretion history for the cluster halos. We find that the unrelaxed clusters (non-Gaussian velocity distributions) in the simulation show recent accretion and active merger histories compared to relaxed systems. When considering three-dimensional positions and velocities in the simulation, we show that projection effects play a significant role and that one-dimensional velocity information is not sufficient to classify cluster dynamical state on a cluster-by-cluster basis. Large samples of clusters are therefore needed to mitigate these effects for ensemble samples.

In Chapter 4 we investigate SFR and morphology of galaxies in relaxed and unrelaxed clusters. With a large sample of SDSS clusters we identify relaxed and unrelaxed clusters according to the shape of their velocity distributions. We show that unrelaxed galaxy clusters host a larger proportion of star-forming galaxies compared to relaxed clusters. The fact that unrelaxed clusters show higher fractions of star-forming galaxies, than do relaxed clusters, may be related to the fact that times-since-infall for satellite galaxies are systematically shorter in unrelaxed clusters compared to relaxed systems (see Chapter 3). It is also plausible that quenching mechanisms, such as ram-pressure stripping, may be less efficient in unrelaxed clusters due to an underdense ICM.

In Chapter 5 we study the quenching of cluster galaxies directly as a function of the density of the ICM in their host systems. To do so, we compile a sample of SDSS galaxy clusters which also have high-quality, archival *Chandra* data available. This dataset allows us to derive ICM density profiles for each cluster in the sample and, given the radial position of satellite galaxies in their host cluster,

estimate the ICM density at the location of each galaxy. We find that for all stellar masses, quenched fractions increase with increasing ICM density. Low-mass galaxies show evidence for a broken powerlaw relation between quenched fraction and ICM density, implying excess quenching at the highest ICM densities. With an observationally motivated toy model, coupled to galaxy velocity distributions extracted from simulated clusters, we show that the observed upturn in quenching for low-mass galaxies is consistent with ram pressure stripping. This model is consistent with a "slow-then-rapid" (e.g. Maier et al., 2019) framework for satellite quenching.

In Chapter 6 we study ram pressure stripping in the nearby Coma Cluster by visually identifying a sample of Coma galaxies which show signatures of ongoing stripping. "Stripping candidates" are visually identified by inspecting *ugi* images from the Canada-France-Hawaii Telescope, and flagging galaxies showing evidence of stripped tails or highly asymmetric star formation. These disturbed galaxies are outliers in common morphological planes, such as concentration-asymmetry and Gini-M_{20}, and also show stripped tails pointing away from the cluster centre. These stripping candidates also show enhanced star formation, both relative to "normal" Coma galaxies and relative to galaxies in the field. This enhanced star formation is likely being catalyzed by enhanced gas densities driven by ram pressure. The results of this work suggest that ram pressure stripping is ubiquitous throughout all regions of the Coma cluster.

Finally, in Chapter 7 I provide a discussion and summary of the primary results presented in this thesis. This discussion will include some of the larger picture implications, as well as highlight the next steps to be taken given the availability of new data and new facilities moving forward.

Bibliography

Abraham, Roberto G., Sidney van den Bergh, and Preethi Nair (2003). *ApJ* 588.1, pp. 218–229.

Alam, Shadab et al. (2017). *MNRAS* 470.3, pp. 2617–2652.

Allen, Steven W., August E. Evrard, and Adam B. Mantz (2011). *Annual Review of Astronomy and Astrophysics* 49.1, pp. 409–470.

Alpaslan, M. et al. (2015). *MNRAS* 451, pp. 3249–3268.

Alpher, R. A., H. Bethe, and G. Gamow (1948). *Physical Review* 73.7, pp. 803–804.

Anderson, T. W. and D. A. Darling (1952). *The Annals of Mathematical Statistics* 23, p. 193.

André, P. et al. (2014). *Protostars and Planets VI*. Ed. by Henrik Beuther, Ralf S. Klessen, Cornelis P. Dullemond, and Thomas Henning, p. 27.

Araya-Melo, Pablo A. et al. (2009). *MNRAS* 399.1, pp. 97–120.

Arnaud, M. (2009). *A&A* 500.1, pp. 103–104.

Baldry, I. K. et al. (2006). *MNRAS* 373, pp. 469–483.

Balogh, M. L., J. F. Navarro, and S. L. Morris (2000). *ApJ* 540, pp. 113–121.

Bamford, S. P. et al. (2009). *MNRAS* 393, pp. 1324–1352.

Bastian, Nate, Kevin R. Covey, and Michael R. Meyer (2010). *AR&AA* 48, pp. 339–389.

Behroozi, Peter S., Risa H. Wechsler, and Charlie Conroy (2013). *ApJ* 770.1, 57, p. 57.

Binney, J. and S. Tremaine (2008). Princeton University Press.

Bird, C. M. and T. C. Beers (1993). *AJ* 105, pp. 1596–1606.

Birkinshaw, M. (1999). *Physics Reports* 310, pp. 97–195.

Birnboim, Y. and A. Dekel (2003). *MNRAS* 345, pp. 349–364.

Blanton, M. R. and J. Moustakas (2009). *ARAA* 47, pp. 159–210.

Blanton, M. R. and S. Roweis (2007). *AJ* 133, pp. 734–754.

Böhringer, H. et al. (2010). *A&A* 514, A32, A32.

Böhringer, Hans and Norbert Werner (2010). *A&A Rev.* 18.1-2, pp. 127–196.

Bolatto, Alberto D., Mark Wolfire, and Adam K. Leroy (2013). *AR&AA* 51.1, pp. 207–268.

Bolton, Adam S. et al. (2008). *ApJ* 682.2, pp. 964–984.

Bond, J. Richard, Lev Kofman, and Dmitry Pogosyan (1996). *Nature* 380.6575, pp. 603–606.

Brinchmann, J. et al. (2004). *MNRAS* 351, pp. 1151–1179.

Brown, T. et al. (2015). *MNRAS* 452, pp. 2479–2489.

Brown, Toby et al. (2017). *MNRAS* 466.2, pp. 1275–1289.

Bundy, K. et al. (2010). *ApJ* 719, pp. 1969–1983.

Burke, Claire, Matt Hilton, and Chris Collins (2015). *MNRAS* 449.3, pp. 2353–2367.

Butcher, H. and A. Oemler Jr. (1978). *ApJ* 219, pp. 18–30.

Cameron, E. (2011). *PASA* 28, pp. 128–139.

Campbell, Duncan et al. (2015). *MNRAS* 452.1, pp. 444–469.

Carnall, A. C., R. J. McLure, J. S. Dunlop, and R. Davé (2018). *MNRAS* 480.4, pp. 4379–4401.

Carnall, Adam C. et al. (2019). *ApJ* 873.1, 44, p. 44.

Carollo, C. M. et al. (2013). *ApJ* 776, 71, p. 71.

Catinella, Barbara et al. (2010). *MNRAS* 403.2, pp. 683–708.

Cattaneo, A., A. Dekel, J. Devriendt, B. Guiderdoni, and J. Blaizot (2006). *MNRAS* 370, pp. 1651–1665.

Cautun, Marius, Rien van de Weygaert, Bernard J. T. Jones, and Carlos S. Frenk (2014). *MNRAS* 441.4, pp. 2923–2973.

Cavaliere, A. and R. Fusco-Femiano (1976). *A&A* 500, pp. 95–102.

Chabrier, G. (2003). *PASP* 115, pp. 763–795.

Christlein, D. and A. I. Zabludoff (2004). *ApJ* 616, pp. 192–198.

Chung, A., J. H. van Gorkom, J. D. P. Kenney, H. Crowl, and B. Vollmer (2009). *AJ* 138, pp. 1741–1816.

Chung, A., J. H. van Gorkom, J. D. P. Kenney, and B. Vollmer (2007). *ApJl* 659, pp. L115–L119.

Colless, M. et al. (2001). *MNRAS* 328, pp. 1039–1063.

Connor, Thomas et al. (2018). *ApJ* 867.1, 25, p. 25.

Conselice, Christopher J. (2003). *ApJS* 147.1, pp. 1–28.

— (2014). *ARAA* 52, pp. 291–337.

Cortese, L. et al. (2016). *MNRAS* 459.4, pp. 3574–3584.

Crain, Robert A. et al. (2015). *MNRAS* 450.2, pp. 1937–1961.

Davies, L. J. M. et al. (2015). *MNRAS* 452, pp. 616–636.

de Carvalho, R. R. et al. (2017). *AJ* 154.3, 96, p. 96.

De Lucia, G. and J. Blaizot (2007). *MNRAS* 375, pp. 2–14.

Deason, A. J., V. Belokurov, N. W. Evans, and I. G. McCarthy (2012). *ApJ* 748.1, 2, p. 2.

Domínguez Sánchez, H., M. Huertas-Company, M. Bernardi, D. Tuccillo, and J. L. Fischer (2018). *MNRAS* 476.3, pp. 3661–3676.

Dressler, A. (1980). *ApJ* 236, pp. 351–365.

— (1984). *Annual Review of Astronomy and Astrophysics* 22.1, pp. 185–222.

Dressler, A. and S. A. Shectman (1988). *AJ* 95, pp. 985–995.

Driver, Simon P. et al. (2009). *Astronomy and Geophysics* 50.5, pp. 5.12–5.19.

Duarte, Manuel and Gary A. Mamon (2014). *MNRAS* 440.2, pp. 1763–1778.

Einasto, J. (1965). *Trudy Astrofizicheskogo Instituta Alma-Ata* 5, pp. 87–100.

Ellison, S. L., D. R. Patton, L. Simard, and A. W. McConnachie (2008). *AJ* 135, pp. 1877–1899.

Ellison, S. L., H. Teimoorinia, D. J. Rosario, and J. T. Mendel (2016). *MNRAS* 458, pp. L34–L38.

Epps, Seth D. and Michael J. Hudson (2017). *MNRAS* 468.3, pp. 2605–2613.

Ettori, Stefano et al. (2013). *Space Science Reviews* 177.1-4, pp. 119–154.

Fabian, A. C. (2012). *A&AA* 50, pp. 455–489.

Fabian, Andrew C. (2002). *Lighthouses of the Universe: The Most Luminous Celestial Objects and Their Use for Cosmology*. Ed. by Marat Gilfanov, Rashid Sunyeav, and Eugene Churazov, p. 24.

Fillingham, S. P. et al. (2015). *MNRAS* 454, pp. 2039–2049.

Franco, J. and S. N. Shore (1984). *ApJ* 285, pp. 813–817.

Fujita, Y. (1998). *ApJ* 509, pp. 587–594.

Fujita, Yutaka (2004). *PASJ* 56, pp. 29–43.

Gabor, J. M. and R. Davé (2015). *MNRAS* 447, pp. 374–391.

Galametz, M. et al. (2013). *MNRAS* 431.2, pp. 1956–1986.

Geha, M., M. R. Blanton, R. Yan, and J. L. Tinker (2012). *ApJ* 757.1, 85, p. 85.

George, M. R. et al. (2012). *ApJ* 757, 2, p. 2.

Girardi, M., A. Biviano, G. Giuricin, F. Mardirossian, and M. Mezzetti (1993). *ApJ* 404, p. 38.

Girardi, Marisa, Giuliano Giuricin, Fabio Mardirossian, Marino Mezzetti, and Walter Boschin (1998). *ApJ* 505.1, pp. 74–95.

Gladders, M. D. and H. K. C. Yee (2000). *AJ* 120, pp. 2148–2162.

Gladders, Michael D. et al. (2013). *ApJ* 770.1, 64, p. 64.

Governato, F. et al. (2007). *MNRAS* 374.4, pp. 1479–1494.

Groves, Brent A. et al. (2015). *ApJ* 799.1, 96, p. 96.

Gunn, J. E. and J. R. Gott III (1972). *ApJ* 176, p. 1.

Gupta, A., S. Mathur, Y. Krongold, F. Nicastro, and M. Galeazzi (2012). *ApJL* 756.1, L8, p. L8.

Gürkan, G. et al. (2015). *MNRAS* 452, pp. 3776–3794.

Guth, Alan H. (1981). *Phys. Rev. D* 23.2, pp. 347–356.

Haines, C. P., F. La Barbera, A. Mercurio, P. Merluzzi, and G. Busarello (2006). *ApJL* 647, pp. L21–L24.

Haines, C. P. et al. (2015). *ApJ* 806, 101, p. 101.

Hernquist, L. (1990). *ApJ* 356, pp. 359–364.

Hinshaw, G. et al. (2003). *ApJS* 148, pp. 135–159.

Hoekstra, Henk et al. (2013). *Space Sci. Rev.* 177.1-4, pp. 75–118.

Hopkins, Philip F., Eliot Quataert, and Norman Murray (2011). *MNRAS* 417.2, pp. 950–973.

— (2012). *MNRAS* 421.4, pp. 3522–3537.

Hou, A., L. C. Parker, W. E. Harris, and D. J. Wilman (2009). *ApJ* 702, pp. 1199–1210.

Hou, A. et al. (2013). *MNRAS* 435, pp. 1715–1726.

Hu, Wayne and Scott Dodelson (2002). *ARA&A* 40, pp. 171–216.

Hubble, E. P. (1926). *ApJ* 64.

Huchra, J. P. and M. J. Geller (1982). *ApJ* 257, pp. 423–437.

Hudson, M. J. et al. (2015). *MNRAS* 447, pp. 298–314.

Jáchym, Pavel et al. (2019). *ApJ* 883.2, 145, p. 145.

Jian, Hung-Yu, Lihwai Lin, and Tzihong Chiueh (2012). *ApJ* 754.1, 26, p. 26.

Jog, C. J. and P. M. Solomon (1984). *ApJ* 276, pp. 114–126.

Kafle, P. R. et al. (2016). *MNRAS* 463.4, pp. 4194–4209.

Katayama, H., K. Hayashida, F. Takahara, and Y. Fujita (2003). *ApJ* 585, pp. 687–693.

Kauffmann, G. et al. (2003). *MNRAS* 346, pp. 1055–1077.

Kawata, D. and J. S. Mulchaey (2008). *ApJl* 672, L103, p. L103.

Kawinwanichakij, Lalitwadee et al. (2017). *ApJ* 847.2, 134, p. 134.

Keller, B. W., J. Wadsley, S. M. Benincasa, and H. M. P. Couchman (2014). *MNRAS* 442, pp. 3013–3025.

Kelvin, Lee S. et al. (2014). *MNRAS* 444.2, pp. 1647–1659.

Kenney, J. D. P., J. H. van Gorkom, and B. Vollmer (2004). *AJ* 127, pp. 3361–3374.

Kennicutt, Robert C. and Neal J. Evans (2012). *ARAA* 50, pp. 531–608.

Khosroshahi, H. G. et al. (2017). *ApJ* 842, 81, p. 81.

Kim, Suk et al. (2014). *ApJS* 215.2, 22, p. 22.

Kimm, T. et al. (2009). *MNRAS* 394, pp. 1131–1147.

Klypin, A. A., S. Trujillo-Gomez, and J. Primack (2011). *ApJ* 740, 102, p. 102.

Klypin, A., G. Yepes, S. Gottlöber, F. Prada, and S. Heß (2016). *MNRAS* 457, pp. 4340–4359.

Kravtsov, Andrey V. and Stefano Borgani (2012). *AR&AA* 50, pp. 353–409.

Kroupa, Pavel (2001). *MNRAS* 322.2, pp. 231–246.

Kuutma, Teet, Antti Tamm, and Elmo Tempel (2017). *A&A* 600, L6, p. L6.

Lanzuisi, G. et al. (2015). *A&A* 573, A137, A137.

Larson, R. B., B. M. Tinsley, and C. N. Caldwell (1980). *ApJ* 237, pp. 692–707.

Leja, Joel, Adam C. Carnall, Benjamin D. Johnson, Charlie Conroy, and Joshua S. Speagle (2019). *ApJ* 876.1, 3, p. 3.

Li, I. H., H. K. C. Yee, and E. Ellingson (2009). *ApJ* 698, pp. 83–98.

Lilly, S. J., O. Le Fevre, F. Hammer, and David Crampton (1996). *ApJL* 460, p. L1.

Linde, A. D. (1982). *Physics Letters B* 116.5, pp. 335–339.

Lintott, C. J. et al. (2008). *MNRAS* 389, pp. 1179–1189.

Lopes, Paulo A. A. et al. (2018). *MNRAS* 478, pp. 5473–5490.

Lotz, J. M. et al. (2011). *ApJ* 742, 103, p. 103.

Lotz, Jennifer M., Joel Primack, and Piero Madau (2004). *AJ* 128.1, pp. 163–182.

Madau, P. and M. Dickinson (2014). *ARA&A* 52, pp. 415–486.

Madau, P., L. Pozzetti, and M. Dickinson (1998). *ApJ* 498, pp. 106–116.

Maier, C., M. Hayashi, B. L. Ziegler, and T. Kodama (2019). *A&A* 626, A14, A14.

Martig, M., F. Bournaud, R. Teyssier, and A. Dekel (2009). *ApJ* 707, pp. 250–267.

Mather, J. C. et al. (1990). *ApJl* 354, pp. L37–L40.

Matthee, Jorryt et al. (2017). *MNRAS* 465.2, pp. 2381–2396.

Mayer, L., C. Mastropietro, J. Wadsley, J. Stadel, and B. Moore (2006). *MNRAS* 369, pp. 1021–1038.

McCarthy, I. G. et al. (2008). *MNRAS* 383.2, pp. 593–605.

McConnachie, Alan W. (2012). *AJ* 144.1, 4, p. 4.

McDonald, M. et al. (2016). *ApJ* 817, 86, p. 86.

McGee, S. L., M. L. Balogh, R. G. Bower, A. S. Font, and I. G. McCarthy (2009). *MNRAS* 400, pp. 937–950.

Merloni, A. et al. (2012). *arXiv e-prints*, arXiv:1209.3114, arXiv:1209.3114.

Merritt, David, Alister W. Graham, Ben Moore, Jürg Diemand, and Balša Terzić (2006). *AJ* 132.6, pp. 2685–2700.

Mihos, J. C. and L. Hernquist (1994a). *ApJl* 425, pp. L13–L16.

— (1994b). *ApJl* 431, pp. L9–L12.

Mo, H. J. and S. D. M. White (2002). *MNRAS* 336.1, pp. 112–118.

Mo, H., F. van den Bosch, and S. White (2010). Galaxy Formation and Evolution. Cambridge University Press.

Montes, Mireia and Ignacio Trujillo (2018). *MNRAS* 474.1, pp. 917–932.

— (2019). *MNRAS* 482.2, pp. 2838–2851.

Moore, B., N. Katz, G. Lake, A. Dressler, and A. Oemler (1996). *Nature* 379, pp. 613–616.

Moore, Ben, George Lake, and Neal Katz (1998). *ApJ* 495.1, pp. 139–151.

Moorman, Crystal M. et al. (2016). *ApJ* 831.2, 118, p. 118.

Mullaney, J. R. et al. (2015). *MNRAS* 453, pp. L83–L87.

Murphy, E. J. et al. (2011). *ApJ* 737.2, 67, p. 67.

Nair, P. B. and R. G. Abraham (2010). *ApJS* 186, pp. 427–456.

Navarro, J. F., C. S. Frenk, and S. D. M. White (1997). *ApJ* 490, pp. 493–508.

Newman, J. A. et al. (2013). *ApJS* 208, 5, p. 5.

Nolthenius, R. and S. D. M. White (1987). *MNRAS* 225, pp. 505–530.

Ntelis, Pierros et al. (2017). *Journal of Cosmology and Astroparticle Physics* 2017.6, 019, p. 019.

Nulsen, P. E. J. (1982). *MNRAS* 198, pp. 1007–1016.

Nurgaliev, D. et al. (2013). *ApJ* 779, 112, p. 112.

Nurgaliev, D. et al. (2017). *ApJ* 841, 5, p. 5.

Old, L. et al. (2014). *MNRAS* 441.2, pp. 1513–1536.

Old, L. et al. (2018). *MNRAS* 475, pp. 853–866.

Ota, Naomi, Tetsu Kitayama, Kuniaki Masai, and Kazuhisa Mitsuda (2006). *ApJ* 640.2, pp. 673–690.

Peebles, P. J. E. (1965). *ApJ* 142, p. 1317.

— (1980).

Peebles, P. J. E. and J. T. Yu (1970). *ApJ* 162, p. 815.

Peng, Y.-j. et al. (2010). *ApJ* 721, pp. 193–221.

Peng, Y., R. Maiolino, and R. Cochrane (2015). *Nature* 521, pp. 192–195.

Penzias, A. A. and R. W. Wilson (1965). *ApJ* 142, pp. 419–421.

Perlmutter, S. et al. (1999). *ApJ* 517.2, pp. 565–586.

Peterson, J. R. and A. C. Fabian (2006). *Phys. Rep.* 427.1, pp. 1–39.

Pimbblet, K. A., S. S. Shabala, C. P. Haines, A. Fraser-McKelvie, and D. J. E. Floyd (2013). *MNRAS* 429.2, pp. 1827–1839.

Planck Collaboration et al. (2014). *A&A* 571, A16, A16.

Planck Collaboration et al. (2018). *arXiv e-prints*, arXiv:1807.06209, arXiv:1807.06209.

Poggianti, B. M. et al. (2017). *ApJ* 844, 48, p. 48.

Posti, Lorenzo and Amina Helmi (2019). *A&A* 621, A56, A56.

Press, W. H. and M. Davis (1982). *ApJ* 259, pp. 449–473.

Press, W. H. and P. Schechter (1974). *ApJ* 187, pp. 425–438.

Quilis, V., B. Moore, and R. Bower (2000). *Science* 288, pp. 1617–1620.

Rasmussen, J. et al. (2012). *ApJ* 757, 122, p. 122.

Rhee, J. et al. (2017). *ApJ* 843, 128, p. 128.

Ribeiro, A. L. B. et al. (2013). *MNRAS* 434, pp. 784–795.

Richard, Johan et al. (2010). *MNRAS* 404.1, pp. 325–349.

Riess, Adam G., Stefano Casertano, Wenlong Yuan, Lucas M. Macri, and Dan Scolnic (2019). *ApJ* 876.1, 85, p. 85.

Riess, Adam G. et al. (1998). *AJ* 116.3, pp. 1009–1038.

Roberts, I. D., L. C. Parker, G. D. Joshi, and F. A. Evans (2015). *MNRAS* 448, pp. L1–L5.

Roberts, M. S. (1962). *AJ* 67, pp. 437–446.

Robotham, A. S. G. et al. (2011). *MNRAS* 416.4, pp. 2640–2668.

Ruszkowski, M. and V. Springel (2009). *ApJ* 696, pp. 1094–1102.

Safronov, V. S. (1960). *Annales d'Astrophysique* 23, p. 979.

Saintonge, A. et al. (2017). *ApJS* 233, 22, p. 22.

Sanderson, A. J. R., A. C. Edge, and G. P. Smith (2009). *MNRAS* 398, pp. 1698–1705.

Santini, P. et al. (2012). *A&A* 540, A109, A109.

Santos, J. S., P. Tozzi, P. Rosati, and H. Böhringer (2010). *A&A* 521, A64, A64.

Santos, J. S. et al. (2008). *A&A* 483.1, pp. 35–47.

Sawala, Till, Cecilia Scannapieco, Umberto Maio, and Simon White (2010). *MNRAS* 402.3, pp. 1599–1613.

Scannapieco, C. et al. (2012). *MNRAS* 423.2, pp. 1726–1749.

Scoville, N. et al. (2007). *ApJS* 172, pp. 1–8.

Sérsic, J. L. (1963). *Boletin de la Asociacion Argentina de Astronomia La Plata Argentina* 6, pp. 41–43.

Shirley, Yancy L. (2015). *PASP* 127.949, p. 299.

Sivanandam, S., M. J. Rieke, and G. H. Rieke (2014). *ApJ* 796, 89, p. 89.

Sivanandam, Suresh, Marcia J. Rieke, and George H. Rieke (2010). *ApJ* 717.1, pp. 147–162.

Sofue, Yoshiaki and Vera Rubin (2001). *ARA&A* 39, pp. 137–174.

Springel, V. et al. (2005). *Nature* 435, pp. 629–636.

Stanek, R., A. E. Evrard, H. Bohringer, P. Schuecker, and B. Nord (2006). *ApJ* 648.2, pp. 956–968.

Stanley, F. et al. (2015). *MNRAS* 453, pp. 591–604.

Sunyaev, R. A. and Y. B. Zeldovich (1970). *Ap&SS* 7, pp. 3–19.

Tielens, A.G.G.M. (2005). Cambridge University Press.

Toomre, A. (1964). *ApJ* 139, pp. 1217–1238.

Urquhart, S. A., J. P. Willis, H. Hoekstra, and M. Pierre (2010). *MNRAS* 406, pp. 368–381.

Vincent, R. Anthony and Barbara S. Ryden (2005). *ApJ* 623.1, pp. 137–147.

Vogelsberger, Mark et al. (2014). *MNRAS* 444.2, pp. 1518–1547.

von der Linden, A., V. Wild, G. Kauffmann, S. D. M. White, and S. Weinmann (2010). *MNRAS* 404, pp. 1231–1246.

Wagner, Cory R., Michael McDonald, and Stéphane Courteau (2018). *ApJ* 867.1, 14, p. 14.

Wagoner, Robert V., William A. Fowler, and F. Hoyle (1967). *ApJ* 148, p. 3.

Walcher, J., B. Groves, T. Budavári, and D. Dale (2011). *Astrophys. Space Sci.* 331, pp. 1–52.

Wang, J. et al. (2014). *MNRAS* 441, pp. 2159–2172.

Wetzel, A. R., J. L. Tinker, and C. Conroy (2012). *MNRAS* 424, pp. 232–243.

Wetzel, A. R., E. J. Tollerud, and D. R. Weisz (2015). *ApJL* 808, L27, p. L27.

Wheeler, C., J. I. Phillips, M. C. Cooper, M. Boylan-Kolchin, and J. S. Bullock (2014). *MNRAS* 442, pp. 1396–1404.

Whitaker, K. E., P. G. van Dokkum, G. Brammer, and M. Franx (2012). *ApJl* 754, L29, p. L29.

White, Simon D. M. and Carlos S. Frenk (1991). *ApJ* 379, p. 52.

Wilman, D. J. and P. Erwin (2012). *ApJ* 746, 160, p. 160.

Woo, Joanna et al. (2013). *MNRAS* 428.4, pp. 3306–3326.

Wurster, J. and R. J. Thacker (2013). *MNRAS* 431.3, pp. 2513–2534.

Wyse, Rosemary F. G., Gerard Gilmore, and Marijn Franx (1997). *ARA&A* 35, pp. 637–675.

Yahil, A. and N. V. Vidal (1977). *ApJ* 214, pp. 347–350.

Yang, X., H. J. Mo, F. C. van den Bosch, and Y. P. Jing (2005). *MNRAS* 356, pp. 1293–1307.

Yang, X. et al. (2007). *ApJ* 671, pp. 153–170.

Yao, Y., M. A. Nowak, Q. D. Wang, N. S. Schulz, and C. R. Canizares (2008). *ApJL* 672.1, p. L21.

York, D. G. et al. (2000). *AJ* 120, pp. 1579–1587.

Zeldovich, Yaa B. (1972). *MNRAS* 160, 1P.

Zwicky, F. (1933). *Helvetica Physica Acta* 6, pp. 110–127.

— (1937). *ApJ* 86, p. 217.

2 | Connecting Optical and X-ray Tracers of Galaxy Cluster Relaxation

This chapter represents an unchanged version of the paper, *Connecting Optical and X-ray Tracers of Galaxy Cluster Relaxation*, published in the refereed journal, *Monthly Notices of the Royal Astronomical Society.* The full reference is given below:

Roberts I.D.[1], Parker L.C.[1], Hlavacek-Larrondo J.[2], 2018, MNRAS, Volume 475, Issue 4, pp. 4704-4716

[1] *Department of Physics & Astronomy, McMaster University, Hamilton ON L8S 4M1*

[2] *Département de Physique, Université de Montréal, Montréal QC H3C 3J7*

Abstract

Substantial effort has been devoted in determining the ideal proxy for quantifying the morphology of the hot intracluster medium in clusters of galaxies. These proxies, based on X-ray emission, typically require expensive, high-quality X-ray observations making them difficult to apply to large surveys of groups and clusters. Here, we compare optical relaxation proxies with X-ray asymmetries and centroid shifts for a sample of Sloan Digital Sky Survey clusters with high-quality, archival X-ray data from *Chandra* and *XMM-Newton*. The three optical relaxation measures considered are the shape of the member-galaxy projected velocity distribution – measured by the Anderson-Darling (AD) statistic, the stellar mass gap between the most-massive and second-most-massive cluster galaxy, and the offset between the most-massive galaxy (MMG) position and the luminosity-weighted cluster centre. The AD statistic and stellar mass gap correlate significantly with X-ray relaxation proxies, with the AD statistic being the stronger correlator. Conversely, we find no evidence for a correlation between X-ray asymmetry or centroid shift and the MMG offset. High-mass clusters ($M_{\rm halo} > 10^{14.5}\,{\rm M}_{\odot}$) in this sample have X-ray asymmetries, centroid shifts, and Anderson-Darling statistics which are systematically larger than for low-mass systems. Finally, considering the dichotomy of Gaussian and non-Gaussian clusters (measured by the AD test), we show that the probability of being a non-Gaussian cluster correlates significantly with X-ray asymmetry but only shows a marginal correlation with centroid shift. These results confirm the shape of the radial velocity distribution as a useful proxy for cluster relaxation, which can then be applied to large redshift surveys lacking extensive X-ray coverage.

2.1 Introduction

The majority of galaxies in the local Universe do not evolve in isolation but instead inhabit dense environments such as groups and clusters (e.g. Geller and Huchra, 1983; Eke et al., 2005). In addition to internal processes (e.g. active galactic nucleus feedback, Dubois et al. 2013; Gürkan et al. 2015; Mullaney et al. 2015; Bongiorno et al. 2016; bar-driven evolution, Knapen et al. 1995; Kormendy and Kennicutt 2004; Sheth et al. 2005; morphological quenching, Martig et al. 2009; virial gas heating, Birnboim and Dekel 2003; Cattaneo et al. 2006; Gabor and Davé 2015; etc.), interactions with local environments play a significant role in shaping the observed properties of galaxies. For example, mechanisms acting in dense environments such as ram-pressure stripping (e.g. Gunn and Gott, 1972) and starvation (e.g. Larson, Tinsley, and Caldwell, 1980; Peng, Maiolino, and Cochrane, 2015) can remove the cold and hot gas components from galaxies, respectively. Galaxy interactions, such as mergers and impulsive high-speed encounters, can drive gas to the central regions and induce starburst events which may exhaust a galaxy's gas reserves (e.g. Mihos and Hernquist, 1994a; Mihos and Hernquist, 1994b; Ellison et al., 2008; Davies et al., 2015). These interactions can also influence galaxy morphology through the growth of a strong bulge component, and the end products of major mergers tend to be bulge dominated galaxies with classical de Vaucouleurs profiles (Barnes, 1989). Finally, tidal interactions can also influence gas content through direct stripping or by transporting gas outwards allowing it to be more easily stripped by other mechanisms (e.g. Mayer et al., 2006; Chung et al., 2007). It is generally accepted that these mechanisms can act on galaxies in dense environments, though the relative balance between different mechanisms in different environments remains an outstanding question.

Understanding the influence of environment is contingent on being able to identify and quantify galaxy environments. Common environmental measures include the projected number density of galaxies out to the Nth nearest neighbour, the halo mass of a host group or cluster, or the projected separation from the centre of a group or cluster. Star formation and morphology of galaxies correlate well with these environment proxies, with galaxies in high density regions (or alternatively, high halo mass or small group/cluster-centric radius) being preferentially

red, passive, and early type (Dressler, 1980; Goto et al., 2003; Poggianti et al., 2008; Kimm et al., 2009; Li, Yee, and Ellingson, 2009; Wetzel, Tinker, and Conroy, 2012; Wilman and Erwin, 2012; Fasano et al., 2015; Haines et al., 2015). An alternative way to parametrize the environment of a host group or cluster is to classify the degree to which a system is dynamically relaxed. A relaxed, dynamically old group or cluster should be characterized by a central galaxy which is the brightest (most massive) member by a significant margin (e.g. Khosroshahi, Ponman, and Jones, 2007; Dariush et al., 2010; Smith et al., 2010) and is located near the minimum of the potential well (e.g. George et al. 2012; Zitrin et al. 2012, however also see Skibba et al. 2011), satellite galaxies which are distributed in velocity space according to a Gaussian profile (e.g. Yahil and Vidal, 1977; Bird and Beers, 1993; Hou et al., 2009; Martínez and Zandivarez, 2012), and diffuse X-ray emission which is symmetric about the group/cluster centre (e.g. Rasia, Meneghetti, and Ettori, 2013; Weißmann et al., 2013; Parekh et al., 2015). The dynamical state of clusters is related to the age of the halo and the time since infall for member galaxies, which simulations have shown is an important quantity in determining the degree to which galaxy properties are affected by environment (e.g. Wetzel et al., 2013; Oman and Hudson, 2016; Joshi, Wadsley, and Parker, 2017). Unrelaxed groups and clusters are systems which formed more recently or which have recently experienced a significant merger event, and in either case it would be expected that the time-since-infall on to the current halo for member galaxies will be relatively short. Therefore galaxies in unrelaxed groups may have properties which have been less influenced by environment compared to galaxies in more relaxed systems.

Recent studies have attempted to determine the degree to which galaxy properties depend on the "'relaxedness" of a given group or cluster. It has been shown that galaxies in relaxed groups tend to be redder than counterparts in unrelaxed systems, using relaxation definitions based on the presence of a well-defined central galaxy (e.g. Carollo et al., 2013) as well as the shape of the satellite velocity distribution (e.g. Ribeiro, Lopes, and Trevisan, 2010; Ribeiro et al., 2013). Previously, we have shown that low-mass galaxies in the inner regions of Gaussian (G) groups have reduced star-forming fractions relative to non-Gaussian (NG) groups

(Roberts and Parker, 2017). We have also shown that star-forming and disc fractions for low-mass galaxies are enhanced in X-ray underluminous (XRW) groups, and shown that galaxies in XRW groups have velocity distributions consistent with being unrelaxed systems (at least relative to X-ray strong groups, Roberts, Parker, and Karunakaran 2016).

Building from our recent work, here we aim to further investigate the connection between X-ray and optical measures of group relaxedness. The shape of the diffuse X-ray component of a group or cluster is among the most direct probes of the degree to which a group/cluster is relaxed or recently disturbed. The downside, however, is that measuring this morphology requires deep, high-quality X-ray observations which are not available for large surveys containing thousands of groups and clusters. To address this challenge, we use a sample of galaxy clusters with existing X-ray observations to investigate the relationship between the X-ray relaxation and three previously used optical probes of relaxation: the shape of the satellite velocity distribution, the stellar mass gap between the most-massive and second-most-massive group galaxy, and the offset between the position of the most-massive galaxy and the luminosity-weighted centre of the group. We determine the effectiveness of these optical relaxation measures (which are applicable to large redshift surveys) by comparing them to measured X-ray morphology, a more direct probe of relaxation.

The outline of this paper is as follows. In Section 2.2 we describe the optical group catalogue as well as the archival X-ray data used in this work. In Section 2.3 we outline the cluster relaxation estimators, both optical and X-ray, that we consider. In Section 2.4 we present the main results, comparing optical and X-ray cluster relaxation measures. In Section 2.5 we discuss these results and provide a summary in Section 2.6.

This paper assumes a flat Λ cold dark matter cosmology with $\Omega_M = 0.3$, $\Omega_\Lambda = 0.7$, and $H_0 = 70\,\mathrm{km\,s^{-1}\,Mpc}$. The h-dependence of important calculated properties are: $M_{\mathrm{halo}} \sim h^{-1}$, $M_\star \sim h^{-2}$, $R_{500} \sim h^{-1}$.

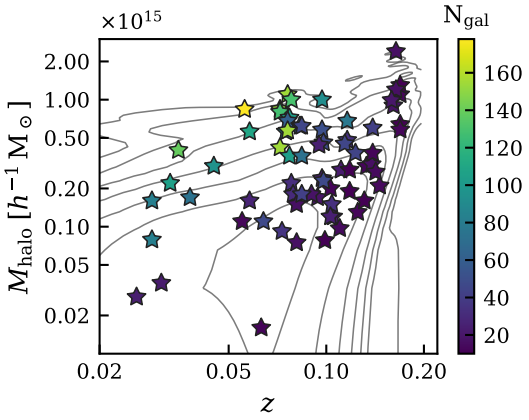

FIGURE 2.1: Cluster halo mass versus redshift for Yang clusters. Stars correspond to the X-ray matched clusters used in this work, coloured by the number of galaxies identified in each system. Grey contours show the distribution for the parent sample of $N > 10$ Yang clusters.

2.2 Data

2.2.1 Optically Identified Galaxy Clusters

We use galaxy clusters identified from the seventh release of the Sloan Digital Sky Survey (SDSS DR7; Abazajian et al. 2009) by Yang et al. (2005) and Yang et al. (2007) who construct a group sample with a "halo-based" group finder which aims to improve upon the classic friends-of-friends (FoF) algorithm (e.g. Huchra and Geller, 1982; Press and Davis, 1982). For a full description of the algorithm see Yang et al. (2005) and Yang et al. (2007), however in short, the groups are initially populated by connecting galaxies through a standard FoF approach (with very small linking lengths) and group memberships are iteratively updated under the assumption that the distribution of galaxies in phase space follows that of a spherical NFW profile (Navarro, Frenk, and White, 1997). Each iteration yields an updated estimate of the group mass, size, and velocity dispersion and iterations continue until memberships stabilize. Final group halo masses ($M_{\rm halo}$) obtained via abundance matching are given in the Yang catalogue (in particular, we use the sample III); we use galaxy stellar masses ($M_\star$) given in the New York University

Value-Added Galaxy Catalogue (Blanton et al., 2005) determined with fits to the galaxy spectra and broad-band photometric measurements following the procedure of (Blanton and Roweis, 2007). We note that the Yang catalogue contains a mixture of what would generally be considered groups ($M_{\rm halo} < 10^{14}\,{\rm M}_{\odot}$) as well as galaxy clusters ($M_{\rm halo} \geq 10^{14}\,{\rm M}_{\odot}$), for the sake of brevity we will refer to all systems as clusters regardless of halo mass as the majority of the systems we consider have $M_{\rm halo} \geq 10^{14}\,{\rm M}_{\odot}$.

Cluster-centric radii are computed for galaxies with the redshift and the angular separation between the galaxy position and the luminosity-weighted centre of the cluster. We normalize all cluster-centric radii by R_{500} (the radius at which the average interior density is 500 times the critical density of the Universe) of each cluster which we compute as

$$R_{500} = R_{200m}/2.7, \tag{2.1}$$

where

$$R_{200m} = 1.61\,{\rm Mpc}\left(\frac{M_{\rm halo}}{10^{14}\,{\rm M}_{\odot}}\right)^{1/3}(1+z_{\rm group})^{-1} \tag{2.2}$$

is the radius at which the average interior density is equal to 200 times the critical mass density of the Universe (Yang et al., 2007; Tinker et al., 2008), and we have assumed an NFW density profile (Navarro, Frenk, and White, 1997) with a concentration given by the concentration-mass relation of Macciò et al. (2007) (Wang et al., 2014). Our sample of galaxy clusters is a subset of the Yang catalogue including only clusters with ten or more member galaxies (2559 clusters). The cut-off in membership is chosen in order to be able to classify the shape of the velocity profile for each cluster with relative accuracy (Hou et al., 2009). Fig. 2.1 shows the $M_{\rm halo}$-redshift distribution for the parent sample (grey contours) with the 58 X-ray matched clusters (see Section 2.2) overplotted as stars colour-coded by the number of galaxies identified in each cluster. As expected, at fixed redshift the observed cluster richness increases with halo mass and at fixed halo mass the observed cluster richness decreases with redshift. The latter is a selection effect due to increasing incompleteness at higher redshift. To check whether this incompleteness may be biasing our results we repeat our analysis on "low-z" ($z < 0.10$) and "high-z" ($z \geq 0.10$) subsamples (results not shown) and find no difference between the

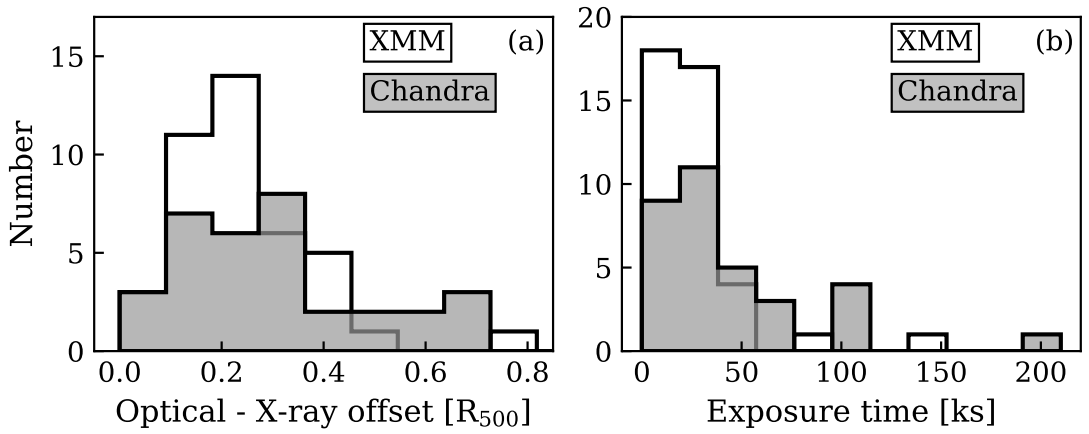

FIGURE 2.2: Distribution of the offset between the X-ray peak and cluster luminosity-weighted centre (left) and X-ray exposure time (right) for the clusters in our sample, for *Chandra* (grey) and *XMM-Newton* (white).

conclusions drawn from either redshift subsample. Therefore moving forward, we consider the entire redshift range.

2.2.2 X-ray Matched Clusters

In order to make connections between optical measures of cluster relaxedness and the shape of the cluster extended X-ray profile we searched the *Chandra* and *XMM-Newton* science archives at the positions of the luminosity-weighted centres of each of the 2559 $N > 10$ Yang clusters. With a search radius of 5 arcmin we matched observations of extended X-ray emission to the corresponding optically identified cluster, only including observations with clean exposure times ≥ 10 ks. We also exclude systems where multiple Yang ($N > 10$) clusters are matched to the same X-ray observation to avoid the potential overlap of X-ray emission from physically distinct systems in projection (this was only the case for < 5 per cent of matches). This matching results in 58 Yang clusters with X-ray coverage. Fig. 2.2a shows the projected separation between the luminosity-weighted centre and the X-ray centre of each Yang cluster for *Chandra* (grey) and *XMM-Newton* (white), whereas Fig. 2.2b shows the respective filtered exposure times for the observations. X-ray centres are calculated as the position of the brightest pixel in

the X-ray image after smoothing with a Gaussian kernel with a bandwidth of 40 kpc (as in Nurgaliev et al. 2013). As shown in Fig. 2.2a, the offset between the optical and X-ray centres is far smaller than the virial radius for all systems.

Chandra observations were reprocessed, cleaned, and calibrated with the latest version of CIAO (CIAO version 4.9, CALDB version 4.7.5). Charge transfer inefficiency and time-dependent gain corrections were applied and observations were filtered for background flares with the LC_CLEAN script with a 3σ threshold. Exposure corrected images are then created with exposure maps generated at an energy of 1.5 keV, the average peak emission of our sample. Images were created in the 0.5-5 keV energy band to maximize the ratio between cluster and background flux (Nurgaliev et al., 2013). Point sources are identified with the WAVDETECT script and are filled with local Poisson noise with DMFILTH, blank sky background images are generated for each observation with the BLANKSKY and BLANKSKY_IMAGE scripts. All observations are then checked by eye to ensure that no obvious point sources were missed by the algorithm. For systems with multiple observations, combined images and exposure maps were generated with the MERGE_OBS script and blank sky background images were combined with REPROJECT_IMAGE.

Data reduction for *XMM-Newton* observations was done with the Extended Source Analysis Software within the *XMM-Newton* Science Analysis System (SAS, version 16.0.0). Calibrated event files were generated with the EMCHAIN script, and filtered event lists were generated with MOS-FILTER. Exposure corrected images were created in the 0.5-5 keV band, and point sources were identified with the CHEESE script and subsequently filled with local Poisson noise with the CIAO script DMFILTH. Again, images are checked by eye to ensure no obvious point sources are missed. For *XMM-Newton* observations we only use the MOS exposures to avoid the complications of the many chip gaps on the PN detector. MOS exposures are combined with the COMB script to give merged images, exposure maps, and background images. For systems with multiple observations, images, exposure maps, and background images are merged with the CIAO script REPROJECT_IMAGE.

The pixel scale of the resulting images is 0.5 arcsec for *Chandra* and 2.5 arcsec for *XMM-Newton*. We calculate X-ray asymmetries and centroid shifts at these

native resolutions to avoid losing information from the higher resolution *Chandra* images, however we note that binning the *Chandra* images to the *XMM-Newton* resolution does not alter the results. Furthermore, when we compare asymmetries and centroid shifts computed for systems which are observed by both *Chandra* and *XMM-Newton*, we see no bias introduced by the resolution difference.

2.3 Cluster Relaxation Measures

2.3.1 Optical

In this study we implement three previously used optical measures to parametrize the relaxation of clusters: the Anderson-Darling statistic, the stellar mass ratio between the second most-massive and the most-massive cluster galaxy (M_2/M_1), and the offset between the position of the MMG and the luminosity-weighted centre of the cluster (MMG offset).

Anderson-Darling Statistic

The Anderson-Darling (AD) test is a statistical normality test which measures the "distance" between the cumulative distribution functions (CDFs) corresponding to the data as well as the ideal case of a normal distribution (Anderson and Darling, 1952). The distance between the CDFs is parametrized by the AD statistic (A^2), in the sense that large values of this statistic correspond to larger deviations from normality. The AD statistic, A^2 is given by

$$A^2 = -n - \frac{1}{n}\sum_{i=1}^{n}[2i-1][\ln \Phi(x_i) + \ln(1-\Phi(x_{n+1-i}))] \tag{2.3}$$

where x_i are the length-n ordered data and $\Phi(x_i)$ is the CDF of the hypothetical underlying distribution (Gaussian in this application).

In the context of cluster evolution, it is expected that galaxies in evolved, dynamically old clusters should display projected velocity profiles which are well fit by a normal distribution; conversely more unrelaxed clusters will show larger deviations from normality (Yahil and Vidal, 1977; Bird and Beers, 1993; Ribeiro et al., 2013). The AD test can therefore be applied to the velocity distributions of

member galaxies to discriminate between relaxed and unrelaxed clusters (e.g. Hou et al., 2009). In this work we use the AD statistic as a proxy for cluster relaxedness, where increasing values of A^2 are indicative of progressively more unrelaxed clusters. It is also common in the literature to use the p-value associated with the AD statistic to define a dichotomy between Gaussian and non-Gaussian clusters (e.g. Hou et al., 2009; Martínez and Zandivarez, 2012; Roberts and Parker, 2017), which we consider in Section 2.4.3.

Stellar Mass Gap

The second optical parameter we use to classify the relaxation of galaxy clusters is the stellar mass ratio between the second most-massive and most-massive galaxies in a given cluster. Since the MMG should sit near the centre of the cluster potential, it will progressively grow in stellar mass by dominating gas accretion within the cluster, and more importantly, by cannibalizing galaxies through minor mergers (e.g. De Lucia and Blaizot, 2007; Ruszkowski and Springel, 2009; Lin et al., 2013; McDonald et al., 2016). This MMG mass growth will therefore drive down M_2/M_1 in dynamically old clusters, whereas more unrelaxed systems will have had less time to establish a dominant MMG.

The reliability of M_2/M_1 is contingent on correctly identifying both the MMG and M_2. A particular concern when using SDSS data is the potential for galaxies missing spectra due to fibre collisions; this has an increasing impact in the dense inner regions of groups and clusters where one would expect to find the MMG and M_2. In an attempt to mitigate the effects of fibre collisions we use sample III from the Yang group catalogue which corrects for fibre collisions by assigning fibre collision galaxies the redshift of the galaxy they 'collide' with. While this procedure accounts for fibre collisions it also introduces potential impurities to the group catalogue (some fibre collision galaxies will have redshifts which are catastrophically different from the one they are assigned), we delay a more detailed discussion of these effects until Section 2.5.2 though we urge the reader to keep these caveats in mind when interpreting results in Section 2.4.1.

MMG Offset

The final optical relaxation parameter we consider is the projected offset between the MMG and the luminosity-weighted cluster centre, $\delta R_{\rm MMG}$. There is currently no consensus regarding the best observational definition of group centre, with the position of the MMG, the position of the X-ray peak, and the luminosity or mass-weighted centre all being popular choices (e.g. George et al., 2012). For relaxed clusters it is expected that all of the aforementioned centre definitions will be relatively consistent with one another, but more unrelaxed clusters may show significant offsets between different cluster centre choices. In particular, many unrelaxed clusters host MMGs with large offsets from other cluster centre definitions (e.g. Katayama et al., 2003; Sanderson, Edge, and Smith, 2009; Carollo et al., 2013; Khosroshahi et al., 2017), therefore the offset between MMG position and luminosity-weighted centre can be a useful measure of cluster relaxation.

As with the stellar mass gap, there are potential complications with regards to interpreting the MMG offset as a relaxation probe. For example, it is based on the assumption that in a relatively relaxed system the MMG (or brightest galaxy) will be located at rest at the centre of the dark matter potential well – the so-called central galaxy paradigm (CGP). However, some recent studies have called into question whether or not the CGP is valid in all systems (van den Bosch et al., 2005; Coziol et al., 2009; Skibba et al., 2011; Sehgal et al., 2013; Lauer et al., 2014; Hoshino et al., 2015). Additionally, even in relaxed systems the MMG may oscillate about the centre of a cored dark-matter potential (e.g. Harvey et al., 2017) further complicating the interpretation of the radial offset of the central galaxy. Yet again, we will defer a full discussion of these effects to Section 2.5.2.

2.3.2 X-ray

Photon Asymmetry

Photon asymmetry is a novel technique to measure the asymmetry of X-ray profiles which is model-independent and robust across a wide range in X-ray counts and background level (Nurgaliev et al., 2013). In this work we will give a brief

discussion of the photon asymmetry computation, but for a complete description, including tests of robustness, we direct the reader to Nurgaliev et al. (2013).

The photon asymmetry measures the degree to which the count profile of an X-ray observation is axisymmetric around the X-ray peak, or phrased alternatively, the degree to which the polar angles of X-ray counts are distributed uniformly over the range $0 \leq \phi \leq 2\pi$. This is accomplished quantitatively with Watson's U2 test which compares the polar angle CDF for observed counts to a uniform CDF corresponding to an idealized axisymmetric profile (Watson, 1961). In a given radial annulus, the distance between the observed count distribution and a uniform distribution is given by

$$\hat{d}_{N,C} = \frac{N}{C^2}\left(U_N^2 - \frac{1}{12}\right), \tag{2.4}$$

where N is the total number of counts within the annulus, C is the number of counts intrinsic to the cluster (i.e. above the background) within the annulus, and U_N^2 is Watson's statistic. We follow Nurgaliev et al. (2013) and compute Watson's statistic with the following relation (see Watson 1961):

$$\begin{aligned} U_N^2(\phi_0) = \frac{1}{12N} + \sum_{i=0}^{N-1}\left(\frac{2i+1}{2N} - F(\phi_i)\right)^2 \\ - N\left(\frac{1}{2} - \frac{1}{N}\sum_{i=0}^{N-1} F(\phi_i)\right)^2, \end{aligned} \tag{2.5}$$

where ϕ_i are the observed count polar angles, ϕ_0 is the origin polar angle on the circle, and F is the uniform CDF. To obtain the final value for U_N^2 we minimize the statistic over all origin angles on the circle

$$U_N^2 = \min_{\text{origin on circle, } \phi_o} U_N^2(\phi_0). \tag{2.6}$$

The final value for the photon asymmetry, A_{phot}, is given by the cluster weighted average of $\hat{d}_{N,C}$ in each radial annulus, namely

$$A_{\text{phot}} = 100 \sum_{k=1}^{N_{\text{ann}}} C_k \hat{d}_{N_k,C_k} \Big/ \sum_{k=1}^{N_{\text{ann}}} C_k. \tag{2.7}$$

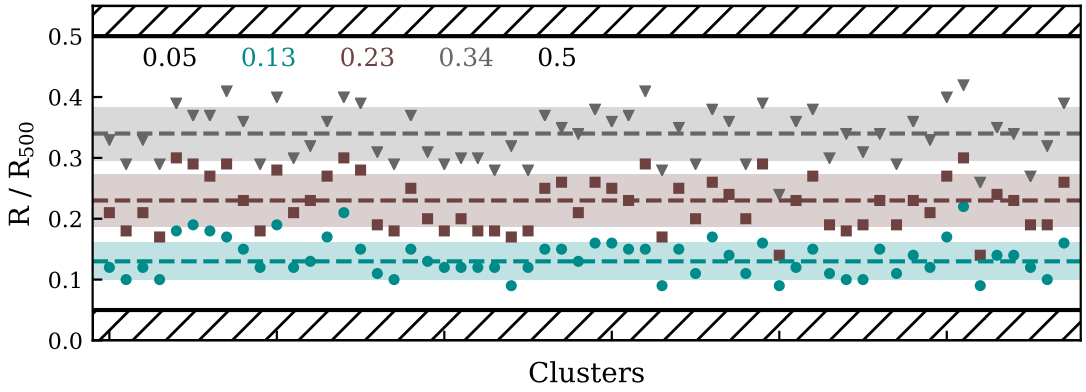

FIGURE 2.3: "Optimal annuli" positions (constant cluster counts) for each cluster in the X-ray matched sample. For four annuli, this amounts to two fixed end points (black) and three inner boundaries with variable positions (teal circles, maroon squares, grey triangles). Dashed lines correspond to the median value for each annulus boundary (values of the boundaries are also printed at the top of the figure), which we take to be our final annuli positions when computing asymmetries. Hatched areas denote radial regions not included in the asymmetry calculation (see Section 3.2.1) and shaded regions show the 1σ scatter for each annuli position.

We assume a uniform background which we estimate from blank-sky images for each observation and subsequently compute the number of cluster counts, C, by subtracting the expected number of background counts within the annulus from the total number of observed counts. Following Nurgaliev et al. (2013) we compute $\hat{d}_{N,C}$ in four radial annuli, which in this work range between $0.05\,R_{500}$ and $0.5\,R_{500}$. This choice of four annuli ensures that we will obtain at least hundreds of cluster counts in each annulus for the low-count observations (∼a few thousand counts). Optimal annuli are selected by requiring an approximately constant number of cluster counts within each annulus. We define the annuli radii as those which minimize the variance in cluster counts across each of the annuli. In Fig. 2.3 we show the optimal annuli positions for each of the 58 clusters in the X-ray matched sample. We note that while there is some variation in optimal annuli from cluster to cluster, in general the scatter is relatively small and there is no overlap between the 1σ scatter of neighbouring annuli. The final annuli edges are taken to be the median values across all of the clusters, which corresponds to $\{0.05, 0.13, 0.23, 0.34, 0.50\} \times R_{500}$. The inner boundary of $0.05\,R_{500}$ is set to avoid pixelation artefacts at small radii (Nurgaliev et al., 2013), and the outer boundary of $0.5\,R_{500}$ is chosen to enclose the majority of the emission while still ensuring chip coverage. The large angular sizes of some of the high-mass, low-redshift systems ($R_{500} \sim 15 - 20$ arcmin) prevents us from computing $A_{\rm phot}$ out to a full R_{500} since they extend beyond the edge of the detector. Statistical uncertainties on $A_{\rm phot}$ are estimated following Nurgaliev et al. (2013) by randomly resampling half of the observed counts 500 times and recalculating $A_{\rm phot}$ for each iteration. For clusters with both *Chandra* and *XMM-Newton* observations, we compute $A_{\rm phot}$ for the *Chandra* and *XMM* data separately and then combine them as a count-weighted average.

Centroid Shift

A commonly used X-ray relaxation proxy is the centroid shift, w, which measures the shift of the X-ray surface brightness centroid in different radial apertures. For a system in dynamical equilibrium, the centre of mass of the ICM (i.e. the centroid) should be independent of scale, whereas an unrelaxed system with substructure can have a centre of mass which depends on radius (e.g. Mohr, Fabricant, and Geller,

1993). To compute centroid shifts we use the following relation (e.g. Böhringer et al., 2010):

$$w = \left[\frac{1}{N-1}\sum_i (\Delta_i - \langle\Delta\rangle)^2\right]^{1/2} \times \frac{1}{R_{\rm max}}, \tag{2.8}$$

where Δ_i is the offset between the X-ray peak and the centroid position within the ith aperture, N is the number of apertures, and $R_{\rm max}$ is the radius of the largest aperture. Centroids are determined from the moments of the exposure-corrected X-ray images [1], and the X-ray peak is considered to be the position of the brightest pixel after smoothing with a Gaussian kernel with a bandwidth of 40 kpc. The smallest aperture that we consider is $R < 0.1\,R_{500}$ and we progressively increase the aperture radius by $0.05\,R_{500}$ out to a maximum of $0.5\,R_{500}$, for a total of nine apertures. These aperture choices are motivated by previous studies (Böhringer et al., 2010; Nurgaliev et al., 2013; Rasia, Meneghetti, and Ettori, 2013; Weißmann et al., 2013) as well as ensuring chip coverage as was done to measure $A_{\rm phot}$ in Section 3.2.1. As with $A_{\rm phot}$, uncertainties for the centroid shift are determined from randomly resampling the X-ray images and recalculating w, and for clusters with observations from *Chandra* and *XMM-Newton* w is computed as a count-weighted average.

2.4 Results

2.4.1 Relationship between X-ray and Optical Relaxation Proxies

To explore the consistency between group relaxation measures in the X-ray and optical, we measure the correlations between photon asymmetry and centroid shifts and the three optical relaxation parameters (A^2, M_2/M_1, $\delta R_{\rm MMG}$). To quantify the correlations between these parameters, we use two different methods:

1. We fit a simple power law to each relationship and derive uncertainties on the slope and normalization with bootstrap resampling.

[1] `http://photutils.readthedocs.io/en/stable/photutils/centroids.html`

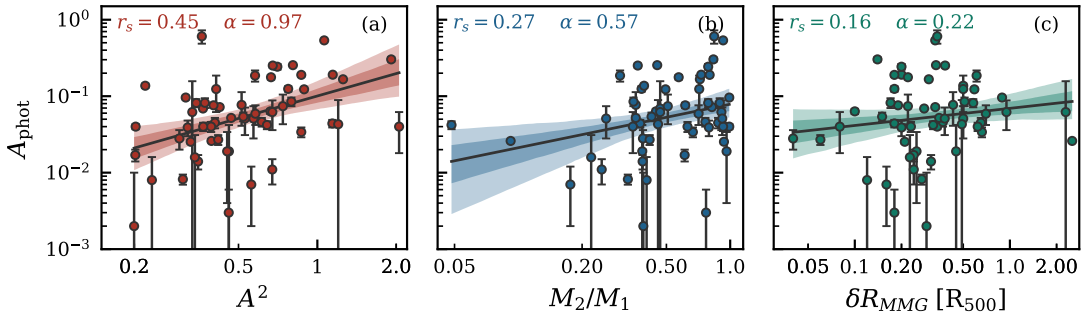

FIGURE 2.4: Photon asymmetry versus optical relaxation parameters (A^2, M_2/M_1, $\delta R_{\rm MMG}$), error bars are 1σ resampling uncertainties. The solid line is the best-fitting power-law relationship and the shaded regions correspond to the 68 and 95 per cent bootstrap confidence intervals. The Spearman correlation coefficient, r_s, and the best-fitting power-law slope, α, are indicated in the upper region of each panel.

2. We compute Spearman's rank correlation coefficient, r_s, (which is preferred over the Pearson correlation due to its non-parametric nature) for each relationship to quantify the percentile at which the data are consistent with a correlation.

Photon Asymmetry

In Figs 2.4a-c we show the relationship between photon asymmetry and the three optical relaxation proxies. The $A_{\rm phot} - A^2$ relationship shows a significant correlation as measured by both the power-law fit and by the Spearman test. The best-fitting power law has a positive slope at 3.5σ and the Spearman test gives a positive correlation at the >99.9 per cent level. The $A_{\rm phot} - M_2/M_1$ relationship shows a weaker (but still significant) correlation with a positive slope at 2.9σ and a Spearman correlation at the 96 per cent level. In contrast, the $A_{\rm phot} - \delta R_{\rm MMG}$ relationship does not display a significant correlation by either measure, with a power law slope consistent with zero and a Spearman p-value of 0.23.

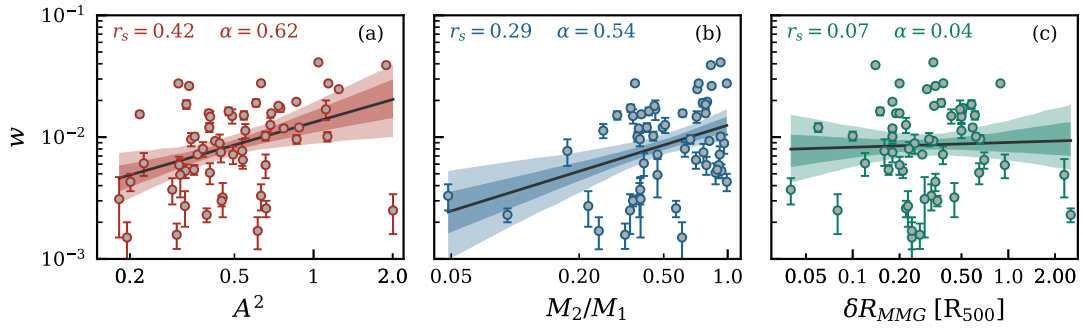

FIGURE 2.5: Same as Fig. 2.4 but for the centroid shift instead of photon asymmetry.

Centroid Shift

In Figs 2.5a-c we now show the relationship between the optical relaxation parameters and the centroid shift as the X-ray relaxation proxy. The results in Fig. 3.5 are very similar to those in Fig. 3.4, with the optical relaxation proxies tracing the centroid shift analogously to photon asymmetry. The $w - A^2$ relationship has a best-fitting positive slope at 2.8σ and the Spearman test gives a positive correlation at the 99.9 per cent level. The $w - M_2/M_1$ again shows a significant correlation as well with a positive slope at 3.6σ and a positive Spearman correlation at the 97 per cent level. Finally, we find no evidence for a correlation between the centroid shift and the MMG offset, with a power-law slope consistent with zero and a Spearman p-value of 0.62.

Based on the results from this section we conclude that Anderson-Darling statistic provides the best correlation with X-ray asymmetry among the three optical relaxation measures, as it shows the strongest Spearman correlations with the X-ray relaxation proxies, and the $A_{\rm phot} - A^2$ and $w - A^2$ relationships have positive power-law slopes at $\geq 3\sigma$. Modulo scatter, this correlation lends credence to the use of the Anderson-Darling test to quantify cluster relaxation for a large sample, as the shape of the diffuse X-ray profile is an independent (and arguably more direct) probe of the degree to which groups are unrelaxed/disturbed. Therefore, for the remainder of this paper we will focus on the $A_{\rm phot} - A^2$ and $w - A^2$ relationships. In the next section, we extend this analysis by investigating the halo mass dependence of the $A_{\rm phot} - A^2$ and $w - A^2$ relations.

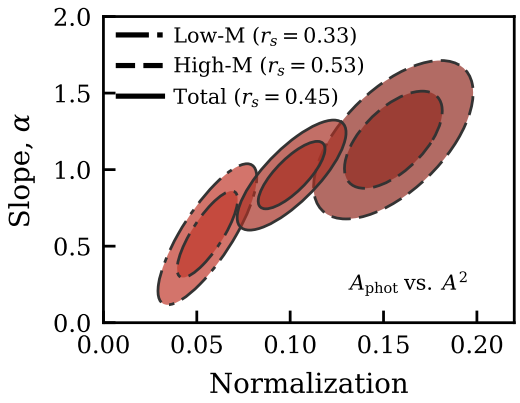

FIGURE 2.6: 68 and 95 per cent confidence ellipses for the photon asymmetry versus AD statistic best-fitting power-law parameters for low-mass haloes ($M_{\rm halo} < 10^{14.5}\,{\rm M}_\odot$, dot-dashed), high-mass haloes ($M_{\rm halo} \leq 10^{14.5}\,{\rm M}_\odot$, dashed), and the total sample (solid). Spearman correlation coefficients are denoted for each sample.

2.4.2 Halo Mass Dependence of X-ray-Optical Relations

In Section 2.4.1 we presented a significant correlation between the AD statistic for a given cluster and X-ray relaxation parameters (the photon asymmetry and the centroid shift). In this section we further divide the sample into systems with small halo masses and those with large halo masses to investigate if the $A_{\rm phot} - A^2$ and $w - A^2$ correlations vary with cluster halo mass. We choose the median halo mass of our cluster sample, $M_{\rm halo,\,med} = 10^{14.5}\,{\rm M}_\odot$, to make this division.

Photon Asymmetry

In Fig. 2.6 we show the confidence ellipses (68 and 95 per cent levels) corresponding to the power-law fit results to the $A_{\rm phot} - A^2$ relationship for high- and low-mass haloes (as well as the total sample). The separation between the high- and low-mass ellipses suggests that high- and low-mass clusters follow somewhat different scaling relations between $A_{\rm phot} - A^2$. For high-mass haloes a significant correlation is still seen, with a best-fitting slope of $1.15^{+0.42}_{-0.39}$ and a Spearman correlation significant at the 99.4 per cent level. For low-mass haloes the correlation is somewhat

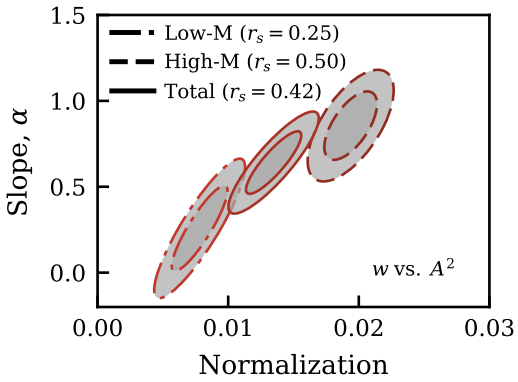

FIGURE 2.7: Same as Fig. 2.6 but for the centroid shift instead of photon asymmetry.

weaker with a best-fitting power law slope of $0.61^{+0.44}_{-0.33}$ and a Spearman correlation significant at the 94 per cent level. The best-fitting slopes for the low- and high-mass haloes are equal within uncertainties, but the normalization is larger for high-mass haloes at the $> 2\sigma$ level. Additionally, we find that high-mass haloes have a slightly larger median $A_{\rm phot}$ (0.08 ± 0.03) than low-mass haloes (0.04 ± 0.01).

Centroid Shift

In Fig. 2.7 we now show the power-law fit results to the $w - A^2$ relationship for the two halo mass subsamples. We find qualitatively similar results when considering centroid shift instead of photon asymmetry, with the high-mass haloes displaying a clear correlation (slope: $0.86^{+0.27}_{-0.24}$, Spearman p-value: 0.005) whereas the correlation for low-mass haloes is marginal and not statistically significant (slope: $0.24^{+0.35}_{-0.30}$, Spearman p-value: 0.19). We also find that the median centroid shift is larger for high-mass haloes (0.015 ± 0.002) than low-mass haloes (0.007 ± 0.001).

2.4.3 The Discrete Case: X-ray Asymmetry of Gaussian and non-Gaussian Groups

Thus far we have treated the shape of the velocity distribution in a continuous fashion with the AD statistic, though it is commonplace in the literature to define

a dichotomy between "'Gaussian" and "non-Gaussian" clusters (Hou et al., 2009; Ribeiro et al., 2013; de Carvalho et al., 2017; Roberts and Parker, 2017). We use the AD test and choose a critical p-value of 0.10 to define G and NG groups – where G groups have $p_{AD} \geq 0.10$ and NG groups have $p_{AD} < 0.10$ (though our results are not sensitive to the precise p-value chosen over a reasonable range).

To quantify the relationship between photon asymmetry and whether a cluster is classified as G or NG we employ the method of logistic regression (e.g. Cox, 1958). Logistic regression is a classification tool used to estimate the probability of a binary response as a function of one (or many) independent variables, which may be numeric or categorical. For this application, a galaxy cluster is classified as either G or NG (the Boolean, dependent variable) and we are interested in the probability of a galaxy cluster being NG as a function of photon asymmetry or centroid shift (the numeric, independent variable). The estimated probability is then

$$\hat{p} = \frac{e^{\beta_1 x + \beta_0}}{1 + e^{\beta_1 x + \beta_0}} \tag{2.9}$$

where β_0 and β_1 are parameters of the fit, and for this work we have $\hat{p} = \hat{p}(NG)$ and $x = \log A_{\rm phot}$ or $\log w$.

Photon Asymmetry

In Fig. 2.8 we show the photon asymmetry for G (0, green) and NG (1, purple) clusters along with the best-fitting logistic curve (black line, equation 9) describing the probability of being classified as NG as a function of $A_{\rm phot}$. It is clear from Fig. 2.8 that the probability of a cluster being NG increases with photon asymmetry, we obtain a best-fitting coefficient of $\beta_1 = 2.1 \pm 0.8$ indicating a significant correlation at 2.6σ. According to our logistic model, the $A_{\rm phot}$ value where the probability of being an NG cluster reaches 50 per cent is $A_{\rm phot} = 0.14$ and the asymmetry where the probability reaches 75 per cent is $A_{\rm phot} = 0.46$. Additionally in Fig. 2.8 we show the median photon asymmetry and the 1σ standard error for G and NG clusters, NG clusters have a larger median asymmetry of 0.13 ± 0.03 compared to 0.05 ± 0.02 for G clusters.

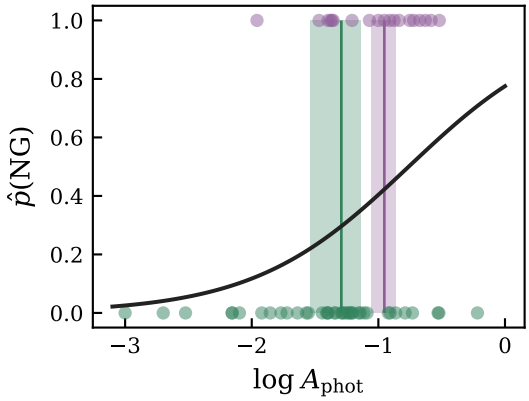

FIGURE 2.8: Estimated probability of a cluster being non-Gaussian as a function of photon asymmetry. Photon asymmetry data points are shown for Gaussian (0, green) and non-Gaussian (1, purple) clusters and the black line shows the best-fitting logistic curve. Shaded vertical lines show the median asymmetry and 1σ standard error for Gaussian and non-Gaussian groups.

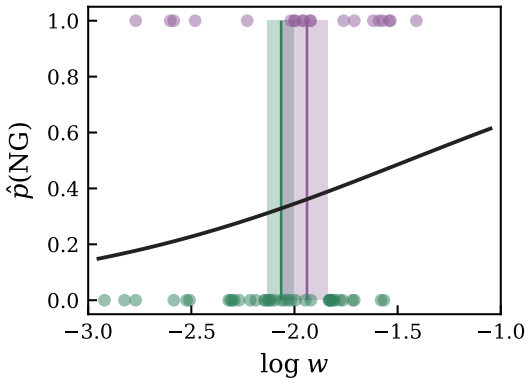

FIGURE 2.9: Same as Fig. 2.8 but for the centroid shift instead of photon asymmetry.

Centroid Shift

In Fig. 2.9 we show an analogous logistic regression to Fig. 2.8, with the centroid shift as the numeric variable. Examining Fig. 2.9 it is clear that the distinction between G and NG clusters is not as strong as it was with photon asymmetry. From the fit we obtain a best-fitting coefficient of $\beta_1 = 1.2 \pm 0.8$, indicating only a marginal correlation at 1.5σ. From this fit the value of w where $\hat{p}(NG)$ reaches 50 per cent is $w = 0.04$. We also show the median value for w for G (green) and NG (purple) clusters, and find that while the median centroid shift is slightly larger for NG clusters, this difference is not significant (G: 0.009 ± 0.001, NG: 0.012 ± 0.003).

2.5 Discussion

2.5.1 The Anderson-Darling Test as a Relaxation Proxy

The primary result from this paper is the strong correlation detected between X-ray relaxation measures and both the AD statistic for a given cluster (Figs 2.4a and 2.5a), as well as the probability of a system being NG when considering the dichotomy of G and NG clusters (at least for $A_{\rm phot}$, Fig. 2.8). We argue that this is an important confirmation of the usefulness of the AD test to quantitatively identify unrelaxed/disturbed systems. This, however, is only true in the statistical sense as there is still significant scatter around the $A_{\rm phot} - A^2$ and $w - A^2$ relations. The AD test may or may not accurately classify the dynamical state of an individual cluster, but applied to a large statistical sample it is a useful tool to identify systems which are on average relaxed or unrelaxed. It is also worth considering whether the group finder preferentially selects G or NG clusters. The Yang et al. group finder constructs clusters assuming that the galaxy phase-space distribution follows a spherical NFW profile, which could bias the group finder in favour of G clusters (i.e. assuming a spherical, symmetric distribution). The analysis presented here does not account for any such bias, but since the clusters are all selected with the same algorithm the correlations found are robust for this sample.

The AD test has become a relatively common tool used to identify unrelaxed systems from large redshift surveys (e.g. Hou et al., 2009; Ribeiro, Lopes, and

Trevisan, 2010; Martínez and Zandivarez, 2012; Hou et al., 2013; Ribeiro et al., 2013; Roberts and Parker, 2017), though its efficacy has only been tested in detail with Monte Carlo simulations sampling from idealized parent distributions (both Gaussian and non-Gaussian, Hou et al. 2009; Ribeiro et al. 2013). These tests have provided useful insight into the strengths and limitations of the AD test, but it is also important to test this technique in a more physical setting. The comparison to diffuse X-ray morphology in this work provides one such test in an astronomical context. In an upcoming paper we perform a detailed analysis on the AD test applied to groups and clusters in large, cosmological, N-body simulations. This will allow us to explore outcomes such as the false-positive rate, as well as potential differences in satellite time-since-infall or halo age for G and NG systems in a cosmological context.

The results of Section 2.4.3 can also be used to constrain the dividing line between relaxed and unrelaxed clusters. Based on the logistic regression model, the value of $A_{\rm phot}$ above which the probability of being an NG cluster exceeds 50 per cent is $A_{\rm phot} = 0.14$ and the value above which the probability exceeds 75 per cent is $A_{\rm phot} = 0.46$. Correspondingly, the median $A_{\rm phot}$ for NG clusters is 0.13 ± 0.03, suggesting that $A_{\rm phot} \gtrsim 0.10 - 0.50$ may be a useful dividing line between relaxed and unrelaxed clusters, depending on the desired level of purity. In McDonald et al. (2017) a threshold of $A_{\rm phot} < 0.10$ is chosen to identify relaxed clusters, while this threshold was chosen arbitrarily we have shown here that this is a reasonable choice based on cluster velocity distribution measurements. The threshold used to identify unrelaxed clusters in McDonald et al. (2017) is $A_{\rm phot} > 0.50$, which also shows excellent agreement with the dividing lines that we derive from velocity measurements. The choice of $A_{\rm phot} > 0.50$ is motivated by simulations of cluster major mergers from Nurgaliev et al. (2017) who suggest that $A_{\rm phot} \gtrsim 0.2 - 0.6$ is a useful threshold to identify disturbed clusters, again corresponding very closely to the range we determine in this work. This shows that using the AD test (in this case with a p-value of 0.10) to identify relaxed and unrelaxed clusters corresponds very closely to previous results using X-ray techniques.

When using the centroid shift, w, instead of photon asymmetry, the logistic regression model does not separate G and NG clusters as distinctly, but we can still use the model to constrain a dividing line. In particular, the regression model

suggests that the probability of being a NG cluster reaches 50 per cent at $w = 0.040$. This is larger by a factor of a few than the boundary between regular and disturbed objects in previous X-ray analyses, which ranges between $w \simeq 0.01$ and $w \simeq 0.02$ (O'Hara et al., 2006; Cassano et al., 2010; Weißmann et al., 2013). Given that the logistic regression only detects a marginal correlation between $\hat{p}(NG)$ and w, the dividing line that we derive here is likely not well constrained.

We can also contrast the two different X-ray relaxation proxies by highlighting any differences in the photon asymmetry and centroid shift relationships with the AD statistic. When considering the continuous case in Section 2.4.1 we see very similar behaviour in the $A_{\rm phot}-A^2$ and $w-A^2$ relationships, consistent with the fact that photon asymmetry and centroid shift have been shown to correlate strongly (Nurgaliev et al., 2013). However the discrete case in Section 2.4.3 shows that G and NG clusters are more clearly segregated in terms of photon asymmetry than centroid shift, perhaps suggesting that photon asymmetry is a slightly stronger identifier of dynamically unrelaxed clusters, though a larger sample is required to robustly determine this.

Finally, in Section 2.4.2 we explored the halo mass dependence of the $A_{\rm phot}-A^2$ and $w-A^2$ relationships by separating the sample into subsamples of low-mass ($M_{\rm halo} < 10^{14.5}\,{\rm M}_\odot$) and high-mass clusters ($M_{\rm halo} \geq 10^{14.5}\,{\rm M}_\odot$). We find small differences between the low-mass and high-mass relations, namely, both the $A_{\rm phot}-A^2$ and $w-A^2$ relationships for high-mass clusters have larger normalizations, whereas the slopes are consistent between the high- and low-mass samples. In addition, the median values for $A_{\rm phot}$ and w are slightly larger for high-mass clusters compared to low-mass clusters. Nurgaliev et al. (2013) show that the $A_{\rm phot}$ and w statistics are robust against varying numbers of X-ray counts above ∼2000 counts ($A_{\rm phot}$ is robust even below 2000 counts). All of the systems in this work have $N_{\rm counts} > 2000$, therefore it is unlikely that these differences in asymmetry and centroid shift are being driven by the relatively high-count observations of massive systems. This result hints that low-mass and high-mass clusters may follow slightly different scaling relations when it comes to $A_{\rm phot}$ or w versus A^2, though a larger sample is necessary to build up the statistics required to conclude this with high confidence. In principle, this difference could be explained through simple hierarchical growth where low-mass haloes are on average more virialized than

higher-mass clusters at the present day. High-mass clusters will be more recently formed through mergers and accretion which can in turn increase $A_{\rm phot}$ and w (e.g. Cassano et al., 2010; Nurgaliev et al., 2017). From the optical perspective, we also find that high-mass clusters have velocity distributions which are less Gaussian than low-mass systems, in agreement with previous studies (de Carvalho et al., 2017; Roberts and Parker, 2017). Although it is important to note that it is easier to statistically identify departures from normality for high-mass systems with many members.

2.5.2 Interpretting MMG-based Relaxation Parameters

The second optical relaxation proxy that shows a significant correlation with X-ray relaxation proxies is the stellar mass gap between the two most-massive cluster galaxies (see Section 2.4.1). The correlations between X-ray relaxation proxies and M_2/M_1 are found to be weaker than for A^2 (especially as measured by the Spearman correlation), potentially suggesting that M_2/M_1 is a poorer (though still useful) tracer of diffuse X-ray morphology. This may be expected given that satellite galaxies (i.e. the velocity distribution) and the diffuse hot gas profile should both trace the larger-scale cluster potential relatively directly, whereas central galaxy growth is governed more by dynamical interactions and gas accretion at the cluster centre. It is also possible that the $A_{\rm phot} - M_2/M_1$ and $w - M_2/M_1$ trends are being affected by selection effects related to the difficulty indentifying the true MMG (and second most massive galaxy) in these clusters. A particular concern regarding the SDSS is the impact of fibre collisions in the dense inner regions of clusters, as it has been estimated that up to 30 per cent of clusters may be missing a spectrum for the true BCG (Von Der Linden et al., 2007). In an attempt to mitigate the effect of fibre collisions we use the systems from sample III in the Yang group catalogue which attaches redshifts to galaxies that lack spectra due to fibre collisions by assigning these galaxies the redshift of the galaxy it "collided" with. While this procedure allows the group finder to include galaxies which otherwise would be missed due to fibre collisions, the trade-off is uncertainty regarding whether the added galaxies are true group members. $\sim$60 per cent of fibre collision galaxies have redshifts within $500\,{\rm km\,s^{-1}}$ of the estimated value (Zehavi et al., 2002), though this still leaves a significant number of fibre

collision galaxies which may have true redshifts that differ substantially from the assigned value. To ensure that our results are not being affected by the inclusion of these fibre collision galaxies we re-test the $A_{\rm phot} - M_2/M_1$, $w - M_2/M_1$, and $A_{\rm phot} - \delta R_{\rm MMG}$, $w - \delta R_{\rm MMG}$ relationships for correlations, now removing any systems where the MMG (and in the case of M_2/M_1, the second-most-massive galaxy as well) is a fibre collision galaxy. 26 per cent of the clusters in the sample have an MMG which is a fibre collision galaxy and 39 per cent of the sample have either the MMG or the second-most-massive galaxy as a fibre collision galaxy. Re-testing these relationships for correlations leaves the Spearman correlation coefficient virtually unchanged from Sections 2.4.1 and 2.4.1, suggesting that fibre collision galaxies are not biasing the results.

In Section 2.4.1 we find no evidence for a correlation between $A_{\rm phot}$ or w and $\delta R_{\rm MMG}$, which suggests that the MMG offset is not a reliable tracer of cluster relaxation. One caveat which is important to consider is the assumptions made to justify the use of M_2/M_1 and $\delta R_{\rm MMG}$ as relaxation proxies, in particular that for relaxed systems the MMG (or brightest galaxy) resides at rest at the centre of the dark matter potential – the so-called CGP. For example, if the MMG is instead a satellite galaxy then the use of M_2/M_1 as a relaxation measure may not be valid as it is predicated on the MMG being the central and growing through accretion and mergers at the centre of the potential well. Similarly, if the MMG is a satellite then its offset from the luminosity-weighted centre would not be expected to trace cluster relaxation. Many recent studies have called into question the ubiquity of the CGP by highlighting the fact that a substantial fraction of brightest cluster galaxies (BCGs) are significantly offset from the cluster centroid, both in terms of projected distance and velocity (van den Bosch et al., 2005; Coziol et al., 2009; Skibba et al., 2011; Sehgal et al., 2013; Lauer et al., 2014; Hoshino et al., 2015)). In particular, Skibba et al. (2011) find that the fraction of haloes where the brightest galaxy is in fact a satellite ($f_{\rm BNC}$) ranges from ∼25 per cent in low-mass haloes ($10^{12} \leq M \leq 2\times10^{13}\,h^{-1}\,{\rm M}_\odot$) to ∼40 per cent in high-mass haloes ($M \geq 5\times10^{13}\,h^{-1}\,{\rm M}_\odot$). Furthermore, Hoshino et al. (2015) find $f_{\rm BNC} \sim 20-30$ per cent for galaxies in redMaPPer clusters, and in terms of velocity Coziol et al. (2009) show that the median peculiar velocity for BCGs in a sample of Abell clusters is ∼1/3 of the cluster velocity dispersion. It is plausible that systems

where the CGP is not valid are diluting stronger trends between $A_{\rm phot}$ or w and M_2/M_1, or perhaps masking trends between $A_{\rm phot}$ or w and $\delta R_{\rm MMG}$. Unfortunately, identifying systems where the CGP is violated is difficult on a case-by-case basis, limited by observing in projection, and is generally done in the statistical sense for large samples (i.e. thousands) of groups and clusters (e.g. van den Bosch et al., 2005; Skibba et al., 2011). Therefore we continue to argue that the AD test (or some other measure of the velocity distribution shape, see e.g. Ribeiro et al. 2013) is a better optical relaxation proxy as it is not complicated by CGP assumptions.

2.6 Summary

In this paper we present a comparison between diffuse X-ray morphology and cluster relaxation proxies based on optical measures. With the Yang et al. (2007) SDSS group catalogue we match optically identified clusters with $N \geq 10$ members to X-ray observations from both the *Chandra* and *XMM-Newton* X-ray observatories. With a sample of 58 X-ray matched clusters we compare X-ray asymmetry and centroid shift to three different optical relaxation probes: the Anderson-Darling statistic, the stellar mass gap, and the MMG offset. The main conclusions of this work are as follows:

1. We detect a significant positive correlation between X-ray relaxation proxies (photon asymmetry, centroid shift) and Anderson-Darling statistic at $\sim 3-4\sigma$ as measured by both a power-law fit and by the Spearman correlation test, and a weaker correlation ($\sim 2-3\sigma$) between X-ray relaxation proxies and stellar mass gap (between two most-massive cluster galaxies).

2. We do not detect a significant correlation between X-ray asymmetry or centroid shift and the MMG offset.

3. We find that the $A_{\rm phot} - A^2$ and $w - A^2$ relationships vary somewhat for low-mass ($M_{\rm halo} < 10^{14.5}\,{\rm M}_\odot$) and high-mass ($M_{\rm halo} \geq 10^{14.5}\,{\rm M}_\odot$) clusters. Specifically, high-mass clusters have a best-fitting relationship with a larger normalization, and the median asymmetry and centroid shift are larger in high-mass systems. However, a definitive measure of the halo mass dependence awaits a larger sample.

4. When considering a dichotomy between Gaussian ($p_{AD} \geq 0.10$) and non-Gaussian ($p_{AD} < 0.10$) clusters we find that the probability of being a non-Gaussian system (as measured by a logistic regression) correlates clearly with X-ray asymmetry. Additionally, the median asymmetry of non-Gaussian clusters is larger than that of Gaussian clusters. When using the centroid shift as the X-ray relaxation proxy the correlation is marginal.

Though the scatter in the above-mentioned relations limits the reliability of this approach on a case-by-case basis, these results confirm the effectiveness of the shape of the projected velocity distribution as a proxy for cluster relaxation, when applied to a large sample.

Acknowledgments: We thank the Natural Sciences and Engineering Research Council of Canada for funding. This work made use of many open-source software packages, such as: `astropy` (Astropy Collaboration 2013), `matplotlib` (Hunter 2007), `numpy` (van der Walt, Colbert & Varoquaux 2011), `pandas` (McKinney 2010), `photutils` (Bradley et al. 2016), `scipy` (Jones et al. 2001), `statsmodels` (Seabold & Perktold 2010), and `topcat` (Taylor 2005).

Funding for the Sloan Digital Sky Survey IV has been provided by the Alfred P. Sloan Foundation, the U.S. Department of Energy Office of Science, and the Participating Institutions. SDSS-IV acknowledges support and resources from the Center for High-Performance Computing at the University of Utah. The SDSS web site is `www.sdss.org`.

SDSS-IV is managed by the Astrophysical Research Consortium for the Participating Institutions of the SDSS Collaboration including the Brazilian Participation Group, the Carnegie Institution for Science, Carnegie Mellon University, the Chilean Participation Group, the French Participation Group, Harvard-Smithsonian Center for Astrophysics, Instituto de Astrofísica de Canarias, The Johns Hopkins University, Kavli Institute for the Physics and Mathematics of

the Universe (IPMU)/University of Tokyo, Lawrence Berkeley National Laboratory, Leibniz Institut für Astrophysik Potsdam (AIP), Max-Planck-Institut für Astronomie (MPIA Heidelberg), Max-Planck-Institut für Astrophysik (MPA Garching), Max-Planck-Institut für Extraterrestrische Physik (MPE), National Astronomical Observatories of China, New Mexico State University, New York University, University of Notre Dame, Observatário Nacional/MCTI, The Ohio State University, Pennsylvania State University, Shanghai Astronomical Observatory, United Kingdom Participation Group, Universidad Nacional Autónoma de México, University of Arizona, University of Colorado Boulder, University of Oxford, University of Portsmouth, University of Utah, University of Virginia, University of Washington, University of Wisconsin, Vanderbilt University, and Yale University.

Bibliography

Abazajian, K. N. et al. (2009). *ApJS* 182, 543-558, pp. 543–558.

Anderson, T. W. and D. A. Darling (1952). *The Annals of Mathematical Statistics* 23, p. 193.

Barnes, J. E. (1989). *Nature* 338, pp. 123–126.

Bird, C. M. and T. C. Beers (1993). *AJ* 105, pp. 1596–1606.

Birnboim, Y. and A. Dekel (2003). *MNRAS* 345, pp. 349–364.

Blanton, M. R. and S. Roweis (2007). *AJ* 133, pp. 734–754.

Blanton, M. R. et al. (2005). *AJ* 129, pp. 2562–2578.

Böhringer, H. et al. (2010). *A&A* 514, A32, A32.

Bongiorno, A. et al. (2016). *A&A* 588, A78, A78.

Carollo, C. M. et al. (2013). *ApJ* 776, 71, p. 71.

Cassano, R. et al. (2010). *ApJl* 721, pp. L82–L85.

Cattaneo, A., A. Dekel, J. Devriendt, B. Guiderdoni, and J. Blaizot (2006). *MNRAS* 370, pp. 1651–1665.

Chung, A., J. H. van Gorkom, J. D. P. Kenney, and B. Vollmer (2007). *ApJl* 659, pp. L115–L119.

Cox, D. R. (1958). *Journal of the Royal Statistical Society. Series B (Methodological)* 20.2, pp. 215–242.

Coziol, R., H. Andernach, C. A. Caretta, K. A. Alamo-Martínez, and E. Tago (2009). *AJ* 137, 4795-4809, pp. 4795–4809.

Dariush, A. A. et al. (2010). *MNRAS* 405, pp. 1873–1887.

Davies, L. J. M. et al. (2015). *MNRAS* 452, pp. 616–636.

de Carvalho, R. R. et al. (2017). *AJ* 154.3, 96, p. 96.

De Lucia, G. and J. Blaizot (2007). *MNRAS* 375, pp. 2–14.

Dressler, A. (1980). *ApJ* 236, pp. 351–365.

Dubois, Y., R. Gavazzi, S. Peirani, and J. Silk (2013). *MNRAS* 433, pp. 3297–3313.

Eke, V. R. et al. (2005). *MNRAS* 362, pp. 1233–1246.

Ellison, S. L., D. R. Patton, L. Simard, and A. W. McConnachie (2008). *AJ* 135, pp. 1877–1899.

Fasano, G. et al. (2015). *MNRAS* 449, pp. 3927–3944.

Gabor, J. M. and R. Davé (2015). *MNRAS* 447, pp. 374–391.

Geller, M. J. and J. P. Huchra (1983). *ApJS* 52, pp. 61–87.

George, M. R. et al. (2012). *ApJ* 757, 2, p. 2.

Goto, T. et al. (2003). *MNRAS* 346, pp. 601–614.

Gunn, J. E. and J. R. Gott III (1972). *ApJ* 176, p. 1.

Gürkan, G. et al. (2015). *MNRAS* 452, pp. 3776–3794.

Haines, C. P. et al. (2015). *ApJ* 806, 101, p. 101.

Harvey, D., F. Courbin, J. P. Kneib, and I. G. McCarthy (2017). *ArXiv e-prints*.

Hoshino, H. et al. (2015). *MNRAS* 452, pp. 998–1013.

Hou, A., L. C. Parker, W. E. Harris, and D. J. Wilman (2009). *ApJ* 702, pp. 1199–1210.

Hou, A. et al. (2013). *MNRAS* 435, pp. 1715–1726.

Huchra, J. P. and M. J. Geller (1982). *ApJ* 257, pp. 423–437.

Joshi, G. D., J. Wadsley, and L. C. Parker (2017). *MNRAS* 468, pp. 4625–4634.

Katayama, H., K. Hayashida, F. Takahara, and Y. Fujita (2003). *ApJ* 585, pp. 687–693.

Khosroshahi, H. G., T. J. Ponman, and L. R. Jones (2007). *MNRAS* 377, pp. 595–606.

Khosroshahi, H. G. et al. (2017). *ApJ* 842, 81, p. 81.

Kimm, T. et al. (2009). *MNRAS* 394, pp. 1131–1147.

Knapen, J. H., J. E. Beckman, C. H. Heller, I. Shlosman, and R. S. de Jong (1995). *ApJ* 454, p. 623.

Kormendy, J. and R. C. Kennicutt Jr. (2004). *ARA&A* 42, pp. 603–683.

Larson, R. B., B. M. Tinsley, and C. N. Caldwell (1980). *ApJ* 237, pp. 692–707.

Lauer, T. R., M. Postman, M. A. Strauss, G. J. Graves, and N. E. Chisari (2014). *ApJ* 797, 82, p. 82.

Li, I. H., H. K. C. Yee, and E. Ellingson (2009). *ApJ* 698, pp. 83–98.

Lin, Y.-T. et al. (2013). *ApJ* 771, 61, p. 61.

Macciò, A. V. et al. (2007). *MNRAS* 378, pp. 55–71.

Martig, M., F. Bournaud, R. Teyssier, and A. Dekel (2009). *ApJ* 707, pp. 250–267.

Martínez, H. J. and A. Zandivarez (2012). *MNRAS* 419, pp. L24–L28.

Mayer, L., C. Mastropietro, J. Wadsley, J. Stadel, and B. Moore (2006). *MNRAS* 369, pp. 1021–1038.

McDonald, M. et al. (2016). *ApJ* 817, 86, p. 86.

McDonald, M. et al. (2017). *ApJ* 843, 28, p. 28.

Mihos, J. C. and L. Hernquist (1994a). *ApJl* 425, pp. L13–L16.

— (1994b). *ApJl* 431, pp. L9–L12.

Mohr, J. J., D. G. Fabricant, and M. J. Geller (1993). *ApJ* 413, pp. 492–505.

Mullaney, J. R. et al. (2015). *MNRAS* 453, pp. L83–L87.

Navarro, J. F., C. S. Frenk, and S. D. M. White (1997). *ApJ* 490, pp. 493–508.

Nurgaliev, D. et al. (2013). *ApJ* 779, 112, p. 112.

Nurgaliev, D. et al. (2017). *ApJ* 841, 5, p. 5.

O'Hara, T. B., J. J. Mohr, J. J. Bialek, and A. E. Evrard (2006). *ApJ* 639, pp. 64–80.

Oman, K. A. and M. J. Hudson (2016). *MNRAS* 463, pp. 3083–3095.

Parekh, V., K. van der Heyden, C. Ferrari, G. Angus, and B. Holwerda (2015). *A&A* 575, A127, A127.

Peng, Y., R. Maiolino, and R. Cochrane (2015). *Nature* 521, pp. 192–195.

Poggianti, B. M. et al. (2008). *ApJ* 684, 888-904, pp. 888–904.

Press, W. H. and M. Davis (1982). *ApJ* 259, pp. 449–473.

Rasia, E., M. Meneghetti, and S. Ettori (2013). *The Astronomical Review* 8.1, pp. 40–70.

Ribeiro, A. L. B., P. A. A. Lopes, and M. Trevisan (2010). *MNRAS* 409, pp. L124–L127.

Ribeiro, A. L. B. et al. (2013). *MNRAS* 434, pp. 784–795.

Roberts, I. D. and L. C. Parker (2017). *MNRAS* 467, pp. 3268–3278.

Roberts, I. D., L. C. Parker, and A. Karunakaran (2016). *MNRAS* 455, pp. 3628–3639.

Ruszkowski, M. and V. Springel (2009). *ApJ* 696, pp. 1094–1102.

Sanderson, A. J. R., A. C. Edge, and G. P. Smith (2009). *MNRAS* 398, pp. 1698–1705.

Sehgal, N. et al. (2013). *ApJ* 767, 38, p. 38.

Sheth, Kartik, Stuart N. Vogel, Michael W. Regan, Michele D. Thornley, and Peter J. Teuben (2005). *ApJ* 632.1, pp. 217–226.

Skibba, R. A. et al. (2011). *MNRAS* 410, pp. 417–431.

Smith, Russell J. et al. (2010). *MNRAS* 408.3, pp. 1417–1432.

Tinker, J. et al. (2008). *ApJ* 688, 709-728, pp. 709–728.

van den Bosch, F. C. et al. (2005). *MNRAS* 361, pp. 1203–1215.

Von Der Linden, A., P. N. Best, G. Kauffmann, and S. D. M. White (2007). *MNRAS* 379, pp. 867–893.

Wang, J. et al. (2014). *MNRAS* 441, pp. 2159–2172.

Watson, G. S. (1961). *Biometrika* 48.1-2, p. 109.

Weißmann, A., H. Böhringer, R. Šuhada, and S. Ameglio (2013). *A&A* 549, A19, A19.

Wetzel, A. R., J. L. Tinker, and C. Conroy (2012). *MNRAS* 424, pp. 232–243.

Wetzel, A. R., J. L. Tinker, C. Conroy, and F. C. van den Bosch (2013). *MNRAS* 432, pp. 336–358.

Wilman, D. J. and P. Erwin (2012). *ApJ* 746, 160, p. 160.

Yahil, A. and N. V. Vidal (1977). *ApJ* 214, pp. 347–350.

Yang, X., H. J. Mo, F. C. van den Bosch, and Y. P. Jing (2005). *MNRAS* 356, pp. 1293–1307.

Yang, X. et al. (2007). *ApJ* 671, pp. 153–170.

Zehavi, I. et al. (2002). *ApJ* 571, pp. 172–190.

Zitrin, A., M. Bartelmann, K. Umetsu, M. Oguri, and T. Broadhurst (2012). *MNRAS* 426, pp. 2944–2956.

3 | "Observing" Unrelaxed Clusters in Dark Matter Simulations

This chapter represents an unchanged version of the paper, *"Observing" Unrelaxed Clusters in Dark Matter Simulations*, published in the refereed journal, *Monthly Notices of the Royal Astronomical Society*. The full reference is given below:

Roberts I.D., Parker L.C., 2019, MNRAS, Volume 490, Issue 1, pp. 773-783

Department of Physics & Astronomy, McMaster University, Hamilton ON L8S 4M1

Abstract

We present a detailed study of relaxed and unrelaxed galaxy clusters in a large dark matter only simulation. Recent work has demonstrated clear differences between the galaxy populations in clusters that have Gaussian velocity distributions (relaxed) compared to those that do not (unrelaxed). To directly compare with observations, we identify unrelaxed clusters in simulations with one-dimensional velocity distributions. We show that non-Gaussian clusters have had recent major mergers and enhanced rates of galaxy infall relative to systems with Gaussian velocity profiles. Furthermore, we find that the fraction of non-Gaussian clusters increases strongly with cluster mass and modestly with redshift. For comparison, we also make use of three-dimensional information available in the simulations to explore the impact of projection on observational measurements. Differences between Gaussian and non-Gaussian clusters are much stronger when three-dimensional information is considered, which demonstrates that the strength of observed trends with cluster dynamics is diluted because observed velocity information is limited to one line-of-sight.

3.1 Introduction

Galaxy clusters represent the largest virialized objects in the local Universe. As such, galaxy clusters are important laboratories to understand the build-up of massive galaxy environments as well as the influence of such extreme environments on satellite galaxy evolution. However, observations of cluster substructures, both in the optical (e.g. Dressler and Shectman, 1988; Girardi et al., 1997; Flin and Krywult, 2006; Hou et al., 2012) and in the X-ray (e.g. Schuecker et al., 2001; Jeltema et al., 2005; Zhang et al., 2009), suggest that many clusters are not fully virialized. These unrelaxed signatures are likely due to ongoing cluster formation or a recent disruptive merger event. The precise dynamical state of a given cluster can have a significant impact on measured cluster properties as well as the evolution of galaxy members. For instance, clusters that are not in dynamical equilibrium have measured velocity dispersions which are larger than the intrinsic cluster dispersion; this will lead to dynamical mass estimates that are biased high (e.g. Old et al., 2018). Additionally, unrelaxed clusters may support an underdense intracluster medium (ICM) leading to low X-ray luminosities relative to relaxed systems (Popesso et al., 2007; Roberts, Parker, and Karunakaran, 2016; Giles et al., 2017). This difference in ICM properties may have important implications for satellite quenching in clusters of different dynamical states. Finally, if clusters appear unrelaxed due to ongoing formation and/or recent mergers, then the average time since infall for the satellite population should be relatively short compared to relaxed clusters. This will lead to satellite populations that have been exposed to the dense cluster environment for less time, and whose properties have therefore been comparatively less influenced by environment.

Reliably identifying relaxed and unrelaxed clusters observationally is an active research topic, with two main approaches being commonly employed. (1) The use of X-ray observations, either photometrically by identifying unrelaxed clusters with disturbed X-ray morphology or spectroscopically by identifying relaxed clusters based on the presence of an X-ray cool core (e.g. Nurgaliev et al., 2013; Weißmann et al., 2013). (2) A dynamical analysis of cluster galaxies, for example through phase-space analyses (e.g. Wojtak, 2013), by identifying galaxy

substructures (e.g. Hou et al., 2012), or by classifying the shape of the member-galaxy velocity distribution (e.g. Hou et al., 2009; Ribeiro et al., 2013). X-ray techniques are reliable and relatively straightforward to apply, but require deep, high-resolution X-ray observations that are not available for most systems. Dynamical approaches can easily be applied to large samples of groups and clusters from redshift surveys, but rely on high completeness and accurate determination of cluster membership. Furthermore, both X-ray and dynamical approaches are complicated by the unavoidable fact that we lose information by observing galaxy clusters in projection.

One of the simplest methods to classify cluster dynamical state is to examine the shape of the member-galaxy velocity distribution. In Roberts, Parker, and Hlavacek-Larrondo (2018), we demonstrated that clusters with velocity distributions well fitted by a Gaussian (G) have X-ray morphologies that are symmetric on average, whereas clusters with non-Gaussian (NG) velocity profiles show X-ray morphologies with significant asymmetries. This suggests that the use of velocity distributions is a reliable way to determine cluster dynamical state. Previous studies have found that NG clusters host an excess of blue, star-forming galaxies relative to G systems (Ribeiro, Lopes, and Trevisan, 2010; Roberts and Parker, 2017). Velocity dispersion profiles (VDPs) also systematically differ between G and NG clusters, with relaxed clusters showing VDPs that decline with radius compared to rising or flat VDPs in unrelaxed clusters (Hou et al., 2009; Bilton and Pimbblet, 2018; Costa, Ribeiro, and de Carvalho, 2018).

A key missing ingredient in understanding G versus NG clusters is a detailed analysis of such systems in simulations. Observations have established dependences between galaxy properties and host-cluster dynamical state, and simulations give us access to key "unobservables" such as cluster merger and infall history as well as three-dimensional position and velocity information. Given that cluster dynamics are dominated by the dark matter component, we use a dark matter only simulation large enough to contain many galaxy cluster-sized haloes. In this study, we use the MultiDark Planck 2 (MDPL2) simulation to study G and NG clusters. We identify G and NG clusters from the simulation box with the same technique applied to observed clusters, which allows us to estimate unobservable properties such as time since last major merger (MM) and time since infall for satellites in

clusters. Furthermore, given detailed merger trees we can trace cluster haloes back through time and constrain the time-scales over which clusters appear NG. Finally, we can gauge the effect of observational projection and determine whether observed trends are being diluted by misidentifying NG clusters in projection. Again, given that we identify NG clusters with observational techniques, these properties are directly comparable to observed systems and can aid in interpreting observed differences between G and NG systems.

The structure of this paper is as follows. In Section 3.2, we introduce the simulation, our method for identifying galaxy-mass subhaloes, and our method for identifying NG clusters. In Section 3.3, we investigate the influence of projection on identifying G and NG clusters. We explore the connection between NG clusters and recent MMs as well as satellite time since infall in Sections 3.5 and 3.6, respectively. In Section 3.7, we investigate the evolution of NG clusters with redshift. Finally, in Section 3.8, we present and discuss the conclusions from this work.

3.2 Methods

3.2.1 MultiDark Planck 2 Simulation

This paper uses data from the MDPL2 (Prada et al., 2012; Klypin et al., 2016) simulation, a dark matter only simulation with a box size of $(1000\,h^{-1}\,\mathrm{Mpc})^3$, assuming a flat ΛCDM cosmology with $h = 0.6777$, $\Omega_\Lambda = 0.692885$, $\Omega_m = 0.307115$, $\Omega_b = 0.048206$, $n_s = 0.96$, and $\sigma_8 = 0.8228$. The simulation contains 3840^3 particles with a mass resolution of $1.51 \times 10^9\,h^{-1}\,\mathrm{M}_\odot$, therefore resolving haloes $> 10^{11}\,h^{-1}\,\mathrm{M}_\odot$ with ≥ 100 particles.

In each snapshot bound haloes are identified with the phase-space friends-of-friends (FoF) algorithm ROCKSTAR (Behroozi, Wechsler, and Wu, 2013) and merger trees are generated with CONSISTENT TREES (Behroozi et al., 2013). Halo catalogues are output for 126 snapshots between $z = 15$ and $z = 0$. Halo properties are calculated according to the virial overdensity, $\Delta_{\mathrm{vir}}(z)$, from Bryan and Norman (1998)

$$\Delta_{\mathrm{vir}}(z) = 18\pi^2 + 82[\Omega(z) - 1] - 39[\Omega(z) - 1]^2, \tag{3.1}$$

where for a flat cosmology

$$\Omega(z) = \frac{\Omega_{m,0}(1+z)^3}{\Omega_{m,0}(1+z)^3 + \Omega_\Lambda}. \tag{3.2}$$

3.2.2 Identifying Galaxy Analogues

In the dark matter only simulation, we identify subhaloes of groups and clusters at z = 0 and keep those with peak masses consistent with galaxies, following the procedure of Joshi, Parker, and Wadsley (2016) and Joshi, Wadsley, and Parker (2017). In brief, starting with distinct haloes at the top of the subhalo hierarchy, we select "'galaxy analogues" with the following criteria.

1. If the peak halo mass, M_{peak}, is $< 10^{11}\,h^{-1}\,\text{M}_\odot$, the halo and its subsequent branches are not considered.

2. If $M_{\text{peak}} > 10^{12.5}\,h^{-1}\,\text{M}_\odot$, the halo is eliminated but each of its subhaloes are put through criteria 1-4.

3. If $10^{11} < M_{\text{peak}} < 10^{12.5}\,h^{-1}\,\text{M}_\odot$ and the halo has no subhaloes with $M_{\text{peak}} > 10^{11}\,h^{-1}\,\text{M}_\odot$, the halo is considered a galaxy analogue and its subsequent branches are eliminated.

4. If $10^{11} < M_{\text{peak}} < 10^{12.5}\,h^{-1}\,\text{M}_\odot$, then the quantity $M_{\text{rem}} = M_{\text{peak}} - \sum M_{\text{subhalo, peak}}$ is considered. If $10^{11} < M_{\text{rem}} < 10^{12.5}\,h^{-1}\,\text{M}_\odot$ then the halo is accepted as a galaxy analogue and each of its subhalos are put through criteria 1-4.

The above mass limits are chosen to correspond to the stellar mass range of galaxies in observational surveys ($M_\star \sim 10^9 - 10^{11}\,\text{M}_\odot$, assuming a Hudson et al. 2015 stellar-to-halo mass relationship). The upper mass limit is chosen to avoid including group haloes as part of our galaxy sample, but this cut may miss some massive central galaxies. This is not a problem in this analysis because satellite galaxies are the primary tracers of the host cluster dynamical state. It is also worth noting that halo finders struggle to accurately identify central substructure (e.g. Knebe et al., 2011; Joshi, Parker, and Wadsley, 2016), meaning that such massive subhaloes sitting at the centre of the potential may be poorly identified. In the $z = 0$

snapshot, we identify 7308 248 galaxy analogues, and for brevity we will refer to galaxy analogues as "galaxies" for the remainder of the paper[1].

3.2.3 Cluster Dynamical States

In order to characterize the velocity distribution of member galaxies with relative accuracy (while still maintaining a large sample of clusters) we only consider clusters with at least 10 members (Hou et al., 2009; Roberts, Parker, and Hlavacek-Larrondo, 2018). In this analysis, we use galaxy analogues identified as cluster members by the ROCKSTAR halo finder. However, our key findings remain the same if instead we assign cluster memberships with cuts in projected radius and 1D velocity dispersion (i.e. more similar to observational memberships). The membership cut restricts the sample size to 2300 045 galaxies in 101 868 clusters. The host clusters (with 10+ members) range between $4.8\times10^{12} < M_{\rm vir} < 3.5\times10^{15}\,{\rm M}_{\odot}$. Despite the large range in mass we refer to all host haloes as clusters for simplicity. When we explicitly consider dependencies on halo mass in the subsequent sections, we will refer to systems with $M_{\rm vir} < 10^{14}\,h^{-1}\,{\rm M}_{\odot}$ as *low-mass clusters* and systems with $M_{\rm vir} \geq 10^{14}\,h^{-1}\,{\rm M}_{\odot}$ as *high-mass clusters*. The halo masses that we quote throughout the paper are the simulation halo masses from the ROCKSTAR catalogues. We note that we have also performed our analysis with dynamical masses estimated from one-dimensional velocity dispersions (a common observational halo mass estimator) and find that our results are unchanged. When estimating dynamical masses we find that measured velocity dispersions for high-mass NG clusters are enhanced by roughly 10 per cent relative to similar G clusters. This is due to the fact that NG clusters are more dynamically disturbed, but we find that this small difference does not impact our results.

In Fig 3.1 we show median cluster membership (i.e. the number of galaxies identified in each parent halo) as a function of parent halo mass. For clusters with $M_{\rm vir} < 4\times10^{13}\,h^{-1}\,{\rm M}_{\odot}$ we note that the median cluster membership is less than 10. This means that by selecting only clusters with 10+ members, we are biasing our sample at halo masses less than $4\times10^{13}\,h^{-1}\,{\rm M}_{\odot}$. In our final sample we only

[1]We emphasize that these "galaxies" are identified purely on dark matter content, with no consideration of stellar or gaseous components

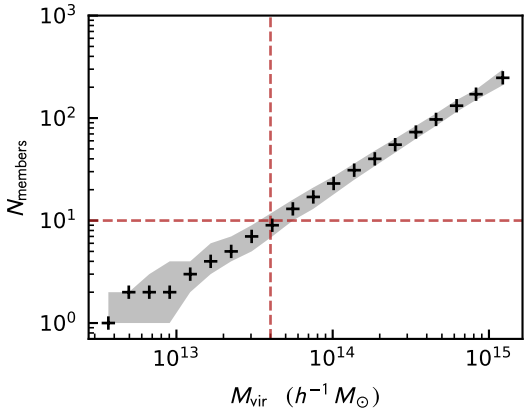

FIGURE 3.1: Median cluster membership (number of galaxies) as a function of cluster mass. Shaded region corresponds to the 50 per cent (25th to 75th percentile) scatter. Dashed lines mark $M_{\rm vir} = 4\times 10^{13}\,{\rm M}_\odot$, which is the cluster mass which corresponds to a median membership of $N_{\rm members} = 10$. In our final sample, we only include clusters with $M_{\rm vir} > 4 \times 10^{13}\,{\rm M}_\odot$.

include clusters with $M_{\rm vir} > 4 \times 10^{13}\,h^{-1}\,{\rm M}_\odot$ in order to avoid these potential biases. This leaves a final sample consisting of 2000 328 galaxies in 77 533 clusters.

To make direct comparisons to observations we consider galaxy positions and velocities in projection. We project each cluster along a random axis mimicking the fact that real clusters are observed along a random line of sight (LOS). We will refer to the two projected position axes as $\tilde{x}$ and $\tilde{y}$ and the projected velocity direction as $\tilde{z}$ for each cluster. We stress that these are randomly projected axes for each cluster and in general do not correspond to the x, y, and z coordinate axes of the simulation box. We classify relaxed and unrelaxed clusters by considering the shape of the projected velocity distribution for member satellite galaxies (e.g. Hou et al., 2009). This method is predicated on the notion that relaxed/dynamically old clusters will be characterized by velocity distributions which are close to G (Yahil and Vidal, 1977; Bird and Beers, 1993). To quantify the degree to which projected velocities are consistent with a G, we apply the Anderson-Darling (AD; Anderson and Darling 1952) normality test to the distribution of $v_{\tilde{z}}$ for each cluster in the sample. Specifically, we consider

$$v_{\rm los} = v_{\tilde{z}} - \bar{v}_{\tilde{z}} \tag{3.3}$$

where $v_{\tilde{z}}$ is the velocity in the random $\tilde{z}$-direction for each galaxy and $\bar{v}_{\tilde{z}}$ is the mean $v_{\tilde{z}}$ for galaxies in the cluster.

The AD normality test is a non-parametric normality test which quantifies the distance between the cumulative distribution function (CDF) of the data and the CDF of a normal distribution. This distance is parametrized by the AD statistic (Anderson and Darling, 1952; D'Agostino and Stephens, 1986) given by

$$A^{*2} = A^2 \times (1.0 + 0.75/n + 2.25/n^2), \tag{3.4}$$

where

$$A^2 = -n - \frac{1}{n}\sum_{i=1}^{n}[2i-1][\ln \Phi(x_i) + \ln(1 - \Phi(x_{n+1-i}))], \tag{3.5}$$

where x_i are the length-n ordered data and $\Phi(x_i)$ is the CDF of the G distribution. A *p-value* is then computed from the value of the AD statistic, A^{*2}, and following previous work (e.g. Hou et al., 2009; Roberts and Parker, 2017) we consider clusters with $p_{AD} < 0.05$ to be NG in one dimension (NG_{1D}) and clusters with $p_{AD} \geq 0.05$ to be G in one dimension (G_{1D}). One important consideration is the fact that statistical normality tests such as the AD test will more readily detect subtle departures from normality when the sample size is large, due to the increasing statistical power of the test (e.g. Mohd Razali and Yap, 2011). In our sample, for a given halo mass, the median cluster membership is the same for G_{1D} and NG_{1D} clusters (this is true at all haloes masses we consider), therefore the fact that the statistical power of the AD test increases with sample size should not introduce any bias between our G_{1D} and NG_{1D} samples. At $z = 0$, we find 72 178 G_{1D} clusters and 5355 NG_{1D} clusters. In Fig. 3.2 we show example clusters which we identify as NG_{1D} (left) and G_{1D} (right), each with masses of $M_{\rm vir} \simeq 4 \times 10^{14}\, h^{-1}\, \mathrm{M}_{\odot}$. The dashed line corresponds to the virial radius of the cluster halo and the circles correspond to the projected ($\tilde{x}$, $\tilde{y}$) positions of member galaxies (sized according to the virial radius of the subhalo and coloured according to their velocity in the $\tilde{z}$-direction).

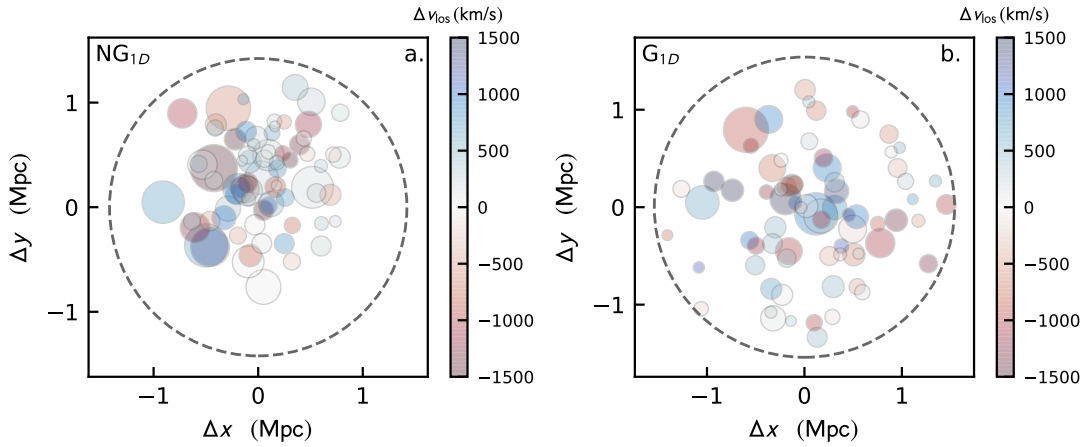

FIGURE 3.2: An example of a G (right) and NG (left) cluster identified by applying the Anderson-Darling test to cluster velocity distributions. Circles correspond to the projected positions of cluster galaxy analogues and the dashed line marks the cluster virial radius. The sizes of the circles are scaled according to the subhalo virial radii and they are coloured according to their v_{los} offset from the cluster centroid.

3.3 Effects of Line-of-Sight Projection

Throughout this paper we will be analysing clusters, which are classified as G or NG according to velocity distributions along a single LOS (G_{1D} and NG_{1D}). The advantage of using simulations is that we can also gauge the effects of misclassification due to projection and quantify the effect of this on the trends that we observe. To do this, we develop an estimate of cluster dynamical state measured along many random LOS, as opposed to just one. Using three-dimensional information allows a more robust understanding of the dynamical state of each cluster. In order to quantify the effects of projection we reproject each cluster along a random LOS 100 times. For the ith random projection we apply the AD test to the one-dimensional velocity distribution and classify the cluster as NG (along that specific LOS) if $p_{AD,i} < 0.05$. For the 100 random projections we compute the fraction of realizations where the cluster is classified as NG, namely

$$F_{\rm NG} = \frac{N(p_i < 0.05)}{N_{\rm tot}}, \tag{3.6}$$

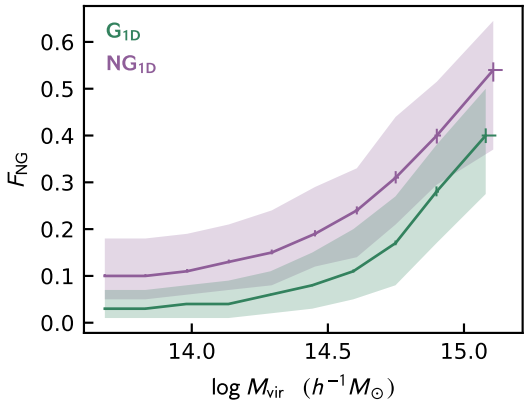

FIGURE 3.3: The fraction of 100 random projections along which a given cluster appears NG ($p_{AD} < 0.05$) as a function of parent virial mass. The purple line corresponds to NG_{1D} clusters and the green line corresponds to the G_{1D}. Error bars correspond to 68 per cent statistical errors estimated from the beta distribution following Cameron (2011), shaded region corresponds to the 50 per cent (25th to 75th percentile) scatter.

where $N(p_i < 0.05)$ is the number of random projections where the cluster is classified as NG and $N_{\rm tot}$ is the total number of random projections (100 in this case). This fraction, $F_{\rm NG}$, is therefore a measure of how unrelaxed a given cluster appears along many LOS as opposed to just the one LOS we are limited to observationally.

We can now compare $F_{\rm NG}$, which is measured for each cluster, for G_{1D} and NG_{1D} clusters. In Fig. 3.3, we plot median F_{NG} versus parent halo mass for clusters in the sample which are G_{1D} (green) and NG_{1D} (purple) at $z = 0$. The error bars correspond to 68 per cent statistical uncertainties and the shaded region shows the 50 per cent (25th to 75th percentiles) scatter. Regardless of dynamical state, halo mass and $F_{\rm NG}$ are strongly correlated, with $F_{\rm NG}$ increasing towards high halo masses. This reflects the fact that high-mass clusters are inherently less virialized than lower mass systems (e.g. Press and Schechter, 1974). The median $F_{\rm NG}$ is systematically larger for NG_{1D} clusters compared to G_{1D} clusters at all halo masses. At low halo masses $F_{\rm NG}$ is small, ~ 0 for G_{1D} clusters and ~ 0.1 for NG_{1D} clusters. At these masses clusters are classified as G along most LOS, even those clusters that were classified as NG along one random LOS (purple). Fig. 3.3 demonstrates the impurity that can be introduced when restricted to observing

along a single LOS; there is always the chance that the observed LOS may not be reflective of the dynamics of the cluster as a whole. On the high-mass end $F_{\rm NG}$ is much larger, $\sim 0.3 - 0.4$ for G_{1D} and ~ 0.5 for NG_{1D} clusters. While on the low-mass end the sample of NG_{1D} clusters is likely contaminated by clusters with relatively relaxed dynamics, on the high-mass end the converse is true. The high impurity for low-mass systems in Fig. 3.3 suggests that the AD test in one dimension struggles to identify truly unrelaxed systems at the low end of our mass range. This could be due to the fact that these systems have fewer member galaxies and therefore with a small number of dynamical tracers we may be undersampling the underlying halo velocity profile. The fact that $F_{\rm NG} \sim 0.3 - 0.4$ for high-mass G_{1D} clusters suggests that the G_{1D} sample contains some clusters which show complex dynamical states along many LOS. Therefore despite the fact that high-mass G_{1D} clusters appear relaxed along a single, random LOS many of these clusters may look much less relaxed with three-dimensional information.

Regardless of the value of $F_{\rm NG}$, the fact that $F_{\rm NG}$ is systematically larger for NG_{1D} clusters compared to G_{1D} clusters demonstrates that the AD test is selecting NG_{1D} clusters that are inherently less relaxed than their G_{1D} counterparts, at all halo masses. Therefore this method works on average when applied to a large sample of clusters, but not necessarily for an individual system.

3.4 Mass-matched Cluster Sample

Fig. 3.3 shows a clear dependence between cluster mass and the shape of the velocity profile, namely high-mass clusters are far more likely to be classified as NG. This is further illustrated in Fig. 3.4(a) where we show the distribution of virial mass for G_{1D} (green) and NG_{1D} (purple) clusters. It is apparent that there is a small excess of NG_{1D} clusters at the highest cluster masses. This excess has also been previously reported in samples of observed clusters (de Carvalho et al., 2017; Roberts and Parker, 2017). Given this dependence of classified dynamical state on cluster mass, it is important to mass match the G_{1D} and NG_{1D} samples to ensure that any differences between G_{1D} and NG_{1D} clusters are not resulting from different cluster mass distributions.

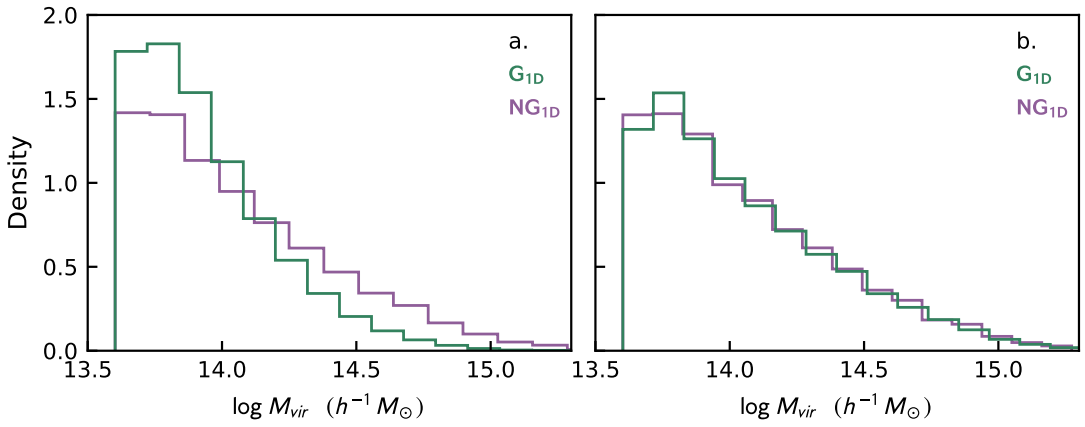

FIGURE 3.4: Virial mass distributions for G_{1D} (green) and NG_{1D} (purple) clusters in the sample. *Left:* Distributions for the total sample. *Right:* Distributions for the mass-matched sample.

In order to construct a mass-matched sample of G_{1D} and NG_{1D} clusters, for each NG_{1D} cluster we select 10 G_{1D} clusters, which have virial masses within 0.1 dex of the NG_{1D} cluster. The 10:1 is chosen to roughly match the ratio of G_{1D} to NG_{1D} clusters identified by the AD test (see section 3.2.3). In Fig. 3.4(b) we now plot the virial mass distributions for G_{1D} and NG_{1D} clusters in the mass-matched sample, clearly showing that the mass distributions of the two subsamples are now well matched. For the remainder of the paper, any results comparing properties of G_{1D} and NG_{1D} clusters will show trends for both the original sample of G_{1D} and NG_{1D} clusters as well as the mass-matched sample. The differences seen between G_{1D} and NG_{1D} clusters cannot be explained by differences in the cluster mass distributions (see Figs 3.5 and 3.8).

3.5 Time Since Last Major Merger

A useful proxy for the dynamical age of a cluster halo is the time since last MM (e.g. Rowley, Thomas, and Kay, 2004). The scale factor of the last MM for each halo is given in the ROCKSTAR halo catalogues (defining a major merger to have a mass ratio greater than 0.3), which is easily converted to a time since last MM given our assumed cosmology. In Fig. 3.5(a) we show the kernel density distribution of time

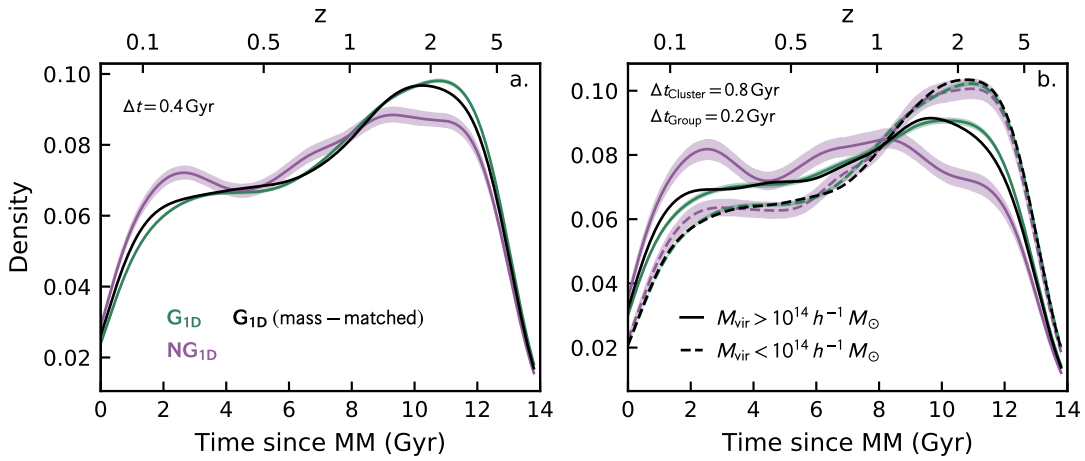

FIGURE 3.5: Distribution of time since last major merger for G_{1D} (green) and NG_{1D} (purple) clusters. The solid black line corresponds to the G_{1D} sample, which is mass matched to the NG_{1D} sample (see section 3.4). Distributions are generated with a G kernel density estimation. Shaded regions show the 68 per cent confidence region from 1000 random bootstrap resamplings. *Left:* Distributions for the entire sample. *Right:* Distributions split into low-mass ($M_{\mathrm{vir}} < 10^{14}\,h^{-1}\,\mathrm{M}_{\odot}$) and high-mass ($M_{\mathrm{vir}} \geq 10^{14}\,h^{-1}\,\mathrm{M}_{\odot}$) clusters. The median time difference between G_{1D} and NG_{1D}, Δt, is shown for each sample.

since last MM for G_{1D} (green) and NG_{1D} (purple) clusters. The distributions for both G_{1D} and NG_{1D} clusters peak at early times ($t_{\rm lookback} \sim 10 - 12\,{\rm Gyr}$) corresponding to early cluster assembly, and at late times ($t_{\rm lookback} \lesssim 4\,{\rm Gyr}$) the distribution of NG_{1D} systems shows a secondary peak corresponding to late-time MMs which is smaller for G_{1D} clusters. As a whole, the median time since last MM is 0.4 Gyr shorter for NG_{1D} clusters compared to G_{1D} systems. Therefore the AD test for cluster dynamics is sensitive to physical differences in cluster merger history, namely NG_{1D} systems have preferentially short times since MM. This difference is subtle but systematic, suggesting that the AD test applied to large samples of groups and clusters can identify statistical differences in merger history.

Fig. 3.5(b) we show the same distributions, but now divided into low-mass (dashed, $M_{\rm vir} < 10^{14}\,h^{-1}\,{\rm M}_{\odot}$) and high-mass (solid, $M_{\rm vir} \geq 10^{14}\,h^{-1}\,{\rm M}_{\odot}$) clusters. Nearly all of the difference seen in Fig. 3.5(a) is driven by the high-mass clusters, as low-mass G_{1D} and NG_{1D} clusters have virtually identical time since last MM distributions. When considering only the high-mass clusters, the difference from Fig. 3.5(a) becomes larger with a median difference between G_{1D} and NG_{1D} of 0.8 Gyr. The little difference in time since MM distributions for low-mass G_{1D} and NG_{1D} clusters suggests that the AD test is not identifying clear physical differences (at least in terms of MMs) for low-mass clusters like it is for high-mass clusters. Indeed, the fraction of low-mass NG_{1D} ($M_{\rm vir} < 10^{14}\,h^{-1}\,{\rm M}_{\odot}$) is only 5.5 per cent. Given that the fraction of low-mass NG_{1D} clusters is close to the *p-value* used to identify NG_{1D} systems ($p_{AD} = 0.05$), we cannot rule out that many of the low-mass clusters that we identify as NG_{1D} are false-positives with intrinsic velocity distributions drawn from a G. Indeed, in Fig. 3.3 we show that low-mass clusters which are classified as NG_{1D} actually appear G along most LOS.

3.5.1 Increasing the Purity of the Unrelaxed Sample

To construct a sample of NG clusters with higher purity we use $F_{\rm NG}$ (see section 3.3, equation 3.6). A reminder that $F_{\rm NG}$ corresponds to the fraction of random projections, for a given cluster, along which the cluster is classified as NG. Therefore a sample of clusters with large values of $F_{\rm NG}$ will be a sample of unrelaxed clusters with relatively high purity. If the AD test is identifying physical differences between clusters classified as G and NG then we expect the properties

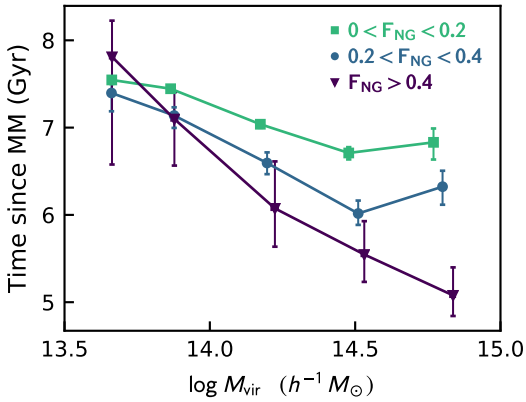

FIGURE 3.6: Time since MM as a function of cluster mass, in bins of $F_{\rm NG}$ (see equation 3.6). Error bars are 68 per cent uncertainties estimated non-parametrically as: |16/84th percentile - median|/sqrt(N).

of relaxed and unrelaxed clusters to differ more strongly as $F_{\rm NG}$ increases. In other words, the differences between relaxed and unrelaxed samples should increase as the purity of the unrelaxed sample increases. In Fig. 3.6 we plot the average time since MM as a function of cluster mass, for different bins of $F_{\rm NG}$. Given the mass dependence of $F_{\rm NG}$ it is important to compare $F_{\rm NG}$ at fixed cluster mass. The errorbars in Fig. 3.6 are computed non-parametrically as: |16/84th percentile - median|/sqrt(N). Fig. 3.6 shows different trends for different cluster masses. For low-mass clusters there is no trend between time since MM and $F_{\rm NG}$, which may be related to the fact that low-mass clusters have relatively few recent MMs (see Figs 3.5b and 3.7b). Furthermore, the frequency of MMs over the entire cluster lifetime is lower for low-mass clusters compared to high-mass systems (plot not shown). On the other hand, for high-mass clusters there is a clear anticorrelation between time since MM and $F_{\rm NG}$. For high-mass clusters, a large fraction of projections that show NG dynamics corresponds to relatively short time since MM. The difference in time since MM between the smallest and largest values of $F_{\rm NG}$ ranges from $\sim$ 1 to 2 Gyr for the higher mass clusters. This difference highlights the inherent information lost when restricted to observing along a single LOS. While a systematic difference in time since MM between G_{1D} and NG_{1D} clusters

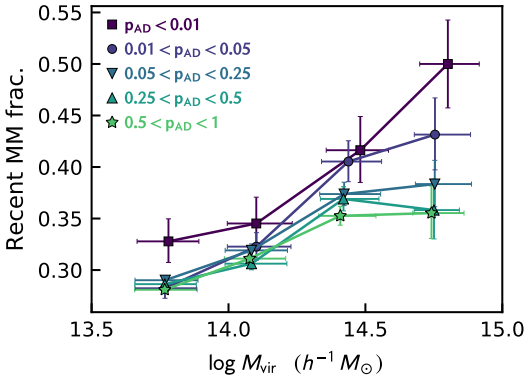

FIGURE 3.7: Fraction of $z = 0$ clusters with a MM within the past 5 Gyr as a function of cluster mass, for bins of AD *p-value*. The errors correspond to 68 per cent statistical errors estimated from the beta distribution following Cameron (2011).

is seen for the one-dimensional case (Fig. 3.5), when considering a more pure sample of unrelaxed clusters (high values of $F_{\rm NG}$) the difference is strongly enhanced (Fig. 3.6).

3.5.2 Recent Merger Fractions

Given that the distribution of time since MM for NG_{1D} clusters in this sample appears bimodal, it is natural to divide the population into two classes: clusters which have experienced a recent MM, and those which have not. Based on the distributions in Fig. 3.5 we define a recent MM to be an MM within the last 5 Gyr, though our results are not sensitive to the specific dividing line that we choose. In Fig. 3.7 we show the fraction of clusters that have experienced a recent MM (time since MM $<$ 5 Gyr) as a function of cluster virial mass, for different bins of AD *p-value*. For all values of AD *p-value* there is a correlation between recent MM fraction and cluster mass. Recent MM fraction increases most strongly with cluster mass for the low values of AD *p-value*, specifically for clusters which we classify as NG_{1D} ($p_{AD} < 0.05$). Furthermore, at fixed cluster mass the recent MM fraction increases with decreasing AD *p-value*. This is most obvious at the high-mass end where the recent MM fractions are clearly highest for the smallest

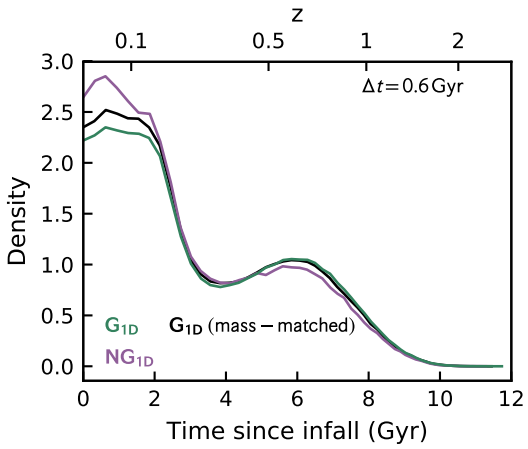

FIGURE 3.8: Distribution of time since infall for galaxies in G_{1D} (green) and NG_{1D} (purple) clusters. The solid black line corresponds to the G_{1D} sample which is mass matched to the NG_{1D} sample (see section 3.4). The median time difference between G_{1D} and NG_{1D} clusters, Δt, is shown.

p-values. In other words, the fraction of clusters which have experienced a recent MM is highest for systems which appear very dynamically disturbed.

3.6 Satellite Time Since Infall

We now consider the infall history of galaxies on to their present-day parent haloes. Infall history is related to time since last MM, since mergers are a source of newly infalling satellites, but clusters are also continuously accreting new satellites which are not associated with rare MMs. Time since infall for satellite galaxies is particularly interesting for exploring environmental quenching of star formation in galaxies, as observed quenched fractions are reproduced well by models which directly tie quenching to an infall time threshold (e.g. Haines et al., 2015). It is possible that differences in observed quenched fractions between G and NG clusters (e.g. Roberts and Parker, 2017) may be directly related to differences in time since infall.

We derive time since infall onto the current parent halo for each galaxy by tracing the galaxy's most-massive progenitor (MMP) back through the merger

trees[2]. We consider infall to be the first time that an MMP of a galaxy becomes a subhalo of the MMP of the galaxy's present-day parent halo. In Fig. 3.8 we plot the time since infall distributions for the G_{1D} and NG_{1D} samples. Galaxies in NG_{1D} systems have systematically shorter times since infall, with a median difference of 0.6 Gyr. Again, the difference between G_{1D} and NG_{1D} clusters is subtle but systematic. Similarly, observational studies have reported enhanced accretion in NG clusters relative to G clusters (de Carvalho et al., 2017). In both G_{1D} and NG_{1D} clusters, recent accretion dominates and the peak in time since infall occurs within the past 2 Gyr.

The bimodal shape seen in Fig. 3.8 is likely driven by backsplashing galaxies (Yun et al., 2019). Membership is restricted to those galaxies which are within the virial radius of the parent halo at $z = 0$, therefore any galaxies which have made a pericentric passage and then "backsplashed" beyond the virial radius will not be included as members. The characteristic time-scale required for a galaxy to infall, make a pericentric passage, and then backsplash beyond the virial radius is of order ∼few Gyr (e.g. Oman, Hudson, and Behroozi, 2013). Therefore the deficit of satellites which have time since infall of 3-4 Gyr is likely related to those satellites backsplashing at $z = 0$ and not being identified as members. The distributions in Fig. 3.8 also do not account for satellites which were once members but have since been destroyed by tidal interactions or have merged with another galaxy.

3.6.1 Increasing the Purity of the Unrelaxed Sample

Analogously to Fig. 3.6, we now investigate average time since infall as a function of cluster mass, for bins of the fraction of random projections along which a cluster is classified as NG, $F_{\rm NG}$, in Fig. 3.9(a). We normalize the y-axis such that we are plotting the percentage change in time since infall relative to clusters with $F_{\rm NG} = 0$ (relaxed in all random projections). Namely

$$\Delta\,\text{time since infall} = 100 \times \frac{t_{\text{since infall}}(F_{\rm NG}) - t_{\text{since infall}}(F_{\rm NG=0})}{t_{\text{since infall}}(F_{\rm NG=0})}, \tag{3.7}$$

[2] `https://ytree.readthedocs.io/`

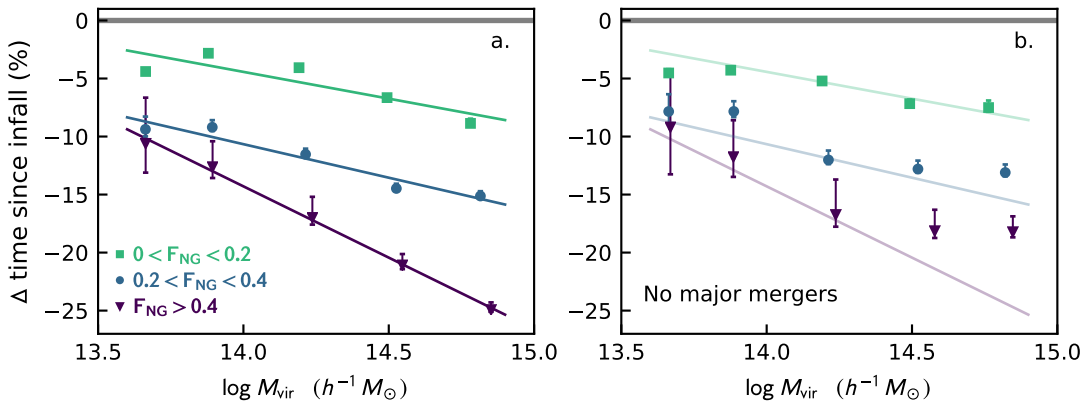

FIGURE 3.9: Percent change in time since infall (relative to 'purely' G systems, $F_{\rm NG} = 0$) as a function of cluster mass, for bins of $F_{\rm NG}$ (see equation 3.6). Solid lines correspond to linear fits to the data in panel (a). Error bars are 68 per cent uncertainties estimated non-parametrically as: |16/84th percentile - median|/sqrt(N). *Left:* Time since infall for all clusters in the sample. *Right:* Time since infall since the last MM for galaxies in clusters that have not had a major merger in the past 8 Gyr, separating the contribution of infall from MMs from panel (a).

where $t_{\rm since\ infall}(F_{\rm NG})$ is the average time since infall for galaxies as a function of $F_{\rm NG}$. The shaded horizontal line in Fig. 3.9 corresponds to the average time since infall for satellites of haloes with $F_{\rm NG} = 0$, which in this case is Δ time since infall $= 0$ by construction. For high-mass clusters we see a qualitatively similar trend to Fig. 3.6 (time since MM), where time since infall decreases with increasing $F_{\rm NG}$. High-mass clusters which appear dynamically unrelaxed along many LOS host satellites which have recently become members. The trend for low-mass systems is clearly different when comparing satellite time since infall to time since MM. Whereas no strong trend is seen between time since MM and $F_{\rm NG}$ (see Fig. 3.6), a clear trend is apparent between satellite time since infall and $F_{\rm NG}$. Specifically, time since infall decreases with increasing $F_{\rm NG}$. While the trend is weaker in low-mass clusters compared to high-mass clusters, a clear anticorrelation is present.

The combination of Figs 3.6 and 3.9 suggest that for low-mass systems the AD test is likely tracing satellite time since infall more than time since MM. Infalling satellites on to clusters can be sourced through MMs or more continuous accretion of small groups and individual galaxies. Given the lack of dependence between

$F_{\rm NG}$ and time since MM for low-mass clusters (see Fig. 3.6), it appears that the AD test is tracing continuous accretion as opposed to MMs for these lower mass systems. Since low-mass clusters also have low galaxy memberships, it may be that this continuous accretion can have a larger impact on the dynamics of the host system.

MMs will always facilitate the infall of new satellite galaxies on to a cluster, therefore the trends that we see in Fig. 3.9(a) are a superposition of infall associated with MMs as well as continuous accretion. We separate the effect due to infall from continuous accretion versus MMs by selecting a subset of clusters which have not experienced any recent MMs, and therefore any recent accretion of satellites on to these systems will be driven by minor mergers and isolated accretion. Specifically, we select all clusters which have not experienced a MM in the last 8 Gyr and consider only satellite infall occurring after the last MM. This cut completely excludes the MM peak at late times (see Fig. 3.5a), and we note that these results are not particularly sensitive to the specific dividing line chosen.

In Fig. 3.9(b) we show Δ time since infall versus $F_{\rm NG}$ for galaxies which have infallen since the last MM on to clusters that have not had an MM for at least 8 Gyr. Therefore we have effectively removed the contribution from accretion via MMs from Fig. 3.9(a). To guide the eye we also show solid lines corresponding to weighted least-squares linear fits to the data in panel (a). For both low-mass and high-mass clusters there is still a residual trend between time since infall and $F_{\rm NG}$ suggesting the AD test is sensitive to physical differences in infall history, even in the absence of MMs. For the lowest mass clusters there is little difference between panels (a) and (b), which is consistent with the lack of clear correlation between $F_{\rm NG}$ and time since MM which was previously shown (Fig. 3.6). As expected, removing the contribution from MM accretion has only a small effect for low-mass systems. Conversely, the trend for high-mass clusters differs between Figs 3.9(a) and (b) (especially for large values of $F_{\rm NG}$), showing that the both MMs and accretion contribute to the trend for high-mass systems. Upon removing the MM contribution the trend between time since infall and $F_{\rm NG}$ becomes flatter. This is especially clear when comparing the $F_{\rm NG} > 0.4$ best-fitting line from panel (a) (solid purple line in panel b) to the $F_{\rm NG} > 0.4$ data points in panel (b). These results suggest that for massive clusters the AD test traces dynamical disruptions

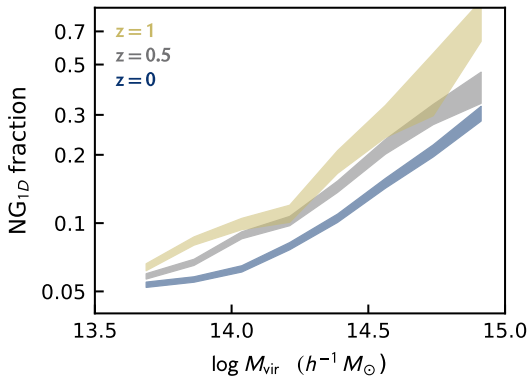

FIGURE 3.10: The fraction of NG_{1D} clusters versus halo mass for three different redshift snapshots. The shaded regions correspond to 68 per cent statistical errors estimated from the beta distribution following Cameron (2011).

from MMs and continuous accretion, whereas for lower mass clusters the AD test seems to be primarily sensitive to continuous accretion and not MMs.

3.7 Redshift Evolution

3.7.1 Fraction of Unrelaxed Clusters

In Fig. 3.10 we show the evolution of the fraction of clusters classified as NG_{1D} ($p_{AD} < 0.05$ along one random LOS) as a function of halo mass and redshift, for three redshift snapshots (z = 0, 0.5, 1). Fig. 3.10 reveals two clear trends. First, at all redshifts the fraction of NG_{1D} clusters increases with halo mass, and second, at fixed halo mass the fraction of NG_{1D} clusters increases modestly with redshift. Both the trend with redshift and the trend with halo mass can be explained through simple virialization. At all redshifts high-mass clusters are, on average, less virialized than lower mass haloes, leading to more NG_{1D} clusters at high halo mass; and at all masses haloes are, on average, less virialized at earlier epochs compared to the present day.

These trends with halo mass and redshift are in qualitative agreement with observations of G and NG clusters. Observations have shown that the proportion of NG to G systems increases at high halo mass (Ribeiro, Lopes, and Rembold,

2013; de Carvalho et al., 2017; Roberts and Parker, 2017). As well, observations of G and NG systems at different redshifts have demonstrated that the fraction of NG clusters tends to increase with redshift (Hou et al., 2013).

3.7.2 How Long Have z=0 Clusters Appeared Unrelaxed?

With the available redshift snapshots and merger trees we can probe how long NG_{1D} systems remain in the NG state. Given that NG_{1D} clusters are associated with transient events like MMs (see section 3.5), it is interesting to estimate the characteristic time required for clusters, on average, to return to a relaxed dynamical state. To do this we trace the MMP of each redshift zero cluster back through the merger trees out to a given redshift. We then keep all $z = 0$ NG_{1D} clusters whose MMPs have at least 10 member galaxies in all snapshots back to this redshift, which ensures that we can apply the AD test to the cluster MMPs in each snapshot. We note that for this part of the analysis we consider one-dimensional velocities measured along the z-axis of the simulation box as opposed to the one random LOS used up until this point. The reason is that this is a simple way to ensure that we are measuring velocities along the same axis for clusters and all of their MMPs as we trace them back through the merger trees.

To probe the rate at which NG $z = 0$ systems cease to be classified as NG, we consider the survival curve[3] for NG_{1D} clusters. We measure the fraction of NG_{1D} systems at $z = 0$ that "survive" as we move to simulation snapshots at higher redshift. We consider a NG_{1D} system at $z = 0$ to have survived out to a redshift, z, if the MMPs of that cluster are classified as NG ($p_{AD} < 0.05$) in all redshift snapshots between $z = 0$ and z. NG_{1D} clusters at $z = 0$ whose MMPs are classified as G in some snapshot between $z = 0$ and z are considered to not have survived at redshift z. These "surviving fractions" give us a quantitative measure of how quickly the population of NG_{1D} clusters evolves back to the G_{1D} state. We trace the MMPs of $z = 0$ NG_{1D} systems back to the redshift where the surviving fraction of all NG_{1D} systems reaches ~ 1 per cent. This corresponds to $z \sim 0.15$ or a lookback time of ~ 2 Gyr.

[3]Survival curves are commonly used in radiobiology to determine the fraction of surviving cells as a function of radiation dose (e.g. Deacon, Peckham, and Steel, 1984).

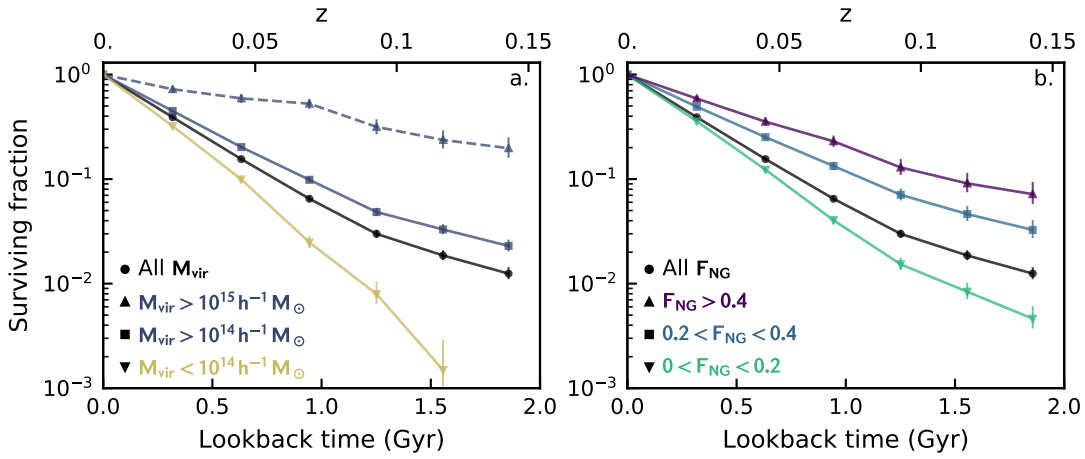

FIGURE 3.11: Surviving fraction for $z = 0$ unrelaxed clusters as a function of lookback time. The surviving fraction is the fraction of $z = 0$ unrelaxed clusters whose MMPs are also classified as unrelaxed ($p_{AD} < 0.05$) in subsequent redshift snapshots. Once the MMP of a cluster is classified as relaxed ($p_{AD} \geq 0.05$) in a snapshot, then the cluster is considered to have not survived. Errorbars correspond to 68 per cent statistical errors estimated from the beta distribution following Cameron (2011). *Left:* Divided by parent halo mass. *Right:* Divided by $F_{\rm NG}$ (see equation 3.6).

In Fig. 3.11 we plot the surviving fractions of $z = 0$ NG_{1D} clusters as a function of lookback time. At a lookback time of 0.0 Gyr the surviving fraction is unity, by construction, and then the surviving fraction decreases towards higher redshift. In Fig. 3.11(a) the black line corresponds to the surviving fraction for all unrelaxed clusters, and the coloured lines correspond to subsamples of halo mass. The solid yellow line shows the surviving fraction for all low-mass clusters ($M_{\rm vir} < 10^{14}\,{\rm M}_{\odot}$), the solid blue line shows the surviving fraction for all high-mass clusters ($M_{\rm vir} \geq 10^{14}\,{\rm M}_{\odot}$), and the dashed blue line shows the surviving fraction for very high mass clusters ($M_{\rm vir} \geq 10^{15}\,{\rm M}_{\odot}$). The decline in surviving fraction depends on halo mass, with the surviving fractions for low-mass clusters falling off the most quickly and the fractions for the most massive haloes declining at the slowest rate. At a lookback time of ~ 2 Gyr, the surviving fractions for the vast majority of haloes are $\lesssim$ a few per cent. Only the clusters with ($M_{\rm vir} \geq 10^{15}\,{\rm M}_{\odot}$) have surviving fractions which persist above 10 per cent for longer than 1 Gyr. Therefore clusters identified as NG in one dimension at $z = 0$ do not appear NG for long (on average), though the precise time-scales depend on halo mass.

In Fig. 3.11(b) we now show surviving fraction divided by $F_{\rm NG}$ instead of halo mass. A reminder that $F_{\rm NG}$ is the fraction of random projections along which a given group/cluster is classified as NG, therefore it is a measure of how unrelaxed a system is along many LOS as opposed to just one. In Fig. 3.11(b) the green line corresponds to $0 < F_{\rm NG} < 0.2$, the blue line corresponds to $0.2 < F_{\rm NG} < 0.4$, the purple line corresponds to $F_{\rm NG} > 0.4$, and the black line corresponds to all values of $F_{\rm NG}$ (same line as in panel a). A clear trend is visible, where clusters with the lowest values of $F_{\rm NG}$ also have the lowest survival fractions. As $F_{\rm NG}$ increases so does the survival fraction. This is expected as subsamples with high $F_{\rm NG}$ are samples of NG clusters with high purity (i.e. fewer clusters misidentified as NG due to projection). We emphasize that while Figs 3.11(a) and (b) are not independent since $M_{\rm vir}$ and $F_{\rm NG}$ are correlated (see Fig. 3.3), throughout this paper we continue to see trends with $F_{\rm NG}$ at fixed cluster mass and vice versa.

We can define a "half-life" for $z = 0$ NG_{1D} clusters to be the lookback time at which point the surviving fraction is equal to 50 per cent. For the total population this half-life is roughly 0.5 Gyr, considering subsamples with high halo mass or high purity (high $F_{\rm NG}$) extends this half-life up to ~ 1 Gyr. The fact that low-mass

clusters have very low surviving fractions is consistent with our finding that many low-mass NG_{1D} clusters are seemingly quite relaxed and just misidentified due to projection (Fig. 3.3). We reiterate that whether or not an NG_{1D} cluster survives is based on measurements of the one-dimensional velocity distribution, which is analogous to what observers measure for galaxy clusters.

3.8 Discussion and Conclusions

In this study we identify G and NG galaxy clusters in a large dark matter only simulation with an observational technique based on the one-dimensional cluster velocity profile. The main objective of this work is to test how well the one-dimensional AD test is able to identify physical differences between clusters haloes. By classifying G_{1D} and NG_{1D} clusters with observational methods, we can directly compare the results of this work to observed clusters. The main results of this work are the following:

1. Time since last MM is systematically shorter for NG_{1D} systems compared to G_{1D} systems (Fig. 3.5). This difference is strongest for high-mass clusters, whereas little difference is seen for lower mass systems.

2. The time since infall (on to the present-day parent halo) is systematically shorter for satellites in NG_{1D} systems relative to G_{1D} systems (Fig. 3.8).

3. The non-Gaussianity of high-mass cluster velocity profiles is due to both major mergers as well as minor mergers and the accretion of isolated galaxies. However, for low-mass clusters the non-Gaussianity seems to trace minor mergers and isolated accretion and not major mergers (Figs 3.6 and 3.9).

4. The fraction of NG_{1D} clusters increases as a function of both halo mass and redshift. The stronger increase is with halo mass, while the proportion of NG_{1D} systems increases more modestly with redshift (Fig. 3.10).

5. On average, NG_{1D} systems remain NG for 0.5-1 Gyr (Fig. 3.11).

6. The difference between G and NG systems becomes much stronger when using three-dimensional information to construct a sample of NG clusters with

higher purity. This suggests that the intrinsic dependencies of galaxy and cluster properties on dynamical state are likely underestimated observationally due to only having access to projected positions and velocities (Figs 3.6 and 3.9).

3.8.1 Implications for Galaxy Quenching

It is possible to use these results to interpret observational trends with cluster dynamic state. For example, previous works have established that galaxies in NG systems tend to show signatures of being a relatively blue, star-forming, and active population compared to G systems (Ribeiro, Lopes, and Trevisan, 2010; Hou et al., 2012; Roberts and Parker, 2017). It is possible that these differences are related to differences in time since infall. The fact that galaxies in NG clusters have been exposed to a dense environment for less time would naturally give rise to a galaxy population which is preferentially blue and star-forming relative to galaxies in G systems, without the need to invoke any specific quenching mechanism. In an upcoming paper, we plan to use the infall history extracted from these simulations along with a quenching model to test whether differences in time since infall are sufficient to explain the dependence of star-forming fraction on cluster dynamical state observed in Roberts and Parker (2017). A second possibility is that these observed differences are related to physical differences between the haloes of relaxed and unrelaxed clusters. For example, unrelaxed clusters may have underdense and disturbed ICMs, which can affect the efficiency with which the cluster is able to environmentally quench satellites. For example, Roberts, Parker, and Karunakaran (2016) show that X-ray underluminous systems show signatures of disturbed dynamics (see also Popesso et al. 2007) and also host an excess of star-forming galaxies. Environmental quenching mechanisms which involve interactions between galaxies and the ICM, such as ram pressure stripping or starvation, may therefore be less efficient in such systems.

3.8.2 Estimating Dynamical State Along a Single Line-of-Sight

Observations of galaxy cluster dynamics are unavoidably restricted to one-dimensional LOS velocity measurements, which is why we focus the majority of this analysis on NG clusters identified only in one dimension. However, working with simulation data allows us to analyse a more pure sample where clusters have NG velocity distributions in a large fraction of random cluster projections. We find that the separation between properties of G and NG clusters is consistently enhanced when considering a sample of NG clusters with a higher purity compared to the one-dimensional case. This is due to the fact that observationally we only have access to one LOS, and the fact that a cluster looks unrelaxed along one, random, LOS is not enough to say conclusively that a given cluster is unrelaxed on the whole. Indeed, many of the simulated clusters in this work which appear NG along one random projection, show little evidence for disturbed dynamics along other projections.

In some sense this is discouraging, as the three-dimensional information required to more accurately classify cluster dynamical state is not accessible observationally. On the other hand, the fact that we still see systematic differences in cluster properties such as time since MM and satellite time since infall, between G and NG clusters identified in one dimension is encouraging. These differences demonstrate that given a large enough sample, NG clusters identified in one dimension are indeed preferentially unrelaxed relative to G clusters, despite the sample impurity. As a result of this observational impurity, the differences which have been observed between large samples of G and NG clusters (Hou et al., 2009; Ribeiro, Lopes, and Trevisan, 2010; Carollo et al., 2013; Ribeiro et al., 2013; Roberts and Parker, 2017; Costa, Ribeiro, and de Carvalho, 2018; Roberts, Parker, and Hlavacek-Larrondo, 2018; Nascimento et al., 2019) are almost certainly lower limits to the true, underlying dependencies of cluster properties on dynamical state. On a system-by-system basis, this impurity suggests that simply classifying the one-dimensional velocity profile is not enough to classify the underlying dynamical state with confidence. To get a more comprehensive picture of cluster dynamics on a system-by-system basis, it is more useful to combine other dynamic probes

alongside LOS velocities, such as: X-ray morphology (e.g. Roberts, Parker, and Hlavacek-Larrondo, 2018), BCG offsets (e.g. Lopes et al., 2018), magnitude gaps (e.g. Lopes et al., 2018), galaxy spatial distributions (e.g. Wen and Han, 2013), velocity dispersion profiles (e.g. Bilton and Pimbblet, 2018), and more. Many of these observational relaxation proxies are easily derived for groups and clusters in large redshift surveys (excluding X-ray proxies), and therefore identifying samples of unrelaxed systems with many observational tests will help mitigate some of the inherent uncertainty of individual probes.

Acknowledgments: We thank the anonymous referee for their detailed comments that have significantly improved the manuscript. IDR and LCP are supported by the Natural Science and Engineering Research Council of Canada. This work was made possible thanks to a large number of open-source software packages, including: ASTROPY (Astropy Collaboration 2013), MATPLOTLIB (Hunter, 2007), NUMPY (Walt, Colbert, and Varoquaux, 2011), PANDAS (McKinney, 2010), SCIPY (Jones, Oliphant, Peterson, et al., 2001), TOPCAT (Taylor, 2005), YTREE (Smith and Lang, 2018).

The CosmoSim data base used in this paper is a service by the Leibniz-Institute for Astrophysics Potsdam (AIP). The MultiDark data base was developed in cooperation with the Spanish MultiDark Consolider Project CSD2009-00064. The authors gratefully acknowledge the Gauss Centre for Supercomputing e.V. (`www.gauss-centre.eu`) and the Partnership for Advanced Supercomputing in Europe (PRACE, `www.prace-ri.eu`) for funding the MultiDark simulation project by providing computing time on the GCS Supercomputer SuperMUC at Leibniz Supercomputing Centre (LRZ, `www.lrz.de`).

Bibliography

Anderson, T. W. and D. A. Darling (1952). *The Annals of Mathematical Statistics* 23, p. 193.

Behroozi, P. S., R. H. Wechsler, and H.-Y. Wu (2013). *ApJ* 762, 109, p. 109.

Behroozi, P. S. et al. (2013). *ApJ* 763, 18, p. 18.

Bilton, L. E. and K. A. Pimbblet (2018). *MNRAS*.

Bird, C. M. and T. C. Beers (1993). *AJ* 105, pp. 1596–1606.

Bryan, G. L. and M. L. Norman (1998). *ApJ* 495, pp. 80–99.

Cameron, E. (2011). *PASA* 28, pp. 128–139.

Carollo, C. M. et al. (2013). *ApJ* 776, 71, p. 71.

Costa, A. P., A. L. B. Ribeiro, and R. R. de Carvalho (2018). *MNRAS* 473, pp. L31–L35.

D'Agostino, Ralph B and Michael A Stephens, eds. (1986). New York, NY, USA: Marcel Dekker, Inc.

de Carvalho, R. R. et al. (2017). *AJ* 154.3, 96, p. 96.

Deacon, Jane M, Michael J Peckham, and Galvanized Steel (1984). *Radiotherapy and oncology : journal of the European Society for Therapeutic Radiology and Oncology* 2 4, pp. 317–23.

Dressler, A. and S. A. Shectman (1988). *AJ* 95, pp. 985–995.

Flin, P. and J. Krywult (2006). *A&A* 450, pp. 9–14.

Giles, P. A. et al. (2017). *MNRAS* 465, pp. 858–884.

Girardi, M. et al. (1997). *ApJ* 482, pp. 41–62.

Haines, C. P. et al. (2015). *ApJ* 806, 101, p. 101.

Hou, A., L. C. Parker, W. E. Harris, and D. J. Wilman (2009). *ApJ* 702, pp. 1199–1210.

Hou, A. et al. (2012). *MNRAS* 421, pp. 3594–3611.

Hou, A. et al. (2013). *MNRAS* 435, pp. 1715–1726.

Hudson, M. J. et al. (2015). *MNRAS* 447, pp. 298–314.

Hunter, J. D. (2007). *Computing In Science & Engineering* 9.3, pp. 90–95.

Jeltema, T. E., C. R. Canizares, M. W. Bautz, and D. A. Buote (2005). *ApJ* 624, pp. 606–629.

Jones, Eric, Travis Oliphant, Pearu Peterson, et al. (2001).

Joshi, G. D., L. C. Parker, and J. Wadsley (2016). *MNRAS* 462, pp. 761–777.

Joshi, G. D., J. Wadsley, and L. C. Parker (2017). *MNRAS* 468, pp. 4625–4634.

Klypin, A., G. Yepes, S. Gottlöber, F. Prada, and S. Heß (2016). *MNRAS* 457, pp. 4340–4359.

Knebe, Alexander et al. (2011). *MNRAS* 415.3, pp. 2293–2318.

Lopes, Paulo A. A. et al. (2018). *MNRAS* 478, pp. 5473–5490.

McKinney, Wes (2010). *Proceedings of the 9th Python in Science Conference*. Ed. by Stéfan van der Walt and Jarrod Millman, pp. 51–56.

Mohd Razali, Nornadiah and Bee Yap (2011). *J. Stat. Model. Analytics* 2.

Nascimento, R. S., P. A. A. Lopes, A. L. B. Ribeiro, A. P. Costa, and D. F. Morell (2019). *MNRAS* 483, pp. L121–L126.

Nurgaliev, D. et al. (2013). *ApJ* 779, 112, p. 112.

Old, L. et al. (2018). *MNRAS* 475, pp. 853–866.

Oman, K. A., M. J. Hudson, and P. S. Behroozi (2013). *MNRAS* 431, pp. 2307–2316.

Popesso, P., A. Biviano, H. Böhringer, and M. Romaniello (2007). *A&A* 461, pp. 397–410.

Prada, F., A. A. Klypin, A. J. Cuesta, J. E. Betancort-Rijo, and J. Primack (2012). *MNRAS* 423, pp. 3018–3030.

Press, W. H. and P. Schechter (1974). *ApJ* 187, pp. 425–438.

Ribeiro, A. L. B., P. A. A. Lopes, and S. B. Rembold (2013). *A&A* 556, A74, A74.

Ribeiro, A. L. B., P. A. A. Lopes, and M. Trevisan (2010). *MNRAS* 409, pp. L124–L127.

Ribeiro, A. L. B. et al. (2013). *MNRAS* 434, pp. 784–795.

Roberts, I. D. and L. C. Parker (2017). *MNRAS* 467, pp. 3268–3278.

Roberts, I. D., L. C. Parker, and J. Hlavacek-Larrondo (2018). *MNRAS* 475, pp. 4704–4716.

Roberts, I. D., L. C. Parker, and A. Karunakaran (2016). *MNRAS* 455, pp. 3628–3639.

Rowley, D. R., P. A. Thomas, and S. T. Kay (2004). *MNRAS* 352, pp. 508–522.

Schuecker, P., H. Böhringer, T. H. Reiprich, and L. Feretti (2001). *A&A* 378, pp. 408–427.

Smith, Britton and Meagan Lang (2018).

Taylor, M. B. (2005). *Astronomical Data Analysis Software and Systems XIV*. Ed. by P. Shopbell, M. Britton, and R. Ebert. Vol. 347. Astronomical Society of the Pacific Conference Series, p. 29.

Walt, S. van der, S. C. Colbert, and G. Varoquaux (2011). *Computing in Science Engineering* 13.2, pp. 22–30.

Weißmann, A., H. Böhringer, R. Šuhada, and S. Ameglio (2013). *A&A* 549, A19, A19.

Wen, Z. L. and J. L. Han (2013). *MNRAS* 436, pp. 275–293.

Wojtak, Radosław (2013). *A&A* 559, A89, A89.

Yahil, A. and N. V. Vidal (1977). *ApJ* 214, pp. 347–350.

Yun, Kiyun et al. (2019). *MNRAS* 483, pp. 1042–1066.

Zhang, Y.-Y., T. H. Reiprich, A. Finoguenov, D. S. Hudson, and C. L. Sarazin (2009). *ApJ* 699, pp. 1178–1195.

4 | Evidence of pre-processing and a dependence on dynamical state for low-mass satellite galaxies

This chapter represents an unchanged version of the paper, *Evidence of Pre-Processing and a Dependence on Dynamical State for Low-Mass Satellite Galaxies*, published in the refereed journal, *Monthly Notices of the Royal Astronomical Society*. The full reference is given below:

Roberts I.D., Parker L.C., 2017, MNRAS, Volume 467, Issue 3, pp. 3268-3278

Department of Physics & Astronomy, McMaster University, Hamilton ON L8S 4M1

Abstract

We study the dependence of satellite star formation rate and morphology on group dynamics for a sample of Sloan Digital Sky Survey groups. We classify the group dynamical state and study satellite properties for populations of galaxies at small and large group-centric radii. For galaxies at large radii we find no differences in the star-forming or disc fraction for those in Gaussian groups compared to those in non-Gaussian groups. By comparing the star-forming and disc fractions of infalling galaxies to field galaxies we find evidence for the pre-processing of both star formation rate and morphology. The strength of pre-processing increases with halo mass and is highest for low-mass galaxies infalling on to high-mass haloes. We show that the star formation rate of galaxies at small radii correlates with group dynamical state, with galaxies in non-Gaussian groups showing enhanced star-forming fractions compared to galaxies in Gaussian groups. Similar correlations are not seen for the disc fractions of galaxies at small radii. This seems to suggest that either the mechanisms driving star formation quenching at small halo-centric radii are more efficient in dynamically relaxed groups or that non-Gaussian groups have assembled more recently and therefore satellites of the groups will have been exposed to these transforming mechanisms for less time.

4.1 Introduction

In the first half of the twentieth century, it was beginning to be realized that populations of high-mass clusters were predominantly made up of early-type galaxies, with Hubble and Humason (1931) stating that "the predominance of early types is a conspicuous feature of clusters in general". Many subsequent observational studies have cemented the now familiar environmental dependence of galaxy properties (e.g. Butcher and Oemler, 1978; Dressler, 1980; Postman and Geller, 1984; Dressler et al., 1999; Blanton et al., 2005; Wetzel, Tinker, and Conroy, 2012). Namely, galaxies in clusters tend to be red in colour with low star formation rates and early-type morphologies. On the other hand, the low-density field is preferentially populated by blue, star-forming, spiral galaxies. A third environment, galaxy groups are the most common environment in the local Universe (Geller and Huchra, 1983; Eke et al., 2005) and also represent an intermediate-mass regime in which significant populations of both star-forming spirals and passive ellipticals are observed (e.g. Wilman et al., 2005; McGee et al., 2011).

Not only do galaxy properties correlate with the type of haloes in which they reside, but also with distance from the halo centre. In particular, galaxies at large radii show enhanced star formation and are more likely to have spiral morphologies compared to galaxies near the centre of the halo (Whitmore, Gilmore, and Jones, 1993; Goto et al., 2003; Postman et al., 2005; Rasmussen et al., 2012; Wetzel, Tinker, and Conroy, 2012; Fasano et al., 2015; Haines et al., 2015). Therefore, in order to probe the environmentally driven aspects of galaxy evolution it is crucial to account for both the dependence on the host halo environment and the radial position within the group or cluster.

The aforementioned environmental dependences are strongest for low-mass galaxies and it appears that properties of high-mass galaxies are less dependent on environment (Haines et al., 2006; Bamford et al., 2009). For high-mass galaxies, quenching is thought to be driven by internal, secular processes such as feedback from AGN (e.g. Schawinski et al., 2009). This dichotomy between high- and low-mass galaxies is presented in Peng et al. (2010) where it is argued that in the local Universe galaxies below $\sim 10^{10.5}\,\mathrm{M}_{\odot}$ are environmentally quenched as satellite galaxies and galaxies above that mass are primarily quenched by internal processes

(so-called mass quenching).

While it appears that the majority of low-mass galaxies are primarily quenched as satellites, there are still open questions regarding the details of the process(es) involved. One such question is which are the dominant mechanism(s) responsible for suppressing star formation in satellite galaxies? Galaxy harassment (e.g. Moore et al., 1996), mergers (e.g. Mihos and Hernquist, 1994), starvation (e.g. Kawata and Mulchaey, 2008) and ram-pressure stripping (e.g. Gunn and Gott, 1972) have all been invoked; but no consensus exists on their relative importance in different environments. Additionally, while all of these mechanisms are capable of quenching galaxies (either through inducing rapid star formation, and thus quickly using up cold gas reserves, or the stripping of gas), not all would have a strong effect on galaxy morphology. Recently, starvation and/or ram-pressure stripping are often favoured as satellite quenching mechanisms (Muzzin et al., 2014; Fillingham et al., 2015; Peng, Maiolino, and Cochrane, 2015; Weisz et al., 2015; Wetzel, Tollerud, and Weisz, 2015) but it is not clear that either would strongly impact morphology; therefore in order to explain the observed correlation between galaxy star formation and morphology it seems that an additional process to efficiently drive morphological transformations is perhaps required (e.g. Christlein and Zabludoff, 2004).

Also of importance is determining the characteristic haloes in which most satellite galaxies are quenched and experience morphological transformations. Do galaxies remain actively forming stars with late-type morphologies until passing the virial radius of high-mass clusters, or are they transformed in smaller groups prior to or during cluster infall (known as "pre-processing") (e.g. Fujita, 2004)? Pre-processing is often invoked to explain observational results such as passive and red fractions at large cluster-centric radii which are enhanced significantly relative to the field (Lu et al., 2012; Wetzel, Tinker, and Conroy, 2012; Bahé et al., 2013; Haines et al., 2015; Just et al., 2019), as well as the prevalence of S0 galaxies in large clusters (Kodama and Smail, 2001; Helsdon and Ponman, 2003; Moran et al., 2007; Wilman et al., 2009). Studies have also found evidence for pre-processing by measuring the fraction of galaxies which are part of a group subhalo during infall on to a cluster, with both simulations (McGee et al., 2009; De Lucia, Fontanot, and Wilman, 2012; Bahé et al., 2013) and observations (Dressler et al., 2013; Hou,

Parker, and Harris, 2014).

This pre-processing and recent infall of galaxies can imprint itself on the dynamical profile of a group or cluster. For a dynamically relaxed group it is expected that the projected velocity profile of member galaxies will resemble a Gaussian distribution whereas groups which are dynamically young and unrelaxed tend to display velocity profiles which are less Gaussian in nature (e.g. Yahil and Vidal, 1977; Bird and Beers, 1993; Martínez and Zandivarez, 2012; Ribeiro et al., 2013). The degree to which galaxy properties correlate with the dynamical state of their host groups is still an open question (e.g. Biviano et al., 2002; Ribeiro, Lopes, and Rembold, 2013), though it may be expected that such correlations exist. For example, dynamically complex groups are preferentially X-ray underluminous (Popesso et al., 2007; Roberts, Parker, and Karunakaran, 2016) which indicates an underdense intra-group medium. Considering that many quenching mechanisms operate through interactions with the intra-group medium, it may be expected that such mechanisms will be less efficient in non-Gaussian (NG) groups. Furthermore, if NG groups represent younger systems then galaxy properties could be affected (compared to Gaussian systems) simply due to galaxies being exposed to a dense environment for less time. Previous work has suggested that galaxies in relaxed groups tend to be redder than galaxies in unrelaxed groups (Ribeiro, Lopes, and Trevisan, 2010; Carollo et al., 2013; Ribeiro et al., 2013). However, less work has been done studying the dynamical dependences of star formation and morphology directly. One example is the work of Hou et al. (2013) who find no detectable difference between the quiescent fractions of galaxies in Gaussian versus NG groups as a function of redshift.

Previously, we have shown that the star formation and morphology of low-mass galaxies depend not only on stellar and halo mass but also on the X-ray luminosity of the host group (Roberts, Parker, and Karunakaran, 2016). Here we investigate the dependence of star-forming and morphological properties of galaxies on group dynamical state. In particular, we study these properties within different radial regions of the halo to explore whether galaxy properties correlate with group dynamical state and whether any correlations show radial dependence.

The outline of this paper is as follows. In Section 4.2 we describe the sample of galaxies in groups as well as our field sample. In Section 4.3 we analyse the

dependence of galaxy star formation and morphology on dynamics for galaxies at large radii. In Section 4.4 we do the same for galaxies in the inner regions of the halo. We discuss our results in Section 4.5 and summarize in Section 4.6.

In this paper we assume a flat Λ cold dark matter cosmology with $\Omega_M = 0.3$, $\Omega_\Lambda = 0.7$ and $H_0 = 70\,\mathrm{km\,s^{-1}\,Mpc^{-1}}$.

4.2 Data

4.2.1 Group Sample

For this work we employ the group catalogue of Yang et al. (2007), which is constructed by applying the halo-based galaxy group finder from Yang et al. (2005) and Yang et al. (2007) to the New York University Value-Added Galaxy Catalogue (NYU-VAGC; Blanton et al. 2005). The NYU-VAGC is a low-redshift galaxy catalogue consisting of $\sim 700\,000$ galaxies in the Sloan Digital Sky Survey Data Release 7 (SDSS-DR7; Abazajian et al. 2009). We will briefly describe the halo-based group finding algorithm used to generate the Yang group catalogue; but for a more complete description please see Yang et al. (2005) and Yang et al. (2007).

First, the centres of potential groups are identified. Galaxies are initially assigned to groups with a traditional "friends-of-friends" (FOF) algorithm (e.g. Huchra and Geller, 1982) with very small linking lengths. The luminosity-weighted centres of FOF groups with at least two members are then taken as the centres of potential groups and all galaxies not yet associated with a FOF group are treated as tentative centres for potential groups. A characteristic luminosity, $L_{19.5}$, defined as the combined luminosity of all group members with ${}^{0.1}M_r - 5\log h \leq -19.5$, is calculated for each tentative group and an initial halo mass is assigned with an assumption for the group mass-to-light ratio, $M_H/L_{19.5}$. Utilizing this tentative group halo mass, velocity dispersions and a virial radius are calculated for each group. Next, galaxies are assigned to groups under the assumption that the distribution of galaxies in phase space follows that of dark matter particles – the distribution of dark matter particles is assumed to follow a spherical NFW profile (Navarro, Frenk, and White, 1997). With the new group memberships, group

centres are recalculated and the procedure is iterated until group memberships no longer change.

We take group halo masses, M_H, from the Yang catalogue calculated with a characteristic group stellar mass, $M_{\star,\mathrm{grp}}$, and assuming that there is a one-to-one relation between $M_{\star,\mathrm{grp}}$ and M_H. Yang et al. (2007) define $M_{\star,\mathrm{grp}}$ as

$$M_{\star,\mathrm{grp}} = \frac{1}{g(L_{19.5},\, L_{\mathrm{lim}})} \sum_i \frac{M_{\star,i}}{C_i} \tag{4.1}$$

where $M_{\star,i}$ is the stellar mass of the ith member galaxy, C_i is the completeness of the survey at the position of that galaxy, and $g(L_{19.5},\, L_{\mathrm{lim}})$ is a correction factor which accounts for galaxies missed due to the magnitude limit of the survey. While we utilize halo masses derived from group stellar mass in this paper, we have run the same analysis with halo masses derived from group luminosity in the Yang catalogue and see no changes in observed trends. Campbell et al. (2015) show that the choice between stellar mass and luminosity as a halo mass predictor can introduce biases in mass estimates. For example, when group luminosity is assumed to be the primary property determining halo occupation in mock catalogues, halo masses inferred from group stellar mass are systematically larger for haloes with a red central compared to haloes with a blue central (Campbell et al., 2015). For the samples of Gaussian and NG groups which are frequently compared in this paper (see Section 4.2.3), we find that the fraction of groups with passive centrals is 94 per cent in both cases; therefore the aforementioned effects should not preferentially bias one sample more than the other.

The Yang catalogue contains both haloes which would be broadly classified as groups ($10^{12} \leq M_H \leq 10^{14}\,\mathrm{M}_\odot$) as well as clusters ($M_H \leq 10^{14}\,\mathrm{M}_\odot$); but for brevity we will refer to all haloes as groups regardless of halo mass unless otherwise specified.

We calculate group-centric radii for all group members within the sample with the redshift of the group and the angular separation of the galaxy from the luminosity-weighted centre of the host halo. Radii are normalized by the virial radius, R_{200}, of the group which is defined as (Yang et al., 2007; Tinker et al.,

2008)

$$R_{200} = \left[\frac{M_H}{200(4/3)\pi\Omega_{m,0}\rho_{c,0}(1+z)^3}\right]^{1/3} \tag{4.2}$$

For the cosmology assumed in this work, Equation 4.2 becomes

$$R_{200} = 1.13\,h^{-1}\,\mathrm{Mpc}\left(\frac{M_H}{10^{14}\,h^{-1}\,\mathrm{M}_\odot}\right)^{1/3}(1+z_{\mathrm{group}})^{-1}. \tag{4.3}$$

For our group sample, we consider galaxies which have projected group-centric radii within R_{200}.

To study specific characteristics of galaxies within the group sample, we match various public SDSS galaxy catalogues to the group sample. We utilize galaxy stellar masses and k-corrected absolute magnitudes given in the NYU-VAGC, which are obtained through fits to galaxy spectra and broad-band photometric measurements following the procedure of Blanton and Roweis (2007).

For our star formation indicator we use fibre-corrected specific star formation rates (SSFR = SFR/$M_\star$) from the MPA-JHU DR7 catalogue (Brinchmann et al., 2004). These SSFRs are primarily derived from emission lines, with an exception for galaxies with no clear emission lines or AGN contamination in which case SSFRs are based on the 4000 Å break. SSFRs for galaxies with S/N > 2 in Hα are determined with only the Hα line and SSFRs for galaxies with S/N > 3 in all four BPT lines are determined with a combination of emission lines. For this work we define star-forming galaxies to be all galaxies with $\log \mathrm{SSFR} \geq -11$, Wetzel, Tinker, and Conroy (2012) show that in the local Universe the division between the red sequence and the blue cloud is consistently found at $\log \mathrm{SSFR} \simeq -11$ across a wide range of halo masses.

For our morphology indicator we use a global Sérsic index, n, taken from the single component Sérsic fits in Simard et al. (2011), and define disc galaxies as all galaxies with $n \leq 1.5$. While the distribution of Sérsic index is not as clearly bimodal as the SSFR distribution, we find that our observed trends are insensitive to our exact choice of dividing Sérsic index. We also weight all of the data by $1/\mathrm{V}_{\mathrm{max}}$ as given in Simard et al. (2011) to account for the stellar-mass incompleteness of the sample. This does not explicitly account for the fact that completeness is also a function of galaxy colour, with star-forming galaxies being visible at higher

redshift than passive galaxies (e.g. Taylor et al., 2011). While the sample will be biased towards detecting star-forming galaxies at high redshift, we do not expect that this bias will affect galaxies in Gaussian groups differently than galaxies in NG groups. Furthermore, the fact that we match all samples by redshift (see Section 4.2.4) should help to ensure that the completeness (as a function of colour) of the different galaxy samples does not vary substantially. We note that we do not use a stellar mass complete sample in this work due to the fact that the sample size would be significantly reduced, and in particular, the sample of galaxies in NG groups would be very small.

For our analysis we consider only satellite galaxies within groups. Central galaxies are defined as the most-massive galaxy (MMG) within a group and subsequently removed from the data set. We note that it has been shown that the most-massive (or brightest) group galaxy does not always correspond to the group central (i.e. the galaxy closest to the centre of the potential), for example Skibba et al. (2011) show that the fraction of galaxies which are brightest but do not reside at the centre of the potential ranges from $\sim$25 per cent for group-mass haloes to $\sim$40 per cent for high-mass clusters. To gauge any potential influence that removing the MMG has on the results, we repeat the analysis both with no removal of the MMG and also with removing the second MMG instead of the MMG. In both cases, this does not alter the observed trends qualitatively or quantitatively.

To ensure reasonable statistics when classifying the dynamical states of the groups Section 4.2.3 we only include groups from the Yang catalogue which have eight or more member galaxies. In total, this gives an initial group sample of 47 961 galaxies in 2 662 groups.

4.2.2 Infalling and Field Samples

We also define samples of "infalling" and "field" galaxies for further comparisons.

To populate the infalling sample we take all galaxies in single-member groups from the Yang catalogue which have projected distances from luminosity-weighted group centres between 1 and 3 virial radii, and have line-of-sight (LOS) velocities less than 1.5σ from the group centroid, where velocity dispersions, σ, are calculated with Equation (6) from Yang et al. (2007). We further define a "strict" infalling sample with the same velocity threshold but only containing galaxies between 2

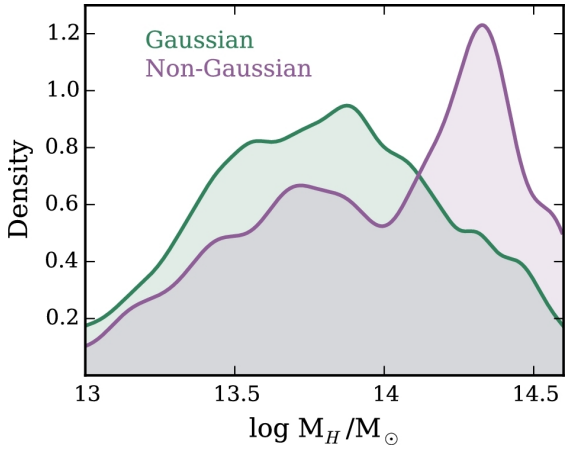

FIGURE 4.1: Halo mass distributions, smoothed with a Gaussian kernel, for galaxies in the unmatched G and NG samples.

and 3 virial radii. Galaxies which satisfy these criteria for multiple groups are assigned as infalling on to the group which they are closest to. The infall sample consists of 19 598 galaxies infalling on to 2 396 groups.

Our field sample is defined as all galaxies in single-member groups which are not members of the infalling sample, and are separated from their nearest "bright" neighbour by at least 1 Mpc in projected distance and 1000 km s^{-1} in LOS velocity, though our results are insensitive to the exact isolation criteria chosen. We define bright neighbours as all galaxies which are brighter than the survey r-band absolute magnitude limit at $z = 0.2$ (our redshift upper limit), which corresponds to $M_{r,\mathrm{lim}} = -21.3$. Without this condition, the strictness of our isolation criteria would vary with redshift. We also remove any galaxies which are within 1 Mpc of a survey edge, or are within 1000 km s^{-1} of our maximum redshift to ensure that all galaxies truly satisfy the isolation criteria. The field sample consists of 352 262 galaxies.

Stellar masses, absolute magnitudes, SSFRs and Sérsic indices for the infall and field sample are obtained from the same sources discussed in Section 4.2.1.

4.2.3 Group Dynamics

To classify the dynamical state of the haloes in the data set we use a combination of two statistical tests: the Anderson-Darling (AD) normality test (Anderson and

Darling 1952; see Hou et al. 2009; Hou et al. 2013 for an astronomical application) and the Dip test (Hartigan and Hartigan 1985; see Ribeiro et al. 2013 for an astronomical application).

The AD test is a non-parametric test of normality based upon the comparison between the cumulative distribution function (CDF) of a measured data sample and the CDF of a Gaussian distribution. Under the assumption that the data are in fact normally distributed, the AD test determines the probability (p) that the difference between the CDFs of the data and a normal distribution equals or exceeds the observed difference. We apply the AD test to the velocity distributions of the member galaxies of each group in the sample, thereby broadly classifying the dynamical state of each halo. Our first criterion in classifying a group as Gaussian (G) is that the p-value given by the AD test be greater than or equal to 0.05.

Our second criterion required for a group to be classified as G is that its velocity distribution be unimodal. Ideally standard normality tests would detect all instances of multimodality; but this is not always the case. In particular, multimodality in distributions with modes at small separations can be missed by standard statistical techniques (Ashman, Bird, and Zepf, 1994). To gauge the modality of the velocity distribution of a given group we use the Dip test. Like the AD test, the Dip test is also a non-parametric CDF statistic. Where they differ is that the Dip test looks for a flattening of the CDF for the data which would correspond to a "dip" in the distribution being tested. The Dip test operates under the null hypothesis that the data are unimodal, and we consider a group velocity distribution unimodal if the Dip test p-value is greater than or equal to 0.05. Therefore, our G data sample consists of all those groups with $p_{\rm ad} \geq 0.05$ and $p_{\rm dip} \geq 0.05$, whereas our NG data sample consists of all those groups with $p_{\rm ad} < 0.05$ or $p_{\rm dip} < 0.05$.

After applying the above criteria we find a G sample consisting of 42 655 galaxies within 2447 groups and a NG sample consisting of 5306 galaxies within 215 groups. We find that the AD test is the stronger discriminator compared to the Dip test as out of all of the galaxies making up the NG sample, 90 per cent failed the AD test but passed the Dip test, 8 per cent passed the AD test but failed the Dip test, and 2 per cent failed both the AD test and the Dip test. The authors note that it is easier to statistically identify NG groups for groups with high galaxy

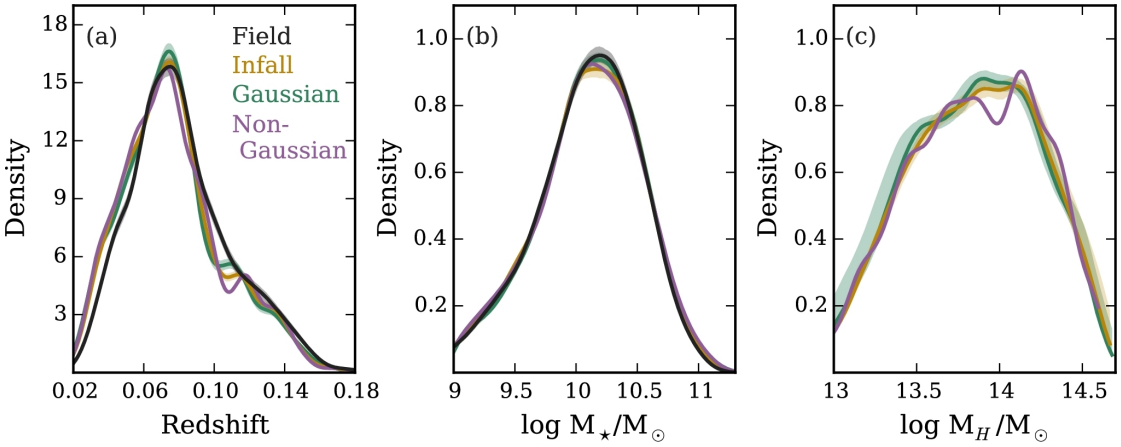

FIGURE 4.2: Distributions for stellar mass, redshift and host halo mass for galaxies in the matched G, NG, infall and field (where applicable) samples, smoothed with a Gaussian kernel. Shaded regions around the G, infall and field lines are 99 per cent Monte Carlo confidence intervals corresponding to the stochastic nature of our matching procedure. The lines corresponding to the NG sample have no shading because it is the NG sample to which the other samples are stochastically matched.

membership, this can lead to the NG sample being skewed towards large halo masses (see Fig. 4.1). To address this we match our G and NG samples by halo mass (as well as stellar mass and redshift), as described in the following section.

4.2.4 Matched Data Set

To ensure a fair comparison between galaxies in different environments (i.e. field galaxies, infall galaxies, galaxies in G groups, and galaxies in NG groups) we match our sample of G group galaxies, NG group galaxies and infalling galaxies by stellar mass, redshift and halo mass. Additionally, we then match our sample of field galaxies by stellar mass and redshift. The matching is particularly important when trying to elucidate information on the effect of group dynamics on galaxy star formation and morphological properties for two main reasons:

First, stellar mass, redshift and halo mass have all been shown to influence galaxy star formation and morphology (e.g. Brinchmann et al., 2004; Feulner et al., 2005; Zheng et al., 2007; Cucciati et al., 2012; Wetzel, Tinker, and Conroy, 2012; Lackner and Gunn, 2013; Tasca et al., 2014); whereas the impact of group

dynamics is less clear (Hou et al., 2013; Ribeiro et al., 2013) which is suggestive of a more modest role. Therefore, to search for trends in galaxy star formation and morphology with group dynamics it is crucial to properly control for these other known correlations.

Secondly, standard statistical normality tests, such as the AD test, are biased towards identifying NG distributions when sample size is large. This is a result of the statistical power of the test increasing with sample size which subsequently allows the detection of more and more subtle departures from normality (Mohd Razali and Yap, 2011). While these subtle departures from normality will perhaps be statistically significant, they may not be physically relevant (in principle, no group is perfectly Gaussian) and what really matters is whether galaxies in groups which show large departures from normality have different properties than galaxies in groups which show smaller departures from normality. Since group richness generally scales with halo mass, in the absence of any matching procedure, a sample of NG groups will be biased towards large halo masses compared to a similar sample of G groups – even though many high halo mass NG groups may have been identified on the basis of very small departures from normality. Ensuring that our G and NG samples have similar halo mass distributions allows us to make a fairer comparison between the two samples.

Our algorithm for matching the G and NG samples is as follows:

1. The list of galaxies found in NG groups is iterated through, for each galaxy one "matching" galaxy from the G sample is found. To be considered matching the two galaxies must have stellar masses within 0.1 dex, redshifts within 0.01 and halo masses within 0.1 dex.

2. Step 1 is repeated until no more matches are found. The end result is a list of galaxies from the NG sample each of which will have one or more matching galaxies from the G sample assigned to them.

3. The matched G sample is generated by including two galaxies from the G sample for every one matching galaxy from the NG sample. By definition this excludes any galaxies in the NG sample which have only one identified match. However, 85 per cent of galaxies in the NG sample have two or more matches so although we reduce the NG sample size by 15 per cent it allows

us to increase the matched G sample size twofold. It is worth noting that when we run our analysis keeping only one matched G galaxy instead of two, we find no changes in the trends observed.

4. In the case where a given galaxy in the NG sample has more than two identified matches, the two matching galaxies from the G sample are chosen randomly. This introduces a stochastic nature to our analysis as each generation of the matched G sample will not contain exactly the same galaxies. To account for this, any quantities calculated with the matched G sample are done so in a Monte Carlo sense where the median of 1000 stochastic generations is quoted.

The infall and field sample are subsequently matched to the NG sample following the same procedure and the same method is used to account for the stochastic nature of the matching procedure. Fig. 4.2 shows smoothed density distributions of stellar mass, redshift and halo mass for the matched G, NG, infall and field samples. For the remainder of the paper all analysis is done with the matched samples, therefore from this point forward any reference to the G, NG, infall or field samples refers to the matched samples.

4.3 Galaxy Properties at Large Radii

We first consider the star-forming and morphological properties of galaxies at large group-centric radii, and for comparison show the same trends for galaxies within the infall and field samples. We separate galaxies at large and small radii at $1/2\,R_{200}$ which is close to the median group-centric radius for the sample of $0.43\,R_{200}$. We apply a lower stellar mass cut at $10^{9.5}\,\mathrm{M}_{\odot}$ in order to avoid including galaxies with large $1/V_{\mathrm{max}}$ weights.

In Fig. 4.3 we show star-forming ($\log \mathrm{SSFR} > -11$) and disc ($n < 1.5$) fractions versus stellar mass for the four different galaxy samples. The bottom panels show the difference in star-forming/disc fractions between the NG and G samples ($NG - G$) coarsely binned into low-mass ($M_{\star} < 10^{10.2}\,\mathrm{M}_{\odot}$) and high-mass ($M_{\star} > 10^{10.2}\,\mathrm{M}_{\odot}$) galaxies, where $10^{10.2}\,\mathrm{M}_{\odot}$ is the median stellar mass of the sample. We estimate uncertainties on star-forming and disc fractions with two

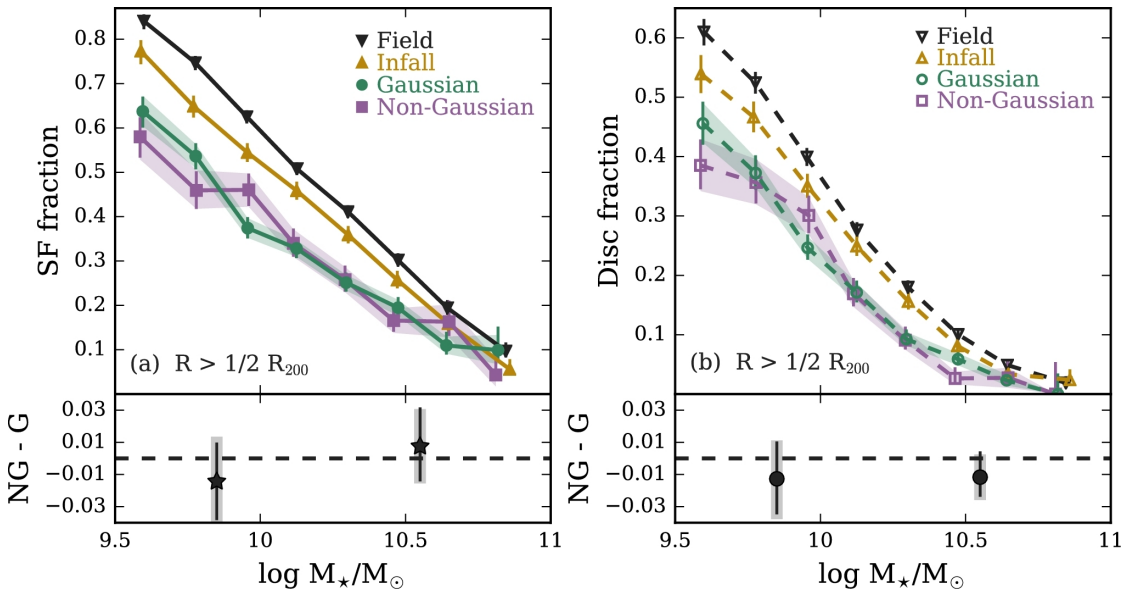

FIGURE 4.3: Star-forming (left) and disc (right) fraction versus stellar mass for field galaxies, infalling galaxies and galaxies at large radii (outside $1/2\,R_{200}$) in the G and NG samples. Error bars correspond to 68 per cent binomial confidence intervals as given in Cameron (2011), and shaded regions are 68 per cent confidence intervals derived from 1000 bootstrap re-samplings over individual groups. Lower panels show the difference in star-forming/disc fractions between G and NG groups, for low-mass ($M_\star < 10^{10.2}\,\mathrm{M}_\odot$) and high-mass ($M_\star > 10^{10.2}\,\mathrm{M}_\odot$) galaxies.

methods. First, we follow Cameron (2011) who advocate the use of Bayesian binomial confidence intervals derived from the quantiles of the beta distribution to estimate statistical uncertainties on population fractions. The error bars on the fractions correspond to 68 per cent confidence intervals obtained with this method. Secondly, we quote 68 per cent bootstrap confidence intervals derived by bootstrapping over the member galaxies of individual groups; the confidence intervals derived from 1000 bootstrap realizations are shown as shaded regions.

In Fig. 4.3 we see a distinct trend in terms of star-forming and disc fractions, where field galaxies show the highest fractions, followed by infalling galaxies, followed by large-radius group members. Focusing now on the two dynamical samples we see no systematic difference between the star-forming or disc fractions for galaxies at large-radii within G groups compared to galaxies in NG groups. This suggests that any influence that the dynamical state of the group has on star-forming or morphological properties is not in place at large radii within the groups. This is apparent in the lower panels of Fig. 4.3 where the value of $NG - G$ is consistent with zero for both star-forming and disc fractions, regardless of stellar mass. As stated in Section 4.2.3 we have used a p-value of 0.05 to divide the sample into G and NG groups; but we note that the results in Fig. 4.3 are not sensitive to the specific choice from a reasonable range of p-values (see Appendix 4.A).

We also see that the star-forming and disc fractions for galaxies at large radii are significantly below the values for the field sample. Previous studies (Lewis et al., 2002; Gray et al., 2004; Rines et al., 2005; Verdugo, Ziegler, and Gerken, 2008) have similarly found that star formation of galaxies within infall regions remains suppressed compared to the field out to radii of $\sim 2-3\,R_{200}$. This suppression is often attributed to backsplash galaxies which have already made a passage through the halo centre, the pre-processing of galaxies in small groups prior to infall, or some combination of the two. We are particularly interested in determining how much of this difference can be accounted for by pre-processing. It is expected that pre-processing should play a more important role in large clusters compared to smaller groups, as a larger fraction of galaxies infalling on to clusters will have been a part of a group prior to infall. This is a result of the hierarchical build-up of structure; regions of space around large clusters are not average but are preferentially populated with other dense structures such as group haloes (e.g. Mo

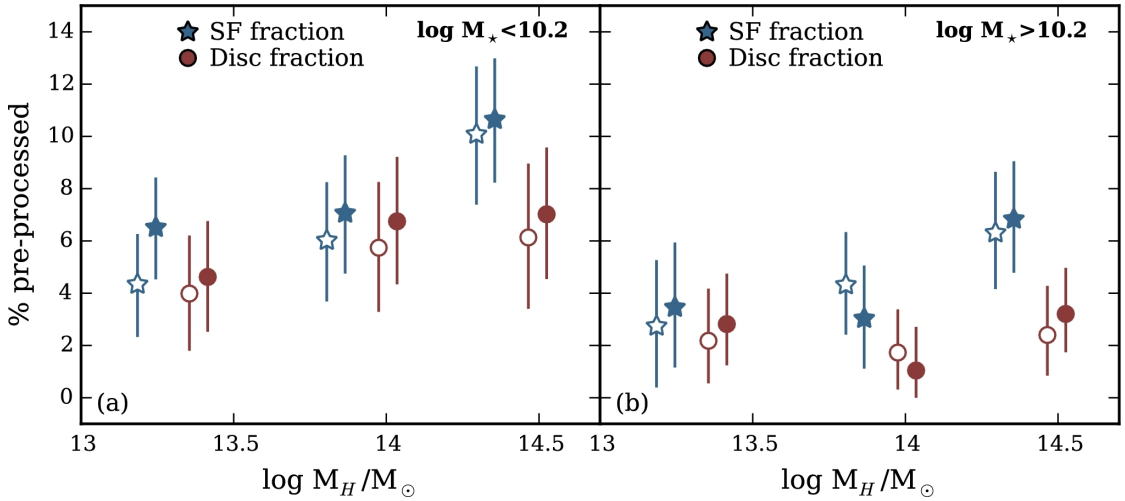

FIGURE 4.4: Percentage of infalling galaxies which have had star formation (stars) or morphology (circles) pre-processed for both low-mass ($M_\star < 10^{10.2}\,\mathrm{M}_\odot$, left) and high-mass ($M_\star > 10^{10.2}\,\mathrm{M}_\odot$, right) galaxies, as a function of halo mass. Filled markers correspond to the whole infall sample ($1 < R < 3\,R_{200}$) and open markers correspond to the strict infall sample ($2 < R < 3\,R_{200}$). Error bars are 68 per cent binomial confidence intervals (Cameron, 2011)

and White, 1996; Wang et al., 2008).

We look for evidence of pre-processing by examining the "field excess", which we define as the difference in star forming or disc fraction between field and infalling galaxies at a given stellar mass, for different halo mass ranges. The range in group-centric radii for galaxies in the infall sample ($1 < R < 3\,R_{200}$) is susceptible to contamination from galaxies backsplashing beyond the virial radius after first pericentric passage (e.g. Bahé et al., 2013). To address this, we also show pre-processing results for our "strict" infall sample ($2 < R < 3\,R_{200}$) which should be less susceptible to backsplash contamination, as many previous studies have shown that the majority of backsplashing galaxies are found within two virial radii (Mamon et al., 2004; Mahajan, Mamon, and Raychaudhury, 2011; Oman, Hudson, and Behroozi, 2013; Haines et al., 2015). If contamination from backsplash galaxies is low, this field excess should approximate the fraction of galaxies which have been pre-processed prior to infalling on to their present-day group. We investigate the halo mass dependence of pre-processing by splitting the group sample into

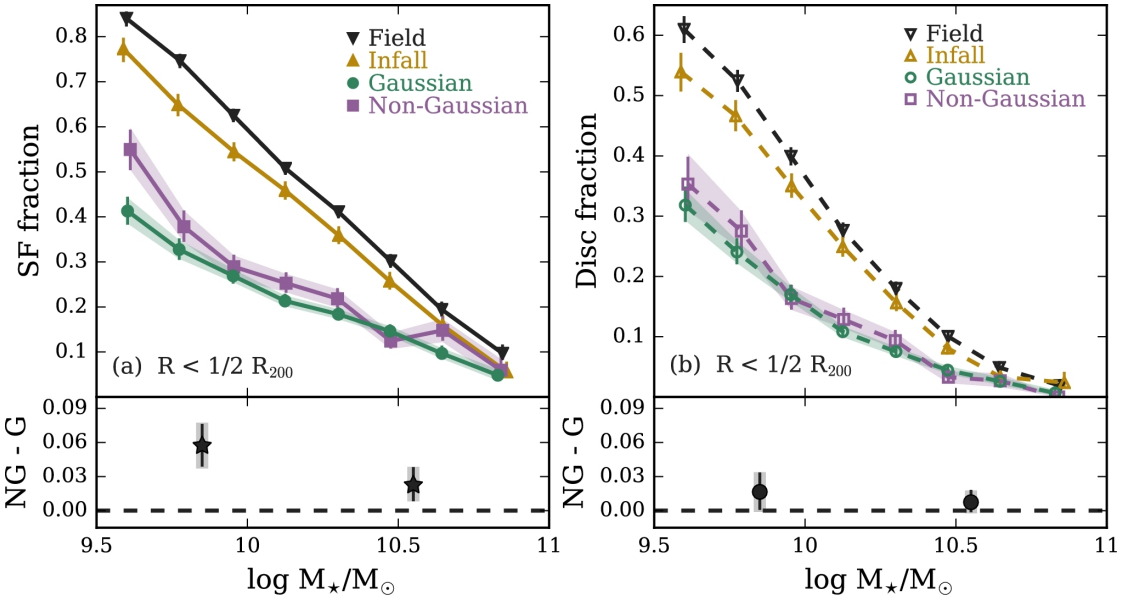

FIGURE 4.5: Star-forming (left) and disc (right) fraction versus stellar mass for field galaxies, infalling galaxies and galaxies at small radii (within the median group-centric radius) in the G and NG samples. Error bars correspond to 68 per cent binomial confidence intervals as given in Cameron (2011), and shaded regions are 68 per cent confidence intervals derived from 1000 bootstrap re-samplings over individual groups. Lower panels show the difference in star-forming/disc fractions between G and NG groups, for low-mass ($M_\star < 10^{10.2}\,\mathrm{M}_\odot$) and high-mass ($M_\star > 10^{10.2}\,\mathrm{M}_\odot$) galaxies.

three halo mass bins each containing an approximately equal number of galaxies: $10^{13} < M_H \leq 10^{13.7}\,\mathrm{M}_\odot$, $10_{13.7} < M_H \leq 10^{14.1}\,\mathrm{M}_\odot$ and $10^{14.1} < M_H \leq 10^{15}\,\mathrm{M}_\odot$, as well as two stellar mass bins (for each range in halo mass): $M_\star < 10^{10.2}\,\mathrm{M}_\odot$ and $M_\star > 10^{10.2}\,\mathrm{M}_\odot$. In Fig. 4.4 we show the percentage of low-mass and high-mass galaxies which have been pre-processed in terms of star-forming fraction and disc fraction, and its dependence on halo mass, for the infall sample (filled markers) and the strict infall sample (open markers).

4.4 Galaxy Properties at Small Radii

We now consider star-forming and disc fractions for galaxies at small radii within the halo, and again consider the differences among the G, NG, infall and field

samples. Fig. 4.5 shows star-forming and disc fractions versus stellar mass for the four galaxy samples. In contrast to the outer region of the halo, when considering star-forming fractions for galaxies at small radii a dependence on group dynamics emerges. In particular, galaxies in G groups have the lowest star-forming fractions and galaxies in NG groups have intermediate values – larger star-forming fractions than galaxies in G groups but significantly smaller than infalling galaxies or the field. As shown in the lower panels of Fig. 4.5, this difference between G and NG groups is significant for low-mass galaxies (2.9σ) but not for high-mass galaxies (1.6σ). When considering disc fraction, we do not detect a significant enhancement in NG groups for low- or high-mass galaxies (0.9σ and 0.8σ, respectively). As was the case for galaxies at large radii, we show results corresponding to different p-value choices in Appendix 4.A. The observed trends do not depend strongly on p-value. If anything, choosing a larger p-value only strengthens the observed difference between G and NG at large stellar mass (see Appendix 4.A).

4.5 Discussion

4.5.1 The Impact of Group Dynamical State

The question of how much group dynamical state influences galaxy properties has not yet been conclusively answered. In this study we find that star formation of galaxies within the inner regions of haloes shows a dependence on group dynamics. In particular, we find that compared to G groups galaxies at small radii in NG groups show an increase in star-forming fraction.

Carollo et al. (2013) study the differences between galaxies in "relaxed" and "unrelaxed" groups (defined based upon the presence, or lack thereof, of a well-defined central group galaxy) in the Zurich Environmental Study. Carollo et al. (2013) find that $<10^{10}\,\mathrm{M}_{\odot}$ satellites show slightly redder colours in relaxed groups compared to unrelaxed groups. Given the general correlations between galaxy colour and star formation, this agrees well with the findings of this work. Ribeiro et al. (2013) use a statistical metric designed to quantify the distance between probability density functions, known as the Hellinger distance, to discriminate between G and NG groups with a FOF catalogue of SDSS group galaxies (Berlind

et al., 2006). They find no dependence on group dynamics for bright galaxies ($M_r \leq -20.7$); but they find that properties of faint galaxies ($-20.7 < M_r \leq -17.9$) do depend on whether they live in a G or NG group. Relevant to this work, (Ribeiro et al., 2013) show that faint galaxies in G groups are redder than their NG counterparts. As well, (Ribeiro, Lopes, and Trevisan, 2010) find that galaxies in G groups are redder than galaxies in NG groups out to $4\,R_{200}$.

Hou et al. (2013) have explored the dependence of quiescent fraction on group dynamical state as a function of redshift with a combination of groups from the SDSS and the Group Environment and Evolution Collaboration (GEEC). For their low-redshift galaxies, Hou et al. find no difference between the quiescent fraction of galaxies in NG versus G groups, though they use a stellar mass complete sample and are only able to probe masses of ($M_\star > 10^{10}\,\mathrm{M}_\odot$). This is consistent with the result from this work showing that any correlations with dynamical state are subtle and only seen for low-mass galaxies.

The results of this paper can be used to further constrain the connection between group dynamics and the quenching of star formation as well as morphological transformations. The main result is that we observe a dependence of star formation on dynamics in the inner region of the halo but not for galaxies at large radii, whereas morphology is not found to correlate with dynamics at any radius. This seems to suggest that quenching is primarily taking place near the centres of groups, and is more efficient in G groups than NG groups. Alternatively, the observed excess of star-forming galaxies in NG groups could be due to the more dynamically complex NG groups having assembled more recently, therefore galaxies in G groups will have been exposed to quenching mechanisms within the group environment for longer.

It is also worth noting that the unusual structure in velocity space of the NG groups could be a result of poorly identified groups which have undergone "fusing" (i.e. two separate haloes which group finders have combined into one group) or "fracturing" (i.e. one distinct halo which has been split into multiple groups by group finders). Recent works (Duarte and Mamon, 2014; Campbell et al., 2015) have investigated the degree to which standard group finding techniques can accurately reproduce groups from mock catalogues. Campbell et al. (2015) show that

these misidentifications can bias some colour-dependent statistics, such as red fraction which is directly related to the star-forming fraction considered in this work. It would be useful in future work to apply the same statistics used here to discriminate between G and NG groups on mock catalogues in order to determine what fraction of identified NG groups are in fact unrelaxed, dynamically young systems as opposed to systems which have simply been misidentified by the group finder.

4.5.2 Pre-processing of Infalling Galaxies

In addition to star formation quenching and morphological transformations within the current host halo, we also find evidence for pre-processing in both star formation and morphology. To probe pre-processing we measure the "field excess" (i.e. the degree to which star-forming and disc fractions are enhanced in the field relative to the infalling region of groups). Assuming that any environmentally driven quenching or morphological transformations occur within the virial radius of a halo, the field excess will correspond to the fraction of infalling galaxies which have been pre-processed. With this we quantitatively determine the level of pre-processing by computing the field excess for low-mass and high-mass galaxies (divided at the median stellar mass of our sample, $M_\star \geq 10^{10.2}\,\mathrm{M}_\odot$) in our three halo mass bins. As shown in Fig. 4.4, we find that the fraction of pre-processed low-mass galaxies ranges between 4 and 11 per cent when considering star-forming fraction and between 4 and 7 per cent when considering disc fraction. For high-mass galaxies the pre-processed fraction is smaller and generally only marginally significant.

Prior studies have aimed to constrain the fraction of pre-processed galaxies. One common approach is to measure the fraction of galaxies which fall on to a cluster as a member of a smaller group, either directly with simulations or by measuring substructure or clustering observationally. For clusters with mass $\sim 10^{14}\,\mathrm{M}_\odot$, De Lucia et al. (2012) use semi-analytic models (SAMs) and find that the fraction of satellite galaxies which are accreted in groups with $M_H \gtrsim 10^{13}\,\mathrm{M}_\odot$ is highest for low-mass galaxies, corresponding to ~ 28 per cent. Also with SAMs, McGee et al. (2009) find that the fraction of galaxies accreted on to the ultimate cluster as members of $\gtrsim 10^{13}\,h^{-1}\,\mathrm{M}_\odot$ groups depends strongly on the cluster halo mass, ranging from ~ 0.1 for $10^{13.5}\,h^{-1}\,\mathrm{M}_\odot$ haloes to ~ 0.45 for haloes with masses of $10^{15}\,h^{-1}\,\mathrm{M}_\odot$. Bahé et al. (2013) use the GIMIC suite

of zoom-in simulations and find that the fraction of galaxies which have been satellites of a $> 10^{13}\,\mathrm{M}_{\odot}$ halo prior to accretion on to the ultimate host ranges from < 10 per cent for a host with halo mass $< 10^{13.5}\,\mathrm{M}_{\odot}$, up to as high as ~ 60 per cent for a host halo mass of $10^{15.2}\,\mathrm{M}_{\odot}$. Observationally, Hou, Parker, and Harris (2014) use the Dressler-Schectman test (Dressler and Shectman, 1988) to identify infalling subhaloes and find for $< 10^{14}\,\mathrm{M}_{\odot}$ groups that less than 5 per cent of infalling galaxies are part of a subhalo, whereas for haloes with masses $10^{14} < M_H < 10^{14.5}\,\mathrm{M}_{\odot}$ the fraction of galaxies infalling in subhaloes is ~ 10 per cent and ~ 25 per cent, respectively. Qualitatively, the pre-processing trends observed in this work are consistent with these previous studies, namely the fraction of pre-processed galaxies tends to decrease with increasing galaxy stellar mass and increase with the halo mass of the host which the galaxies are infalling on to. The subhalo fraction found in these works can be interpreted as an upper limit on the field excess quantity which we quote. This is because only some fraction of galaxies within subhaloes during infall will be pre-processed, whereas the field excess more closely measures the fraction of galaxies which have actually been pre-processed. Therefore, the fact that our values for the fraction of pre-processed galaxies are consistently smaller than the quoted subhalo fractions is still consistent.

Studying the star-forming fractions of cluster galaxies, Haines et al. (2015) use a simple toy model in an attempt to reproduce the trend between cluster-centric radius and star-forming fraction. They find that in order to reproduce the observational trend, a 19 per cent decrease in the star-forming fraction of cluster galaxies relative to the field is required on top of star formation quenching occurring within the virial radius. Haines et al. suggest that pre-processing is a possible mechanism to generate this 19 per cent decrease. In this work we find that the fraction of high-mass (the Haines et al. sample consists of galaxy stellar masses $> 2 \times 10^{10.2}\,\mathrm{M}_{\odot}$) pre-processed galaxies for high-mass clusters is at most 7 ± 2 per cent. Therefore, this work is only able to account for a portion of the amount of pre-processing required by the Haines et al. (2015) model, although a more complete comparison would require samples matched in halo mass and galaxy stellar mass.

At $\sim z = 0.2$, Lu et al. (2012) find that blue fractions of low- and intermediate-mass cluster galaxies are lower than the field values (at the same stellar mass)

out to radii of 7 Mpc, but the most massive galaxies show no difference from the field. This is similar to the stellar mass trends observed in this work where we see stronger pre-processing for low-mass galaxies.

Recent studies have examined pre-processing of morphology (e.g. Kodama and Smail, 2001; Helsdon and Ponman, 2003; Moran et al., 2007; Wilman et al., 2009) and star formation (e.g. Cortese et al., 2006; Wetzel, Tinker, and Conroy, 2012; Bahé et al., 2013; Haines et al., 2015) separately; but we are not aware of other works which have made direct quantitative comparisons between the amount of pre-processing of star formation and morphology. In Fig. 4.4, we see evidence for pre-processing in both star formation and morphology, though due to the relatively large error bars it is unclear whether one is more strongly pre-processed than the other. The largest difference between star formation and morphology is in the highest halo mass bin, where star formation shows marginally stronger pre-processing than morphology. Additionally if we consider the entire data set (without subdividing by halo mass) we find that the pre-processing of star formation rate is marginally enhanced relative to morphology at the $\sim 2\sigma$ level. Understanding the relative strength of pre-processing of star formation versus morphology could help to disentangle environmentally driven galaxy evolution mechanisms and should be explored further.

4.6 Summary and Conclusions

In this paper we investigate the dependence of galaxy properties (namely, star-forming and disc fractions) on host group dynamics. To do so we construct a carefully matched sample of galaxies housed in Gaussian groups, galaxies housed in NG groups, as well as infalling and field galaxies, all with similar distributions in stellar mass, redshift and (field galaxies excluded) halo mass. We then compare the properties of these different samples for two different radial regions within the halo. The main findings of this work are as follows.

1. Star-forming and disc fractions of galaxies at large group-centric radius do not show any dependence on the dynamical state of their host group.

2. We detect pre-processing by measuring the difference between the star-forming and disc fractions for field galaxies compared to infalling galaxies. Infalling galaxies have had both star formation and morphology pre-processed, with low-mass galaxies infalling on to high-mass haloes showing the largest degree of pre-processing.

3. Galaxy star formation in the inner region of the halo shows a clear dependence on group dynamical state, with enhanced star-forming fractions for galaxies in NG groups compared to galaxies in Gaussian groups at the same stellar mass. We do not detect a significant dependence of disc fraction on group dynamical state in the same inner region.

Acknowledgements: We thank the referee for their insightful comments and suggestions, which have improved this paper significantly. IDR thanks the Ontario Graduate Scholarship programme and the National Science and Engineering Research Council of Canada for funding. LCP thanks the National Science and Engineering Research Council of Canada for funding. The authors thank F. Evans for matching together the various SDSS catalogues used in this research. We thank X. Yang et al. for making their SDSS DR7 group catalogue publicly available, L. Simard et al. for the publication of their SDSS DR7 morphology catalogue, J. Brinchmann et al. for publication of their SDSS SFRs, and the NYU-VAGC team for the publication of their SDSS DR7 catalogue. This research would not have been possible without access to these public catalogues.

Funding for the SDSS has been provided by the Alfred P. Sloan Foundation, the Participating Institutions, the National Science Foundation, the U.S. Department of Energy, the National Aeronautics and Space Administration, the Japanese Monbukagakusho, the Max Planck Society, and the Higher Education Funding Council for England. The SDSS Web Site is `http://www.sdss.org/`.

The SDSS is managed by the Astrophysical Research Consortium for the Participating Institutions. The Participating Institutions are the American Museum of Natural History, Astrophysical Institute Potsdam, University of Basel, University of Cambridge, Case Western Reserve University, University of Chicago, Drexel University, Fermilab, the Institute for Advanced Study, the Japan Participation Group, Johns Hopkins University, the Joint Institute for Nuclear Astrophysics,

the Kavli Institute for Particle Astrophysics and Cosmology, the Korean Scientist Group, the Chinese Academy of Sciences (LAMOST), Los Alamos National Laboratory, the Max-Planck-Institute for Astronomy (MPIA), the Max-Planck-Institute for Astrophysics (MPA), New Mexico State University, Ohio State University, University of Pittsburgh, University of Portsmouth, Princeton University, the United States Naval Observatory and the University of Washington.

Bibliography

Abazajian, K. N. et al. (2009). *ApJS* 182, 543-558, pp. 543–558.

Anderson, T. W. and D. A. Darling (1952). *The Annals of Mathematical Statistics* 23, p. 193.

Ashman, Keith M., Christina M. Bird, and Stephen E. Zepf (1994). *AJ* 108, p. 2348.

Bahé, Y. M., I. G. McCarthy, M. L. Balogh, and A. S. Font (2013). *MNRAS* 430, pp. 3017–3031.

Bamford, S. P. et al. (2009). *MNRAS* 393, pp. 1324–1352.

Berlind, Andreas A. et al. (2006). *ApJS* 167.1, pp. 1–25.

Bird, C. M. and T. C. Beers (1993). *AJ* 105, pp. 1596–1606.

Biviano, A., P. Katgert, T. Thomas, and C. Adami (2002). *A&A* 387, pp. 8–25.

Blanton, M. R. and S. Roweis (2007). *AJ* 133, pp. 734–754.

Blanton, M. R. et al. (2005). *AJ* 129, pp. 2562–2578.

Brinchmann, J. et al. (2004). *MNRAS* 351, pp. 1151–1179.

Butcher, H. and A. Oemler Jr. (1978). *ApJ* 219, pp. 18–30.

Cameron, E. (2011). *PASA* 28, pp. 128–139.

Campbell, Duncan et al. (2015). *MNRAS* 452.1, pp. 444–469.

Carollo, C. M. et al. (2013). *ApJ* 776, 71, p. 71.

Christlein, D. and A. I. Zabludoff (2004). *ApJ* 616, pp. 192–198.

Cortese, L. et al. (2006). *A&A* 453.3, pp. 847–861.

Cucciati, O. et al. (2012). *A&A* 539, A31, A31.

De Lucia, G., F. Fontanot, and D. Wilman (2012). *MNRAS* 419, pp. 1324–1330.

De Lucia, G., S. Weinmann, B. M. Poggianti, A. Aragón-Salamanca, and D. Zaritsky (2012). *MNRAS* 423, pp. 1277–1292.

Dressler, A. (1980). *ApJ* 236, pp. 351–365.

Dressler, A. and S. A. Shectman (1988). *AJ* 95, pp. 985–995.

Dressler, A. et al. (1999). *ApJS* 122, pp. 51–80.
Dressler, A. et al. (2013). *ApJ* 770, 62, p. 62.
Duarte, Manuel and Gary A. Mamon (2014). *MNRAS* 440.2, pp. 1763–1778.
Eke, V. R. et al. (2005). *MNRAS* 362, pp. 1233–1246.
Fasano, G. et al. (2015). *MNRAS* 449, pp. 3927–3944.
Feulner, Georg et al. (2005). *ApJL* 633.1, pp. L9–L12.
Fillingham, S. P. et al. (2015). *MNRAS* 454, pp. 2039–2049.
Fujita, Yutaka (2004). *PASJ* 56, pp. 29–43.
Geller, M. J. and J. P. Huchra (1983). *ApJS* 52, pp. 61–87.
Goto, T. et al. (2003). *MNRAS* 346, pp. 601–614.
Gray, M. E. et al. (2004). *MNRAS* 347.4, pp. L73–L77.
Gunn, J. E. and J. R. Gott III (1972). *ApJ* 176, p. 1.
Haines, C. P., F. La Barbera, A. Mercurio, P. Merluzzi, and G. Busarello (2006). *ApJL* 647, pp. L21–L24.
Haines, C. P. et al. (2015). *ApJ* 806, 101, p. 101.
Hartigan, J. A. and P. M. Hartigan (1985). *Ann. Statist.* 13.1, pp. 70–84.
Helsdon, Stephen F. and Trevor J. Ponman (2003). *MNRAS* 339.4, pp. L29–L32.
Hou, A., L. C. Parker, and W. E. Harris (2014). *MNRAS* 442, pp. 406–418.
Hou, A., L. C. Parker, W. E. Harris, and D. J. Wilman (2009). *ApJ* 702, pp. 1199–1210.
Hou, A. et al. (2013). *MNRAS* 435, pp. 1715–1726.
Hubble, E. and M. L. Humason (1931). *ApJ* 74, p. 43.
Huchra, J. P. and M. J. Geller (1982). *ApJ* 257, pp. 423–437.
Just, Dennis W. et al. (2019). *ApJ* 885.1, 6, p. 6.
Kawata, D. and J. S. Mulchaey (2008). *ApJl* 672, L103, p. L103.
Kodama, Tadayuki and Ian Smail (2001). *MNRAS* 326.2, pp. 637–642.
Lackner, C. N. and J. E. Gunn (2013). *MNRAS* 428, pp. 2141–2162.
Lewis, Ian et al. (2002). *MNRAS* 334.3, pp. 673–683.
Lu, T., D. G. Gilbank, S. L. McGee, M. L. Balogh, and S. Gallagher (2012). *MNRAS* 420, pp. 126–140.
Mahajan, S., G. A. Mamon, and S. Raychaudhury (2011). *MNRAS* 416, pp. 2882–2902.
Mamon, G. A., T. Sanchis, E. Salvador-Solé, and J. M. Solanes (2004). *A&A* 414, pp. 445–451.

Martínez, H. J. and A. Zandivarez (2012). *MNRAS* 419, pp. L24–L28.

McGee, S. L., M. L. Balogh, R. G. Bower, A. S. Font, and I. G. McCarthy (2009). *MNRAS* 400, pp. 937–950.

McGee, S. L. et al. (2011). *MNRAS* 413, pp. 996–1012.

Mihos, J. C. and L. Hernquist (1994). *ApJl* 425, pp. L13–L16.

Mo, H. J. and S. D. M. White (1996). *MNRAS* 282.2, pp. 347–361.

Mohd Razali, Nornadiah and Bee Yap (2011). *J. Stat. Model. Analytics* 2.

Moore, B., N. Katz, G. Lake, A. Dressler, and A. Oemler (1996). *Nature* 379, pp. 613–616.

Moran, Sean M. et al. (2007). *ApJ* 671.2, pp. 1503–1522.

Muzzin, A. et al. (2014). *ApJ* 796, 65, p. 65.

Navarro, J. F., C. S. Frenk, and S. D. M. White (1997). *ApJ* 490, pp. 493–508.

Oman, K. A., M. J. Hudson, and P. S. Behroozi (2013). *MNRAS* 431, pp. 2307–2316.

Peng, Y.-j. et al. (2010). *ApJ* 721, pp. 193–221.

Peng, Y., R. Maiolino, and R. Cochrane (2015). *Nature* 521, pp. 192–195.

Popesso, P., A. Biviano, H. Böhringer, and M. Romaniello (2007). *A&A* 461, pp. 397–410.

Postman, M. and M. J. Geller (1984). *ApJ* 281, pp. 95–99.

Postman, M. et al. (2005). *ApJ* 623, pp. 721–741.

Rasmussen, J. et al. (2012). *ApJ* 757, 122, p. 122.

Ribeiro, A. L. B., P. A. A. Lopes, and S. B. Rembold (2013). *A&A* 556, A74, A74.

Ribeiro, A. L. B., P. A. A. Lopes, and M. Trevisan (2010). *MNRAS* 409, pp. L124–L127.

Ribeiro, A. L. B. et al. (2013). *MNRAS* 434, pp. 784–795.

Rines, Kenneth, Margaret J. Geller, Michael J. Kurtz, and Antonaldo Diaferio (2005). *AJ* 130.4, pp. 1482–1501.

Roberts, I. D., L. C. Parker, and A. Karunakaran (2016). *MNRAS* 455, pp. 3628–3639.

Schawinski, Kevin et al. (2009). *ApJl* 692.1, pp. L19–L23.

Simard, L., J. T. Mendel, D. R. Patton, S. L. Ellison, and A. W. McConnachie (2011). *ApJS* 196, 11, p. 11.

Skibba, R. A. et al. (2011). *MNRAS* 410, pp. 417–431.

Tasca, L. A. M. et al. (2014). *A&A* 564, L12, p. L12.

Taylor, Edward N. et al. (2011). *MNRAS* 418.3, pp. 1587–1620.

Tinker, J. et al. (2008). *ApJ* 688, 709-728, pp. 709–728.

Verdugo, M., B. L. Ziegler, and B. Gerken (2008). *A&A* 486.1, pp. 9–24.

Wang, Yu et al. (2008). *ApJ* 687.2, pp. 919–935.

Weisz, D. R. et al. (2015). *ApJ* 804, 136, p. 136.

Wetzel, A. R., J. L. Tinker, and C. Conroy (2012). *MNRAS* 424, pp. 232–243.

Wetzel, A. R., E. J. Tollerud, and D. R. Weisz (2015). *ApJL* 808, L27, p. L27.

Whitmore, B. C., D. M. Gilmore, and C. Jones (1993). *ApJ* 407, pp. 489–509.

Wilman, D. J. et al. (2005). *MNRAS* 358, pp. 88–100.

Wilman, D. J. et al. (2009). *ApJ* 692.1, pp. 298–308.

Yahil, A. and N. V. Vidal (1977). *ApJ* 214, pp. 347–350.

Yang, X., H. J. Mo, F. C. van den Bosch, and Y. P. Jing (2005). *MNRAS* 356, pp. 1293–1307.

Yang, X. et al. (2007). *ApJ* 671, pp. 153–170.

Zheng, Xian Zhong et al. (2007). *ApJL* 661.1, pp. L41–L44.

4.A Appendix: Dependence on the Definition of NG Groups

To discriminate between G and NG groups we use a critical p-value of 0.05 for both the AD test and the Dip test (see Section 4.2.3). While this choice of 0.05 is standard, it is still an arbitrary choice and it is therefore important to investigate the effect of varying this dividing p-value.

Figs 4.6 and 4.7 show star-forming and disc fractions for galaxies in the outer and inner regions of G and NG groups (similar to Figs 4.3 and 4.5), for different choices of the dividing p-value between G and NG groups. The lower panels in Figs 4.3 and 4.5 show NG-G for different choices of p-value, with the height of the data marker corresponding to 68 per cent confidence intervals derived from either bootstrapping or the methodology of Cameron (2011) (whichever is larger). Please note that the data markers are offset from one another for visibility. Lines range in decreasing transparency from p-values of 0.05 to 0.20.

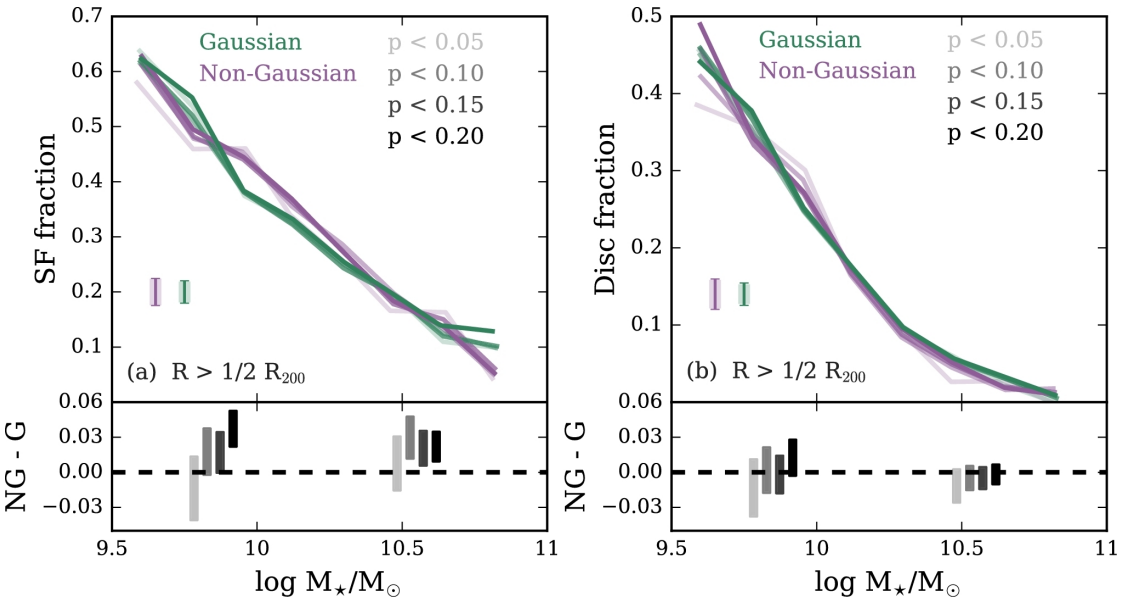

FIGURE 4.6: Star-forming (left) and disc (right) fraction versus stellar mass for galaxies at large radius in the G and NG samples. The lines of varying transparency correspond to different definitions of the NG sample, where the listed p-value is the critical value used in the AD and Dip tests to identify NG groups. Characteristic uncertainties are shown for 68 per cent confidence intervals from Cameron (2011, error bars) and from 1000 bootstrap re-samplings (shaded regions). Lower panels show the difference between star-forming fractions in G and NG groups (left) and similarly for disc fraction (right), for low-mass ($M_\star < 10^{10.2}\,\mathrm{M}_\odot$) and high-mass ($M_\star > 10^{10.2}\,\mathrm{M}_\odot$) galaxies.

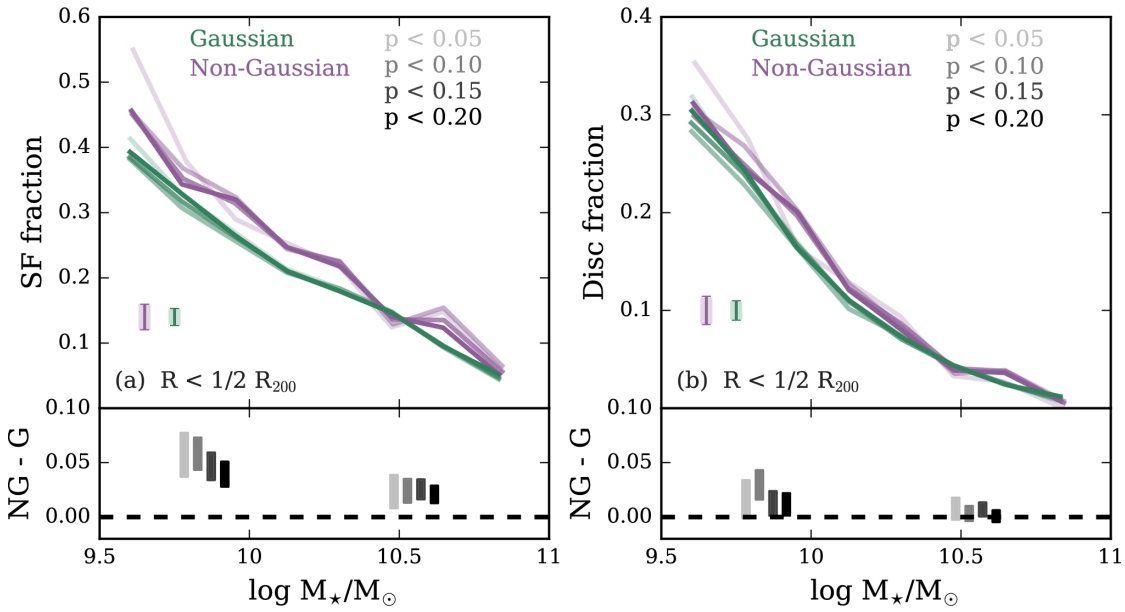

FIGURE 4.7: Star-forming (left) and disc (right) fraction versus stellar mass for galaxies at small radius in the G and NG samples. The lines of varying transparency correspond to different definitions of the NG sample, where the listed p-value is the critical value used in the AD and Dip tests to identify NG groups. Characteristic uncertainties are shown for 68 per cent confidence intervals from Cameron (2011, error bars) and from 1000 bootstrap re-samplings (shaded regions). Lower panels show the difference between star-forming fractions in G and NG groups (left) and similarly for disc fraction (right), for low-mass ($M_\star < 10^{10.2}\,\mathrm{M}_\odot$) and high-mass ($M_\star > 10^{10.2}\,\mathrm{M}_\odot$) galaxies.

5 | Quenching Low-mass Satellite Galaxies: Evidence for a Threshold ICM Density

This chapter represents an unchanged version of the paper, *Quenching Low-mass Satellite Galaxies: Evidence for a Threshold ICM Density*, published in the refereed journal, *The Astrophysical Journal*. The full reference is given below:

Roberts I.D.[1], Parker L.C.[1], Brown T.[1], Joshi G.D.[2], Hlavacek-Larrondo J.[3], Wadsley J.[1], 2019, ApJ, Volume 873, Issue 1, pp. 42-57

[1] *Department of Physics & Astronomy, McMaster University, Hamilton ON L8S 4M1*

[2] *Max Planck Institute for Astronomy D-69117 Heidelberg, Germany*

[3] *Département de Physique, Université de Montréal, Montréal QC H3C 3J7*

Abstract

We compile a sample of Sloan Digital Sky Survey (SDSS) galaxy clusters with high-quality Chandra X-ray data to directly study the influence of the dense intracluster medium (ICM) on the quenching of satellite galaxies. We study the quenched fractions of satellite galaxies as a function of ICM density for low- ($10^9 \lesssim M_\star \lesssim 10^{10}\,\mathrm{M}_\odot$), intermediate- ($10^{10} \lesssim M_\star \lesssim 10^{10.5}\,\mathrm{M}_\odot$), and high-mass ($M_\star \gtrsim 10^{10.5}\,\mathrm{M}_\odot$) satellite galaxies with >3000 satellite galaxies across 24 low-redshift ($z < 0.1$) clusters. For low-mass galaxies we find evidence for a broken power-law trend between satellite quenched fraction and local ICM density. The quenched fraction increases modestly at ICM densities below a threshold before increasing sharply beyond this threshold toward the cluster center. We show that this increase in quenched fraction at high ICM density is well matched by a simple, analytic model of ram pressure stripping. These results are consistent with a picture where low-mass cluster galaxies experience an initial, slow-quenching mode driven by steady gas depletion, followed by rapid quenching associated with ram pressure of cold-gas stripping near (one-quarter of the virial radius, on average) the cluster center.

5.1 Introduction

It is now firmly established that local environment plays a pivotal role in dictating the properties of galaxy populations. Galaxies located in the underdense field tend to be blue in color, with young stellar populations, disk (late-type) morphologies, and high star formation rates (SFRs). In contrast, dense environments such as galaxy clusters, embedded within massive ($\gtrsim 10^{14}\,M_{\odot}$) dark matter (DM) halos, host galaxy populations that are on average red, with bulge-dominated (early-type) morphologies, old stellar populations, and little ongoing star formation. The first clear evidence for such a paradigm was presented in early seminal works (e.g. Oemler, 1974; Davis and Geller, 1976; Butcher and Oemler, 1978; Dressler, 1980; Postman and Geller, 1984), and has since been cemented by more recent studies with large, detailed spectroscopic surveys of galaxies across a variety of environments (e.g. Blanton and Moustakas, 2009; Kimm et al., 2009; Peng et al., 2010; Wetzel, Tinker, and Conroy, 2012; Wilman and Erwin, 2012). Even within individual clusters, galaxy properties are a strong function of environment. Galaxies that inhabit the dense cluster interior are preferentially red, of early type, and quiescent relative to galaxies at large cluster-centric radius (e.g. Postman et al., 2005; Blanton and Roweis, 2007; Prescott et al., 2011; Rasmussen et al., 2012; Fasano et al., 2015; Haines et al., 2015). Ultimately, if we are to understand galaxy evolution, we must understand which physical mechanisms drive these observed trends by quenching star formation and transforming morphology as a function of galaxy environment.

In addition to environmental quenching occurring in a galaxy's present-day cluster, there is increasing evidence that a large fraction of galaxies may have their star formation quenched in smaller groups prior to cluster infall. It has been estimated that nearly half of present-day cluster galaxies may have infallen as a part of smaller groups (e.g. McGee et al., 2009), and quenched fractions at the cluster virial radius tend to be enhanced relative to the field – indicating that star formation is influenced environmentally prior to infall (von der Linden et al., 2010; Haines et al., 2015; Roberts and Parker, 2017). This "pre-processing" of galaxy properties is a natural consequence of a hierarchical growth of dense structures in the universe.

Many physical mechanisms have been proposed that in principle are capable of quenching star formation in dense environments. These mechanisms can be broadly divided into two classes: hydrodynamic interactions between galaxies and the intracluster medium (ICM); and dynamical interactions between member galaxies, or between galaxies and the cluster halo potential. Examples of hydrodynamic mechanisms include "starvation" (e.g. Larson, Tinsley, and Caldwell, 1980; Balogh, Navarro, and Morris, 2000; Peng, Maiolino, and Cochrane, 2015), where the high virial temperature of the cluster ($\gtrsim 10^7$ K) prevents cold-flow accretion of gas onto the disk of satellite galaxies; and "ram pressure stripping" (e.g. Gunn and Gott, 1972; Quilis, Moore, and Bower, 2000), where a galaxy passing through the dense ICM will feel a ram pressure "wind" that is strong enough to directly strip cold gas from the galactic disk. Dynamical interactions thought to be relevant include galaxy mergers (e.g. Mihos and Hernquist, 1994a; Mihos and Hernquist, 1994b), where the final end products in dense environments tend to be quiescent galaxies with early-type morphologies; "harassment" (e.g. Moore et al., 1996), where repeated impulsive interactions between galaxies can induce strong starbursts, thereby quickly exhausting cold-gas reserves; and gravitational tidal forces (e.g. Mayer et al., 2006; Chung et al., 2007), which can directly strip gas from a galaxy, or in the less extreme case, transport gas to less bound orbits where it will be more susceptible to hydrodynamic effects such as ram pressure. While it is understood that all of these processes should be affecting galaxies in dense environments, it is the balance between these mechanisms, and the dependence of this balance on environment, that fuels substantial debate.

Recently, starvation or ram pressure stripping (or a combination of the two) has been favored as the primary quenching mechanism in galaxy groups and clusters (Muzzin et al., 2014; Fillingham et al., 2015; Peng, Maiolino, and Cochrane, 2015; Wetzel, Tollerud, and Weisz, 2015; Brown et al., 2017; Foltz et al., 2018). Substantial effort has been devoted to determine how to distinguish between these two quenching pathways observationally. A common technique is to constrain the timescale over which quenching occurs, which is expected to be relatively long ($\gtrsim 3-4$ Gyr) for starvation but short ($\lesssim 1$ Gyr) for ram pressure stripping. It is important to note, however, that ram pressure stripping of cold gas will not be immediately efficient upon cluster infall and a delay time is likely necessary for

the galaxy to reach the dense interior ICM before quenching begins. Therefore the total quenching timescale for ram pressure (delay + quenching) should be on the order of the cluster dynamical time. Starvation should begin to act immediately after infall as the galaxy encounters the hot, virialized halo, but quenching by starvation will still produce an excess of quenched galaxies in the cluster interior (relative to the outskirts) as the time-since-infall for these central galaxies will be relatively long.

The effects of ram pressure stripping can, in some cases, be studied directly by observing cluster galaxies with extended HI distributions (Kenney, van Gorkom, and Vollmer, 2004; Chung et al., 2007; Chung et al., 2009; Kenney, Abramson, and Bravo-Alfaro, 2015), HI deficient disks (post-stripping, Kenney and Young 1989; Boselli and Gavazzi 2006; Jaffé et al. 2016), and by observing "jellyfish galaxies" with extended, stripped "tentacles" of gas and stars (Poggianti et al., 2017; Jaffé et al., 2018). Ram pressure also lends itself well to analytic modeling through the simple balance between the restoring potential of a galactic disk and the strength of ram pressure given by $\rho_{\rm ICM} v^2_{\rm galaxy}$ (Gunn and Gott, 1972). Such an approach has been used to constrain the regions in cluster phase-space where stripping should be efficient, finding that the "stripping" regions tend to be populated by galaxies that are HI deficient and show morphological signs of ongoing stripping (Jaffé et al., 2015; Jaffé et al., 2016; Jaffé et al., 2018).

In this paper we compile a statistical sample (> 3000) of satellite galaxies in 24 low-redshift ($z < 0.1$) clusters observed with the *Chandra* X-ray observatory to directly study the connection between galaxy quenching and ICM density. We can then estimate the physical ICM density (based on density profiles for each cluster) around each satellite galaxy and constrain the impact of ram pressure stripping with a simple analytic model. This represents the first systematic study of environmental quenching directly as a function of ICM density for a large, statistical sample of galaxies across many clusters.

The paper is organized as follows: in Section 5.2 we describe the sample of cluster satellite galaxies, as well as the optical and X-ray data for the host clusters; in Section 5.3 we present the dependence of satellite quenched fraction on ICM density; in Section 5.4 we describe an analytic ram pressure stripping model we construct and make comparisons to the observed trends; in Section 5.5 we

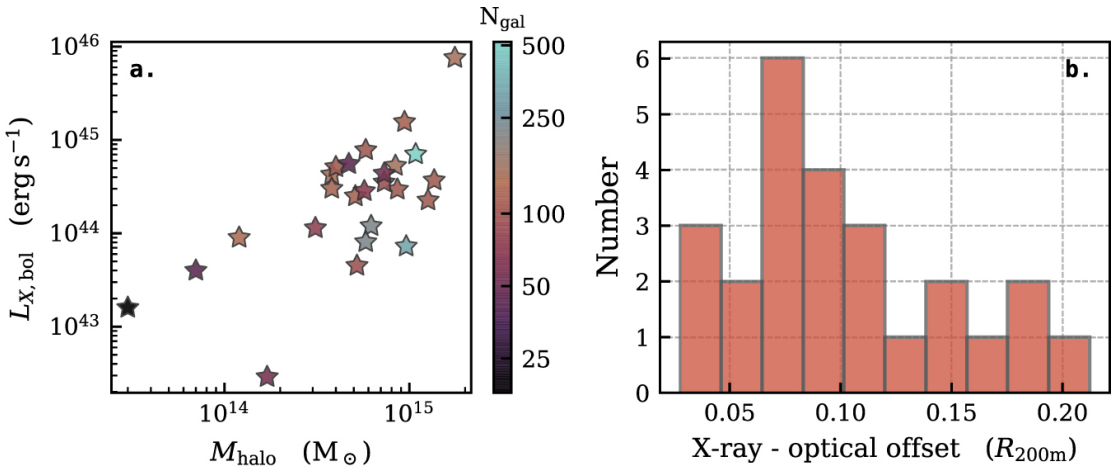

FIGURE 5.1: Left: Literature bolometric X-ray luminosity (from the ACCEPT cluster sample when available: Cavagnolo et al. 2009, otherwise from the SDSS-RASS sample: Wang et al. 2014a) vs. halo mass (Yang et al., 2007) for the 24 clusters in the sample. Markers are colored according to the number of galaxies identified in each cluster. Right: Projected offset between the X-ray peak and optical luminosity-weighted center for each cluster in the sample.

constrain quenching timescales assuming a "slow-then-rapid" framework for satellite quenching; and finally, in Sections 5.6 and 5.8 we discuss and summarize our results.

This paper assumes a flat Λ cold DM cosmology with $\Omega_M = 0.3$, $\Omega_\Lambda = 0.7$, and $H_0 = 70\,\mathrm{km\,s^{-1}\,Mpc^{-1}}$. Throughout this paper we use lowercase r to represent galactocentric radii (in cylindrical coordinates), and uppercase R to represent cluster-centric radii.

5.2 Data

5.2.1 Cluster Sample

We construct a sample of low-redshift galaxy clusters with high-quality, archival X-ray observations, starting with all clusters in the Yang et al. (2005) and Yang et al. (2007) Sloan Digital Sky Survey (SDSS) DR7 catalog at $z < 0.1$ with 10 or more member galaxies. We then query the Chandra data archive at the positions of the

TABLE 5.1: Galaxy cluster sample

Name	Yang ID[a]	$z_{\rm cluster}$[b]	$M_{\rm halo}$[c] ($10^{14}\,{\rm M}_{\odot}$)	R_{500} (kpc)	$L_{X,{\rm bol}}$[d] ($10^{44}\,{\rm erg\,s^{-1}}$)	$N_{\rm gal}/N_{\rm Yang}$[e]	Exp. time (ks)	*Chandra* ObsID
Coma	1	0.024	10.8	1150	7.1*	517/652	479	13993,13994,13995 13996,14406,14410 14411,14415
Abell 2147	2	0.036	9.6	1078	0.7	329/383	18	3211
Abell 1367	3	0.022	6.2	955	1.2*	223/352	402	514,17199,17200 17201,17589,17590 17591,17592 18704,18705,18755
Abell 2199	5	0.030	5.8	920	0.8	221/302	158	497,498,10748 10803,10804,10805
Abell 85	11	0.056	8.4	1030	5.3	152/178	198	904,15173,15174 16263,16264
Abell 2063	18	0.035	3.8	799	4.3	132/156	50	4187,5795,6262 6263
Abell 2670	19	0.076	12.6	1115	2.3*	107/154	40	4959
Abell 2029	20	0.077	9.4	1041	15.6	114/154	128	891,4977,6101
Abell 2065	21	0.072	8.6	1013	3.0	104/154	55	3182,7689
Abell 2142	22	0.090	17.6	1259	75.9	149/153	205	5005,15186,16564 16565
MKW 8	23	0.027	1.2	697	0.9	132/150	104	4942,18266,18850
Abell 2107	24	0.041	3.8	787	3.0	119/149	36	4960
Abell 2052	25	0.035	4.0	815	5.1	103/141	654	890,5807,10477 10478,10479,10480 10879,10914,10915 10916,10917
Abell 2255	27	0.082	13.6	1167	3.7	107/130	44	894,7690
Abell 2061	29	0.078	5.1	1072	2.5*	115/129	55	4965
Abell 1795	32	0.063	5.8	895	7.8	103/125	105	493,494,10432,17228
ZwCl 1215	45	0.077	7.3	954	3.5	93/103	12	4184
Abell 1991	52	0.058	5.2	862	0.5	96/99	38	3193
MKW 3S	57	0.045	3.1	743	1.1	77/95	57	900
MKW 4	62	0.021	1.7	625	0.03	58/88	30	3234
Abell 1775	71	0.075	5.7	880	2.8*	70/82	99	12891,13510
Abell 1650	86	0.084	7.3	947	4.4	56/72	251	4178,5822,5823 6356,6357,6358 7242,7691
AWM 4	145	0.032	0.7	564	0.4*	44/55	74	9423
Abell 2244	191	0.098	4.7	805	5.5	44/47	65	4179,7693 13192,13193
NGC 4325	611	0.026	0.3	336	0.2*	18/24	30	3232

NOTES. [a]Group ID from sample III in the Yang catalogue (Yang et al., 2007); [b]Cluster redshift from Yang catalogue; [c]Halo mass from Yang catalogue determined with the ranking of cluster stellar mass; [d]Bolometric X-ray luminosities taken from the ACCEPT catalogue (Cavagnolo et al., 2009) when available, and otherwise taken from the ROSAT all-sky survey (marked by *, Wang et al. 2014b) ; [e]Number of cluster members in the final sample after matching with SFRs and B+D decompositions, compared to the number of cluster members identified in the Yang catalogue.

luminosity-weighted centers of the Yang clusters in this initial sample. We require that any matches have at least 25,000 X-ray counts above the background (after combining all Chandra archival observations for a given cluster), which results in 24 clusters that both are in the Yang et al. catalog and are observed with Chandra to sufficient depth. Table 5.1 lists the clusters in this sample, Figure 5.1(a) shows the $L_X - M_{\rm halo}$ relation for these clusters, and Figure 5.1(b) shows the projected offset between the position of the X-ray peak and the luminosity-weighted cluster center, showing that typical offsets are only a small fraction of the virial radius (Equation 5.2). X-ray centers are calculated as the position of the brightest pixel in the X-ray image after smoothing with a Gaussian kernel with a bandwidth of 40 kpc (Nurgaliev et al., 2017; Roberts, Parker, and Hlavacek-Larrondo, 2018), and luminosity-weighted centers are computed with the positions of member galaxies from the Yang et al. catalog. Bolometric X-ray luminosities are archival and are taken from the ACCEPT cluster sample (Cavagnolo et al., 2009) when available, and otherwise from the Rosat All Sky Survey (RASS; Wang et al. 2014a). Cluster halo masses are taken from the Yang et al. catalog. They are computed with abundance matching based on the ranking of the characteristic group stellar mass, given by Equation (13) in Yang et al. (2007). We normalize all cluster-centric radii by R_{500} (the radius at which the interior density is 500 times the critical density of the universe) or by R_{200m}, which are computed as

$$R_{500} = R_{200m}/2.7 \tag{5.1}$$

where

$$R_{200m} = 1.61\,{\rm Mpc}\left(\frac{M_{\rm halo}}{10^{14}\,{\rm M}_\odot}\right)^{1/3}(1+z_{\rm cluster})^{-1} \tag{5.2}$$

is the radius enclosing an average density equal to 200 times the critical mass density of the Universe (Yang et al., 2007; Tinker et al., 2008; Wang et al., 2014a).

5.2.2 ICM Density Profiles

The Chandra observations were downloaded, reprocessed, cleaned, and calibrated with CIAO (CIAO version 4.9, CALDB version 4.7.7). We apply charge transfer inefficiency and time-dependent gain corrections and filter for background flares with

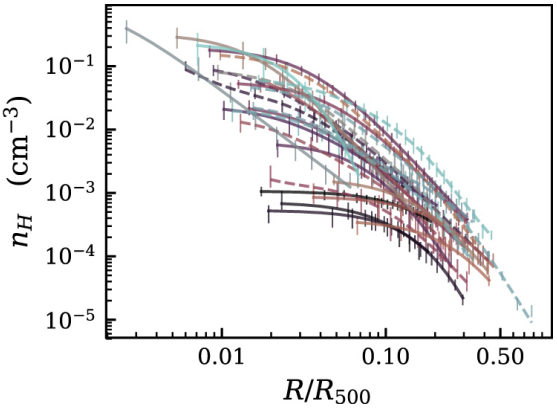

FIGURE 5.2: Best-fit ICM density profile, assuming a single- or double-beta model (whichever gives the lowest AIC) for each cluster in the sample. Clusters that are better fit by a double-beta model are marked as dashed lines. Error bars correspond to 1σ statistical uncertainties on the measured densities.

the CIAO script `lc_clean` with a 3σ threshold. Point sources are identified and masked with the `wavdetect` script. Backgrounds were estimated with the blanksky event file output from the CIAO script `blanksky`, which is normalized to the ratio of observed-to-blanksky background counts in the 9-12 keV band. To determine the ICM density as a function of radius, we extract X-ray spectra in radial annuli from the source and the background data sets with the CIAO script `specextract` in the 0.5-7 keV energy band. Annuli are centered on the X-ray peak and extend out to the edge of the chip coverage. Weighted response files and redistribution matrices were generated with a count-weighted map across the extent of the extraction regions. We then fit the X-ray spectra in radial annuli for each cluster in the sample. We set a minimum of 5000 counts (after background subtraction) per annulus, which is based on the merged data set for clusters with multiple observations (see Table 5.1), and then group spectra to have 25 counts per energy channel (i.e., S/N = 5). We only consider clusters with at least 5 radial annuli (i.e., 25,000 counts), and set an upper limit of 20 annuli per cluster – this means that clusters with deep *Chandra* observations will have far more than 5000 counts per annulus. To gain insight into the physical densities in each annulus, we deproject the spectra with the code DSDEPROJ (Sanders and Fabian, 2007; Russell, Sanders, and Fabian, 2008), which is a model-independent deprojection method assuming

only spherical symmetry. We then fit the deprojected spectrum in each annulus with an absorbed single-temperature APEC model[1], with temperature, abundance, and normalization as free parameters. For clusters with multiple *Chandra* observations, we extract a spectrum for each data set and then simultaneously fit all spectra in SHERPA[2]. The redshift is fixed at the cluster redshift from the Yang catalog. The Galactic hydrogen column density is estimated from the spectrum extracted over the entire cluster region, which gives sufficient counts to obtain a good constraint. We then assume that the Galactic hydrogen column density (N_H) is constant across the cluster and fix N_H at this fitted value for the spectral fits within each radial annulus. The fitted hydrogen column densities agree well with the observed values from Kalberla et al. (2005). The spectral normalization is then converted into a hydrogen number density with the following relation:

$$n_H = \sqrt{\frac{4\pi D_A^2 (1+z)^2 \eta \cdot 10^{14}}{1.2V}}, \tag{5.3}$$

where D_A is the angular diameter distance to the cluster at redshift, z, η is the spectral normalization, V is the volume corresponding to a given annulus, and we have assumed $n_e = 1.2n_H$. The deprojected density profile for each cluster is then fit with both a single (Equation 5.4) and a double (Equation 5.5) beta model,

$$n_H = n_{H,0}\left[1 + \left(\frac{R}{R_c}\right)^2\right]^{-\frac{3}{2}\beta} \tag{5.4}$$

$$n_H = n_{H,01}\left[1 + \left(\frac{R}{R_{c1}}\right)^2\right]^{-\frac{3}{2}\beta_1} + n_{H,02}\left[1 + \left(\frac{R}{R_{c2}}\right)^2\right]^{-\frac{3}{2}\beta_2} \tag{5.5}$$

with the central density, $n_{H,0}$, core radii, R_c, and beta indices, β, as free parameters. Given the single- and double-beta fit for each cluster, we use the fit that gives the lowest Akaike information criterion[3] (AIC; Akaike 1974) value. Allowing clusters to be parameterized by a double-beta model when necessary allows for the

[1] `http://www.atomdb.org/`

[2] `http://cxc.harvard.edu/sherpa/`

[3] The AIC is a model-selection tool used to quantify the information lost when describing a set of data with a particular model. When comparing two models, the model with the lowest AIC value is preferred. The AIC also includes a penalty for increasing the number of fits parameters, thereby accounting for obtaining "better" fits by increasing the model complexity

more accurate modeling of systems with strong cool cores, but we note that using a single-beta model for all clusters in the sample does not change the conclusions of this paper. The data prefer a double-beta model for 8 of the clusters in the sample, with the remaining 16 preferring a single-beta fit. The ICM density profile fits are made with the MCMC code EMCEE[4] (Foreman-Mackey et al., 2013) assuming a flat prior; best-fit parameters are taken to be the median values from each chain after burn-in. Figure 5.2 shows the best-fit profiles for each cluster as well as 1σ error bars corresponding to the measured densities. These fits allow us to determine the local, azimuthally averaged, ICM density for each satellite galaxy at a given cluster-centric radius (extrapolating the fits to larger cluster-centric radii when necessary).

5.2.3 Galaxy Sample

We compile a sample of cluster satellite galaxies beginning with the member galaxies for the clusters in Table 5.1 from the Yang et al. DR7 catalog (we remove the most massive galaxy from each cluster). Galaxies are then matched to SFRs from the Max-Planck-Institut für Astrophysik and Johns Hopkins University (MPA-JHU) collaboration[5] (Brinchmann et al., 2004), with the updated prescriptions from Salim et al. (2007). To determine specific SFRs (sSFR = SFR/$M_\star$) we use stellar masses from Mendel et al. (2014) derived via fits to galaxy broadband spectral energy distributions (SEDs). Mendel et al. also derive bulge and disk stellar masses with the bulge+disk (B+D) decompositions from Simard et al. (2011); assuming an exponential disk and a De Vaucouleurs bulge), which we use in our ram pressure stripping model (see Section 5.4). After matching the Yang et al. member galaxies to the SFR, stellar mass, and structural catalogs, we are left with a total of 3250 galaxies in 24 clusters.

We also make use of the isolated field sample from Roberts and Parker (2017) for comparison to the cluster sample. The field sample is composed of all galaxies in single-member groups from the Yang et al. catalog with a minimum separation of 1 Mpc and 1000 km s^{-1} from their nearest "bright" neighbor. Bright neighbors

[4] `http://dfm.io/emcee/current/`
[5] `https://www.mpa-garching.mpg.de/SDSS/DR7`

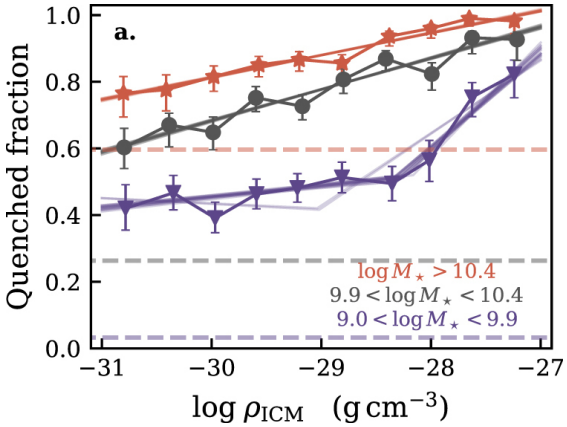

FIGURE 5.3: Quenched fraction ($\log \mathrm{sSFR} < -11\,\mathrm{yr}^{-1}$) vs. ICM density for low- (purple), intermediate- (gray), and high-mass (red) galaxies. Faded lines show fits to the data (single power-law for intermediate- and high-mass galaxies, double power-law for low-mass galaxies) after rebinning, ranging from 10 to 20 bins. Quenched fractions for an isolated field sample in each mass bin are shown by the dashed horizontal lines. Error bars correspond to 68% Bayesian confidence intervals estimated from the beta distribution (Cameron, 2011). Uncertainty ranges on the field quenched fractions are smaller than the line widths shown in the figure.

correspond to galaxies that are brighter than the r-band limiting absolute magnitude of the survey at $z = 0.1$, which ensures that the strictness of the isolation criteria is redshift independent. Finally, any galaxies within 1 Mpc of the survey edge, or $1000\,\mathrm{km\,s}^{-1}$ of the maximum redshift, are removed. Stellar masses and SFRs are obtained for the field sample from the same sources discussed above, resulting in an isolated field sample of 164,193 galaxies.

5.3 Satellite Quenching versus ICM Density

It is well established by previous works that the fraction of quenched galaxies is a strong function of cluster-centric radius, from the local universe out to at least $z \sim 1$ (Bamford et al., 2009; Muzzin et al., 2012; Wetzel, Tinker, and Conroy, 2012; Haines et al., 2015). Given the fact that there is significant scatter in the cluster-centric radius versus ICM density relation across different clusters (see Figure 5.2), it is interesting to explore quenched fraction trends as a function of ICM density

directly. These trends can be used to explore quenching mechanisms such as ram pressure stripping (see Section 5.4.1), the strength of which depends explicitly on ICM density. Figure 5.3 shows quenched fraction ($\log \mathrm{sSFR} < -11\,\mathrm{yr}^{-1}$, Wetzel et al. 2013) versus ICM density for low- (purple), intermediate- (gray), and high-mass (red) galaxies, computed in equally spaced bins of ICM density. Galaxy stellar mass subsamples are defined such that there are an equal number of galaxies in each mass bin. We also mark the quenched fraction for the isolated field sample (described in Section 5.2.1) in each mass bin as the dashed horizontal lines in Figure 5.3.

We find that the quenched fraction at the lowest ICM densities, which corresponds to the vicinity of the virial radius (R_{200m}; Equation 5.2), is significantly enhanced relative to the value for the field, at the same stellar mass. This is particularly true for the two lower mass bins, whereas the trend for the highest mass galaxies approaches the field value. Numerous previous studies (e.g. Lu et al., 2012; Bahé et al., 2013; Haines et al., 2015; Roberts and Parker, 2017) have identified that the quenched fraction in the cluster outskirts can be significantly enhanced relative to the field, a fact that is often attributed to the pre-processing of star formation in less dense environments (i.e., small groups) prior to infall onto galaxy clusters. For the low-mass galaxies specifically, the data interpreted this way would require a pre-processed fraction of $\sim 30\%$.

For intermediate- and high-mass galaxies, the quenched fraction increases smoothly toward high ICM density. The environmental effect on the higher-mass galaxies is weaker than for the lowest-mass galaxies, consistent with previous studies that argued that environment most strongly influences low-mass galaxies ($M_\star \lesssim$ few $\times\, 10^{10}\,\mathrm{M}_\odot$, Haines et al. 2006; Bamford et al. 2009; Peng et al. 2010). To ensure that the observed trends are not being driven by our particular binning scheme, we rebin the data from 10 bins up to 20 bins and fit the resulting trend for intermediate- and high-mass galaxies with a single power-law. The fits to the 10 rebinnings are shown as the faded lines in Figure 5.3. While increasing the number of bins adds noise and increases the statistical uncertainties, the fits remain nearly identical and the underlying trend is robust. Given that the trend with ICM density is seemingly different for low-mass galaxies, these low-mass objects will be the focus of the remainder of the paper; but we present a discussion

of differences between high- and low-mass galaxies in Section 5.6.

The quenched fraction trend for low-mass galaxies shows signs of a broken power-law, with a moderate increase at the lowest ICM densities and a steepening in the densest cluster regions. To quantify this trend, we fit the quenched fraction trend for low-mass galaxies with both a single (SPL) and a broken power-law[6] (BPL) and compare the best fits. With the AIC as our model comparison tool, we find a lower value for the AIC for the BPL fit compared to the SPL fit; this is true for each of the rebinnings (faded lines Figure 5.3). This suggests that the AIC prefers a BPL, despite the penalty for increasing the number of fit parameters. We note that this is not the case for the higher-mass bins, where a SPL is always preferred. For the BPL the power-law slope is $\alpha_1 = 0.04^{+0.01}_{-0.03}$ at low ICM densities, and $\alpha_2 = 0.30^{+0.09}_{-0.10}$ at high ICM densities. For the SPL fit, the reduced chi-squared values range between 1.6 and 2.9 for the various rebinnings with a median of 2.2. In comparison, the reduced chi-squared for the BPL ranges between 0.5 and 1.5 with a median of 0.8.

This apparent BPL trend for low-mass galaxies is an intriguing result, and if robust, has important implications for the quenching of cluster satellites. Further work is required to test the validity of this result. We devote more time to the discussion of single versus double power-law along with other tests of robustness in Section 5.6. However, given the preference for the BPL according to the AIC and the reduced chi-squared, in Sections 5.4 and 5.5 we take the BPL fit at face value in order to explore a potential origin for the shape of this trend and the implications for satellite quenching.

5.4 Ram Pressure Stripping Model

The BPL behavior (for low-mass galaxies) in Figure 5.3 matches the qualitative expectation for quenching via ram pressure stripping – where a galaxy remains star-forming until reaching a threshold density beyond which the ram pressure force becomes strong and quenching proceeds efficiently (see Section 5.4.1, Figures 5.5 and 5.6). The break point in the BPL fit provides an estimate for this threshold density, and for our sample of low-mass galaxies we find a break point

[6] `http://docs.astropy.org/en/stable/modeling/`

of $\log \rho_{\rm thresh} = -28.3^{+0.2}_{-0.7}\,{\rm g\,cm^{-3}}$. We now can test whether a simple, analytic ram pressure stripping model is able to reproduce the trend for low-mass galaxies in Figure 5.3.

To directly constrain the fraction of galaxies susceptible to ram pressure stripping, we take a simple analytic approach, similar to models used previously in literature (e.g. Rasmussen et al., 2008; Jaffé et al., 2015; Jaffé et al., 2018). The basis of the model is the balance between ram pressure and the gravitational restoring force felt by the gas disk in a galaxy (Gunn and Gott, 1972). Specifically, gas will be susceptible to stripping when

$$\rho_{ICM}(R)v^2 > [g_{DM}(r) + g_{d,\star}(r) + g_b(r) + g_{HI}(r) + g_{H_2}(r)]\Sigma_{\rm gas}(r), \tag{5.6}$$

where $\rho_{ICM}(R)$ is the density of the ICM as a function of cluster-centric radius, v is the galaxy speed relative to the cluster center, $\Sigma_{\rm gas}$ is the surface mass density of the atomic+molecular gas component, and $g(r)$ is the maximum restoring gravitational acceleration for the DM halo, the stellar disk $(d, \star)$, bulge (b), atomic gas (HI), and molecular gas (H_2) in the direction perpendicular to the disk. Given a model for the ICM density and the galaxy restoring force, the galactocentric radius at which stripping is efficient can be constrained.

As described in Section 5.2.2, we estimate the local ICM density for each galaxy with the beta profile fits to the deprojected *Chandra* density profiles. To complete the left-hand side of Equation 5.6, we estimate the galaxy speed relative to the cluster center as

$$v = \sqrt{3} \times \frac{|z - z_{\rm cluster}|}{1 + z_{\rm cluster}} \times c, \tag{5.7}$$

where z is the galaxy redshift, $z_{\rm cluster}$ is the cluster redshift from the Yang catalog, and c is the speed of light. The factor of $\sqrt{3}$ is included to convert from line of sight to three-dimensional speed, on average. Following Equation 5.6, the restoring gravitational accelerations for both the gas and stellar components have to be modeled for each satellite galaxy as a function of galactocentric radius. For the stellar distribution, the bulge and disk components are modeled with GIM2D bulge + disk decompositions (exponential disk, De Vaucouleurs bulge; Simard et al. 2011), giving disk scale lengths and bulge effective radii (R_d, R_e) in the r band. We also make use of bulge and disk stellar masses (M_b, M_d) from Mendel et al.

(2014). For the stellar disk, we assume an exponential profile and calculate the restoring gravitational acceleration as

$$g_{d,\star} = 2G\Sigma_{d,\star}(r) = 2G\Sigma_0 e^{-r/R_d}, \tag{5.8}$$

where $\Sigma_{d,\star}(r)$ is the surface density of the stellar disk as a function of radius. Given the disk mass and scale length, the normalization, Σ_0, can be determined by integrating the surface density,

$$M_d = 2\pi \int_0^\infty \Sigma_{d,\star}(r) r \, dr = 2\pi\Sigma_0 R_d^2. \tag{5.9}$$

For the bulge component, we assume a Hernquist profile, as it has a convenient analytic form that is a good approximation to the De Vaucouleurs profile assumed in the bulge+disk decomposition (Hernquist, 1990). The bulge potential, ϕ_b, is then given by

$$\phi_b(r,\, z) = \frac{GM_b}{(r^2 + \mathcal{Z}^2)^{1/2} + a}, \tag{5.10}$$

where $\mathcal{Z}$ corresponds to the distance in direction perpendicular to the disk component and a is related to the bulge effective radius as $a = R_e/1.815$ (Hernquist, 1990). We then calculate the maximum (over the $\mathcal{Z}$ direction) restoring gravitational acceleration as

$$\begin{aligned} g_b(r) &= \max_{\mathcal{Z}} \frac{\partial \phi_b(r,\, \mathcal{Z})}{\partial \mathcal{Z}} \\ &= \max_{\mathcal{Z}} \frac{GM_b}{[(r^2 + \mathcal{Z}^2)^{/2} + a]^2} \frac{\mathcal{Z}}{(r^2 + \mathcal{Z}^2)^{1/2}}, \end{aligned} \tag{5.11}$$

For the DM halo, we also assume a Hernquist profile. The galaxy halo mass is determined with the observed stellar mass and the stellar-to-halo mass relation from Hudson et al. (2015). The scale radius, $a = r_{\rm vir}/c$, is estimated from the concentration and the galaxy r_{200}, assuming a concentration-mass relation from Diemer and Kravtsov (2015). Both the bulge and DM halo profiles are implemented with the COLOSSUS[7] package (Diemer, 2017).

Modeling the gas component is more challenging because unlike the stellar component, these galaxies are generally not observed in atomic or molecular gas. We

[7] `https://bdiemer.bitbucket.io/colossus/`

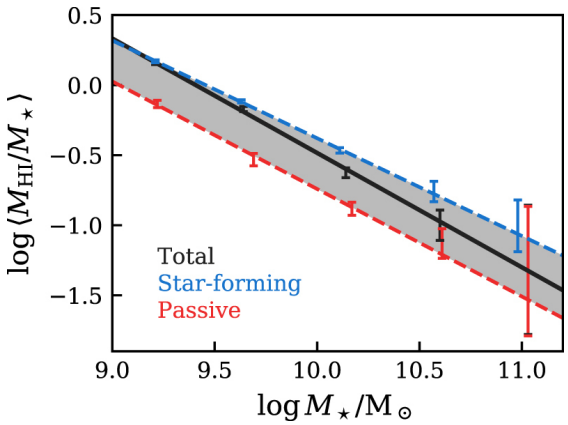

FIGURE 5.4: HI gas fraction-stellar mass scaling relation obtained by stacking ALFALFA spectra (both detections and non-detections) for 14,128 low-redshift SDSS galaxies. Scaling relations are shown for the total sample (black), as well as for only star-forming (blue) and passive (red) galaxies.

assume that the gas distribution consists of an atomic and molecular component, each following an exponential disk with different scale lengths – with the restoring acceleration taking the same exponential form as Equation 5.8. We assume that the atomic gas scale length is twice the optical disk scale length (i.e., $R_{\rm HI} = 2\,R_d$), which is consistent with the observed value for local non-HI deficient galaxy disks (Cayatte et al., 1994; Cortese et al., 2010; Boselli et al., 2014). For the molecular component we assume a scale length equal to the optical disk scale length (i.e., $R_{\rm H_2} = R_d$), again corresponding to molecular gas-to-stellar size ratio for non-deficient galaxy disks (Boselli et al., 2014). Because the galaxies in this sample are not observed in atomic or molecular gas, we assign gas masses statistically with the atomic/molecular gas fraction–stellar mass ($f_{\rm gas}$ versus $M_\star$, $f_{\rm gas} = M_{\rm gas}/M_\star$) scaling relations for representative samples of galaxies. In particular, we assign HI gas fractions for a given stellar mass assuming the $f_{HI} - M_\star$ relation for isolated galaxies. We are therefore approximating the gas fraction that the cluster galaxies in this sample would have had in the field, prior to infall; allowing us to estimate the amount of pre-infall gas that can be stripped by the cluster environment. To do this, we construct the $f_{\rm HI} - M_\star$ relation with the spectral stacking technique (Fabello et al., 2011) applied to a sample of 14,128 isolated, low-redshift ($0.02 < z < 0.05$) SDSS galaxies with processed ALFALFA data (Brown et al.,

2017). We refer to Brown et al. (2015) for a complete description of the parent sample and stacking technique, but most importantly, spectral stacking allows us to exploit both HI detections and non-detections to obtain the $f_{\rm HI} - M_\star$ relation for an unbiased sample of galaxies from low ($\sim 10^9\,{\rm M}_\odot$) to high ($\sim 10^{11}\,{\rm M}_\odot$) stellar mass. Figure 5.4 shows the $f_{\rm HI} - M_\star$ relation for the sample of isolated SDSS galaxies for the total sample (black) as well as for subsamples of star-forming (blue, 10,984 galaxies with $\log {\rm sSFR} > -11\,{\rm yr}^{-1}$) and passive (red, 3144 galaxies $\log {\rm sSFR} < -11\,{\rm yr}^{-1}$) galaxies. A consequence of the spectral stacking technique is that the intrinsic scatter in the $f_{\rm HI} - M_\star$ relation is unknown, therefore we use the difference between the relation for star-forming and passive galaxies as a rough estimate of the scatter. We assign "pre-infall" HI masses to each cluster galaxy by stochastically sampling from the "scatter" in Figure 5.4 (the shaded region) at the stellar mass of the galaxy. The stochastic selection is weighted by the inverse distance from the relation for the total sample (black line), therefore the sampling reflects the fact that the scatter is not symmetric about the trend for the total sample. This process is iterated 1000 times, and final values calculated with the HI mass are taken to be the median of these Monte Carlo resamplings.

Pre-infall molecular gas masses ($M_{\rm H_2}$) are assigned with the $f_{\rm H_2} - M_\star$ relation from xCOLD GASS (Saintonge et al., 2017) obtained from spectral stacking with a representative sample of low-redshift galaxies ($0.01 < z < 0.02$, $M_\star > 10^9\,{\rm M}_\odot$). Saintonge et al. (2017) find that for the stacked sample, the molecular gas fraction is approximately constant at $f_{\rm H_2} \sim 0.1$ for masses $\lesssim 10^{10.5}\,{\rm M}_\odot$ (see Table 5 in Saintonge et al. 2017). For the ram pressure model we focus on low-mass galaxies ($M_\star < 10^{10}\,{\rm M}_\odot$), therefore we choose to assign a constant molecular gas fraction of $f_{\rm H_2} = 0.1$ to our cluster galaxies. We note that at these masses, the gas content of galaxies remains largely dominated by the atomic component (e.g. Saintonge et al., 2017), which is also the component that is most susceptible to environmental interactions. Therefore our specific assumptions regarding the molecular gas component do not strongly affect the results.

With Equation 5.6 combined with the galaxy and ICM models described above, we can determine the stripping radius, $r_{\rm strip}$, the galactocentric radius at which $\rho_{\rm ICM}(R)v^2 > [g_{\rm DM}(r) + g_{d,\star}(r) + g_b(r) + g_{\rm HI}(r) + g_{\rm H_2}(r)]\Sigma_{\rm gas}(r)$. Given the stripping radius, the stripped mass (i.e., the gas mass outside of the stripping radius) can

be calculated as

$$M_{\rm strip} = M_{\rm gas}\, e^{r_{\rm strip}/R_{\rm gas}} \left(\frac{r_{\rm strip}}{R_{\rm gas}} + 1 \right) \tag{5.12}$$

(Binney and Tremaine, 2008). We compute the stripped mass for both the atomic and molecular gas components and then calculate the total stripped gas fraction as

$$f_{\rm strip} = \frac{M_{\rm strip,HI} + M_{\rm strip,H_2}}{M_{\rm HI} + M_{\rm H_2}} \tag{5.13}$$

Uncertainties on the disk scale lengths and bulge effective radii from Simard et al. (2011) introduce uncertainties on the stripped masses of roughly 10%, but do not bias the results in any way.

We stress that the ram pressure stripping model described above makes many simplifying assumptions. This model is not intended to be a detailed treatment of ram pressure stripping, but instead to provide a rough estimate of where ram pressure is expected to significantly influence satellite galaxies. We highlight and discuss the primary assumptions of this model in Appendix 5.A.

5.4.1 Comparison to Observed Quenched Fractions

With this analytic model of ram pressure stripping, we can now make direct comparisons to the observed quenched fractions for the low-mass galaxies in Figure 5.3. Specifically, we aim to constrain whether the apparent quenched fraction upturn at high ICM density and low stellar mass can be reproduced by a simple ram pressure model. Therefore, we isolate the high-density upturn by subtracting the power-law fit to the low ICM density trend ($\rho_{\rm ICM} \lesssim 10^{-28}\,{\rm g\,cm^{-3}}$). This allows us to make a direct comparison between the observed upturn and the output from our ram pressure model. We calculate the fraction of galaxies in the sample in which n-per cent of their cold-gas reserves is susceptible to stripping (where n is a free parameter in the model).

In Figure 5.5 we overlay the rescaled quenched fraction with the low-density power law subtracted on top of output tracks from the ram pressure model. Each track corresponds to the fraction of galaxies in the sample in which at least the given percentage of their cold-gas mass is located beyond the stripping radius (and therefore is susceptible to stripping). We show tracks ranging between >20% and

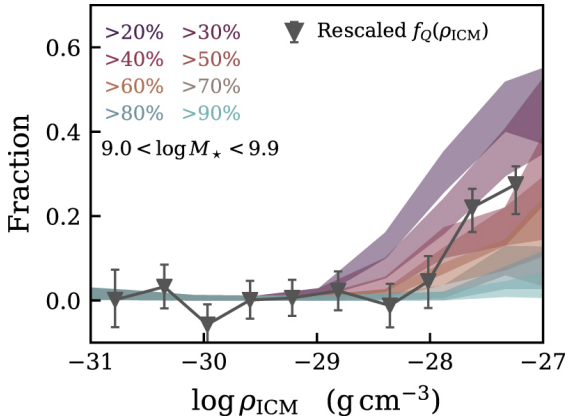

FIGURE 5.5: Fraction of low-mass galaxies with the listed percentage of their gas mass that is susceptible to stripping, as a function of ICM density. Shaded bands correspond to 68% Bayesian confidence intervals estimated from the beta distribution (Cameron, 2011). For comparison to the shape of these tracks, we plot the quenched fraction for low-mass galaxies from Figure 5.3 with the power-law fit at low ICM density subtracted, this permits a direct comparison between ram pressure stripping and the observed quenched fraction upturn at high ICM density.

>90%, and the observed quenched fraction trend is well matched by a model where about half of a galaxy's cold-gas mass is available to be stripped. The stripped fractions in Figure 5.3 correspond to the removal of a parcel of gas entirely from the galaxy, as they are computed with the maximum restoring accelerations (in the direction perpendicular to the disk, Equation 5.6). Considering instead the removal of gas from a typical gaseous disk (scale height of a few hundred parsecs), the data are then well fit by a stripped fraction of $\gtrsim$ 70%. Regardless of the precise definition of gas stripping, we emphasize that the primary insight is the fact that the observed upturn in quenched fraction coincides closely with the onset of a significant ram pressure force relative to the galaxy restoring potential. The results from this simplified ram pressure model are consistent with low-mass cluster galaxies experiencing enhanced quenching due to relatively efficient ram pressure. Below this threshold density, ram pressure seems to be not strong enough, on average, to quench even low-mass galaxies.

5.5 Slow-then-rapid Quenching

A commonly invoked model for environmental quenching is so-called delayed-then-rapid quenching (Wetzel et al., 2013), where satellite quenching does not occur immediately upon infall but proceeds rapidly only after a characteristic delay time. Qualitatively, the low-mass quenched fraction versus ICM density trend found in this work lends itself naturally to a similar interpretation (see Figure 5.3), namely a "slow-then-rapid" quenching framework. We note that a slow-then-rapid scheme for satellite quenching has been independently advocated for by Maier et al. (2019). Again taking the apparent BPL trend at face value (see Section 5.6 for a detailed discussion of the robustness of this trend), we interpret the modest power-law slope between infall and a galaxy reaching the threshold ICM density as the slow-quenching portion, beyond which point the galaxy rapidly quenches as it moves to higher ICM density. This interpretation is illustrated schematically in Figure 5.6 both as an annotated quenched fraction plot and as a diagram showing a toy infall track for a star-forming galaxy onto a cluster.

To be more quantitative and to permit comparisons to previous studies, we derive rough estimates for the time that a satellite galaxy spends on the slow-quenching track after infall ($t_{\rm slow}$) as well as the quenching timescale associated with the rapid-quenching component ($\tau_{Q,\rm rapid}$) with a simple exponential model. The primary simplifying assumption made in this model is that galaxies are quenched exclusively on their first infall on a radial orbit. We note that these assumptions are consistent with recent results from hydrodynamic simulations (Arthur et al., 2019; Lotz et al., 2019).

We calculate the time spent in the slow-quenching mode as

$$t_{\rm slow} = \left(\frac{R_{200m} - R_{\rm thresh}}{v_{\rm slow}} \right), \tag{5.14}$$

where $R_{200m} - R_{\rm thresh}$ is the radial distance traveled between infall and reaching the threshold ICM density, and $v_{\rm slow}$ is the mean galaxy velocity over the "slow-quenching" portion. For each cluster, R_{200m} is given by Equation 5.2, and we measure $R_{\rm thresh}$ given the observed density profile (Figure 5.2). To determine galaxy velocities, we make use of the high-resolution DM only simulations from Joshi,

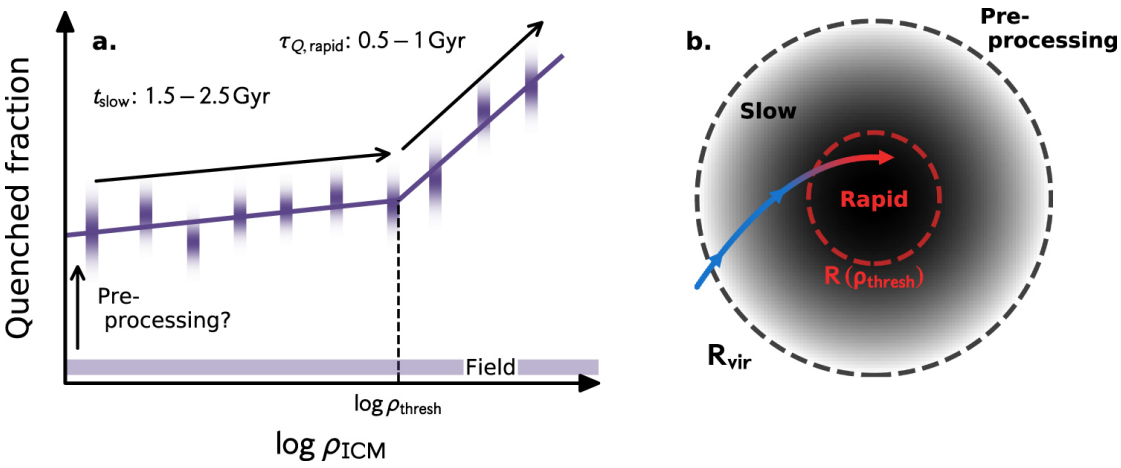

FIGURE 5.6: Schematic diagram illustrating the connection between the results of this paper and a "slow-then-rapid" quenching model. At galaxy infall (at the virial radius), the quenched fraction for infalling galaxies is significantly larger than the corresponding value for isolated field galaxies at the same stellar mass. This offset between the infalling and field populations is consistent with the preprocessing of star formation prior to infall. The slow-quenching phase occurs after galaxy infall prior to reaching a threshold ICM density. Galaxies spend 1.5-2.5 Gyr between infall and reaching the threshold ICM density. At a threshold ICM density ($\rho_{ICM} \sim 10^{-28}\,g\,cm^{-3}$), a significant fraction of a galaxy's cold-gas mass is now susceptible to ram pressure stripping and quenching can occur rapidly on an e-folding time $\tau_Q \sim 1$ Gyr, at ICM densities higher than the threshold value. The left-hand panel annotates this interpretation on the observed quenched fraction vs. ICM density plot, where each data point is shown a Gaussian "smear" indicating the uncertainty. The right-hand panel illustrates this model showing a hypothetical infall track of a star-forming galaxy onto a cluster.

Parker, and Wadsley (2016). Specifically, we consider galaxy cluster subhalos on their first infall, located between R_{200m} and the median $R_{\rm thresh}$ for the clusters in our sample, $0.25 \times R_{200m}$. We only consider subhalos in $> 10^{14}\,\mathrm{M}_{\odot}$ clusters with peak DM masses between $10^{11.1} < M_{\rm peak} < 10^{11.75}\,\mathrm{M}_{\odot}$, which corresponds to our low-mass galaxy stellar mass range of $10^{9} \lesssim M_{\star} \lesssim 10^{10}\,\mathrm{M}_{\odot}$ assuming the stellar-to-halo mass relation from Hudson et al. (2015). We normalize the subhalo velocities by the one-dimensional velocity dispersion of the host clusters in the $z = 0$ snapshot, which is directly comparable to the measured line-of-sight velocity dispersions for the clusters in our sample. The cluster velocity dispersions measured from the DM simulations and the velocity dispersions measured for the observed clusters are both calculated with the biweight estimator (Beers, Flynn, and Gebhardt, 1990). For subhalos on first infall, located between $0.25 < R_{3D} < 1\,\mathrm{R}_{\rm 200m}$, we find that the median velocity is $v = 1.8 \times \sigma_{1D}$. To account for the spread in infall velocities, we calculate $t_{\rm slow}$ in a Monte Carlo sense by sampling velocities, $v_{\rm slow}$, from the full distribution extracted from the simulations. We measure $t_{\rm slow}$ as the median of 1000 random samplings. With Equation 5.14, we obtain an estimate of $t_{\rm slow} = 1.8^{+0.6}_{-0.3}\,\mathrm{Gyr}$. Therefore, infalling galaxies spend $\sim 1.5 - 2.5\,\mathrm{Gyr}$ before reaching the threshold ICM density, beyond which quenching proceeds rapidly. The value for $t_{\rm slow}$ is, unsurprisingly, close to the dynamical time for cluster-mass halos.

For the rapid portion we model the quenched fraction as increasing exponentially over a characteristic e-folding time, τ_Q. The quenched fraction is then given by

$$f_Q = 1 - (1 - f_{Q,0})e^{-t/\tau_Q}. \tag{5.15}$$

Specifically, the e-folding timescale for rapid-quenching is estimated as

$$\tau_{Q,\rm rapid} = t_{\rm rapid} \times \left[\ln\left(\frac{1}{1 - f_{Q,\rm rescaled}(\rho')}\right)\right] \tag{5.16}$$

with

$$t_{\rm slow} = \left(\frac{R_{\rm thresh} - R(\rho')}{v_{\rm rapid}}\right), \tag{5.17}$$

We take $\rho' = 10^{-27}\,\mathrm{g\,cm^{-3}}$ and $f_{Q,\rm rescaled}(\rho') = 0.35$, where $f_{Q,\rm rescaled}$ is the rescaled quenched fraction where the contribution from the low ICM density power law has

been subtracted in order to isolate the high-density upturn (see Figure 5.5). The characteristic infall velocity is again determined from DM simulations, now for subhalos at $R_{3D} < 0.25 \times R_{200m}$. In this inner cluster region we find the median velocity $v = 2.8 \times \sigma_{1D}$, and again estimate the timescale by randomly sampling the simulated velocity distributions. With Equation 5.16, this gives a median quenching e-folding time of $\tau_{Q,\mathrm{rapid}} = 0.6^{+0.1}_{-0.1}$ Gyr.

Our estimates for t_{slow} and $\tau_{Q,\mathrm{rapid}}$ suggest a total quenching time of $\sim 2-3$ Gyr for low-mass galaxies in clusters. Studying cluster dwarf galaxies in the Illustris simulation, Mistani et al. (2016) measure the time elapsed between infall and the first time a galaxy sSFR falls below $10^{-11}\,\mathrm{yr}^{-1}$, finding timescales ranging between $\sim 3-5.5$ Gyr for stellar masses $10^9 \lesssim M_\star \lesssim 10^{10}\,\mathrm{M}_\odot$. Haines et al. (2015) employ a model where galaxies in Local Cluster Substructure Survey (LoCuSS) clusters are quenched instantaneously after a delay time Δt since infall, and find that the surface density of star-forming galaxies based on infrared (UV) observations is best fit by a delay time of $2.1^{+0.8}_{-0.7}$ (3.2 ± 0.4) Gyr. Haines et al. (2015) also derive quenching times of $\sim 1.5-2$ Gyr assuming that star formation declines exponentially upon cluster infall. Wetzel et al. (2013) obtain total quenching times of 4-5 Gyr for low-mass satellites of cluster-mass halos, which are somewhat larger than the estimates derived in this work. With semi-analytic models applied to the Millennium Simulation (Springel et al., 2005) along with observations of galaxies in groups and clusters from the Yang et al. (2007) catalog, De Lucia et al. (2012) argue that on average, galaxies spend 5-7 Gyr in halos $> 10^{13}\,\mathrm{M}_\odot$ before quenching. These timescales are longer than the total quenching timescale that we derive, but given that our sample is dominated by large clusters (median halo mass, $4 \times 10^{14}\,\mathrm{M}_\odot$), it is difficult to make a direct comparison. In fact, we do see evidence for preprocessing, meaning that many galaxies in our cluster sample were likely members of smaller groups ($\sim 10^{13}\,\mathrm{M}_\odot$) prior to cluster infall. Including potential additional time spent as satellites of smaller groups could bring our quenching timescales closer to the De Lucia et al. (2012) estimates. In general, the quenching times that we derive for low-mass cluster galaxies are roughly consistent, if somewhat shorter, than previous estimates from the literature.

5.6 Discussion

5.6.1 Preprocessing

In Figure 5.3 we show that the quenched fraction in the cluster outskirts is significantly enhanced relative to the field, especially for low-mass galaxies. A natural interpretation for this result is that a fraction of infalling galaxies have been preprocessed prior to infall onto the current cluster. The data for low-mass galaxies require a preprocessed fraction of $\sim$0.3 to account for the difference from the field value. This preprocessed fraction estimate, however, is quite crude and does not account for any contamination from backsplashing galaxies, which will have the effect of artificially increasing the apparent level of preprocessing. Therefore, it is more precise to treat this value as an upper limit. With this in mind, this fraction is roughly consistent with estimates for the preprocessed fraction from previous studies. For example, estimates of the fraction of galaxies that infall onto clusters as members of smaller groups (where the galaxies would be susceptible to preprocessing) range from $\sim$25% to $\sim$60% from both simulations (McGee et al., 2009; De Lucia et al., 2012; Bahé et al., 2013) and observations (Hou, Parker, and Harris, 2014). These constraints provide an upper limit to the preprocessed fraction, as not all galaxies infalling as a member of a group will necessarily have been quenched. More direct constraints on the fraction of preprocessed galaxies range from $\sim$ 10% to 30% for cluster galaxies (Haines et al., 2015; Roberts and Parker, 2017; van der Burg et al., 2018). The fraction derived in this work falls on the upper end of this range, but it is again important to note that a portion of the satellite population near the virial radius are actually backsplash galaxies that have already made a pericentric passage (e.g. Mahajan, Mamon, and Raychaudhury, 2011; Bahé et al., 2013; Oman, Hudson, and Behroozi, 2013; Hirschmann et al., 2014). Therefore it is likely that quenched backsplash galaxies at the virial radius are contaminating the "infalling" population and artificially increase the apparent preprocessed fraction.

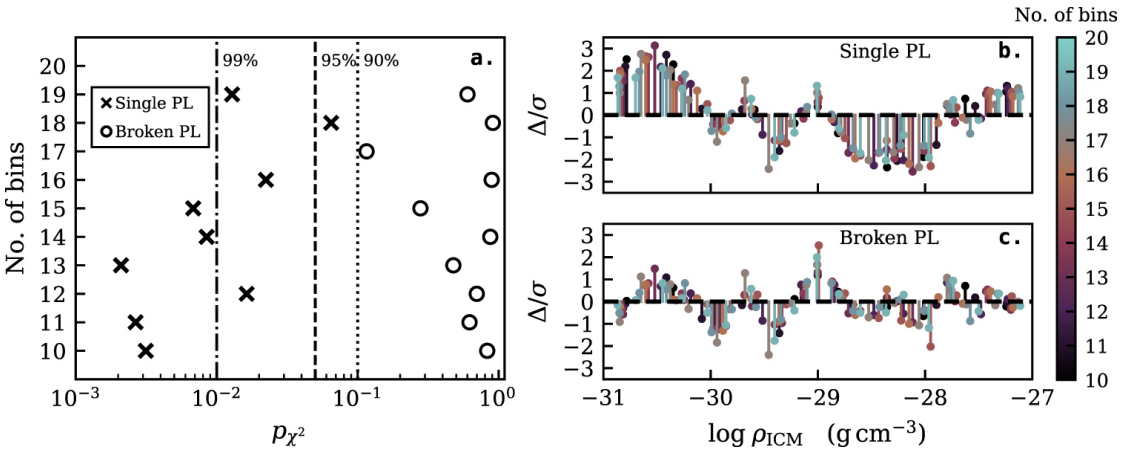

FIGURE 5.7: Left: p-value from chi-squared test for various rebinnings (number of bins, y-axis), for single (crosses) and double (circles) power-law fits. Top right: Residuals from the single power-law fit for each of the rebinnings (see color bar for number of bins). Bottom right: Residuals from the BPL fit for each of the rebinnings (see color bar for number of bins). Residuals are normalized by the 68% uncertainty on data points.

5.6.2 Is a BPL Required for the Low-mass Data?

A key question to address in this study is not only whether the BPL gives a better fit than the SPL to the low-mass data, but also whether the SPL provides an acceptable fit (regardless of the quality of the BPL fit). We have already made use of the AIC as a model discriminator, and as is discussed in Section 5.3, the AIC favors the BPL fit over the SPL fit for the low-mass data and all of the rebinnings of these data. This is certainly clear evidence that the BPL fit is statistically preferred over the simpler SPL, but the AIC says nothing about the quality of individual fits, only whether one fit is better than another.

We also test the significance of the SPL and BPL fits individually by applying a simple chi-squared test. In Figure 5.7 we plot the p-value from the chi-squared test for both the SPL (crosses) and BPL (circles) fits for each of the rebinnings, ranging from 10 to 20 bins on the y-axis. For all of the rebinnings we see evidence (at the 90% level) that the SPL does not provide a sufficient fit to describe the low-mass galaxy trend. This suggests that the SPL fit may not be sufficient based on the chi-squared test. One aspect of the fit that a simple chi-squared test does

not take into account is any structure in the fit residuals. In Figures 5.7(b) and (c) we show the fit residuals (normalized by the uncertainty on each data point) for the single and double power-law fits, respectively. We show the residuals for the fits to all of the rebinnings and mark the number of bins in each fit with the color bar in Figures 5.7(b) and (c). Two trends are clear by comparing Figures 5.7(b) and (c): 1. The amplitude of the residuals is smaller for the BPL fit than for the SPL. 2. For the BPL fit, the residuals seem to be randomly scattered around the zero-line, whereas there is apparent structure in residuals for the SPL fit with a consistent excess of positive residuals between 10^{-31} and $10^{-30}\,\mathrm{g\,cm^{-3}}$ and an excess of negative residuals between 10^{-29} and $10^{-28}\,\mathrm{g\,cm^{-3}}$. This structure in the residuals for the SPL fit is evidence that the SPL model does not fully describe the low-mass quenched fraction data.

5.6.3 Robustness Tests for the BPL Trend

SFR Indicator

When calculating quenched fractions, we use the MPA-JHU SFRs, which are derived from Hα emission (when detected; Brinchmann et al. 2004). Hα has the advantage of being a tracer of star formation on very short timescales ($\lesssim 10\,\mathrm{Myr}$, Kennicutt and Evans 2012) which is especially important when investigating rapid-quenching mechanisms (such as ram pressure). At low SFRs (where emission lines are not detected), the MPA-JHU values are based on the D_n4000 break and are therefore less precise. Given the large number of value-added catalogs available for the SDSS, we are able to reproduce Figure 5.5 for different SFR estimators to test whether the observed shape is driven by our choice of star formation indicator. In Figure 5.8 we show the rescaled quenched fraction (where we have subtracted the low-density power law, as in Figure 5.5) versus ICM density for SFRs derived from UV+optical+mid-IR SED fitting (Salim et al., 2016; Salim, Boquien, and Lee, 2018), optical+IR SED fitting (Chang et al., 2015), rest frame[8] $u-r$ colors (Blanton and Roweis 2007; where we assume that the red fraction corresponds to the quenched fraction), along with the primarily Hα SFRs (Brinchmann et al., 2004) from the main text for reference. For all SFR estimators, we define quenched

[8] k-corrected to $z = 0.1$.

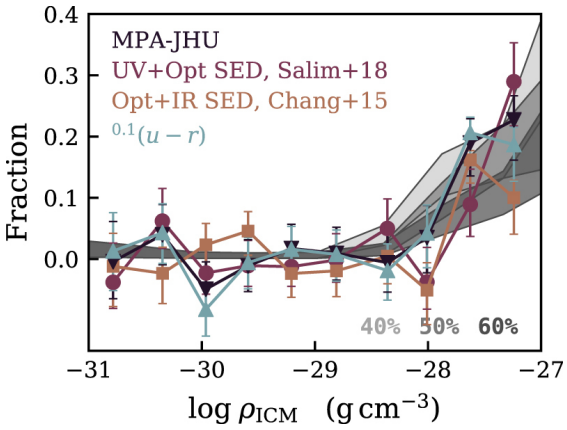

FIGURE 5.8: Baseline-subtracted quenched fraction as a function of ICM density for four different star formation rate tracers: Hα+D_n4000 (downward triangles, Brinchmann et al. 2004), $u-r$ color (upward triangles, Blanton and Roweis 2007), UV+optical SED fitting (circles, Salim et al. 2016; Salim, Boquien, and Lee 2018), and optical+IR SED fitting (squares, Chang et al. 2015). In the background we plot our analytic ram pressure tracks for >40%, >50%, and >60% stripped. The characteristic break at $\rho_{\rm ICM} \simeq 10^{-28}\,{\rm g\,cm^{-3}}$ is present regardless of star formation rate tracer.

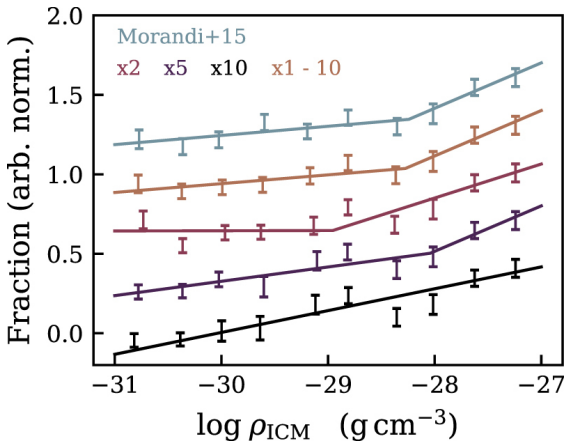

FIGURE 5.9: Quenched fraction (each offset by 0.3 in the vertical direction) vs. ICM density for various assumptions about ICM density beyond R_{500}. $\times 2$, $\times 5$, and $\times 10$ correspond to systematically decreasing the ICM density estimate by the given factor. $\times 1 - 10$ corresponds to randomly decreasing the ICM density for each galaxy by a factor between one and ten. Morandi+15 corresponds to steepening the observed gas density profile slope by a factor between 1 and 1.75 (taken from the observations in Morandi et al. 2015) according to R/R_{500} for each galaxy.

galaxies to have sSFR $< 10^{-11}\,\mathrm{yr}^{-1}$, and for $u-r$ colors, we define quenched galaxies to have ${}^{0.1}(u-r) > 2.4$, which corresponds to the intersection between the red sequence and blue cloud with a double-Gaussian fit. Also plotted for reference are the ram pressure stripping tracks for stripped fractions of >40%, >50%, and >60%. Figure 5.8 shows that the general trend presented in Sections 5.3 and 5.4.1 persists regardless of SFR indicator, and that in all cases, the trend is well matched by a model where quenching becomes efficient when about half of the galactic cold-gas reservoir is susceptible to ram pressure stripping.

ICM Density at Large Radius

Given that the X-ray data used in this work only reach sufficient depth (>5000 counts per annulus) within R_{500}, it is necessary to extrapolate the density profiles to obtain local ICM density estimates for galaxies in the cluster outskirts. Previous work has shown that ICM density profiles tend to steepen at large radius ($\gtrsim R_{500}$) compared to the inner regions (Morandi et al., 2015). In addition, clumpy gas

distributions are common in the cluster outskirts and can introduce biases affecting estimates of the gas density (e.g. Walker et al., 2013; Morandi and Cui, 2014; Ichinohe et al., 2015). This uncertainty in the ICM density profiles at large radius is an important source of uncertainty for this analysis, but it is difficult to quantify on a case-by-case basis without deep X-ray observations out to the virial radius.

Given the observed steepening of density profiles at large radii, by extrapolating profiles we may be overestimating the ICM density in the cluster outskirts. We employ a few different methods to test what effect this could have on the BPL trend we observe. As a simple first test, we arbitrarily decrease the local ICM density estimate for each galaxy beyond R_{500} by a constant factor. The lines labeled $\times 2$, $\times 5$, and $\times 10$ in Figure 5.9 correspond to the quenched fraction trend after assuming a decrease in ICM density by a factor of two, five, and ten beyond R_{500}. Note that the lines in Figure 5.9 have been offset by 0.3 in the vertical direction for readability. For a decrease of a factor of two and five, the BPL shape is still evident (and is still preferred over an SPL by the AIC), but for a factor of ten decrease, there is no evidence for a BPL trend. Unless we systematically overestimate the local ICM density for each galaxy beyond R_{500} by a factor of ≥ 10, the BPL trend therefore appears robust. The line labeled $\times 1 - 10$ in Figure 5.9 corresponds to decreasing the local ICM density randomly by a factor between one and ten. Specifically, the plotted line shows the median of 1000 random Monte Carlo trials, and the presence of the BPL shape is evident and confirmed by the AIC. Finally, Morandi et al. (2015) study a large sample (>300) of galaxy clusters observed by Chandra with coverage out to and beyond the virial radius. For their low-redshift sample ($z < 0.3$), they find that the slope of the gas density profile (β) steadily steepens by a factor of 1.75 between R_{500} and R_{100} (R_{100} is similar to the $R_{200m} \sim R_{\rm vir}$ that we use). Knowing this, we linearly interpolate between a steepening of a factor of 1 at R_{500} and a factor of 1.75 at R_{200m}, and integrate the resulting density profile out to each galaxy's cluster-centric radius to give an updated local ICM density decreased according to Morandi et al. (2015). The result of this is shown with the labeled line in Figure 5.9. Again, the BPL trend is apparent and is preferred over an SPL fit to the data by the AIC.

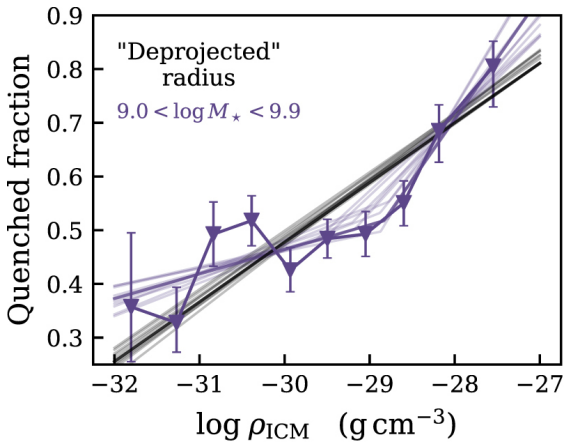

FIGURE 5.10: Quenched fraction vs. ICM density where local ICM densities are determined with "deprojected" cluster-centric radii. Best-fit SPLs and BPLs (gray and black, respectively, for various rebinnings) are shown with the solid lines.

Effect of Projected Radii

The local ICM density estimates in the paper are determined with observed projected cluster-centric radii and observed deprojected ICM density profiles. Observing galaxy positions in projection is unavoidable, but we can attempt to gauge the effect of observing galaxy positions in projection with the aid of simulations. In particular, observed projected radii are a lower limit to the true cluster-centric radius, and small cluster-centric radii (where ICM densities are highest) are where projection effects are most severe. Given that strong mass segregation is not observed in low-redshift clusters (e.g. Roberts et al., 2015; Kafle et al., 2016), projection effects should not bias the low-mass galaxies differentially relative to the higher-mass bins. Therefore, the fact that we see trends that differ in shape between mass bins suggests that projection effects alone are not driving these differences. However, in the interest of completeness, we explore (in an approximate manner) the influence of projected cluster-centric radii on the BPL trend seen for low-mass galaxies.

To roughly deproject observed, projected cluster-centric radii, we make use of DM simulations to obtain three-dimensional radii information. In particular, we again make use of high-resolution DM-only simulations from Joshi, Parker, and Wadsley (2016) that were used to estimate subhalo infall velocities in Section 5.5.

We extract $R_{3D,\mathrm{sim}}/R_{\mathrm{proj,sim}}$ for galaxy-mass subhalos in these simulated galaxy clusters and then measure the median value of $R_{3D,\mathrm{sim}}/R_{\mathrm{proj,sim}}$ in bins of projected cluster-centric radius:

$$R_{\mathrm{proj,sim}} = [0.0,\ 0.1,\ 0.2,\ 0.3,\ 0.4,\ 0.5,\ 0.6,\ 0.7,\ 0.8,\ 0.9,\ 1.0]\, R_{200m}$$

for these radial bins, the median $R_{3D,\mathrm{sim}}/R_{\mathrm{proj,sim}}$ are

$$\frac{R_{3D,\mathrm{sim}}}{R_{\mathrm{proj,sim}}} = [2.59,\ 1.55,\ 1.32,\ 1.21,\ 1.16,\ 1.11,\ 1.08,\ 1.07,\ 1.04,\ 1.01].$$

When computing projected radii from the simulations, we project clusters along a random axis 1000 times and then use median projected radii from these random trials. We perform a linear spline fit to the $R_{3D,\mathrm{sim}}/R_{\mathrm{proj,sim}}$ versus $R_{\mathrm{proj,sim}}$ relationship and then deproject the observed cluster-centric radius,

$$R_{\mathrm{deproj,obs}} = S(R_{\mathrm{proj,obs}}/R_{200m}) \times R_{\mathrm{proj,obs}} \tag{5.18}$$

where $S(R_{\mathrm{proj,obs}}/R_{200m})$ is the spline fit to the $R_{3D,\mathrm{sim}}/R_{\mathrm{proj,sim}}$ versus $R_{\mathrm{proj,sim}}$ relationship interpolated to the observed normalized cluster-centric radius, $R_{\mathrm{proj,obs}}$ is the observed physical cluster-centric radius, and $R_{\mathrm{deproj,obs}}$ is the resulting estimate of the deprojected cluster-centric radius.

In Figure 5.10 we show the quenched fraction as a function of ICM density with local ICM densities determined with the deprojected cluster-centric radii outlined above. For low-mass galaxies the BPL shape is still apparent, despite increased scatter at low-densities. In Figure 5.10 we also show the best-fit SPL (gray) and BPL (purple) fits to the "deprojected" data. The AIC prefers the BPL fit. We emphasize that these are rough deprojections and are only appropriate in an average sense. Unfortunately, obtaining accurate deprojected radii on a galaxy-by-galaxy basis is not possible. A more detailed analysis should include phase-space information to incorporate deprojection not only as a function of radial position, but also as a function of velocity offsets. We note that if we deproject only along the z-axis of the simulation instead of many random halo projections, then the BPL trend in 5.10 becomes less apparent and is only marginally preferred over an SPL fit. It is clear that robustly deprojecting observed radii is still an outstanding issue,

and we do not rule out that projection effects could contribute to the observed BPL trend.

5.7 Mass Dependence of Quenching Mechanisms?

The two most commonly invoked mechanisms to quench satellite star formation in galaxy clusters are ram pressure stripping and starvation (Gunn and Gott, 1972; Quilis, Moore, and Bower, 2000; Wetzel et al., 2013; Wetzel, Tollerud, and Weisz, 2015; Muzzin et al., 2014; Fillingham et al., 2015; Jaffé et al., 2015; Peng, Maiolino, and Cochrane, 2015). It is often argued that the timescale over which these two mechanisms act provides a method of distinguishing. For instance, starvation should quench star formation on relatively long timescales ($\gtrsim 3\,\mathrm{Gyr}$, with the timescale becoming longer for low-mass galaxies) dictated by the gas depletion time, whereas efficient ram pressure stripping will deplete the galaxy of gas, and therefore quench star formation, on much shorter timescales ($\lesssim 1\,\mathrm{Gyr}$ for efficient ram pressure stripping, Quilis, Moore, and Bower 2000; Roediger and Hensler 2005; Steinhauser, Schindler, and Springel 2016). However, this argument can be complicated by the fact that ram pressure stripping may require a significant delay before infalling galaxies encounter the densest regions of the ICM. This delay (which should be on the order of the dynamical time of the cluster) can lead to a total quenching time since infall (delay + quenching) that is similar to that of starvation. The quenched fraction trend for low-mass galaxies in this work is consistent with gas depletion (starvation) driving the slow-quenching phase at low ICM density, and ram pressure driving the rapid-quenching phase in the cluster interior. The high-mass galaxies in this sample, though not investigated in detail in this paper, lack the same ram pressure signature. It has been shown that gas depletion times are shortest for high-mass galaxies (Davé, Finlator, and Oppenheimer, 2011; Fillingham et al., 2015; Saintonge et al., 2017). It is therefore plausible that high-mass galaxies consume their gas reserves and quench via starvation prior to reaching the densest cluster interior where ram pressure becomes efficient. We also note that the deeper potential wells of high-mass galaxies will

make them more resistant to ram pressure stripping in general. Indeed, Yun et al. (2019) show that the fraction of jellyfish galaxies undergoing strong ram pressure stripping in the Illustris-TNG simulation is strongly dependent on stellar mass, with the jellyfish fraction being highest for low-mass galaxies. Furthermore, the quenching of high-mass galaxies may be largely driven by internal mechanisms, regardless of environment (Peng et al., 2010). Star formation in low-mass galaxies should persist for much longer after cluster infall because of the long total gas depletion times, and therefore low-mass galaxies can still be actively forming stars when they reach the densest region of the ICM, where any residual star formation may be quickly quenched as a result of ram pressure stripping. Substantial ram pressure stripping of atomic gas (the more concentrated molecular component is left largely unstripped in our models) can disconnect a galaxy from its cold-gas supply, leaving the galaxy to quench via gas depletion (Cen, 2014). Molecular gas depletion timescales for star-forming, low-mass galaxies are $\sim 1\,\mathrm{Gyr}$ (Saintonge et al., 2017), consistent with the rapid-quenching timescale we derive. The picture that we present here is consistent with what has been described by van der Burg et al. (2018), who suggest a quenching scenario where ram pressure is able to "finish the job" when starvation does not quench satellites rapidly enough. This picture is also consistent with results from hydrodynamic simulations in Bahé and McCarthy (2015).

A mass-dependent transition between starvation and ram pressure stripping has been previously advocated, where it has been argued that dwarf galaxies ($M_\star \lesssim 10^8\,\mathrm{M}_\odot$) are primarily quenched through ram pressure, whereas the quenching of galaxies with $M_\star \gtrsim 10^8\,\mathrm{M}_\odot$ is dominated by starvation (Fillingham et al., 2015; Wetzel, Tollerud, and Weisz, 2015; Rodriguez Wimberly et al., 2019). These conclusions are derived from observations of galaxies primarily in group-mass systems, which are of significantly lower mass than the sample of large clusters in this work. Here we find evidence that this transition mass may be higher ($\sim 10^9 - 10^{10}\,\mathrm{M}_\odot$) in dense clusters, where both the ICM density and relative velocities are high, which leads to a strong ram pressure force.

5.8 Summary

We have used a sample of 24 low-redshift SDSS galaxy clusters observed by Chandra to present the first direct study, with a large sample of cluster galaxies, of the relationship between satellite quenching and measured ICM density. The main results of this paper are the following:

1. Comparing quenched fractions of galaxies at the lowest ICM densities to those for isolated field galaxies, we find evidence that approximately one-third of the cluster galaxies may have been preprocessed prior to infall.

2. The quenched fractions of intermediate- and high-mass cluster galaxies show a modest, continuous increase with ICM density.

3. The quenched fraction versus ICM density trend for low-mass galaxies shows evidence of a BPL trend. The quenched fraction increases modestly at low ICM density before increasing sharply beyond a threshold ICM density. We show that a BPL gives a statistically better fit (even after accounting for extra parameters) than an SPL.

4. The observed BPL trend is still apparent after observed cluster-centric radii are deprojected with galaxy cluster DM simulations, but the strength of the BPL trend shows some dependence on how galaxy positions are deprojected. We do not rule out that projection effects may contribute to the observed trend.

5. The quenched fraction upturn at high ICM density, for low-mass galaxies, is well matched by a simple analytic model of ram pressure stripping, where quenching is efficient when more than about half of a galaxy's cold-gas reservoir becomes susceptible to stripping.

6. These results are consistent with a slow-then-rapid picture of satellite quenching. We argue that the slow-quenching portion is consistent with quenching via steady gas depletion (starvation) and the rapid-quenching portion is consistent with ram pressure stripping "finishing off" the quenching of low-mass satellites.

Acknowledgments: The authors thank the anonymous referee for their many helpful comments which have improved the paper. I.D.R., L.C.P., J.H.L., and J.W. are supported by the National Science and Engineering Research Council of Canada. We thank Adam Muzzin for his helpful comments on an early draft, and we also thank Katy Rodriguez Wimberly for sharing the Ultra-Faint Fat ELVIS color scheme that we used in the figures throughout the manuscript.

The scientific results reported in this article are based on data obtained from the Chandra Data Archive. This research has also made use of software provided by the Chandra X-ray Center (CXC) in the application packages CIAO and Sherpa.

Funding for the Sloan Digital Sky Survey IV has been provided by the Alfred P. Sloan Foundation, the U.S. Department of Energy Office of Science, and the Participating Institutions. SDSS-IV acknowledges support and resources from the Center for High-Performance Computing at the University of Utah. The SDSS website is `www.sdss.org`.

SDSS-IV is managed by the Astrophysical Research Consortium for the Participating Institutions of the SDSS Collaboration including the Brazilian Participation Group, the Carnegie Institution for Science, Carnegie Mellon University, the Chilean Participation Group, the French Participation Group, Harvard-Smithsonian Center for Astrophysics, Instituto de Astrofísica de Canarias, The Johns Hopkins University, Kavli Institute for the Physics and Mathematics of the Universe (IPMU)/ University of Tokyo, the Korean Participation Group, Lawrence Berkeley National Laboratory, Leibniz Institut für Astrophysik Potsdam (AIP), Max-Planck-Institut für Astronomie (MPIA Heidelberg), Max-Planck-Institut für Astrophysik (MPA Garching), Max-Planck-Institut für Extraterrestrische Physik (MPE), National Astronomical Observatories of China, New Mexico State University, New York University, University of Notre Dame, Observatário Nacional/MCTI, The Ohio State University, Pennsylvania State University, Shanghai Astronomical Observatory, United Kingdom Participation Group, Universidad Nacional Autónoma de México, University of Arizona, University of Colorado Boulder, University of Oxford, University of Portsmouth, University of Utah, University of Virginia, University of Washington, University of Wisconsin, Vanderbilt University, and Yale University.

Software: This work was made possible due to a large number of open-source

software packages, including AstroPy (Astropy Collaboration et al., 2013), Colossus (Diemer, 2017), Matplotlib (Hunter, 2007), NumPy (Walt, Colbert, and Varoquaux, 2011), Pandas (McKinney, 2010), Photutils (Bradley et al., 2016), SciPy (Jones, Oliphant, Peterson, et al., 2001), and Topcat (Taylor, 2005).

Bibliography

Akaike, H. (1974). *IEEE Transactions on Automatic Control* 19.6, pp. 716–723.

Arthur, Jake et al. (2019). *MNRAS* 484.3, pp. 3968–3983.

Astropy Collaboration et al. (2013). *A&A* 558, A33, A33.

Bahé, Y. M., I. G. McCarthy, M. L. Balogh, and A. S. Font (2013). *MNRAS* 430, pp. 3017–3031.

Bahé, Yannick M. and Ian G. McCarthy (2015). *MNRAS* 447.1, pp. 969–992.

Balogh, M. L., J. F. Navarro, and S. L. Morris (2000). *ApJ* 540, pp. 113–121.

Bamford, S. P. et al. (2009). *MNRAS* 393, pp. 1324–1352.

Beers, T. C., K. Flynn, and K. Gebhardt (1990). *AJ* 100, pp. 32–46.

Binney, J. and S. Tremaine (2008). Princeton University Press.

Blanton, M. R. and J. Moustakas (2009). *ARAA* 47, pp. 159–210.

Blanton, M. R. and S. Roweis (2007). *AJ* 133, pp. 734–754.

Boselli, A. and G. Gavazzi (2006). *PASP* 118, pp. 517–559.

Boselli, A. et al. (2014). *A&A* 564, A67, A67.

Bradley, Larry et al. (2016).

Brinchmann, J. et al. (2004). *MNRAS* 351, pp. 1151–1179.

Brown, T. et al. (2015). *MNRAS* 452, pp. 2479–2489.

Brown, Toby et al. (2017). *MNRAS* 466.2, pp. 1275–1289.

Butcher, H. and A. Oemler Jr. (1978). *ApJ* 219, pp. 18–30.

Cameron, E. (2011). *PASA* 28, pp. 128–139.

Cavagnolo, K. W., M. Donahue, G. M. Voit, and M. Sun (2009). *ApJS* 182, pp. 12–32.

Cayatte, V., C. Kotanyi, C. Balkowski, and J. H. van Gorkom (1994). *AJ* 107, pp. 1003–1017.

Cen, R. (2014). *ApJ* 781, 38, p. 38.

Chang, Y.-Y., A. van der Wel, E. da Cunha, and H.-W. Rix (2015). *ApJS* 219, 8, p. 8.

Chung, A., J. H. van Gorkom, J. D. P. Kenney, H. Crowl, and B. Vollmer (2009). *AJ* 138, pp. 1741–1816.

Chung, A., J. H. van Gorkom, J. D. P. Kenney, and B. Vollmer (2007). *ApJl* 659, pp. L115–L119.

Cortese, L. et al. (2010). *A&A* 518, L49, p. L49.

Davé, R., K. Finlator, and B. D. Oppenheimer (2011). *MNRAS* 416, pp. 1354–1376.

Davis, M. and M. J. Geller (1976). *ApJ* 208, pp. 13–19.

De Lucia, G., S. Weinmann, B. M. Poggianti, A. Aragón-Salamanca, and D. Zaritsky (2012). *MNRAS* 423, pp. 1277–1292.

Diemer, B. (2017). *ArXiv e-prints*.

Diemer, B. and A. V. Kravtsov (2015). *ApJ* 799, 108, p. 108.

Dressler, A. (1980). *ApJ* 236, pp. 351–365.

Fabello, S. et al. (2011). *MNRAS* 411, pp. 993–1012.

Fasano, G. et al. (2015). *MNRAS* 449, pp. 3927–3944.

Fillingham, S. P. et al. (2015). *MNRAS* 454, pp. 2039–2049.

Foltz, R. et al. (2018). *ApJ* 866.2, 136, p. 136.

Foreman-Mackey, D., D. W. Hogg, D. Lang, and J. Goodman (2013). *PASP* 125, p. 306.

Gunn, J. E. and J. R. Gott III (1972). *ApJ* 176, p. 1.

Haines, C. P., F. La Barbera, A. Mercurio, P. Merluzzi, and G. Busarello (2006). *ApJL* 647, pp. L21–L24.

Haines, C. P. et al. (2015). *ApJ* 806, 101, p. 101.

Hernquist, L. (1990). *ApJ* 356, pp. 359–364.

Hirschmann, Michaela et al. (2014). *MNRAS* 444.3, pp. 2938–2959.

Hou, A., L. C. Parker, and W. E. Harris (2014). *MNRAS* 442, pp. 406–418.

Hudson, M. J. et al. (2015). *MNRAS* 447, pp. 298–314.

Hunter, J. D. (2007). *Computing In Science & Engineering* 9.3, pp. 90–95.

Ichinohe, Y. et al. (2015). *MNRAS* 448.3, pp. 2971–2986.

Jáchym, P., J. Köppen, J. Palouš, and F. Combes (2009). *A&A* 500, pp. 693–703.

Jaffé, Y. L. et al. (2015). *MNRAS* 448, pp. 1715–1728.

Jaffé, Y. L. et al. (2016). *MNRAS* 461, pp. 1202–1221.

Jaffé, Y. L. et al. (2018). *MNRAS*.

Jones, Eric, Travis Oliphant, Pearu Peterson, et al. (2001).

Joshi, G. D., L. C. Parker, and J. Wadsley (2016). *MNRAS* 462, pp. 761–777.

Joshi, Gandhali D., Laura C. Parker, James Wadsley, and Benjamin W. Keller (2019). *MNRAS* 483.1, pp. 235–248.

Kafle, P. R. et al. (2016). *MNRAS* 463.4, pp. 4194–4209.

Kalberla, P. M. W. et al. (2005). *A&A* 440, pp. 775–782.

Kalberla, Peter M. W. and Jürgen Kerp (2009). *ARAA* 47.1, pp. 27–61.

Kenney, J. D. P., A. Abramson, and H. Bravo-Alfaro (2015). *AJ* 150, 59, p. 59.

Kenney, J. D. P., J. H. van Gorkom, and B. Vollmer (2004). *AJ* 127, pp. 3361–3374.

Kenney, J. D. P. and J. S. Young (1989). *ApJ* 344, pp. 171–199.

Kennicutt, Robert C. and Neal J. Evans (2012). *ARAA* 50, pp. 531–608.

Kimm, T. et al. (2009). *MNRAS* 394, pp. 1131–1147.

Larson, R. B., B. M. Tinsley, and C. N. Caldwell (1980). *ApJ* 237, pp. 692–707.

Lotz, Marcel, Rhea-Silvia Remus, Klaus Dolag, Andrea Biviano, and Andreas Burkert (2019). *MNRAS* 488.4, pp. 5370–5389.

Lu, T., D. G. Gilbank, S. L. McGee, M. L. Balogh, and S. Gallagher (2012). *MNRAS* 420, pp. 126–140.

Mahajan, S., G. A. Mamon, and S. Raychaudhury (2011). *MNRAS* 416, pp. 2882–2902.

Maier, C., M. Hayashi, B. L. Ziegler, and T. Kodama (2019). *A&A* 626, A14, A14.

Mayer, L., C. Mastropietro, J. Wadsley, J. Stadel, and B. Moore (2006). *MNRAS* 369, pp. 1021–1038.

McGee, S. L., M. L. Balogh, R. G. Bower, A. S. Font, and I. G. McCarthy (2009). *MNRAS* 400, pp. 937–950.

McKinney, Wes (2010). *Proceedings of the 9th Python in Science Conference*. Ed. by Stéfan van der Walt and Jarrod Millman, pp. 51–56.

Mendel, J. T., L. Simard, M. Palmer, S. L. Ellison, and D. R. Patton (2014). *ApJS* 210, 3, p. 3.

Mihos, J. C. and L. Hernquist (1994a). *ApJl* 425, pp. L13–L16.

— (1994b). *ApJl* 431, pp. L9–L12.

Mistani, P. A. et al. (2016). *MNRAS* 455, pp. 2323–2336.

Moore, B., N. Katz, G. Lake, A. Dressler, and A. Oemler (1996). *Nature* 379, pp. 613–616.

Morandi, A., M. Sun, W. Forman, and C. Jones (2015). *MNRAS* 450, pp. 2261–2278.

Morandi, Andrea and Wei Cui (2014). *MNRAS* 437.2, pp. 1909–1917.

Muzzin, A. et al. (2012). *ApJ* 746, 188, p. 188.

Muzzin, A. et al. (2014). *ApJ* 796, 65, p. 65.

Nurgaliev, D. et al. (2017). *ApJ* 841, 5, p. 5.

O'Brien, J. C., K. C. Freeman, and P. C. van der Kruit (2010). *A&A* 515, A62, A62.

Oemler Jr., A. (1974). *ApJ* 194, pp. 1–20.

Oman, K. A., M. J. Hudson, and P. S. Behroozi (2013). *MNRAS* 431, pp. 2307–2316.

Peng, Y.-j. et al. (2010). *ApJ* 721, pp. 193–221.

Peng, Y., R. Maiolino, and R. Cochrane (2015). *Nature* 521, pp. 192–195.

Poggianti, B. M. et al. (2017). *ApJ* 844, 48, p. 48.

Popping, G., R. S. Somerville, and S. C. Trager (2014). *MNRAS* 442, pp. 2398–2418.

Postman, M. and M. J. Geller (1984). *ApJ* 281, pp. 95–99.

Postman, M. et al. (2005). *ApJ* 623, pp. 721–741.

Prescott, M. et al. (2011). *MNRAS* 417, pp. 1374–1386.

Quilis, V., B. Moore, and R. Bower (2000). *Science* 288, pp. 1617–1620.

Rasmussen, J., T. J. Ponman, L. Verdes-Montenegro, M. S. Yun, and S. Borthakur (2008). *MNRAS* 388, pp. 1245–1264.

Rasmussen, J. et al. (2012). *ApJ* 757, 122, p. 122.

Roberts, I. D. and L. C. Parker (2017). *MNRAS* 467, pp. 3268–3278.

Roberts, I. D., L. C. Parker, and J. Hlavacek-Larrondo (2018). *MNRAS* 475, pp. 4704–4716.

Roberts, I. D., L. C. Parker, G. D. Joshi, and F. A. Evans (2015). *MNRAS* 448, pp. L1–L5.

Rodriguez Wimberly, M. K. et al. (2019). *MNRAS* 483.3, pp. 4031–4039.

Roediger, E. and G. Hensler (2005). *A&A* 433, pp. 875–895.

Russell, H. R., J. S. Sanders, and A. C. Fabian (2008). *MNRAS* 390, pp. 1207–1216.

Saintonge, A. et al. (2017). *ApJS* 233, 22, p. 22.

Salim, S. et al. (2007). *ApJS* 173, pp. 267–292.

Salim, S. et al. (2016). *ApJS* 227, 2, p. 2.

Salim, Samir, Médéric Boquien, and Janice C. Lee (2018). *ApJ* 859.1, 11, p. 11.

Sanders, J. S. and A. C. Fabian (2007). *MNRAS* 381, pp. 1381–1399.

Simard, L., J. T. Mendel, D. R. Patton, S. L. Ellison, and A. W. McConnachie (2011). *ApJS* 196, 11, p. 11.

Springel, V. et al. (2005). *Nature* 435, pp. 629–636.

Steinhauser, D., S. Schindler, and V. Springel (2016). *ArXiv e-prints*.

Taylor, M. B. (2005). *Astronomical Data Analysis Software and Systems XIV*. Ed. by P. Shopbell, M. Britton, and R. Ebert. Vol. 347. Astronomical Society of the Pacific Conference Series, p. 29.

Tinker, J. et al. (2008). *ApJ* 688, 709-728, pp. 709–728.

van der Burg, Remco F. J. et al. (2018). *A&A* 618, A140, A140.

von der Linden, A., V. Wild, G. Kauffmann, S. D. M. White, and S. Weinmann (2010). *MNRAS* 404, pp. 1231–1246.

Walker, S. A., A. C. Fabian, J. S. Sanders, A. Simionescu, and Y. Tawara (2013). *MNRAS* 432.1, pp. 554–569.

Walt, S. van der, S. C. Colbert, and G. Varoquaux (2011). *Computing in Science Engineering* 13.2, pp. 22–30.

Wang, J. et al. (2014a). *MNRAS* 441, pp. 2159–2172.

Wang, L. et al. (2014b). *MNRAS* 439, pp. 611–622.

Wetzel, A. R., J. L. Tinker, and C. Conroy (2012). *MNRAS* 424, pp. 232–243.

Wetzel, A. R., J. L. Tinker, C. Conroy, and F. C. van den Bosch (2013). *MNRAS* 432, pp. 336–358.

Wetzel, A. R., E. J. Tollerud, and D. R. Weisz (2015). *ApJL* 808, L27, p. L27.

Wilman, D. J. and P. Erwin (2012). *ApJ* 746, 160, p. 160.

Yang, X., H. J. Mo, F. C. van den Bosch, and Y. P. Jing (2005). *MNRAS* 356, pp. 1293–1307.

Yang, X. et al. (2007). *ApJ* 671, pp. 153–170.

Yun, Kiyun et al. (2019). *MNRAS* 483, pp. 1042–1066.

5.A Appendix: Ram Pressure Model Assumptions and Considerations

The ram pressure model described in the manuscript makes a number of simplifying assumptions. Below we highlight and briefly discuss the primary assumptions that went in to the ram pressure model.

1. Both the spectral deprojection software and the fact that we fit to azimuthally averaged density profiles assume that the clusters in the sample are spherically symmetric. The majority of clusters in this sample do indeed show relaxed, symmetric X-ray morphologies, and when we exclude the 5 of the 24 clusters (containing $\sim 15\%$ of the low-mass galaxy sample) with clear signs of disturbed morphologies, we find that the observed trends are unchanged.

2. We assume that the fits to the cluster density profile are valid out to the virial radius. Previous work (Morandi et al., 2015) has shown that ICM density profiles for galaxy clusters tend to steepen beyond R_{500}, therefore we may be overestimating the local ICM density for galaxies at $R > R_{500}$. We address this point in detail in Section 5.6.3.

3. We assume that the atomic gas component is distributed in an exponential disk. While this is a common assumption, previous work has suggested that HI profiles may in fact flatten at small radii (Wang et al., 2014b) and flare at large radii (Kalberla and Kerp, 2009; O'Brien, Freeman, and van der Kruit, 2010). We employ an exponential profile because it is easier to construct the analytic surface density given disk masses and scale lengths, but this is at the cost of a more realistic atomic gas distribution.

4. By assigning "pre-infall" gas masses (atomic and molecular) based on $z \approx 0$ observations, we are assuming that the gas fractions for low-mass isolated galaxies at $z \approx 0$ are representative of typical gas fractions at the redshift of infall. Detailed observations of total gas content for large samples of galaxies out to high redshift are not currently feasible, but semianalytic work has found no strong evolution in the $f_{\rm gas} - M_\star$ relationship out to at

least $z \sim 0.5 - 1$ (Popping, Somerville, and Trager, 2014), and the lookback time to these redshifts are well in excess of typical crossing times for clusters in our sample.

5. We assume that galaxies have not undergone significant stellar stripping since infall, consistent with simulations, which show that stellar mass loss after infall is only a minor effect for cluster galaxies (Mistani et al., 2016; Joshi et al., 2019).

6. We assume that the present-day structural properties (i.e., the outputs of the bulge+disk decompositions) of the galaxies have not evolved since infall. Given that the fraction of bulge-dominated galaxies is enhanced in dense clusters (e.g. Wilman and Erwin, 2012), the galaxies in our sample may have had lower bulge-to-total ratios at infall. If this were true, our ram pressure model would overestimate the bulge contribution to the restoring potential of the galaxy.

7. We assume that galaxies interact with the ICM face-on, leading to the maximum ram pressure efficiency. In reality, inclined interactions will reduce the efficiency of stripping, in particular for near edge-on interactions (Jáchym et al., 2009). This means that our model overestimates the amount of stripping in this respect, but the edge-on interactions where this effect plays a significant role are relatively rare.

8. We assume that satellite galaxies are quenched exclusively on their first infall. While some infalling satellites will certainly survive over multiple orbits, in particular those on tangential orbits, simulations suggest that most cluster satellites are indeed quenched during first infall (e.g. Lotz et al., 2019).

6 | Ram pressure stripping candidates in the Coma Cluster: Evidence for enhanced star formation

This chapter represents an unchanged version of the paper, *Ram Pressure Stripping Candidates in the Coma Cluster: Evidence for Enhanced Star Formation*, published in the refereed journal, *Monthly Notices of the Royal Astronomical Society*. The full reference is given below:

Roberts I.D., Parker L.C., 2020, MNRAS, Volume 495, Issue 1, pp. 554-569

Department of Physics & Astronomy, McMaster University, Hamilton ON L8S 4M1

Abstract

The Coma cluster is the nearest massive ($M \gtrsim 10^{15}\,\mathrm{M}_{\odot}$) galaxy cluster, making it an excellent laboratory to probe the influence of the cluster environment on galaxy star formation. Here, we present a sample of 41 galaxies with disturbed morphologies consistent with ram pressure stripping. These galaxies are identified visually with high-quality, multi-band imaging from the Canada-France-Hawaii telescope covering $\sim 9\,\mathrm{deg}^2$ of the Coma cluster. These "stripping candidates" are clear outliers in common quantitative morphological measures, such as concentration-asymmetry and Gini-M_{20}, confirming their disturbed nature. Based on the orientations of observed asymmetries, as well as the galaxy positions in projected phase-space, these candidates are consistent with galaxies being stripped shortly after infall onto the Coma cluster. Finally, the stripping candidates show enhanced star formation rates, both relative to "normal" star-forming Coma galaxies and isolated galaxies in the field. Ram pressure is likely driving an enhancement in star formation during the stripping phase, prior to quenching. On the whole, ram pressure stripping appears to be ubiquitous across all regions of the Coma cluster.

6.1 Introduction

Galaxy properties in the local Universe display a persistent bimodality. The vast majority of local galaxies are either (1) galaxies that have blue colours, are gas-rich, are actively star-forming, and have late-type morphologies; or (2) galaxies that have red colours, are gas-poor, show little-to-no ongoing star formation, and have early-type morphologies. Conventional thinking suggests that these two populations of galaxies represent different points along an evolutionary sequence, with blue, star-forming galaxies (blue cloud) evolving into red, passive galaxies (red sequence). Galaxies that exhibit properties intermediate to the blue cloud and red sequence (known as the "green valley") are often considered transition galaxies currently experiencing star formation quenching (e.g. Salim, 2014). The fact that the green valley is sparsely populated relative to the blue cloud and red sequence, suggests that this transition (quenching) is likely quite rapid. This model works on average, but there are many nuances and exceptions that complicate this simple picture. Some galaxies may transit from the red sequence on to the blue cloud, as opposed to the other direction, due to star formation being rejuvenated (e.g. Clemens et al., 2009; Chauke et al., 2019). Additionally, star formation rates (SFRs) for passive galaxies are often upper limits, which introduces substantial uncertainties in star formation properties for galaxies off the main sequence.

Understanding the physical mechanisms that are driving this star formation quenching requires large, diverse samples of galaxies that span wide ranges in stellar mass and local environment. For example, the fraction of quiescent galaxies depends strongly on stellar mass such that higher mass galaxies are increasingly quiescent, whereas low-mass galaxies are far more likely to be star-forming (e.g. Peng et al., 2010; Geha et al., 2012; Wetzel, Tinker, and Conroy, 2012). The origin of this trend with stellar mass is often ascribed to processes internal to the galaxy such as feedback from supernovae or AGN as well as the high virial temperature of massive galaxy haloes impeding the cooling of gas (e.g. Dekel and Birnboim, 2006; Schawinski et al., 2009). These trends with stellar mass are well established, but, even at fixed stellar mass, galaxy star formation shows a clear trend with local environment (e.g. Wetzel, Tinker, and Conroy, 2012). For example, quiescent fractions scale with halo mass such that galaxies residing in massive clusters are

preferentially quenched compared to field galaxies of the same mass. Even within individual clusters a clear environmental dependence is present, as galaxy populations in the central cluster region are dominated by quiescent galaxies relative to the cluster outskirts (e.g. Postman et al., 2005; Blanton and Roweis, 2007; Prescott et al., 2011; Rasmussen et al., 2012; Fasano et al., 2015; Haines et al., 2015). The balance between internally and externally driven quenching is also a clear function of galaxy mass, with low-mass galaxies ($\log M_{\rm star} \lesssim 10 - 10.5\,{\rm M}_{\odot}$) being significantly more quenched by environment, whereas quenching higher mass galaxies is more strongly associated with internal processes (e.g. Haines et al., 2006; Bamford et al., 2009; Peng et al., 2010).

Galaxy clusters represent the most massive virialized objects in the local Universe, making them the ideal place to probe environmentally driven galaxy evolution. These extreme environments are capable of rapidly shutting down star formation (e.g. Wetzel, Tinker, and Conroy, 2012; Haines et al., 2015; Brown et al., 2017; Roberts et al., 2019) in member galaxies. Many physical mechanisms have been proposed for quenching star formation in galaxy clusters, which can be roughly divided into two classes: (1) interactions between galaxies and the hot, X-ray emitting intracluster medium (ICM) permeating the cluster; and (2) dynamical interactions between cluster galaxies or between galaxies and the cluster halo. Examples belonging to the first category include ram pressure stripping (e.g. Gunn and Gott, 1972; Quilis, Moore, and Bower, 2000), viscous stripping (Nulsen, 1982), and starvation/strangulation (e.g. Larson, Tinsley, and Caldwell, 1980; Peng, Maiolino, and Cochrane, 2015); whereas examples of dynamical interactions include mergers (e.g. Mihos and Hernquist, 1994a; Mihos and Hernquist, 1994b), harassment (e.g. Moore et al., 1996), and tidal interactions (e.g. Mayer et al., 2006; Chung et al., 2007). While all of these mechanisms are capable of affecting cluster galaxies, the key question is which are the primary mechanisms driving quenching and does the dominant mechanism change with halo mass?

Recently, ram pressure stripping and starvation have been favoured for driving quenching in groups and clusters (e.g. Muzzin et al., 2014; Fillingham et al., 2015; Peng, Maiolino, and Cochrane, 2015; Wetzel, Tollerud, and Weisz, 2015; Brown et al., 2017; Foltz et al., 2018; van der Burg et al., 2018; Roberts et al., 2019). Ram pressure stripping involves the direct removal of cold-gas from galactic discs as

galaxies traverse the ICM at high speeds. Signatures of ram pressure stripping include tails of stripped gas or stars trailing behind galaxies in clusters (McPartland et al., 2016; Poggianti et al., 2017), as well as star-forming discs that appear truncated from the outside-in (Schaefer et al., 2017; Finn et al., 2018; Schaefer et al., 2019). On the other hand, starvation is the removal of the gas reservoir for future star formation. This can occur due to the high virial temperature of the cluster preventing hot halo gas from cooling and condensing on to galactic discs, or by the removal of this halo gas from galaxies through stripping. Evidence for starvation can be inferred from galaxy metallicities (Peng, Maiolino, and Cochrane, 2015), from measurements of galaxy's hot gas haloes (Wagner, McDonald, and Courteau, 2018), or indirectly through estimates of quenching times (e.g. Taranu et al., 2014). The relevant time-scale for quenching via starvation is the gas depletion time of a galaxy's present-day cold-gas reserves (since once this gas is consumed it will not be replenished), which is on the order of $\sim 1 - 3\,\mathrm{Gyr}$ (Saintonge et al., 2017). Of course, it is likely that both ram pressure and starvation are acting in concert. Observational studies have argued that starvation may drive an initial reduction in star formation with ram pressure "finishing the job" as galaxies approach the dense cluster centre (van der Burg et al., 2018; Roberts et al., 2019).

One technique for discriminating between quenching mechanisms is to study resolved properties of star formation within individual galaxies. Ram pressure stripping preferentially removes gas from the outskirts of the galaxy where the gas is more loosely bound, which results in outside-in quenching. Radio interferometers provide resolved maps of atomic and molecular hydrogen in galaxies and optical integral field unit (IFU) spectrographs provide resolved maps of common star formation tracers such as Hα emission. With recent large optical IFU surveys such as Mapping Nearby Galaxies at Apache Point Observatory (Bundy et al., 2015), Calar Alto Legacy Integral Field Area survey (Sánchez et al., 2012), and Sydney-AAO Multiobject Integral field spectrograph (Croom et al., 2012), the number of galaxies with resolved Hα spectroscopy has increased rapidly. Some of the galaxies observed by these surveys are located in dense, cluster environments and previous works have studied the resolved Hα properties in galaxy clusters. Some studies have found evidence for outside-in quenching where the Hα profiles decrease rapidly with radius for cluster galaxies (e.g. Schaefer et al., 2017; Schaefer et al.,

2019). Furthermore, the GASP survey has identified many "jellyfish galaxies" in clusters with tails of extended Hα emission (Poggianti et al., 2017). These jellyfish galaxies tend to be located in regions of the cluster where ram pressure forces are expected to be large (Jaffé et al., 2018). Additionally, many galaxies in nearby clusters have been observed to have extended HI tails (e.g. Kenney, van Gorkom, and Vollmer, 2004; Chung et al., 2007; Chung et al., 2009; Kenney, Abramson, and Bravo-Alfaro, 2015). Ram pressure is expected to have a weaker effect on molecular gas (H_2) that is more densely concentrated at the centre of galaxies. The extent to which molecular hydrogen is stripped in galaxy clusters is still an open question (e.g. Vollmer et al., 2012; Jáchym et al., 2019).

Candidates for galaxies undergoing stripping can also be identified with broad-band optical imaging. Imaging in bluer filters in particular can efficiently highlight morphological features associated with ram pressure stripping (McPartland et al., 2016; Poggianti et al., 2016). Follow-up observations of these disturbed cluster galaxies often show prominent ram pressure stripped tails of gas (Poggianti et al., 2017). In this study, we focus on the Coma cluster (Abell 1656), the nearest rich, high-mass galaxy cluster, to constrain the effects of ram pressure stripping on the population of satellite galaxies. We take advantage of high-resolution, archival, multiband imaging from the Canada-France-Hawaii Telescope (CFHT) to identify a sample of galaxies in the Coma cluster that appear to be experiencing stripping. We then explore the observed properties of these "stripping candidates" and compare them to the rest of the Coma satellite population as well as isolated galaxies in the field. The outline of this paper is as follows: in Section 6.2 we describe the Coma and field galaxy datasets, as well as describe the method we use to identify disturbed galaxies, potentially undergoing stripping; in Section 6.3 we compute quantitative morphological parameters for all Coma galaxies in order to compare to our visual classifications; in Section 6.4 we explore the orientation of observed asymmetries in stripping candidates with respect to the cluster centre; in Section 6.5 we consider the position of stripping candidate galaxies in projected phase-space in order to constrain their infall histories; in Section 6.6 we compare star formation rates in stripping candidate galaxies compared to other Coma galaxies and field galaxies; and finally, in Section 6.7 we present the primary conclusions of this work and discuss these results.

This paper assumes a flat Λ cold dark matter cosmology with $\Omega_M = 0.3$, $\Omega_\Lambda = 0.7$, and $H_0 = 70\,\mathrm{km\,s^{-1}\,Mpc^{-1}}$. We assume a redshift for the Coma cluster of $z_{\mathrm{coma}} = 0.024$ and a luminosity distance to the Coma cluster of 105 Mpc.

6.2 Data

6.2.1 Coma Members

We identify spectroscopic members of the Coma cluster with the 12th data release of the Sloan Digital Sky Survey (SDSS DR12; Alam et al. 2015). We consider Coma members to include any galaxies within $1 \times R_{200}$ and $3000\,\mathrm{km\,s^{-1}}$ of the cluster centroid, where R_{200} is the virial radius of 2840 kpc (Kubo et al., 2007). This is a loose membership criterion that may select a small number of galaxies that are not strictly bound to the Coma cluster (in particular at large radius), however, we opt for this approach to ensure that we do not miss galaxies that are just beginning their infall on to the cluster. We use SFRs and stellar masses ($M_\star$) from the medium-deep version of the GSWLC-2 SED fitting catalogue (Salim et al., 2016; Salim, Boquien, and Lee, 2018). These SFRs are derived from UV+optical+mid-IR SED fitting done with the CIGALE[1] code (Boquien et al., 2019). The IR SED is not explicitly fit (as it is not well constrained without far-IR information), instead the total IR luminosity (TIR) is estimated from templates with mid-IR fluxes and this TIR data point is used as a direct constraint in the SED fitting.

We define star-forming galaxies to be all galaxies with $\mathrm{sSFR} > 10^{-11}\,\mathrm{yr^{-1}}$ ($\mathrm{sSFR} = \mathrm{SFR}/M_\star$) and passive galaxies to be all galaxies with $\mathrm{sSFR} \leq 10^{-11}\,\mathrm{yr^{-1}}$. This gives a sample of 296 star-forming Coma members and 388 passive Coma members. We only consider satellite galaxies, and therefore exclude the two central, giant elliptical galaxies in Coma (NGC 4874 and NGC 4889) from our sample. The median stellar mass for star-forming galaxies is $10^{9.1}$ and $10^{10.0}\,\mathrm{M_\odot}$ for passive galaxies. The full range in stellar mass for all satellite galaxies is $M_\star = 10^{8.4} - 10^{11.3}\,\mathrm{M_\odot}$. This sample is stellar mass complete down to roughly $\sim 10^{8.8-9.0}\,\mathrm{M_\odot}$, which means that $\gtrsim 90$ per cent of the satellite galaxy sample is complete. We note that if we restrict our sample to only galaxies with $M_\star > 10^9\,\mathrm{M_\odot}$, all of our conclusions are

[1] `https://cigale.lam.fr/`

unchanged. Finally, we calculate a rest-frame velocity dispersion for our Coma sample with the robust biweight estimator (Beers, Flynn, and Gebhardt, 1990) and only considering the passive galaxy population - which is a better tracer of the cluster potential well (e.g. Biviano et al., 1997; Geller, Diaferio, and Kurtz, 1999). This gives a velocity dispersion of $\sigma_{\rm los} = 930\,{\rm km\,s^{-1}}$, which is similar to previous estimates (e.g. Colless and Dunn, 1996).

6.2.2 Field Galaxies

For comparison, we also compile a sample of field galaxies from the SDSS. We use the field sample described in (Roberts and Parker, 2017), which is derived from $N = 1$ "groups" in the (Yang et al., 2005; Yang et al., 2007) SDSS DR7 group catalogue. This isolated field sample is made up of all $N = 1$ Yang et al. galaxies that are separated from their nearest "bright" neighbour by at least $1\,{\rm Mpc}$ and $1000\,{\rm km\,s^{-1}}$. We restrict the sample to only include galaxies located within $3000\,{\rm km\,s^{-1}}$ of the Coma redshift, and we define a bright neighbour to be any galaxy that is brighter than the SDSS r-band absolute magnitude limit at $z = 0.024$. We also obtain SFRs and stellar masses for the field sample from the medium-deep GSWLC2 catalogue (Salim et al., 2016; Salim, Boquien, and Lee, 2018). These cuts give an isolated field sample consisting of 3575 galaxies that are matched in redshift to the sample of Coma members.

6.2.3 Identifying Stripping Candidates with CFHT Imaging

The primary goal of this work is to study the properties of galaxies potentially undergoing stripping in the Coma cluster. To identify these "stripping candidates", we use high-quality, archival CFHT *ugi* imaging (P.I. Hudson, Run ID 2008AC24) covering Coma out to the virial radius ($\sim 9\,{\rm deg}^2$), with exposure times of 300, 300, and 1360 s, respectively. We use image stacks produced by MEGAPIPE (Gwyn, 2008) that were downloaded from the CADC CFHT Science Archive[2]. The average image quality of the stacks is 0.97, 0.85, and 0.73 arcsec for the u, g, and i bands,

[2] `https://www.cadc-ccda.hia-iha.nrc-cnrc.gc.ca/en/cfht/`

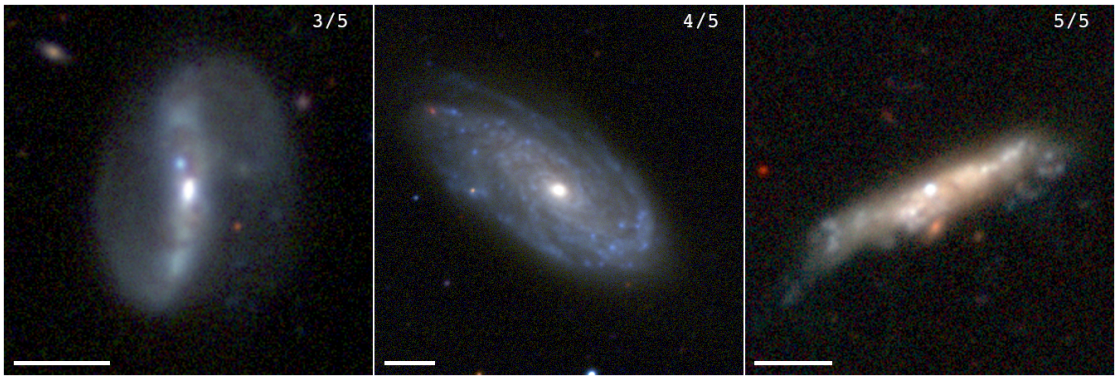

FIGURE 6.1: CFHT *ugi* images for three identified stripping candidates. We show galaxies which received 3/5, 4/5, and 5/5 votes from the classifiers. The scale bar in each image corresponds to a physical size of 5 kpc.

respectively. MEGAPIPE also estimates the 5σ point source detection limit for which the average of the stacks is 26.2, 25.5, and 24.8 mag for the u, g, and i bands, respectively. These magnitude limits are estimated simplistically by finding the faintest point source whose error is 0.198 mag or less. The magnitude error is estimated as

$$\mathrm{mag_{err}} = 2.5\ \log(1 + N/S) \tag{6.1}$$

therefore for $S/N = 5$ this gives

$$\mathrm{mag_{err}} = 2.5\ \log(1.2) = 0.198 \tag{6.2}$$

In practice, this simple method gives magnitude limits that are accurate to $\sim$ 0.3 mag (Gwyn, 2008).

To identify stripping candidates, we visually inspect CFHT three colour *ugi* images for all star-forming Coma member galaxies. Colour cut-out images are made with STIFF[3] (Bertin, 2012) covering a 40×40 kpc box centred on each star-forming galaxy. These images are then visually classified by five experts (including the authors of this work), all of whom are active researchers (see Acknowledgements) studying galaxy evolution with experience identifying galaxies undergoing stripping. The classifiers were all given identical instructions to follow when classifying

[3] `https://www.astromatic.net/software/stiff`

the images. They were instructed to flag any galaxies which exhibited one, or more, of the following features:

1. *The presence of asymmetric tails.* Observed either in u band (blue emission) or in dust (dark red extinction).

2. *Asymmetric star formation.* u-band (blue) emission that is knotty and clearly asymmetric about the galaxy centre.

3. *The presence of bow shocks.* Shock front features may be observed either in u band (blue emission) or in dust (dark red extinction).

4. *Galaxy mergers.* Either obvious mergers based on the presence of two interacting galaxies, or the presence of multiple, bright galaxy nuclei for the case of more evolved mergers.

Galaxies that were flagged as potential mergers by any of the classifiers were then discussed amongst the classifiers at a follow-up meeting. A consensus was reached for each case regarding whether or not clear evidence of a galaxy-galaxy interaction was present. All galaxies deemed to show clear evidence of a galaxy-galaxy interaction were then removed from the sample. The final sample of stripping candidates is defined to include all galaxies flagged as hosting asymmetric tails and/or asymmetric star formation and/or shock features by a majority of the classifiers (i.e. at least 3/5 classifiers). This process results in 41 galaxies identified as stripping candidates out of a parent sample of 296 star-forming Coma members. In the sample of stripping candidates, 17 per cent were identified by 3/5 classifiers, 27 per cent were identified by 4/5 classifiers, and 56 per cent were identified by all classifiers. In Fig 6.1 we show colour images for three example stripping candidates, one identified by 3/5 votes, one identified by 4/5 votes, and one identified by 5/5 votes. The $40 \times 40\,\mathrm{kpc}$ cutouts for all of the stripping candidates, along with a table of basic properties, are shown in Appendix 6.A. Throughout this paper we will consistently refer to four different galaxy subsamples with the following nomenclature: 1. *stripping candidates:* galaxies flagged by a majority of classifiers as potentially undergoing stripping, 2. *star-forming Coma galaxies:* all star-forming Coma member galaxies ($\log \mathrm{sSFR} > -11$) not in the stripping

candidate sample, 3. *passive Coma galaxies:* all passive Coma member galaxies, 4. *field galaxies:* galaxies in the isolated field sample. The galaxies in the three Coma samples were visually inspected, and all merging/interacting galaxies were removed from the samples.

We emphasize that some of our stripping candidates have been previously identified as galaxies undergoing stripping (e.g. Yagi et al., 2007; Smith et al., 2010; Yagi et al., 2010; Yoshida et al., 2012; Gavazzi et al., 2018; Cramer et al., 2019a). We identify 8/13 galaxies with UV tails from Smith et al. (2010) as stripping candidates in this work. Of the remaining five, we flagged one as a potential post-merger (GMP 4555), two do not have SDSS spectroscopic redshifts (GMP 3016, GMP 4232), and two have SDSS DR12 redshifts inconsistent with the Coma Cluster, which prevented them from making it into our initial sample (GMP 2640, GMP 4060). We identify 6/14 galaxies with Hα tails from Yagi et al. (2010) as stripping candidates. Of the remaining eight, five are in our Coma sample but were not identified as stripping candidates (GMP 2923, GMP 3071, GMP 3896, GMP 4017, GMP 4156) – highlighting the fact that galaxies with Hα tails can have relatively undisturbed broad-band morphologies, two are lacking SDSS redshifts (GMP 3016, GMP 4232), and one has an SDSS DR12 redshift inconsistent with the Coma Cluster (GMP 4060). Most previous studies have focused on the core of the Coma Cluster, therefore it is in that region where there is the most overlap with previous studies. Even with this overlap, the majority of galaxies in this paper are newly identified ram pressure stripping candidates.

6.3 Quantitative Measures of Morphology

In Section 6.2 we described our procedure for visually identifying galaxies potentially undergoing stripping. Visual classifications have their advantages when it comes to identifying specific morphological features associated with stripping, but these classifications are inherently qualitative in nature. In this section we compute commonly used morphological measures, such as concentration-asymmetry and Gini-M20, in order to more quantitatively compare the morphologies of galaxies in this sample. The high-quality CFHT images enable us to determine and

compare quantitative morphologies between passive Coma members, star-forming Coma members, and stripping candidates.

6.3.1 Creating Segmentation Maps

A challenge when computing morphological parameters is determining which pixels to include from the galaxy image. This is particularly difficult in dense, low redshift galaxy clusters where fields are often crowded by other cluster galaxies as well as background sources. When computing morphologies we want to ensure, as much as possible, that we are only including pixels which are associated with the galaxy of interest. To do this we create segmentation maps beginning with the $40 \times 40\,\mathrm{kpc}$ cutouts centred on each galaxy from the CFHT imaging of the Coma cluster. We then perform source detection on each cutout with the `detect_threshold` and `detect_sources` functions from the PYTHON package PHOTUTILS[4]. We require that all source pixels be at least 2σ above the background level, where for each cutout a scalar background is estimated with sigma-clipped statistics. We then generate a "first-pass" segmentation map for each cutout, requiring that all sources have at least five connected pixels above the background threshold. For the majority of galaxies in our sample, this first-pass segmentation map provides an accurate description of the pixels associated with a given galaxy of interest. However, a fraction of the identified stripping candidates show trails of stripped debris that can be physically separated from the main galaxy. In this case, the image segmentation identifies this detached stripped material as sources separate from the main galaxy. Since we are interested in describing the morphologies of galaxies undergoing stripping, it is important to include this material in the morphological calculations. Therefore, for each stripping candidate, the first-pass segmentation map is visually inspected next to the *ugi* thumbnail of the same galaxy. With the colour image as a reference, the first-pass segmentation maps are updated such that any distinct sources which appear to be stripped material are now given the same value as the main galaxy in the segmentation map. Visual inspection showed that this amendment to the first-pass segmentation map was necessary for 13/41 stripping candidates. These updated segmentation maps are

[4] `https://photutils.readthedocs.io/en/stable/`

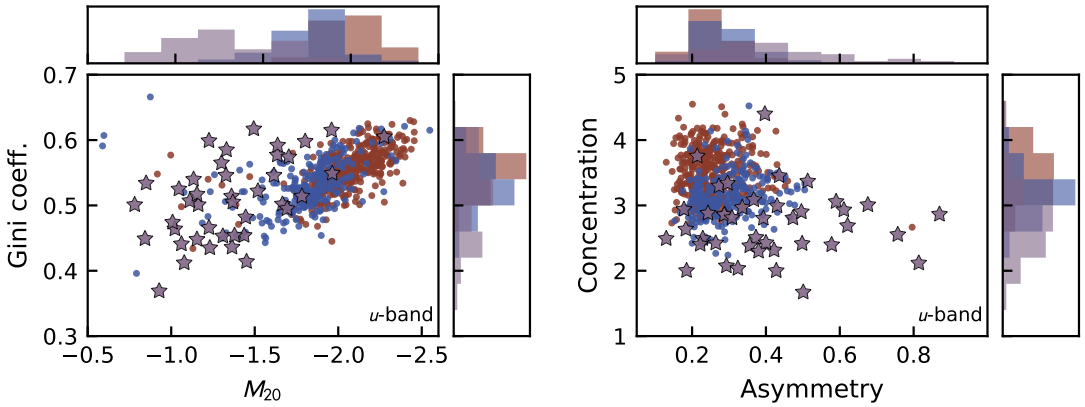

FIGURE 6.2: u-band Gini-M_{20} diagram (left) and Concentration-Asymmetry diagram (right), for passive Coma galaxies (red), non-stripping star-forming galaxies (blue), and stripping candidates (purple). Marginal distributions for each of the axes are shown with histograms.

then used to compute morphological parameters for the stripping candidates. For the non-stripping galaxies, any mergers were identified and removed from the sample and for the remaining galaxies we find that the first pass segmentation maps were all sufficient. We note that the qualitative results (Fig. 6.2) are unchanged when using first-pass segmentation maps for all of the stripping candidates instead of the segmentation maps which were updated manually.

6.3.2 Morphology Diagnostics

For all galaxies we compute a number of quantitative morphological parameters: the "shape asymmetry" and concentration, as well as the Gini coefficient and M_{20}. Below we give a brief description of these morphological measures, but for a more detailed description please see the original papers (Abraham, van den Bergh, and Nair, 2003; Lotz, Primack, and Madau, 2004; Conselice, 2003; Conselice, 2014; Pawlik et al., 2016). We use the PYTHON package STATMORPH to compute all quantitative morphological parameters, for a full description of the implementation please see Rodriguez-Gomez et al. (2019).

Asymmetry

We use the shape asymmetry (A_S) from Pawlik et al. (2016) as our quantitative measure of asymmetry. The shape asymmetry is similar to the asymmetry index from the Concentration-Asymmetry-Clumpiness (CAS) system (Conselice, 2003; Conselice, 2014), but it is computed on a binary detection map (segmentation map) instead of the galaxy image. The shape asymmetry is equivalent to a version of the CAS asymmetry which is not flux-weighted, and because of this, the shape asymmetry increases the sensitivity to low surface brightness features. Because stripped galaxies often show low surface brightness tails or asymmetries we opt to use the shape asymmetry in this work, but we note that all of the qualitative morphological trends that we report are unchanged when using the standard flux-weighted CAS asymmetry as opposed to the shape asymmetry. The shape asymmetry is computed as

$$A_S = \min\left(\frac{\sum |X_0 - X_{180}|}{\sum |X_0|}\right) \tag{6.3}$$

where X_0 corresponds to the binary detection map and X_{180} corresponds to the binary detection map rotated by 180°. The rotation is done about the pixel which minimizes the standard (flux-weighted) asymmetry.

The binary detection map used to compute the shape asymmetry is generated as described in Rodriguez-Gomez et al. (2019). Briefly, a background level is first estimated over a circular annulus with inner and outer annuli of two and four times the Petrosian semimajor axis. Then, a 1σ brightness threshold is defined and the galaxy image is smoothed with a 3×3 boxcar (mean) filter. The binary detection mask is then given by the contiguous group of pixels above the threshold that includes the brightest pixel in the galaxy image. All following references to asymmetry will be referring to the shape asymmetry described above.

Concentration

The concentration parameter is defined as (Conselice, 2003; Conselice, 2014)

$$C = 5 \log\left(\frac{r_{80}}{r_{20}}\right), \tag{6.4}$$

where r_{80} is the radius containing 80 per cent of a galaxy's light and r_{20} is the radius containing 20 per cent of a galaxy's light. The total flux for each galaxy is taken to be the flux contained within $1.5\,r_{\rm petro}$ of the galaxy centroid.

Gini Coefficient

The Gini coefficient originates from economics as a measure to quantify the distribution of wealth over a population. However, it can also be applied to astronomical imaging data to quantify the homogeneity of flux distributed across galaxy pixels (Abraham, van den Bergh, and Nair, 2003; Lotz, Primack, and Madau, 2004). The Gini coefficient is computed as (Glasser, 1962)

$$G = \frac{1}{\bar{X}n(n-1)} \sum_{i=1}^{n} (2i - n - 1) X_i \tag{6.5}$$

where $i = 1, 2, 3, ..., n$ for a set of n pixel flux values X_i. A galaxy with all flux concentrated in one pixel corresponds to $G = 1$, and a galaxy with a perfectly uniform flux distribution corresponds to $G = 0$.

M_{20}

The M_{20} statistic (Lotz, Primack, and Madau, 2004) is a measure of the second-order moment of the galaxy image for the brightest 20 per cent of a galaxy's flux, normalized by the second-order moment for the entire galaxy image. M_{20} is particularly sensitive to bright features offset from the galaxy centre. The "total" moment for the entire image is computed as

$$\mu_{\rm tot} = \sum_{i=1}^{N} \mu_i = \sum_{i=1}^{n} f_i[(x_i - x_c)^2 + (y_i - y_c)^2] \tag{6.6}$$

where x_i, y_i are the coordinates of the ith pixel, f_i is the flux in the ith pixel, and x_c, y_c are the central coordinates which minimize the total moment, $\mu_{\rm tot}$. To compute M_{20}, galaxy pixels are rank-ordered by flux and μ_i is summed over the brightest pixels until the cumulative flux equals 20 per cent of the total flux. This

parameter is then normalized by the total moment, $\mu_{\rm tot}$

$$M_{20} = \log\left(\frac{\sum_i \mu_i}{\mu_{\rm tot}}\right), \text{ while } \sum_i f_i < 0.2\, f_{\rm tot}, \tag{6.7}$$

where $f_{\rm tot}$ is the total flux of the pixels identified by the segmentation map.

In Fig. 6.2 we plot Coma member galaxies (passive: red, star-forming: blue, visual stripping candidates from Section 6.2.3: purple) on the Gini-M20 (left) and concentration-asymmetry (right) diagrams with the calculated morphological parameters. In both cases there is a clear separation between the star-forming/passive Coma galaxies and the stripping candidates. For each panel in Fig. 6.2 we also include 1D histograms corresponding to each axis. Stripping candidates have lower Gini coefficients, less-negative values of M_{20}, lower concentrations, and larger asymmetries compared to other Coma galaxies. The separation between star-forming/passive Coma galaxies and stripping candidates is largest when considering M_{20} or asymmetry. Stripping candidates were selected based on visible signs of asymmetric star formation, asymmetric tails, and shock-front features, therefore it is unsurprising that they show preferentially large measured asymmetries; but it is a reassuring confirmation of the visual classifications. The values of M_{20} for stripping candidates are consistent with a relatively diffuse population of galaxies, which is in turn confirmed by the low concentrations. Furthermore, the fact that M_{20} values for stripping candidates are closer to zero may be driven in part by bright features offset from the galaxy centre in stripping candidates, such as shock fronts or stripped tails/knots of star formation. McPartland et al. (2016) have performed a similar morphological analysis of galaxies undergoing stripping with *HST* observations at intermediate redshift ($z = 0.3 - 0.7$), finding that ram pressure stripping candidates at intermediate redshift occupy distinct regions in the $G - M_{20}$ and $C - A$ planes. Here we find that the morphological results from McPartland et al. (2016) at $z = 0.3 - 0.7$ are consistent with these results from ground-based imaging at low redshift.

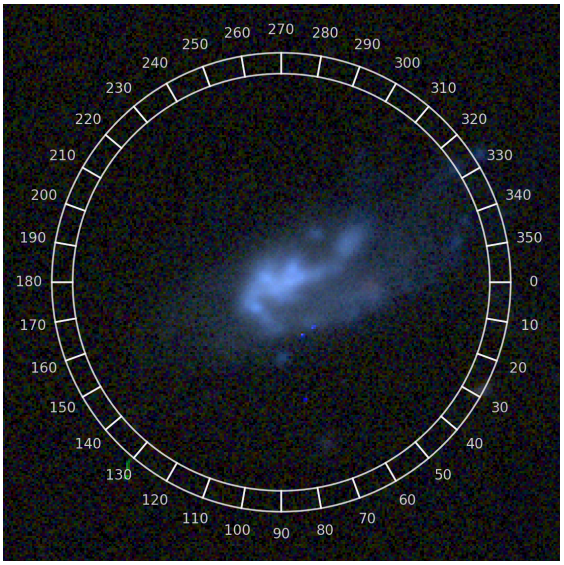

FIGURE 6.3: Example of *ugi* thumbnail with angular guide overlaid in order to determine orientation of observed stripping features.

6.4 Orientation of Stripping Features

A key signature of ram pressure stripping is tails of gas and/or stars trailing behind galaxies opposite to the direction of motion. These ram pressure tails have been observed extensively in cluster galaxies across the electromagnetic spectrum (e.g. Kenney, van Gorkom, and Vollmer, 2004; Smith et al., 2010; Jáchym et al., 2014; Poggianti et al., 2017; Cramer et al., 2019b). Simulations and observations show that galaxies infall onto clusters on largely radial orbits (e.g. Wetzel, 2011; Biviano et al., 2013; Lotz et al., 2019), meaning that tails pointing towards or away from the cluster centre are expected for galaxies undergoing strong stripping. Tails pointing away from the cluster centre indicate galaxies infalling towards the cluster centre; conversely tails pointing towards the cluster centre are suggestive of galaxies "backsplashing" away from the cluster centre after a pericentric passage.

For candidates identified as undergoing stripping, we visually estimate the direction of the stripping features relative to the galaxy centre. In Fig. 6.3 we show an example of a thumbnail used to determine the orientation of the stripping features. These are the same thumbnails used for visual classifications, but now a

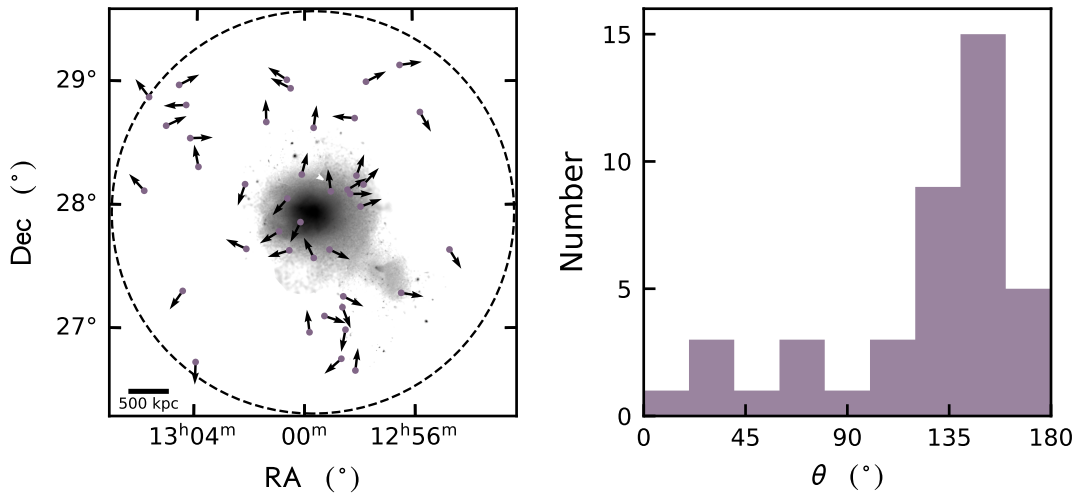

FIGURE 6.4: *Left:* Vector plot showing the orientation at the identified "stripping features" within the Coma cluster. Each point corresponds to a stripping candidate and the arrow points in the direction of the stripping feature, as estimated by eye (see text). The dashed line marks the virial radius, and in the background grayscale we show an 0.5-7 keV XMM-Newton X-ray image. Note that the XMM-Newton observations only cover the inner $\sim 1000 - 1500$ kpc of Coma. *Right:* Histogram of the angle between the stripping feature direction and the direction toward the cluster centre. A majority of galaxies show angles between $\sim 120°$ and 180°, pointing away from the cluster centre.

guide is overlaid marking angles between 0° and 350°. The orientation of the stripping features is determined by selecting the angle (in multiples of 10°) which is most consistent with the observed features. These angles are determined for each galaxy by the five expert classifiers, and the final "asymmetry angle" is taken to be the average of the five estimates for each galaxy. We note that for galaxies where the identified features are relatively subtle, identifying these orientations can be difficult and subjective. By averaging over five classifiers we help to mitigate these difficulties, but some level of subjectivity will persist. For more than half of the cases, there was very good agreement (little-to-no scatter) in the angle estimates. If we only consider galaxies where the selected angles were relatively consistent between the classifiers (i.e. $\sigma/\sqrt{N}$ errors $<15°$), the qualitative results presented below are unchanged compared to using the entire sample. For the example shown in Fig. 6.3, an average angle of 336° was determined through this process. For each thumbnail in Appendix 6.A, we overlay an arrow showing the orientation of the stripping features for each galaxy.

In Fig. 6.4 (left) we show the spatial distribution of stripping candidates within the Coma cluster. The plotted vectors point in the direction of the observed ram pressure features. In the background we plot a 0.5-7 keV X-ray image of the Coma Cluster from *XMM-Newton*, where the main Coma X-ray peak, as well as the secondary peak corresponding to the infalling NGC 4839 group, are both visible. The X-ray data were reduced, imaged, and mosaiced following the standard procedure outlined in the *XMM-Newton* ESAS cookbook[5] (see Roberts, Parker, and Hlavacek-Larrondo 2018 for a detailed description of the reduction process). It is clear by eye that the majority of the vectors are pointing away from the cluster centre, which is consistent with the majority of these galaxies being stripped during infall toward the cluster centre. With these estimated directions, we compute the angle between the direction of the stripping feature and the centre of the cluster. An angle of 0° corresponds to a tail pointing directly toward the cluster centre, and an angle of 180° corresponds to a tail pointing directly away from the cluster centre. In Fig. 6.4 (right) we show a histogram of the angle between the stripping feature and the cluster centre. The majority of stripping galaxies have angles between 120° and 180°. Naively, if these morphological features were not associated with

[5] `https://heasarc.gsfc.nasa.gov/docs/xmm/esas/cookbook/xmm-esas.html`

ram pressure then we would expect to see a uniform distribution of angles instead of the clearly preferred angles seen in Fig. 6.4. For satellites on perfectly radial orbits, ram pressure features should be oriented at angles to the cluster centre of 0° or 180°. While simulations predict that satellites infall on largely radial orbits (e.g. Wetzel, 2011), perfectly radial orbits are an overly simplistic assumption and most galaxy orbits have a non-negligible tangential component (e.g. Biviano et al., 2013). Both variations in orbits and projection effects make it difficult to interpret the observed tail directions. Some ram pressure studies have found strongly peaked distributions of angles (e.g. Chung et al., 2007; Smith et al., 2010), while others have found more random distributions (e.g. McPartland et al., 2016; Poggianti et al., 2016). In a simplistic picture, the distribution of angles observed in this work is consistent with expectations from ram pressure stripping, and the fact that we do not observe a peak at precisely 180° is consistent with orbits which are slightly non-radial on average. Orientations measured in projection will always be inherently uncertain, which must be remembered when interpreting the results in Fig. 6.4

6.5 Phase Space Analysis

An observational tool to study the accretion history of galaxy clusters is the projected phase space (PPS) diagram, which plots 1D velocity offset versus projected cluster-centric distance for member galaxies. Galaxy distributions in PPS tend to trace caustics corresponding to escape velocities from the the host cluster halo. At small cluster-centric distance the velocity range is large due to the high escape velocity, whereas at large distance, where the escape velocity is lower, the velocity range narrows. Furthermore, galaxies first infalling onto a galaxy cluster follow distinct orbits in phase space. They are accelerated to large velocity offsets on their first infall toward the cluster centre, and then over the course of multiple orbits the velocities approach the cluster centroid (see e.g. Fig. 1 in Rhee et al. 2017). This means that galaxies on first infall tend to have large velocity offsets, often near the escape velocity caustic. These infalling tracks in phase space are clear in simulations when using full 3D positions and velocities. In projection, these infalling tracks are far less clear, but infalling galaxies still tend to be found

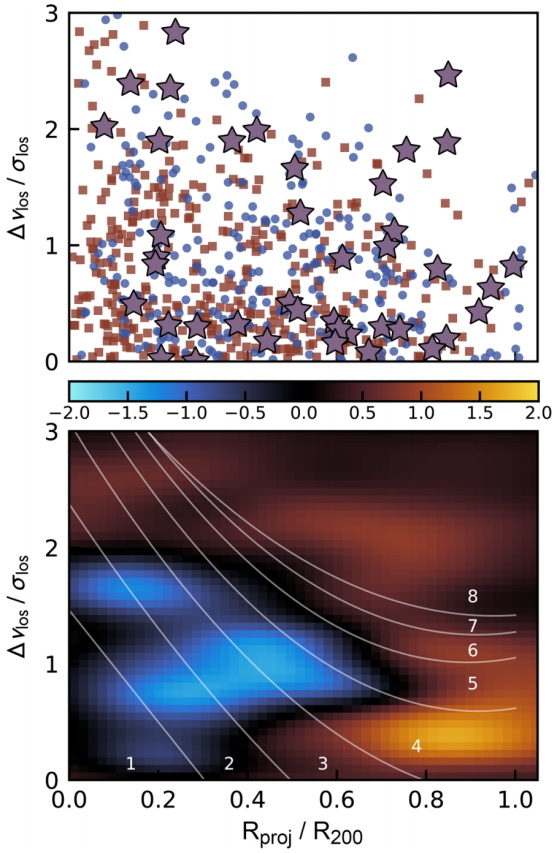

FIGURE 6.5: *Top:* Projected phase space diagram for member galaxies of the Coma cluster. Passive galaxies are shown as red squares, star-forming galaxies are shown as blue circles, and stripping candidates are shown as purple stars. *Bottom:* Difference between the phase space KDE distributions for stripping candidates and normal star-forming Coma galaxies. The colorbar corresponds to the fractional change relative to the mean kernel density. At all radii, there is an excess of stripping candidates (red colour) at large velocity offsets, relative to the bulk star-forming population (blue colour).

at the velocity outskirts of PPS (e.g. Mahajan, Mamon, and Raychaudhury, 2011; Oman, Hudson, and Behroozi, 2013).

In Section 6.4 we showed that the orientation of stripping features is consistent with the majority of stripping candidates being on first infall toward the cluster centre. We further test this by considering the position of stripping candidates in PPS. In Fig. 6.5 (top) we plot the PPS diagram for star-forming (blue) and passive (red) Coma members, as well as stripping candidates (purple stars). There is a collection of stripping candidates extending from $\Delta v_{\rm los} \sim 0.5\,\sigma_{\rm los}$ at the virial radius to $\Delta v_{\rm los} \sim 3\,\sigma_{\rm los}$ near the cluster centre. This is consistent with the PPS positions expected for infalling galaxies. To further compare the distribution of stripping candidates in PPS to that for star-forming Coma galaxies, we measure a 2D gaussian kernel density estimate (KDE) for the PPS distribution for star-forming galaxies and stripping candidates. In Fig. 6.5 (bottom) we show the difference between the KDE distributions for the stripping candidates and the non-stripping star-forming galaxies. Blue regions in this map correspond to an excess of non-stripping galaxies and red/orange regions correspond to an excess of stripping candidates. It is clear that relative to the non-stripping population, the stripping candidates are preferentially found along the infalling track in PPS. This is further evidence that many of these galaxies are being stripped on their first infall toward the cluster centre. At almost all cluster-centric radii, stripping candidates are preferentially found at large velocity offsets. Stripping candidates should therefore be experiencing a stronger ram pressure force (scales with $\sim \rho v^2$), which is evidence that it is ram pressure stripping driving the observed asymmetries in these galaxies. These results are in qualitative agreement with Jaffé et al. (2018) who find that GASP jellyfish galaxies are preferentially found at large peculiar velocities within their host clusters.

With the Yonsei suite of galaxy cluster zoom simulations (in projection), Pasquali et al. (2019) derived regions in PPS of roughly constant time-since-infall. These zones allow us to quantitatively constrain, at least on average, the infall times of Coma galaxies. In Fig. 6.5 (bottom) we show these PPS regions numbered from 1-8. The average time-since-infall for simulated galaxies in these zones from Pasquali et al. (2019) increase monotonically from 1.42 Gyr in zone 8 to 5.42 Gyr in zone

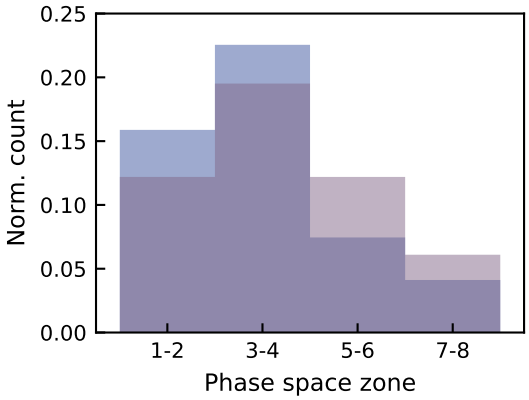

FIGURE 6.6: Normalized histograms showing the distribution of phase space zones from Pasquali et al. (2019) for star-forming Coma members (blue) and stripping candidates (purple). These phase-space zones trace time-since infall, with the average time-since infall increasing monotonically from zone 8 (1.42 Gyr) to zone 1 (5.42 Gyr).

1. In Fig. 6.6 we plot normalized histograms distribution of PPS zones of star-forming Coma galaxies and stripping candidates, showing an excess of stripping candidates in the higher PPS zones, which correspond to shorter times-since-infall. This quantitatively demonstrates that many stripping candidates are likely recent infallers.

6.6 Star Formation in Stripping Galaxies

The effect of ram pressure stripping on galaxy star formation has been a topic of focus of many previous studies (e.g. Dressler and Gunn, 1983; Quilis, Moore, and Bower, 2000; Steinhauser, Schindler, and Springel, 2016; Poggianti et al., 2017; Roberts et al., 2019). Ram pressure stripping is a mechanism which quenches star formation in cluster galaxies through rapid gas removal, but recent simulations and observations have shown that star formation may be briefly enhanced during stripping (Steinhauser et al., 2012; Bekki, 2014; Ebeling, Stephenson, and Edge, 2014; Poggianti et al., 2016; Troncoso Iribarren et al., 2016; Vulcani et al., 2018), prior to gas removal. The star formation enhancement is likely driven by gas compression due to shocks from ram pressure or angular momentum transfer that

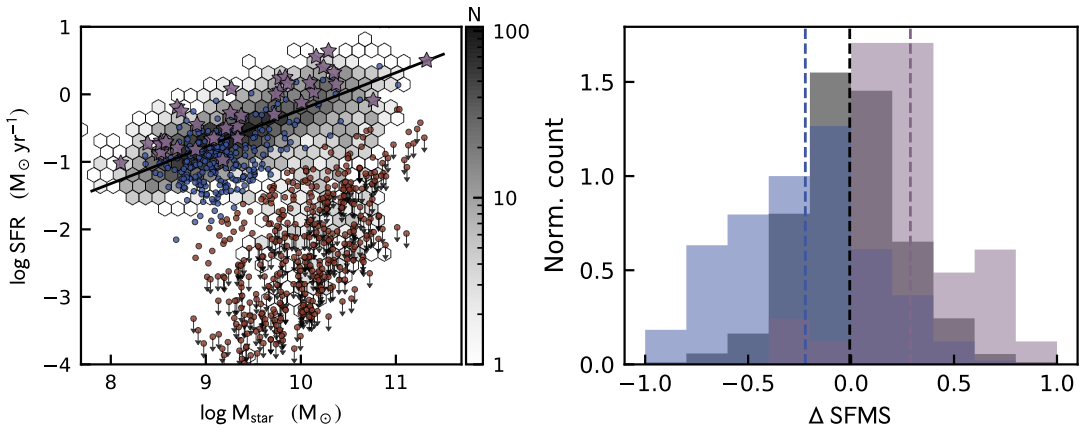

FIGURE 6.7: *Left:* Star formation rate versus stellar mass. Background greyscale shows distribution for galaxies from the isolated field sample and the trend line shows the best-fit to star-forming ($\mathrm{sSFR} > 10^{-11}\,\mathrm{yr}^{-1}$) field galaxies. Blue points correspond to normal star forming Coma galaxies, red points show passive Coma galaxies, and purple stars denote Coma stripping candidates. *Right:* Offset from the field star-forming main sequence for non-stripping star-forming galaxies (blue), field galaxies (black), and stripping candidates (purple). Dashed lines show median offsets from the star-forming main sequence for each population.

catalyzes strong star formation (Schulz and Struck, 2001). The sample of galaxies in this work allow us to further test this prediction.

In Fig. 6.7 (left) we plot star formation rate versus stellar mass for isolated field galaxies (grey 2D histogram), all SDSS Coma galaxies (circles), and stripping galaxies (purple stars). Blue circles correspond to star-forming galaxies and red circles correspond to passive galaxies. We distinguish between star-forming and passive galaxies with a single cut in specific star formation rate at sSFR $= 10^{-11}\,\mathrm{yr}^{-1}$. In Fig. 6.7 we mark the SFRs for all galaxies with sSFR $< 10^{-11.7}\,\mathrm{yr}^{-1}$ as upper limits as suggested by Salim et al. (2016). Finally, for reference we determine a star-forming main sequence (SFMS) by fitting a single powerlaw to the SFR-mass relationship for star-forming field galaxies. We incorporate uncertainties in both stellar mass and SFR to fit the SFMS with LINMIX[6] (Kelly, 2007). We find a main sequence relationship of

$$\log \mathrm{SFR} = 0.55 \times \log M_{\mathrm{star}} - 5.7 \tag{6.8}$$

which is shown in Fig. 6.7 (left) with the solid black line. As expected, the red-sequence is significantly more populated in the Coma cluster relative to the field, furthermore, star-forming Coma galaxies fall slightly below the SFMS suggesting that the cluster environment has an effect even on star-forming Coma galaxies. Consensus is lacking regarding whether the slope and normalization of the SFMS depend on environment. Peng et al. (2010) have found that the SFMS is independent of environment (traced by local galaxy density), whereas other studies have found small offsets, $\sim 0.1-0.2$ dex, between the SFMS in the field versus groups or clusters (Vulcani et al., 2010; Lin et al., 2014; Erfanianfar et al., 2016; Paccagnella et al., 2016; Grootes et al., 2017; Wang et al., 2018). Such an offset may also only be present at low redshift and not in the early Universe (Erfanianfar et al., 2016). The results of this work are consistent with previous studies which find an offset; we measure a small offset of ~ 0.3 dex between the isolated field and Coma cluster SFMS.

At all stellar masses the stripping candidates are found to have significantly higher SFRs relative to the bulk star-forming population in Coma (blue circles).

[6] `https://linmix.readthedocs.io/en/latest/index.html`

This is consistent with predictions that ram pressure can induce temporary enhancements in star formation prior to quenching. When compared to field galaxies the stripping candidates still show enhanced SFRs, with 90 per cent of stripping galaxies falling above the field SFMS. As a test, we randomly draw 41 galaxies (the size of the stripping candidate sample) from the star-forming field population and compute their offsets from the SFMS. We then repeat this Monte-Carlo trial 100 000 times to determine what fraction of galaxies are scattered above the SFMS due to random chance alone. Fractions above the SFMS of >70 per cent from our random samples only occur in 0.05 per cent of trials. This is strong evidence that the SFRs of stripping candidates are systematically enhanced, both relative to other Coma galaxies and relative to isolated field galaxies.

In Fig. 6.7 (right) we show histograms of the offset from the field SFMS for star-forming Coma galaxies (blue), field galaxies (black), and stripping candidates (purple). As previously stated, star-forming Coma galaxies fall preferentially below the field SFMS and stripping candidates fall preferentially above the SFMS. Based on a k-sample Anderson-Darling test (Scholz and Stephens, 1987), a cumulative distribution test which tests the null hypothesis that k-samples are drawn from the same underlying distribution, these three distributions are distinct at greater than 99.99 per cent confidence. Quantitatively, the median offset from the SFMS is enhanced for stripping candidates by 0.5 dex relative to Coma star-forming galaxies and by 0.3 dex relative to field galaxies. This offset from the SFMS of 0.3 dex for stripping candidates is similar to the star formation enhancement of 0.2 dex relative to the SFMS reported by Vulcani et al. (2018) for GASP Jellyfish galaxies.

6.7 Discussion and Conclusions

6.7.1 Are "Stripping-Candidates" Undergoing Ram Pressure Stripping?

The sample of stripping candidates presented in this work were identified based on disturbed, asymmetric morphological features. These visual signatures can be generated by stripping processes or possibly other interactions, such as harassment,

tidal effects, or mergers. As summarized below, we find that the population of stripping candidates is consistent with galaxies undergoing ram pressure stripping, but we note that some individual galaxies may be exceptions with different origins for their disturbed morphologies.

In Fig. 6.4 (right) we show the orientation of stripping features with respect to the cluster centre. The observed distribution of angles, with one prominent peak pointing roughly away from the cluster centre, is consistent with simple expectations from ram pressure stripping. We emphasize that the visual classifiers were given no information regarding positions within the Coma cluster when galaxies were visually classified, therefore this trend is not being driven by any selection biases in the classification process. As in Section 6.4, we emphasize that the interpretation of observed asymmetry orientations is complicated by variations in galaxy orbits as well as projection effects. The observed asymmetries in this work are broadly consistent with a simple picture of ram pressure stripping of galaxies on first infall. Additionally, Fig. 6.5 shows that there is an excess of stripping candidates located at large velocity offsets relative to other Coma satellites. Given that ram pressure scales with ρv^2, this suggests that stripping candidates are currently experiencing a relatively strong ram pressure force. Other cluster processes, such as tidal effects, which could give rise to asymmetric morphologies, should be occurring in regions where galaxy number densities are large. We measure nearest-neighbour number densities for all of the galaxies in this work, and find that stripping candidates actually have marginally *lower* nearest-neighbour number densities (at fixed cluster-centric radius) compared to star-forming Coma galaxies (plot not shown, significant at $2-3\,\sigma$). This suggests that tidal interactions due to densely populated local environments is likely not the driving factor behind the observed morphologies of stripping candidates.

Follow-up observations of these stripping candidates are essential to confirm (or rule out) ram pressure as the driver of their disturbed morphologies. These stripping candidates have been identified largely on the basis of their stellar morphologies, which corresponds to a fairly tightly bound galaxy component. Resolved observations of components more susceptible to stripping, such as atomic hydrogen or ionized gas traced by Hα, would provide even more information on the impacts of ram pressure on these galaxies (e.g. Kenney, van Gorkom, and Vollmer, 2004;

Poggianti et al., 2017).

6.7.2 Star Formation Activity Throughout Ram Pressure Stripping

Assuming that the stripping candidates identified here represent galaxies undergoing ram pressure stripping, this sample provides important constraints on galaxy star formation throughout the stripping process. In Fig. 6.7 we show that the SFRs of stripping candidates are clearly enhanced relative to both star-forming Coma galaxies, as well as star-forming galaxies in the field. This is consistent with previous observational work which has found similar enhancements of SFRs in galaxies experiencing ram pressure stripping (Ebeling, Stephenson, and Edge, 2014; Poggianti et al., 2016; Vulcani et al., 2018), as well as theoretical predictions from hydrodynamic simulations (Steinhauser et al., 2012; Bekki, 2014; Troncoso Iribarren et al., 2016). We note that the SFRs used in this work are derived from UV+optical+TIR SED fitting (Salim et al., 2016; Salim, Boquien, and Lee, 2018), but we also explore dust-corrected Hα fluxes from the SDSS spectra (Thomas et al., 2013). We find that the median Hα flux for stripping candidates is enhanced over the median Hα flux for star-forming field galaxies by a factor of $\sim$2. When considering Hα fluxes we see an even stronger enhancement for stripping candidates over star-forming Coma galaxies. This demonstrates that the observed star formation enhancement for stripping candidates is not only limited to the galaxy disc as a whole, but is also present in galaxy centres traced by the 3″ SDSS fibre ($\sim$1.5 kpc at the redshift of Coma). Furthermore, star formation in stripped tails can make-up a non-negligible portion of the galaxy star formation budget (Poggianti et al., 2019), and such extended star formation is likely not captured by the indicators used in this work. Therefore, we may actually still be underestimating the enhancement of star formation in stripping candidates.

After this period of enhanced star formation, the details of the "quenching phase" associated with ram pressure stripping depend strongly on the efficiency of ram pressure stripping. For example, in the case of extremely efficient stripping, all (or most) atomic and molecular gas reserves may be directly stripped leading to rapid quenching. However, the molecular gas component may be difficult to

strip directly, as it is centrally concentrated and more strongly bound to the the host galaxy. In this case, ram pressure stripping may be able to remove large amounts of atomic hydrogen but leave large molecular gas reserves unstripped. In this case the quenching timescale would then be set by the depletion time of the remaining gas (see e.g. Roberts et al., 2019). This scenario predicts the existence of a "post-stripping" phase where galaxies show residual star formation along with a truncated gas disc due to stripping. Such post-stripping galaxies have been observed in galaxy clusters (e.g. Yoon et al., 2017; Jaffé et al., 2018). The non-stripping population of star-forming galaxies that we identify in Coma is potentially a mixture of these post-stripping galaxies as well as normal star-forming galaxies that have not been strongly affected by ram pressure. If some of these galaxies have begun to quench, that could explain the population of star-forming Coma galaxies located below the SFMS (see Fig. 6.7). With this dataset we cannot measure the fraction of galaxies which may be post-stripping, as that requires resolved maps of star formation or gas in these systems. We can, however, derive rough constraints on the timescales over which galaxies show morphological features of stripping, based on the fact that the vast majority of stripping candidates show morphological features that are pointing away from the cluster centre. There seem to be very few stripping candidates that are on their way out of the cluster centre after a pericentric passage, which suggests that the period over which Coma galaxies show morphological signatures of stripping cannot last much longer than a crossing time. We estimate the crossing time for Coma as $t_{\rm cross} \sim R_{\rm vir}/\sigma_{\rm los}$ which, for $R_{\rm vir} = 2840\,{\rm kpc}$ and $\sigma_{\rm los} = 930\,{\rm km\,s^{-1}}$, gives a crossing time of $\sim 3\,{\rm Gyr}$. Therefore, we can infer an upper limit for the period of strong ram pressure stripping of $\lesssim 3\,{\rm Gyr}$. Further constraints on this timescale requires knowledge of when ram pressure stripping started for each galaxy, which varies depending on galaxy mass, orbits, gas distributions, etc.

6.7.3 Identifying Stripping Galaxies With Rest-Frame Optical Imaging

In this work we visually identify galaxies potentially undergoing stripping with three-colour rest-frame optical imaging. We confirm the validity of these classifications by measuring quantitative morphological parameters for stripping candidates, and show that they occupy unique regions of commonly used morphological planes (see also McPartland et al. 2016). Based on Fig. 6.2, simple cuts in asymmetry or M_{20} select the majority of stripping candidates, with minimal contamination from "normal" cluster galaxies, in an automated fashion. In the era of wide-field photometric surveys, this is a potentially useful way to identify large numbers of candidate stripping galaxies. While such an automated identification also flags mergers and other highly disturbed galaxies, in the cluster environment it is likely that stripping galaxies outnumber mergers. At the very least, such a selection could narrow a prohibitively large sample for follow-up visual classifications. In Fig. 6.2 we show morphological parameters computed with u-band images, as we find the u-band provides the clearest separation between stripping candidates and other cluster galaxies, but we note that we still find a clear separation in the Gini-M_{20} and concentration-asymmetry with g- or i-band images.

6.7.4 Conclusions

In this paper we present a sample of 41 galaxies visually identified as candidates for galaxies undergoing ram pressure stripping in the Coma cluster. While some of these stripping-candidates have been previously identified, the majority of our sample are newly identified ram pressure candidate galaxies. This sizable sample enables a detailed study of the properties of Coma galaxies experiencing stripping. The main conclusions of this work are:

1. Stripping candidates are clear outliers, relative to normal cluster galaxies, in common morphology parameter spaces such as Gini-M_{20} and concentration-asymmetry.

2. Morphological stripping features (e.g. tails, asymmetric star formation, shock fronts) are preferentially oriented radially away from the cluster centre, with

a minority of stripping candidates displaying features directed toward the cluster centre. Virtually no stripping candidates show morphological features perpendicular to the cluster centre.

3. The population of stripping candidates is consistent with most galaxies being on first infall toward the cluster centre.

4. Star formation rates of stripping candidates are clearly enhanced, both relative to other star-forming Coma galaxies, and relative to isolated star-forming field galaxies. This is consistent with ram pressure driving an enhancement in galaxy star formation.

Follow-up observations are essential to confirm the origin of these disturbed galaxies. If confirmed as galaxies in the process of being stripped, that would suggest that ram pressure stripping is ubiquitous in the Coma cluster out to the virial radius.

Acknowledgments: The authors thank Toby Brown, Ryan Chown, and Jacqueline Wightman for carefully classifying the visual morphology of Coma galaxies. IDR thanks the Ontario Graduate Scholarship program for funding, LCP thanks the Natural Science and Engineering Council of Canada for funding. This work was made possible thanks to a large number of publicly available software packages, including: (Astropy Collaboration et al., 2013), CMasher[7], linmix[8], Matplotlib (Hunter, 2007), NumPy (van der Wel, 2008), scikit-learn (Pedregosa et al., 2011), SciPy (Virtanen et al., 2020), statmorph (Rodriguez-Gomez et al., 2019), Stiff (Bertin, 2012), Topcat (Taylor, 2005).

The authors thank Dr. Stephen Gwyn for generating MegaCam image stacks for the central Coma field. This work makes use of observations obtained with MegaPrime/MegaCam, a joint project of CFHT and CEA/DAPNIA, at the Canada-France-Hawaii Telescope (CFHT) which is operated by the National Research Council (NRC) of Canada, the Institut National des Sciences de l'Univers of the Centre National de la Recherche Scientifique of France, and the University of Hawaii. This research used the facilities of the Canadian Astronomy Data Centre

[7] `https://cmasher.readthedocs.io`
[8] `https://linmix.readthedocs.io/en/latest/index.html`

operated by the National Research Council of Canada with the support of the Canadian Space Agency.

Funding for SDSS-III has been provided by the Alfred P. Sloan Foundation, the Participating Institutions, the National Science Foundation, and the U.S. Department of Energy Office of Science. The SDSS-III web site is `http://www.sdss3.org/`.

SDSS-III is managed by the Astrophysical Research Consortium for the Participating Institutions of the SDSS-III Collaboration including the University of Arizona, the Brazilian Participation Group, Brookhaven National Laboratory, Carnegie Mellon University, University of Florida, the French Participation Group, the German Participation Group, Harvard University, the Instituto de Astrofisica de Canarias, the Michigan State/Notre Dame/JINA Participation Group, Johns Hopkins University, Lawrence Berkeley National Laboratory, Max Planck Institute for Astrophysics, Max Planck Institute for Extraterrestrial Physics, New Mexico State University, New York University, Ohio State University, Pennsylvania State University, University of Portsmouth, Princeton University, the Spanish Participation Group, University of Tokyo, University of Utah, Vanderbilt University, University of Virginia, University of Washington, and Yale University.

Bibliography

Abraham, Roberto G., Sidney van den Bergh, and Preethi Nair (2003). *ApJ* 588.1, pp. 218–229.

Alam, Shadab et al. (2015). *ApJS* 219.1, 12, p. 12.

Astropy Collaboration et al. (2013). *A&A* 558, A33, A33.

Bamford, S. P. et al. (2009). *MNRAS* 393, pp. 1324–1352.

Beers, T. C., K. Flynn, and K. Gebhardt (1990). *AJ* 100, pp. 32–46.

Bekki, Kenji (2014). *MNRAS* 438.1, pp. 444–462.

Bertin, E. (2012). *Astronomical Data Analysis Software and Systems XXI*. Ed. by P. Ballester, D. Egret, and N. P. F. Lorente. Vol. 461. Astronomical Society of the Pacific Conference Series, p. 263.

Biviano, A. et al. (1997). *A&A* 321, pp. 84–104.

Biviano, A. et al. (2013). *A&A* 558, A1, A1.

Blanton, M. R. and S. Roweis (2007). *AJ* 133, pp. 734–754.

Boquien, M. et al. (2019). *A&A* 622, A103, A103.

Brown, Toby et al. (2017). *MNRAS* 466.2, pp. 1275–1289.

Bundy, Kevin et al. (2015). *ApJ* 798.1, 7, p. 7.

Chauke, Priscilla et al. (2019). *ApJ* 877.1, 48, p. 48.

Chung, A., J. H. van Gorkom, J. D. P. Kenney, H. Crowl, and B. Vollmer (2009). *AJ* 138, pp. 1741–1816.

Chung, A., J. H. van Gorkom, J. D. P. Kenney, and B. Vollmer (2007). *ApJl* 659, pp. L115–L119.

Clemens, M. S., A. Bressan, B. Nikolic, and R. Rampazzo (2009). *MNRAS* 392.1, pp. L35–L39.

Colless, Matthew and Andrew M. Dunn (1996). *ApJ* 458, p. 435.

Conselice, Christopher J. (2003). *ApJS* 147.1, pp. 1–28.

— (2014). *ARAA* 52, pp. 291–337.

Cramer, W. J. et al. (2019a). *ApJ* 870.2, 63, p. 63.

Cramer, William J. et al. (2019b). *arXiv e-prints*, arXiv:1910.14082, arXiv:1910.14082.

Croom, Scott M. et al. (2012). *MNRAS* 421.1, pp. 872–893.

Dekel, A. and Y. Birnboim (2006). *MNRAS* 368, pp. 2–20.

Dressler, A. and J. E. Gunn (1983). *ApJ* 270, pp. 7–19.

Ebeling, H., L. N. Stephenson, and A. C. Edge (2014). *ApJL* 781.2, L40, p. L40.

Erfanianfar, G. et al. (2016). *MNRAS* 455, pp. 2839–2851.

Fasano, G. et al. (2015). *MNRAS* 449, pp. 3927–3944.

Fillingham, S. P. et al. (2015). *MNRAS* 454, pp. 2039–2049.

Finn, Rose A. et al. (2018). *ApJ* 862.2, 149, p. 149.

Foltz, R. et al. (2018). *ApJ* 866.2, 136, p. 136.

Gavazzi, G., G. Consolandi, M. L. Gutierrez, A. Boselli, and M. Yoshida (2018). *A&A* 618, A130, A130.

Geha, M., M. R. Blanton, R. Yan, and J. L. Tinker (2012). *ApJ* 757.1, 85, p. 85.

Geller, M. J., Antonaldo Diaferio, and M. J. Kurtz (1999). *ApJL* 517.1, pp. L23–L26.

Glasser, Gerald J. (1962). *Journal of the American Statistical Association* 57.299, pp. 648–654.

Godwin, J. G., N. Metcalfe, and J. V. Peach (1983). *MNRAS* 202, pp. 113–124.

Grootes, M. W. et al. (2017). *AJ* 153.3, 111, p. 111.

Gunn, J. E. and J. R. Gott III (1972). *ApJ* 176, p. 1.

Gwyn, Stephen D. J. (2008). *PASP* 120.864, p. 212.

Haines, C. P., F. La Barbera, A. Mercurio, P. Merluzzi, and G. Busarello (2006). *ApJL* 647, pp. L21–L24.

Haines, C. P. et al. (2015). *ApJ* 806, 101, p. 101.

Hunter, J. D. (2007). *Computing In Science & Engineering* 9.3, pp. 90–95.

Jáchym, Pavel, Françoise Combes, Luca Cortese, Ming Sun, and Jeffrey D. P. Kenney (2014). *ApJ* 792.1, 11, p. 11.

Jáchym, Pavel et al. (2019). *ApJ* 883.2, 145, p. 145.

Jaffé, Y. L. et al. (2018). *MNRAS*.

Kelly, Brandon C. (2007). *ApJ* 665.2, pp. 1489–1506.

Kenney, J. D. P., A. Abramson, and H. Bravo-Alfaro (2015). *AJ* 150, 59, p. 59.

Kenney, J. D. P., J. H. van Gorkom, and B. Vollmer (2004). *AJ* 127, pp. 3361–3374.

Kubo, Jeffrey M. et al. (2007). *ApJ* 671.2, pp. 1466–1470.

Larson, R. B., B. M. Tinsley, and C. N. Caldwell (1980). *ApJ* 237, pp. 692–707.

Lin, Lihwai et al. (2014). *ApJ* 782.1, 33, p. 33.

Lotz, Jennifer M., Joel Primack, and Piero Madau (2004). *AJ* 128.1, pp. 163–182.

Lotz, Marcel, Rhea-Silvia Remus, Klaus Dolag, Andrea Biviano, and Andreas Burkert (2019). *MNRAS* 488.4, pp. 5370–5389.

Mahajan, S., G. A. Mamon, and S. Raychaudhury (2011). *MNRAS* 416, pp. 2882–2902.

Mayer, L., C. Mastropietro, J. Wadsley, J. Stadel, and B. Moore (2006). *MNRAS* 369, pp. 1021–1038.

McPartland, Conor, Harald Ebeling, Elke Roediger, and Kelly Blumenthal (2016). *MNRAS* 455.3, pp. 2994–3008.

Mihos, J. C. and L. Hernquist (1994a). *ApJl* 425, pp. L13–L16.

— (1994b). *ApJl* 431, pp. L9–L12.

Moore, B., N. Katz, G. Lake, A. Dressler, and A. Oemler (1996). *Nature* 379, pp. 613–616.

Muzzin, A. et al. (2014). *ApJ* 796, 65, p. 65.

Nulsen, P. E. J. (1982). *MNRAS* 198, pp. 1007–1016.

Oman, K. A., M. J. Hudson, and P. S. Behroozi (2013). *MNRAS* 431, pp. 2307–2316.

Paccagnella, A. et al. (2016). *ApJL* 816.2, L25, p. L25.

Pasquali, A. et al. (2019). *MNRAS* 484.2, pp. 1702–1723.

Pawlik, M. M. et al. (2016). *MNRAS* 456.3, pp. 3032–3052.

Pedregosa, F. et al. (2011). *Journal of Machine Learning Research* 12, pp. 2825–2830.

Peng, Y.-j. et al. (2010). *ApJ* 721, pp. 193–221.

Peng, Y., R. Maiolino, and R. Cochrane (2015). *Nature* 521, pp. 192–195.

Poggianti, B. M. et al. (2016). *AJ* 151.3, 78, p. 78.

Poggianti, B. M. et al. (2017). *ApJ* 844, 48, p. 48.

Poggianti, Bianca M. et al. (2019). *MNRAS* 482.4, pp. 4466–4502.

Postman, M. et al. (2005). *ApJ* 623, pp. 721–741.

Prescott, M. et al. (2011). *MNRAS* 417, pp. 1374–1386.

Quilis, V., B. Moore, and R. Bower (2000). *Science* 288, pp. 1617–1620.

Rasmussen, J. et al. (2012). *ApJ* 757, 122, p. 122.

Rhee, J. et al. (2017). *ApJ* 843, 128, p. 128.

Roberts, I. D. and L. C. Parker (2017). *MNRAS* 467, pp. 3268–3278.

Roberts, I. D., L. C. Parker, and J. Hlavacek-Larrondo (2018). *MNRAS* 475, pp. 4704–4716.

Roberts, I. D. et al. (2019). *ApJ* 873.1, 42, p. 42.

Rodriguez-Gomez, Vicente et al. (2019). *MNRAS* 483.3, pp. 4140–4159.

Saintonge, A. et al. (2017). *ApJS* 233, 22, p. 22.

Salim, S. (2014). *Serbian Astronomical Journal* 189, pp. 1–14.

Salim, S. et al. (2016). *ApJS* 227, 2, p. 2.

Salim, Samir, Médéric Boquien, and Janice C. Lee (2018). *ApJ* 859.1, 11, p. 11.

Sánchez, S. F. et al. (2012). *A&A* 538, A8, A8.

Schaefer, A. L. et al. (2017). *MNRAS* 464.1, pp. 121–142.

Schaefer, A. L. et al. (2019). *MNRAS* 483.3, pp. 2851–2870.

Schawinski, Kevin et al. (2009). *ApJl* 692.1, pp. L19–L23.

Scholz, F. W. and M. A. Stephens (1987). *Journal of the American Statistical Association* 82.399, pp. 918–924.

Schulz, Steven and Curtis Struck (2001). *MNRAS* 328.1, pp. 185–202.

Smith, G. P. et al. (2010). *MNRAS* 409, pp. 169–183.

Steinhauser, D., M. Haider, W. Kapferer, and S. Schindler (2012). *A&A* 544, A54, A54.

Steinhauser, D., S. Schindler, and V. Springel (2016). *ArXiv e-prints*.

Taranu, D. S. et al. (2014). *MNRAS* 440, pp. 1934–1949.

Taylor, M. B. (2005). *Astronomical Data Analysis Software and Systems XIV*. Ed. by P. Shopbell, M. Britton, and R. Ebert. Vol. 347. Astronomical Society of the Pacific Conference Series, p. 29.

Thomas, D. et al. (2013). *MNRAS* 431.2, pp. 1383–1397.

Troncoso Iribarren, Paulina et al. (2016). *Galaxies* 4.4, p. 77.

van der Burg, Remco F. J. et al. (2018). *A&A* 618, A140, A140.

van der Wel, A. (2008). *ApJl* 675, L13, p. L13.

Virtanen, Pauli et al. (2020). *Nature Methods* 17, pp. 261–272.

Vollmer, B. et al. (2012). *A&A* 537, A143, A143.

Vulcani, Benedetta et al. (2010). *ApJL* 710.1, pp. L1–L6.

Vulcani, Benedetta et al. (2018). *ApJL* 866.2, L25, p. L25.

Wagner, Cory R., Michael McDonald, and Stéphane Courteau (2018). *ApJ* 867.1, 14, p. 14.

Wang, L. et al. (2018). *A&A* 618, A1, A1.

Wetzel, A. R. (2011). *MNRAS* 412, pp. 49–58.

Wetzel, A. R., J. L. Tinker, and C. Conroy (2012). *MNRAS* 424, pp. 232–243.

Wetzel, A. R., E. J. Tollerud, and D. R. Weisz (2015). *ApJL* 808, L27, p. L27.

Yagi, Masafumi et al. (2007). *ApJ* 660.2, pp. 1209–1214.

Yagi, Masafumi et al. (2010). *AJ* 140.6, pp. 1814–1829.

Yang, X., H. J. Mo, F. C. van den Bosch, and Y. P. Jing (2005). *MNRAS* 356, pp. 1293–1307.

Yang, X. et al. (2007). *ApJ* 671, pp. 153–170.

Yoon, Hyein, Aeree Chung, Rory Smith, and Yara L. Jaffé (2017). *ApJ* 838.2, 81, p. 81.

Yoshida, Michitoshi et al. (2012). *ApJ* 749.1, 43, p. 43.

6.A Appendix: Ram Pressure Candidates

TABLE 6.1: Ram pressure candidates

Galaxy Name[a]	RA deg	Dec deg	z	$\log M_\star$ [b] $M_\odot$	$\log \mathrm{SFR}$ [b] $M_\odot\ \mathrm{yr}^{-1}$
GMP 4629	194.4593	28.1704	0.0231	8.59	-0.801
GMP 4570	194.4867	27.9918	0.0152	8.11	-1.019
GMP 5382	194.1197	29.1371	0.0316	9.33	-0.475
GMP 5422	194.1191	27.2913	0.0251	10.01	-0.122
GMP 2625	195.1300	28.9505	0.0233	9.18	-0.974
GMP 2599	195.1403	27.6377	0.0250	9.78	0.049
GMP 1616	195.5328	27.6483	0.0230	10.24	0.404
GMP 406	196.1616	28.9727	0.0253	9.06	-0.664
GMP 3779	194.7721	27.6444	0.0181	9.74	0.003
GMP 3816	194.7586	28.1157	0.0314	10.16	0.560
GMP 3618	194.8195	27.1061	0.0280	10.14	0.038
GMP 5821	193.9346	28.7546	0.0275	8.91	-0.448
SDSS J130545.34+285216.8	196.4390	28.8713	0.0266	9.21	-0.502
GMP 2910	195.0381	27.8665	0.0177	9.27	0.080
SDSS J130006.15+281507.8	195.0256	28.2522	0.0212	8.53	-0.692
GMP 4159	194.6472	27.2647	0.0245	9.78	0.242
GMP 4135	194.6553	27.1766	0.0256	9.84	0.251
GMP 4281	194.6064	28.1289	0.0274	9.72	-0.300
GMP 4236	194.6285	26.9949	0.0249	8.39	-0.729
GMP 3143	194.9552	26.9743	0.0235	8.89	-0.820
SDSS J130553.48+280644.7	196.4729	28.1124	0.0246	10.09	0.170
GMP 2544	195.1648	29.0194	0.0242	10.76	-0.089
GMP 4688	194.4321	29.0032	0.0231	8.51	-0.881
GMP 2559	195.1578	28.0580	0.0255	10.29	0.643
GMP 3253	194.9172	28.6308	0.0178	9.37	-0.315
GMP 3271	194.9159	27.5765	0.0167	9.06	-0.662
GMP 6364	193.6752	27.6389	0.0287	8.53	-0.856
GMP 1582	195.5473	28.1725	0.0299	8.70	-0.187
GMP 672	195.9880	26.7295	0.0220	8.70	-0.796
GMP 2374	195.2336	27.7909	0.0266	11.32	0.501
GMP 713	195.9768	28.3106	0.0268	8.74	-0.250
GMP 4437	194.5384	28.7086	0.0254	10.37	0.150
GMP 4333	194.5822	28.0948	0.0239	8.52	-0.733
GMP 4463	194.5386	26.6641	0.0243	9.34	-0.648
GMP 4471	194.5233	28.2426	0.0240	10.88	1.083
GMP 2073	195.3545	28.6772	0.0292	10.35	0.321
GMP 223	196.2776	28.6412	0.0182	8.58	-0.718
GMP 522	196.0945	28.8108	0.0265	9.86	0.159
GMP 455	196.1106	27.3043	0.0184	9.26	-0.274
GMP 4106	194.6664	26.7595	0.0249	9.09	-0.649
GMP 597	196.0547	28.5425	0.0271	8.58	-0.704

NOTES. [a] Galaxy ID from the Godwin, Metcalfe, and Peach (1983) catalog when applicable, otherwise from the SDSS; [b] Medium-deep GSWLC-2 catalogue (Salim et al., 2016; Salim, Boquien, and Lee, 2018)

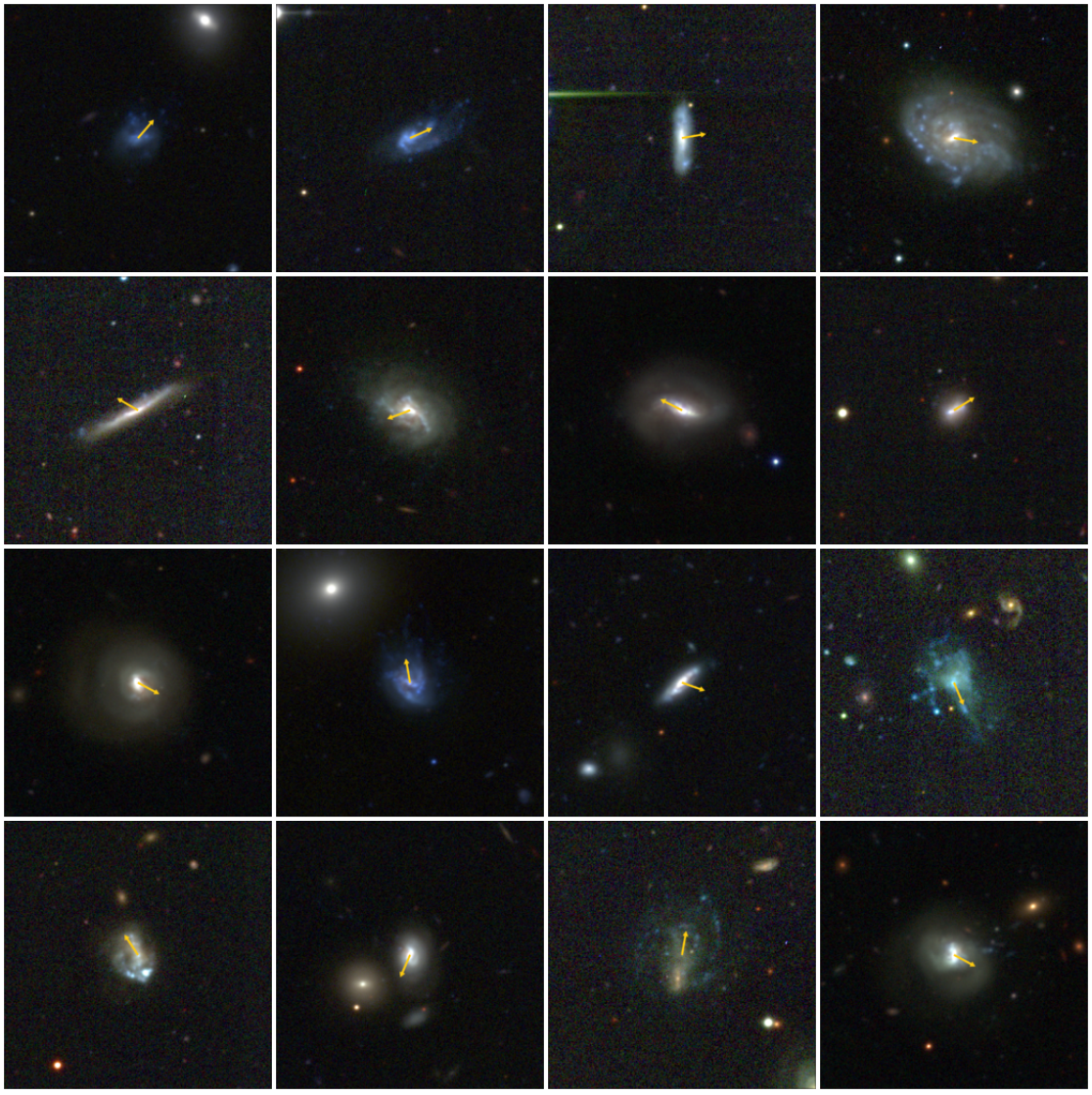

FIGURE 6.8: CFHT *ugi* images for the sample of stripping candidates. All cutout images have physical dimensions of 40×40 kpc. The arrows in each thumbnail mark the estimated orientation of observed stripping features (see section 6.4)

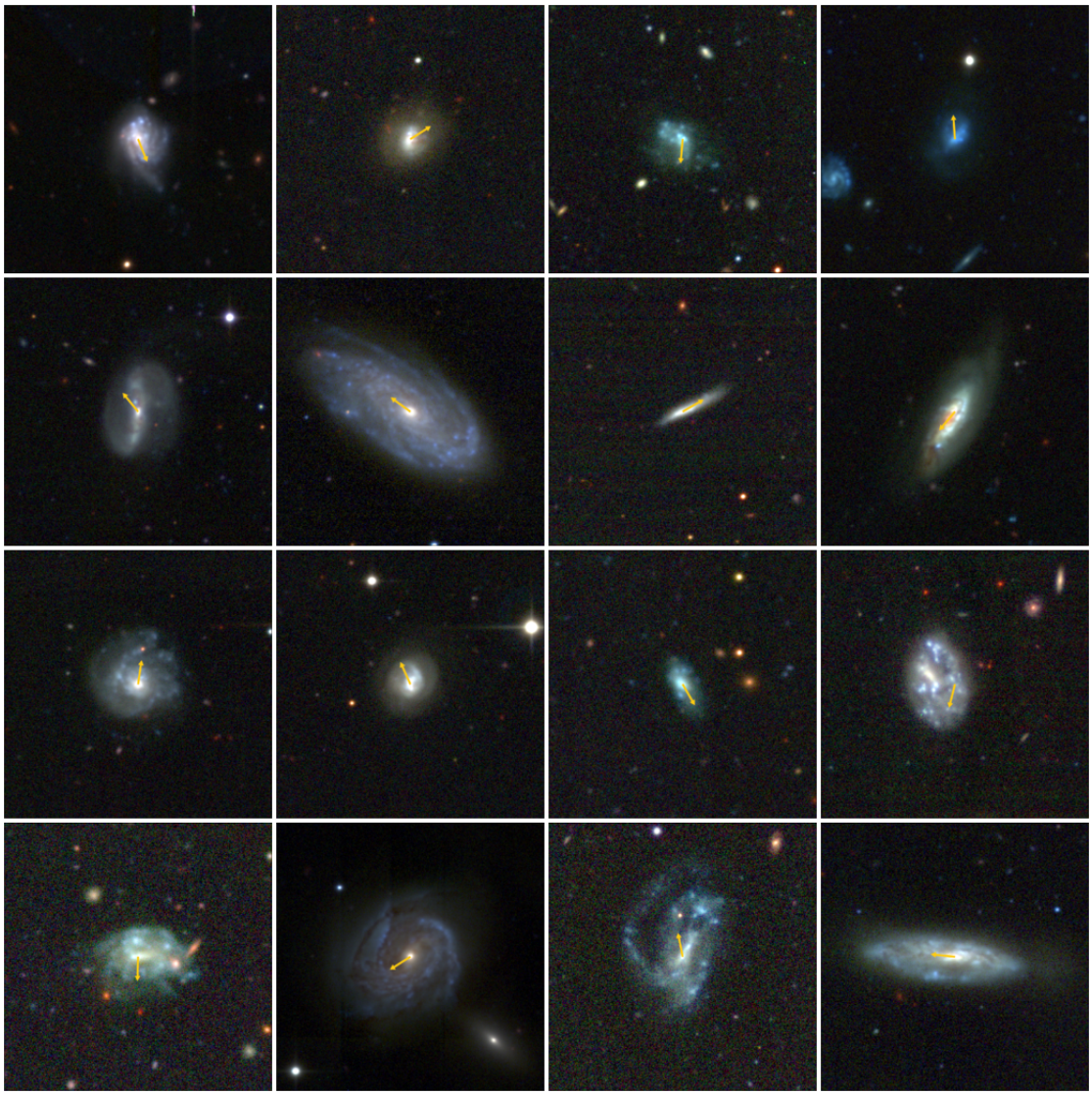

FIGURE 6.9: Continued from Fig. 6.8

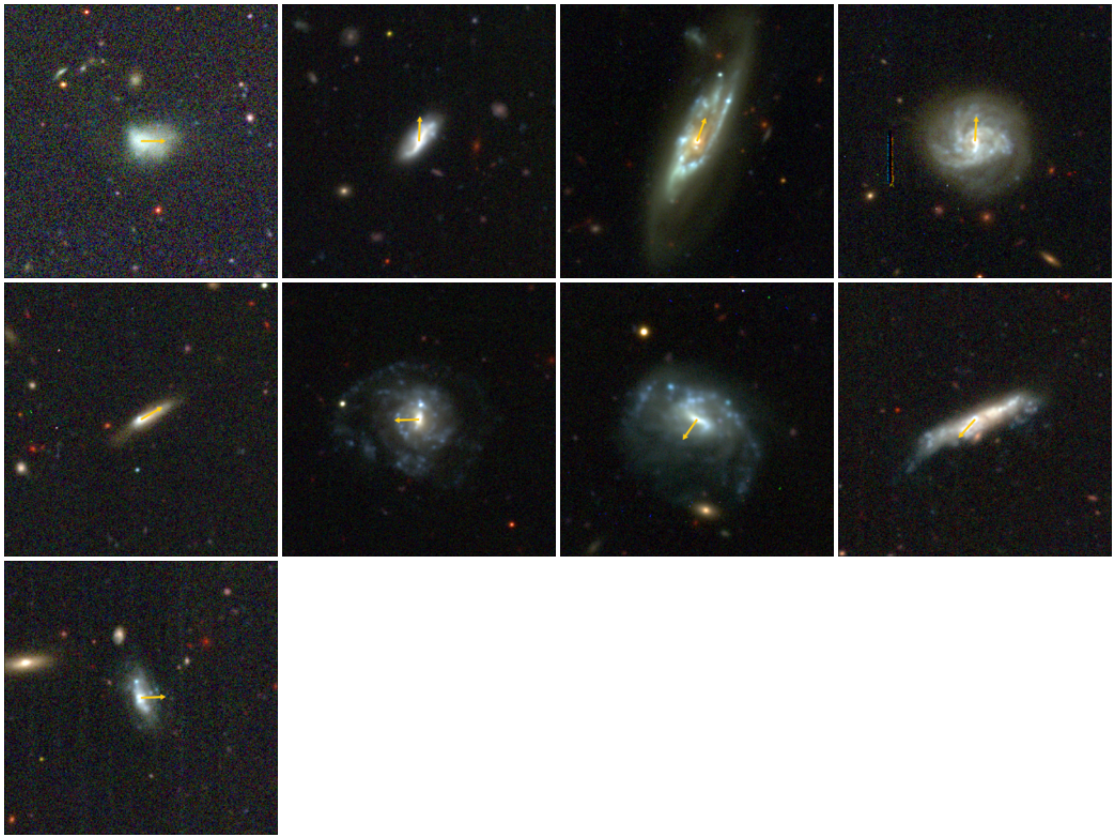

FIGURE 6.10: Continued from Fig. 6.9

7 | Summary and Future Work

7.1 Summary of this Work

Galaxy clusters are extreme environments capable of strongly influencing galaxy properties. However, galaxy clusters are not a homogeneous population, and instead show clear variations in properties like mass/size, richness, dynamical state, X-ray luminosity, etc. When investigating environmentally-driven galaxy evolution, it is important to control for these variations, so that fair comparisons can be made and the underlying physical mechanisms can be explored. In this thesis, I have presented improved methods for characterizing the cluster environment, specifically the dynamical state, as well as a detailed study of the physical mechanisms quenching star formation in galaxy clusters.

In Chapter 2 we compare observational tracers of galaxy cluster dynamical state, with a focus on tracers at X-ray and optical wavelengths. We take X-ray morphology (measured from *Chandra* or *XMM-Newton* imaging) as our "best" proxy for dynamical state, and then test the effectiveness of different optical estimators. By this test, we find that the shape of the galaxy velocity distribution, as measured by the Anderson-Darling (AD) normality test, correlates most strongly with X-ray morphology. We also consider two optical proxies based on the most massive galaxy (MMG), the mass ratio between the most massive and second-most massive cluster galaxies (M_2/M_1), and the offset between the position of the MMG and the luminosity-weighted centre ($\delta_{\rm MMG}$). We find that M_2/M_1 does correlate with X-ray morphology, however less strongly than the AD statistic, but we do not find any evidence for a correlation between X-ray morphology and $\delta_{\rm MMG}$. We also identify relaxed and unrelaxed clusters (Gaussian - G, non-Gaussian - NG) using

the AD test and show that NG clusters have systematically asymmetric X-ray morphologies.

In Chapter 3 we employ the MultiDark-Planck 2 (MDPL2) dark matter simulation to further study the properties of G and NG clusters, and to help interpret the results from Chapters 2 and 4. We project the simulated halos and identify G and NG clusters according their 1D velocity distributions. This allows us to identify G and NG clusters in a similar fashion to observations, while still accessing information exclusive to simulations such as merger and accretion histories. We find that NG clusters have had more recent major mergers and more active accretion of new galaxies relative to G clusters. Additionally, we show that the fraction of NG clusters (relative to the entire cluster population) increases with both cluster mass and redshift. These trends are clear in the simulations, however the differences between G and NG clusters identified in 1D are small. These trends are much stronger when using a sample of NG clusters identified using the full simulation phase space information, showing that projection effects can seriously impact the ability to measure cluster dynamics. Observed trends with cluster dynamics are likely underestimated due to sample impurities introduced by projection.

In Chapter 4 we consider the star formation and morphological properties of satellite galaxies in G and NG systems. After carefully matching G and NG clusters by stellar mass, redshift, and halo mass, we show that there is an excess of low-mass, star-forming galaxies in the central regions of NG clusters compared to G systems. Chapter 4 also explores the prevalence of pre-processing in galaxy groups and clusters. By comparing isolated field galaxies to galaxies in the infall region of groups and clusters, we show that the fraction of galaxies which has been pre-processed is highest for low-mass galaxies which are infalling onto high-mass clusters. This work shows that galaxy star formation has a measurable dependence on cluster dynamics, emphasizing the importance of dynamical classifications for galaxy evolution.

In Chapter 5 we focus on the physical mechanisms driving quenching in galaxy clusters, with a study of the connection between the density of the intracluster medium (ICM) and galaxy star formation. With a sample of Sloan Digital Sky Survey (SDSS) galaxy clusters, along with archival *Chandra* X-ray data, we show that the quenched fraction of satellite galaxies shows a tight correlation with ICM

density. For low-mass galaxies, we present evidence for a broken-powerlaw relation between quenched fraction and ICM density, with an upturn in quenched fraction present at the highest ICM densities. Using a toy model, we show that this upturn in quenching at high ICM density is consistent with predictions from ram pressure stripping. We argue that the results from Chapter 5 are consistent with "slow-then-rapid" quenching for low-mass galaxies, where star formation is slowly reduced by gas depletion until reaching a threshold ICM density, beyond which ram pressure drives rapid quenching.

Finally, in Chapter 6 we perform a search for galaxies undergoing ram pressure stripping in the Coma cluster. With high-resolution Canada-France-Hawaii telescope (CFHT) imaging, we visually identify $\sim$40 ram pressure stripping candidates distributed throughout all regions of the Coma cluster. Based on the direction of observed stripping features, along with the position of stripping candidates in projected phase space, we show that these galaxies are consistent with being stripped on first infall toward the centre of Coma. The stripping candidates show enhanced star formation rates (SFRs), both relative star-forming Coma galaxies and isolated galaxies in the field, which suggests that ram pressure can induce enhanced star formation during the stripping process. Follow-up observations, either in HI or Hα will be critical to confirm these galaxies as undergoing ram pressure stripping.

7.2 Implications

7.2.1 Galaxy Cluster Dynamical State

As shown in Chapter 3, galaxy cluster dynamical state is a tracer of the merger and accretion history of the cluster halo. Readily available in simulations, constraining these properties is observationally challenging, and an accurate characterization of dynamical state provides a tractable method to do so.

The results of this thesis show that the shape of the cluster galaxy velocity distribution is a more reliable probe of dynamical state than proxies based on the MMG. While we found no correlation between X-ray morphology and the offset between the MMG position and luminosity-weighted cluster centre, it is important to note that some studies have found the offset between the MMG position and

the X-ray cluster centre to be a reliable dynamical probe (Lopes et al., 2018). An important take-away from Chapter 3, is that projection effects can seriously impact the ability to observationally measure dynamical state from velocity distributions on a cluster-by-cluster basis. Large samples of G and NG clusters are necessary to overcome the uncertainties introduced by projection effects, giving populations of clusters which are relaxed and unrelaxed, on average. Accurately characterizing dynamical state for a single cluster is significantly more challenging. The velocity distribution is likely unreliable due to projection, however it may be possible to combine multiple dynamical proxies for a more reliable estimator. Depending on the available data, these could include the shape of the velocity distribution, stellar mass or luminosity ratios, MMG offsets, X-ray morphologies, X-ray concentrations, measures of substructure (in galaxies or the ICM), and more.

7.2.2 Star Formation Quenching

In Chapter 5 we present results showing the trend between quenched fraction and ICM density for satellite galaxies in SDSS clusters. The motivation behind this study was the fact that commonly invoked quenching mechanisms in clusters (e.g. ram pressure stripping or starvation) involve interactions between satellite galaxies and the ICM. Therefore insight regarding environmental quenching can be gleaned through a direct study of galaxy star formation as a function of ICM density. We argue that the results in Chapter 5 for low-mass galaxies are consistent with a reduction in star formation driven intially by slow gas depletion (starvation) which is then expedited by ram pressure stripping in the densest regions of the cluster. For intermediate- and high-mass galaxies the observed trend is consistent with solely gas depletion. In Chapter 6 we show that many galaxies in the Coma cluster are currently experiencing ram pressure stripping, especially low-mass galaxies. The enhanced SFRs observed for these stripping candidates demonstrate that ram pressure can induce a temporary enhancement in star formation prior to quenching. This SFR increase has been predicted by simulations of ram pressure stripping (e.g. Steinhauser et al., 2012; Bekki, 2014), and is likely connected to density enhancements in the star-forming gas being driven by the ram pressure interactions. Resolved observations of molecular gas in cluster galaxies will be capable of testing this prediction directly (Jáchym et al., 2019; Moretti et al., 2020).

Despite dichotomies often presented in literature, star formation quenching in galaxy clusters is likely a combination of several different physical mechanisms; and via pre-processing, combinations of different environments. Ram pressure stripping will clearly be most effective in the dense cluster interior, however, before reaching the cluster centre, star formation can still be reduced through gas consumption which cannot be replenished in the cluster environment (starvation). For galaxies which consume their gas reserves very quickly, they may be largely quenched prior to experiencing strong ram pressure. Other galaxies can still be gas rich when approaching the cluster interior, at which point ram pressure stripping may expedite the quenching process (e.g. van der Burg et al., 2018). Additionally, tidal and impulsive galaxy interactions can "puff-up" galaxy gas distributions, allowing gas to be more easily stripped by processes such as ram pressure (Mayer et al., 2006; Chung et al., 2007). Moving forward, instead of advocating for one "favourite" quenching mechanism, it is important to understand how these different physical processes operate in concert and what physical signatures can be observed.

7.2.3 Galaxy Star Formation and Cluster Dynamics

The two primary contributions of this work are: (a) studying observational tracers of cluster dynamical state, and (b) constraining star formation quenching in the cluster environment. These two topics are actually interconnected in important ways. Star formation quenching in clusters is almost certainly a product of galaxy time-since-infall. The longer a galaxy has been part of the harsh cluster environment, the higher the likelihood that that galaxy will be quenched. On average, unrelaxed clusters host galaxies with shorter times-since-infall (see Chapter 3), therefore it could be expected that unrelaxed clusters host more active, star-forming galaxies than more relaxed systems. In Chapter 4 we show that this is the case, and enhanced star-forming fractions are observed in NG clusters relative to G counterparts. This is true even after controlling for the known dependences of star formation on stellar mass and group/cluster mass. There also may be differences in the efficiency of quenching processes in relaxed and unrelaxed clusters. Unrelaxed clusters tend to host underdense ICMs (Popesso et al., 2007; Roberts and Parker, 2017), particularly in the cluster interior, which may

lead to less efficient quenching. That said, predictions have also been made that ram pressure stripping may be *more* effective in unrelaxed, merging clusters (McPartland et al., 2016). The justification is that high infall velocites and dense merger shocks in the ICM may be condusive to ram pressure stripping. All of the examples highlighted above illustrate how star formation quenching can depend on cluster dynamical state, and how one can be used to inform the other.

7.3 Moving Forward

Looking to the future, there are a number of new surveys and new facilities that will continue to advance the work outlined in this thesis.

In Chapter 6 we demonstrated the value of high-quality imaging for identifying galaxies experiencing ram pressure stripping, both through visual classifications and through quantitative morphological estimators. The analysis in Chapter 6 is limited to the Coma cluster, however extending this analysis to more systems will permit constraints on ram pressure stripping as a function of halo mass across groups and clusters. Currently the Canada-France Imaging Survey (CFIS) is imaging thousands of square degrees in the northern sky with MegaCam on the CFHT. This dataset will allow the identification of ram pressure stripping candidates in hundreds of diverse groups and clusters with spectroscopy from the SDSS.

For the past 20 years the most comprehensive X-ray all-sky survey has been the ROSAT All-Sky Survey (RASS), however the depth and resolution of RASS data is not sufficient for quantifying X-ray morphologies and dynamical states for most galaxy groups and clusters. *eROSITA*, the next generation wide-field X-ray observatory, has recently come online and completed an initial all-sky survey[1]. Relative to the RASS, the higher resolution and sensitivity will drastically increase the identified number of X-ray bright groups and clusters, and will also permit the characterization of X-ray morphologies for a subset of these systems. This will drastically increase the number of reliably identified merging and unrelaxed clusters on the sky. A number of merging clusters will also be identified based on radio relics from merger shocks in the ICM, identified by observatories such as the Low-Frequency Array (LOFAR) which will map the entire northern sky. These

[1] `www.mpe.mpg.de/7461761/news20200619`

new surveys and facilities will allow detailed studies of unrelaxed clusters as well as the environmental galaxy evolution taking place in these disturbed systems.

Galaxy star formation is inherently a multiwavelength process, and the signatures of quenching similarly span the electromagnetic spectrum. Important advances in understanding these processes will have to be driven not only by multiwavelength observations, but specifically by multiwavelength observations which are resolved across galaxies. Current instruments such as UVIT, SITELLE, and MUSE provide high-resolution maps of star formation, over large fields of view, which can be complemented by high-resolution observations of cold-gas from ALMA and the VLA. Next generation facilities like CASTOR, JWST, SKA, and ngVLA will continue this effort while making important new progress. This will include advancing our understanding of galaxy evolution in the local Universe, as well as pushing these detailed studies to higher and higher redshift. Ultimately, the end goal is a comprehensive understanding of galaxy evolution and star formation, both as a function of environment and cosmic time.

Bibliography

Bekki, Kenji (2014). *MNRAS* 438.1, pp. 444–462.

Chung, A., J. H. van Gorkom, J. D. P. Kenney, and B. Vollmer (2007). *ApJl* 659, pp. L115–L119.

Jáchym, Pavel et al. (2019). *ApJ* 883.2, 145, p. 145.

Lopes, Paulo A. A. et al. (2018). *MNRAS* 478, pp. 5473–5490.

Mayer, L., C. Mastropietro, J. Wadsley, J. Stadel, and B. Moore (2006). *MNRAS* 369, pp. 1021–1038.

McPartland, Conor, Harald Ebeling, Elke Roediger, and Kelly Blumenthal (2016). *MNRAS* 455.3, pp. 2994–3008.

Moretti, Alessia et al. (2020). *ApJ* 889.1, 9, p. 9.

Popesso, P., A. Biviano, H. Böhringer, and M. Romaniello (2007). *A&A* 461, pp. 397–410.

Roberts, I. D. and L. C. Parker (2017). *MNRAS* 467, pp. 3268–3278.

Steinhauser, D., M. Haider, W. Kapferer, and S. Schindler (2012). *A&A* 544, A54, A54.

van der Burg, Remco F. J. et al. (2018). *A&A* 618, A140, A140.